MEDNARODNA
PODIPLOMSKA ŠOLA
JOŽEFA STEFANA

# 6. ŠTUDENTSKA KONFERENCA MEDNARODNE PODIPLOMSKE ŠOLE JOŽEFA STEFANA

## Zbornik – 1. del

# *6th JOŽEF STEFAN INTERNATIONAL POSTGRADUATE SCHOOL STUDENTS' CONFERENCE*

## *Proceedings – Part 1*



**20. – 22. 05. 2014, LJUBLJANA**

**Zbornik 6. Študentske konference Mednarodne podiplomske šole Jožefa Stefana**
(Proceedings of the 6th Jožef Stefan International Postgraduate School Students Conference)

**Uredniki / Editors:**
Nejc Trdin
Jernej Pavlič
Božidara Cvetković
Nemanja Aničić
Majda Pavlin
Andraž Rešetič

**Fotografije / Photos:**
Nikola Simidjievski

**Založnik / Publisher:**
Mednarodna podiplomska šola Jožefa Stefana, Ljubljana

**Dosegljivo na / Attainable at:**
http://ipssc.mps.si/2014/proceedingsIPSSC2014Papers.pdf

Ljubljana, maj 2014

Konferenco organizira Študentski Svet Mednarodne podiplomske šole Jožefa Štefana
(The Conference is organized by Jožef Stefan International Postgraduate School - IPS Student Council)

CIP - Kataložni zapis o publikaciji
Narodna in univerzitetna knjižnica, Ljubljana

5/6(082)(0.034.2)
378.046-021.68:001.891(497.4)(082)(0.034.2)

MEDNARODNA podiplomska šola Jožefa Stefana. Študentska konferenca (6 ; 2014 ; Ljubljana)
Zbornik [Elektronski vir] : 1. del = Proceedings : part 1 / 6. študentska konferenca Mednarodne
podiplomske šole Jožefa Stefana = 6th Jožef Stefan International Postgraduate School Students' Conference, 20.-22. 05. 2014, Ljubljana ; [organizira študentski svet Mednarodne podiplomske šole Jožefa Štefana = organized by Jožef Stefan International Postgraduate School - IPS Student Council] ; uredili, edited by Nejc Trdin ... [et al.]. - El. knjiga. - Ljubljana : Mednarodna podiplomska šola Jožefa Stefana, 2014

Način dostopa (URL): http://ipssc.mps.si/2014/proceedingsIPSSC2014Papers.pdf

ISBN 978-961-92871-6-3 (pdf)
1. Trdin, Nejc 2. Mednarodna podiplomska šola Jožefa Stefana (Ljubljana)
273807360

# 6. ŠTUDENTSKA KONFERENCA MEDNARODNE PODIPLOMSKE ŠOLE JOŽEFA STEFANA

ZBORNIK - 1. DEL

# *$6^{th}$ JOŽEF STEFAN INTERNATIONAL POSTGRADUATE SCHOOL STUDENTS' CONFERENCE*

*PROCEEDINGS - PART 1*

Uredili / Edited by

Nejc Trdin, Jernej Pavlič, Božidara Cvetković, Nemanja Aničić, Majda Pavlin in Andraž Rešetič

20. - 22. 5. 2014, Ljubljana

## Organizacijski odbor / Organising Committee

Nejc Trdin

Jernej Pavlič

Božidara Cvetković

Nemanja Aničić

Majda Pavlin

Andraž Rešetič

## Redakcijski odbor / Technical Review Committee

Božidara Cvetković

Prof. Dr. Miran Čeh

Dr. Carolina Fortuna

Prof. Dr. Ester Heath

Prof. Dr. Milena Horvat

Dr. Andrej Hrovat

Prof. Dr. Monika Jenko

Prof. Dr. Đani Juričić

Prof. Dr. Spomenka Kobe

Dr. David Kocman

Doc. Dr. Nataša Kopitar-Jerala

Dr. Tina Kosjek

Dr. Primož Kušar

Prof. Dr. Zdravko Kutnjak

Prof. Dr. Darko Makovec

Prof. Dr. Barbara Malič

Doc. Dr. Paul McGuiness

Prof. Dr. Radmila Milačič

Dr. Violeta Mirchevska

Prof. Dr. Nives Ogrinc

Prof. Dr. Veronika Stoka

Prof. Dr. Janez Ščančar

## Beseda predsednika MPŠ

V letošnjem jubilejnem šolskem letu 2013/2014 se je vpisala na Mednarodno podiplomsko šolo Jožefa Stefana - MPŠ že 10. generacija podiplomcev. Do konca leta 2013 je zaključilo s študijem 157 doktorjev znanosti, 29 magistrov znanosti in 24 strokovnih magistrov, kar kaže na to, da je naša podiplomska šola več kot uspešna. Trenutno je vpisanih v tem šolskem letu 142 študentov ter 51 študentov s statusom po zakonu.

Dejstvo je, da se vpisujete na področja delovanja te šole praviloma odlični mladi podiplomci, ki s svojem znanjem, zagnanostjo in dosežki segajo v sam vrh kvalitetnih mladih raziskovalcev. Vaša kvaliteta raziskav se kaže z objavami v uglednih in tudi odličnih mednarodnih revijah. Seveda teh uspehov ne bi bilo brez odličnih mentorjev in somentorjev, ki so prejeli za svoje delo vrsto domačih ter mednarodnih priznanj. Naj omenim še izjemno vzdušje in kolegialne odnose, ki vladajo med podiplomci in njihovimi mentorji. To je posledica tesnega sodelovanja med Institutom Jožef Stefan ter našo podiplomsko šolo, pri čemer imamo na razpolago moderno odlično raziskovalno opremo vključno s Centri odličnosti. Vrhunski kadrovski potenciali in izjemna vpetost v mednarodne povezave na globalnem nivoju omogočajo usposabljanje na najvišji ravni ter prenašanje znanja, pridobljenega na temeljnih in aplikativnih raziskavah, tudi v gospodarstvo. To je misija Mednarodne podiplomske šole ter prispevek k pospešenemu zagonu slovenskega gospodarstva ter hitrejšemu prehodu iz vsesplošne krize v družbo znanja.

Pot do ustanovitve MPŠ je bila dolgotrajna in zahtevna, vendar uspešna. Pričelo se je z razmišljanjem ustanovitve lastne podiplomske šole koncem 90ih let. Po dokajšnih

naporih je Svet za visoko šolstvo Republike Slovenije izdal soglasje za njeno ustanovitev 3.decembra 2003, kar je omogočilo, da so se prvi podiplomski študentje vpisali jeseni leta 2004 na področja nanoznanosti in nanotehnologije, informacijske in komunikacijske tehnologije, ekotehnologije ter s tem povezan menedžment. Ta področja v pretežni meri ni pokrivala univerza, predstavljala pa so in so še vedno moderne usmeritve v svetu. Ustanovitelji te šole so bili poleg Instituta Jožef Stefan še naši industrijski partnerji Gorenje, Kolektor, Salonit in Slovensko zavarovalno združenje, ki so najbolj razumeli potrebe po ustanovitvi te sodobne podiplomske šole. Kasneje so se pridružile šoli tudi druge gospodarske organizacije, Inštitut za kovinske materiale in tehnologije - IMT in prav pred kratkim tudi Nacionalni Institut za Biologijo - NIB.

Današnja predstavitev vaših raziskovalnih dosežkov, že šesta po vrsti, je ponoven dokaz vaše uspešnosti na področju raziskav. Seveda ne smemo pozabiti tudi na odlične publikacije katere ste že mnogi med vami objavili v času študija. Moram omeniti tudi finančna sredstva, saj brez teh si danes ne moremo zamišljati moderne znanosti in iz nje izhajajočih tehnologij ter uspešne konkurenčnosti gospodarstva. Vsa zahvala naj gre Institutu Jožef Stefan, ki s svojim finančnim vložkom v veliki meri omogoča delovanje te šole, da ne omenjamo še enkrat kadrovskega potenciala in odlične raziskovalne opreme, ki je ves čas na voljo.

Slovenija je zapadla v globoko ekonomsko krizo, kateri pa so se v dobri meri izognile države, ki so se pravočasno zavedale pomena vlaganj v odlično znanost in raziskave. Tudi mnoge nove članice EU. Še posebej pa se moramo zavedati, da ekonomsko uspešne države vlagajo velika finančna sredstva v znanost in raziskave in ob tem privabljajo mnoge odlične raziskovalce, pa tudi talentirane podiplomce in dodiplomce na delo in študije za potrebe njihovega nadaljnjega ekonomskega razvoja v tekmi na globalni ravni. Zaradi situacije, v kateri se znašla Slovenija in ki nam je vsem poznana, je nujno, da odgovorni v Republiki Sloveniji končno spoznajo, da brez odličnega znanja in odličnih tehnologij ne bo gospodarskega napredka ter se bomo znašli na samem začelju Evrope.

Mladi ste upravičeni do boljše prihodnosti, kot vam jo ponuja sedanjost! Do novih delovnih mest! Pravico imate, da se vam omogoči uspešno spopadanje z izzivi v domačem okolju, ne pa da iščete izpolnitve svojih ambicij in eksistenčnih možnosti z odhodom v tujino. To desetletje ali še krajša doba bo ključnega pomena za slovensko gospodarstvo ter ekonomsko in politično neodvisnost Slovenije.

Še enkrat bom ponovil, kar sem že pred kratkim rekel: znanje je vrednota, ki omogoča narodu ekonomski razvoj in obstoj. Mladi vrhunski raziskovalci, ki so

pogoj za uspešen gospodarski in vsesplošen razvoj, pa so srce družbe znanja. Očitno so potrebne za to spoznanje globoke družbene spremembe.

prof. dr. Vito Turk
Predsednik MPŠ

## Beseda dekana MPŠ

Mednarodna podiplomska šola Jožefa Stefana (MPŠ) praznuje letos desetletni jubilej svojega delovanja in v njenem okviru že 6. Študentsko konferenco MPŠ.

Vsako jubilejno praznovanje prinaša kak dan veselja. Kaj več pa prinese samo tisti jubilej, ki nas usmerja k pogledu nazaj, da bi bolje začrtali pot naprej.

Na kaj v zadnjem desetletju je MPŠ lahko ponosna? Prav gotovo je to 210 doktorjev in magistrov znanosti, za katere zaposlitev - tudi v več kot dvajsetih drugih državah - ni problem. Odlika so njihovi vrhunski raziskovalni dosežki, med njimi tudi objave v znanstvenih revijah in patentih - visokošolska pravila predpisujejo po eno, doktorji MPŠ jih imajo izjemoma do deset, v povprečju pa tri do pet. Med njimi so tudi objave v tako prestižnih revijah, da celo uveljavljeni raziskovalci ob natisu priredijo praznovanje.

Temu se ob bok postavljajo Študentske konference MPŠ. Njihove visoke odlike so številne. Najprej je to njihova originalnost, saj je bila ta zamisel rojena in gojena na MPŠ ter nima primerjave v visokem šolstvu našega področja. Prav gotovo so odlika tudi odlične predstavitve dosežkov - vse izpolnjujejo tri temeljne zahteve: kakovostno znanstveno poročanje, presojo možnosti za vključevanje dosežkov v gospodarski in socialni razvoj ter opis v takem jeziku, ki je pisan za poučene in nepoučene hkrati. Pisati natančno in strnjeno v takem jeziku je zelo zahtevno, zato je to prispevek k gojenju znanstvene kulture.

Prav posebni odliki vsake Študentske konference sta načrtna predstavitev možnosti in vzpostavljanje načinov za prenos dosežkov v procese dela in odločanja. Tu se prepletajo pristopi temeljnih raziskovalcev in gospodarskih razvojnikov, tu se krešejo

nove ideje in rojevajo razvojne hipoteze, tu se tudi sklepajo poznanstva, včasih celo prijateljstva, ki katalizirajo prenos znanja.

Če pa bi morali izpostaviti največjo odliko teh konferenc, je to prav gotovo skoraj neverjetna samostojnost Študentskega sveta MPŠ, ki snuje, organizira in vodi Študentske konference - od vsakoletnih novih idej, prek pritegovanja podiplomcev in pridobivanja podpore mentorjev, organizacije prispevkov, usklajanja njihove predstavitve, tja do pridobivanja sodelovanja gospodarskih partnerjev. Vse to se ne konča s konferenco in objavo prispevkov. Ambicija seže takoj v analizo doseženega in priprave boljšega.

Študentske konference so prav gotovo pogled nazaj za še boljšo izbiro poti naprej. Zato Študentskemu svetu ob 6. Študentski konferenci iskreno čestitamo!

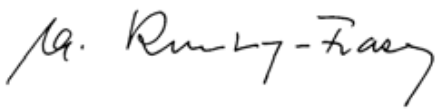

Aleksandra Kornhauser-Frazer
Dekan MPŠ

## Želiš prispevati k trajnostnem razvoju? Spodbudi industrijo s svojo inovacijo!

Po velikem uspehu lanske 5. Študentske konference Mednarodne podiplomske šole Jožefa Stefana, smo se z velikim zagonom in željami po ponovnih presežkih lotili organizacije že 6. Študentske Konference Mednarodne podiplomske šole Jožefa Stefana, ki je namenjena predvsem predstavitvi naših raziskav visokotehnološkim podjetjem in širši publiki, v želji po krepitvi povezav z gospodarstvom. Ker program 6. Študentske konference ravno sovpada z jubilejno 10. letnico naše podiplomske šole, smo v tem letu prvič konferenco organizirali v treh dneh. S tem smo zmanjšali natrpanost urnika konference in tudi naredili prostor za dodatne dogodke ob jubileju.

Ob začetku študijskega leta smo ponudili knjižico s splošnim opisom študentske konference, njenim namenom, dosedanjimi nagrajenci, ter navodili za pripravo prispevkov za sodelovanje na konferenci. V sredini študijskega leta smo organizirali tudi sestanek z mentorji, na katerem smo jim podrobno predstavili študentsko konferenco, zahteve na konferenci in poslanstvo le-te. Prav tako smo tudi vsebino konference promovirali na socialnih omrežjih, z željo po čim večji udeležbi. Vse te zgodnje priprave so se obrestovale, saj smo letos prejeli 31 prispevkov. S tem smo dobili tudi potrditev študentov, da se zavedajo pomembnosti konference in si želijo sodelovanja s podjetji. Študent, ki želi sodelovati na konferenci, mora poslati prispevek v A5 formatu v dolžini 5 do 9 strani s povzetkom, ki je razumljiv širši javnosti, in pripraviti predstavitveni poster. Zaželeno je, da študent v svojem delu poudari morebitno praktično uporabo v industriji oz. drugih sektorjih gospodarstva. S tem skušamo študente dodatno motivirati in jim dati možnost lastnega stališča in opredelitve raziskovalnega problema, s katerim se ukvarjajo. Na konferenci, poleg

naših študentov, sodelujejo tudi dodiplomski študentje in pa študentje drugih fakultet, katerih raziskovalno področje je povezano z našo šolo ali pa z Institutom Jožef Stefan. Namen konference ni samo spodbuditi študente k predstavitvi svojega dela, pač pa tudi v njih vzpodbuditi podjetniško stran raziskovalnega dela. Vsako leto se na konferenco povabi ugledna slovenska podjetja, ki predstavijo svoja stališča in možnosti morebitnega sodelovanja. To je enkratna priložnost, da se podjetje, študent in mentor med seboj povežejo in vzpostavijo morebitno sodelovanje, ki je v trenutnem času ekonomske krize tako zelo pomembno.

Pri tako številnih prispevkih smo želeli zagotoviti visoko kvaliteto le teh, zato smo v letošnjem letu ponovno povečali redakcijski odbor, ki je štel kar 22 članov. Vsak prispevek je bil temeljito pregledan iz strani vsaj enega člana redakcijskega odbora. Recenzenti so se poleg kakovosti prispevkov, tako plakatov, kot člankov, osredotočali tudi na pravilnost, razumljivost besedila in še posebej splošnega povzetka. Splošni povzetek je namenjen širšemu občinstvu, saj je le ta bistvenega pomena za razumevanje naših raziskav s strani podjetij in s tem posledično vzpostavljanje stikov.

Za še dodatno spodbujanje študentskih idej smo letos pripravili tri vabljena predavanja z naslovom »Od ideje do uspeha na trgu«, kamor smo povabili tri slovenska podjetja. V bloku predavanj se bodo predstavile osnovne funkcionalnosti podjetniških inkubatorjev, ter ponujeni servisi takšnih ustanov. Pokrilo se bo vsa teoretična vprašanja snovanja podjetja od ideje, pa vse do končne oblike podjetja, ki uspeva na trgu. Za konkretne probleme pri funkcioniranju podjetja, pa nam bodo na voljo predstavniki dveh podjetij, ki sta začeli z idejo, trenutno pa žanjeta uspehe na ne samo slovenskem, ampak tudi na svetovnem trgu.

Konferenca je idealno sredstvo za samo promocijo šole, tako preko spletnih socialnih omrežij, kot tudi na osebni ravni. S pomočjo konference se študenti naše

šole večkrat pojavijo v kakšnem časopisnem ali radijskem intervjuju, kar kaže na to, da ima šola res kvalitetne študente in da šola sama pridobiva na prepoznavnosti.

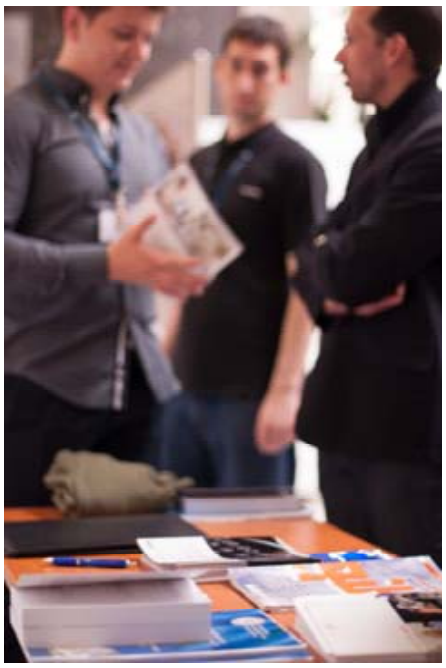

Za tako uspešno konferenco bi se radi v prvi vrsti za sodelovanje in zaupanje zahvalili študentom in njihovim mentorjem, saj njihovi prispevki zelo spodbujajo sodelovanje z gospodarstvom in brez teh prispevkov, konferenca nebi obstajala. Zahvala gre tudi sodelujočim podjetjem, ki so kljub težkim časom pokazala veliko željo za sodelovanje. Brez njih bi konferenca stala na finančno šibkih temeljih, z njimi pa smo lahko pripravili konferenco na visokem nivoju. Posebna zahvala gre še celotnemu osebju Mednarodne podiplomske šole Jožefa Stefana za vso pomoč in podporo. Posebej bi se radi zahvalili dekanji, prof. dr. Aleksandri Kornhauser-Frazer, ki ogromno prispeva k sami konferenci, saj ima odlično vizijo in ideje za sodelovanje z gospodarstvom. Za povezovanje z gospodarstvom bi se radi zahvalili tudi dr. Emilu Rojcu, saj je skrbno kontaktiral podjetja in jih vabil k sodelovanju na konferenci. Zahvalili bi se tudi Tadeji Samec in Maši Matijašević, saj sta nam ves čas nudili veliko podporo pri doseganju zastavljenih ciljev. Nenazadnje pa se zahvaljujemo še članom redakcijskega odbora, ki so temeljito pregledali vse prispevke in s tem pripomogli k višanju nivoja konference.

Uredniški odbor

Kazalo (Table of Contents)

# Ekotehnologija (Ecotechnology)

# Automated method for dissolved gaseous mercury (DGM) measurements

**Ermira Begu**[1, 2], **Jože Kotnik**[1], **Milena Horvat**[1, 2]

[1] Jožef Stefan Institute, Department of environmental Sciences, Jamova 39, Ljubljana 1000, Slovenia

[2] Jožef Stefan International Postgraduate School, Ljubljana, Slovenia

ermira.begu@ijs.si

**Abstract.** Dissolved gaseous mercury (DGM) in natural water includes elemental mercury ($Hg^0$) and dimethyl mercury (DMeHg). $Hg^0$ is the main component (>95%), while DMeHg is unstable and present only deep waters. Due to low water solubility (about 60 μ g/L at 25 °C) and high volatility, $Hg^0$ evaporates from water surfaces and enters into global atmospheric mercury pool. Therefore, accurate measurements of dissolved $Hg^0$ of high importance in global mercury biogeochemical cycle. Dissolved $Hg^0$ is not stable in aqueous solutions, therefore the timing of analysis is of crucial importance. Ideally, continuous measurements with sufficient sensitivity, precision and accuracy would best fit the purpose. In this study, a comparison of manual and automated methods has been performed. The agreement between the methods is relatively good, although the manual method tends to produce slightly higher results (10 to 30%) in the concentration range of 20 to 1500 pg/L. Further improvements of the automated methods is under investigation. Except natural environments, very important application of automated DGM measurements is in the coal burning power plant sector equipped with the wet flue gas desulphurisation equipment (WFGD). Measurements of DGM can be used as a diagnostic tool to control the reduction of $Hg^{2+}$ to elemental Hg which may consequently lead to the emissions of $Hg^0$ through the stack gases to the atmosphere.

**Keywords**: Dissolved gaseous mercury, automated method, natural environments, wet flue gas desulphurisation equipment

# 1 Introduction

Mercury exists in different chemical forms in the environment. Being a global pollutant, the understanding of mercury species transformations and an accurate monitoring of these species and transformations are very important for reliable risk assessment. The chemical form of Hg in natural environments depends on redox and pH conditions, as well as on the concentrations of inorganic and organic complexing agents [1]. It has been estimated that the natural concentration of mercury in marine waters varies from 0.5 ng/L to 3 ng/L, while in estuaries and precipitation it varies from 2 ng/L to 15 ng/L. Transformations of Hg from one form to another plays an important role in the biogeochemical cycle of Hg in aquatic environments [2]. The most important mercury species in the aquatic environment playing an important role in biochemical mercury cycle are reactive mercury (RHg), dissolved gaseous mercury (DGM) and MeHg. DGM consists of total mercury gaseous forms, elemental mercury ($Hg^0$) and dimethylmercury (DMeHg) [1]. Due to its high Henry's law constant and presence in the atmosphere elemental mercury is basically the primary constituent of DGM (about 95 %). In marine waters, represents 10 to 30 % of total Hg. DGM concentrations vary significantly in space and time [3]. Whilst DMeHg is reported to be the dominant organic form of Hg in deeper ocean waters [1]. Several studies have shown that photoproduction [4, 5] and bacterial activity [6] are probably the main sources of volatile $Hg^0$ in surface waters [7]. In open surface freshwater, $Hg^{2+}$ reduction is especially important to Hg cycling due to the evasion of the produced DGM to the atmosphere, particularly on windy summer days [8].

Intensive tectonic activity and geological anomalies may also be an important source of $Hg^0$ especially in the Mediterranean which is tectonically very active [1]. Because of the complex behaviour of $Hg^0$ in aqueous systems and the low concentrations, the DGM determination in non-contaminated surface waters remains a challenge. Very sensitive methods are needed to accurately measure DGM. Existing methods for DGM determination in addition to others, differ from the purging time of the sample, volume of the sample used and the volume of bubbling system [1, 2, 9, 10]. Manual methods have proved so far to be robust and to provide reliable data. Due to dynamic changes of the presence of DGM in time and space, continuous measurements are preferable to manual spot sample analysis.

The most common manual analytical methods for DGM are based on purging of aqueous samples and pre-concentration of $Hg^0$ onto gold traps followed by detection using cold vapour atomic fluorescence spectrophotometry (CV AFS). On the other hand, the automated methods are based on continuous flow of the water sample into the gas liquid separator and the purged $Hg^0$ is continuously swept into the detector (such as cold vapour atomic absorption spectrophotometry – CV AAS) or pre-concentrated on gold in defined short term intervals and subsequently measured by detectors based on absorption or fluorescence principles (CV AAS/CV AFS). The main sources of errors in these methods are related to sampling and calibration of the instruments. Calibration provides the evidence of traceability and comparability in time and space. In this study a comparison of manual and automated method for DGM measurements was performed.

# 2 Experimental

## 2.1 Manual method description

Measurements for DGM were made in double amalgamation system followed by CV AFS detection using Tekran detector, model 2500. The pre-concentration of $Hg^0$ was achieved by gold traps.

The manual method used for $Hg^0$ determination consisted of sampling, purging and measurement steps. 50 to 100 mL of sample was purged in a borosilicate glass purging vessel with a frit by Hg free $N_2$ with a flow of 300 - 400 mL $min^{-1}$. Samples were purged for 10 min and Hg was amalgamated onto sampling gold trap which was then transferred to a double amalgamation system. Hg on sampling trap was then thermally desorbed (300 - 500 °C) for 30 sec into flow of Ar (60 mL $min^{-1}$) to permanent gold trap. Further Hg was thermally desorbed again (heating for 30 sec at the same temperatures) and detected by cold vapour atomic fluorescence spectrometer (Tekran, model 2500). The system was calibrated by gas phase Hg ($Hg^0$) [11] kept at about 4 °C (Tekran, Model 2505, mercury vapour calibration unit). A certain aliquot of $Hg^0$ was transferred with gas-tight syringe (Hamilton, respectively 10, 25 and 50 μL syringes were used) into the double amalgamation system through a septum. Schematic presentation of the system used is presented on Figure. 1.

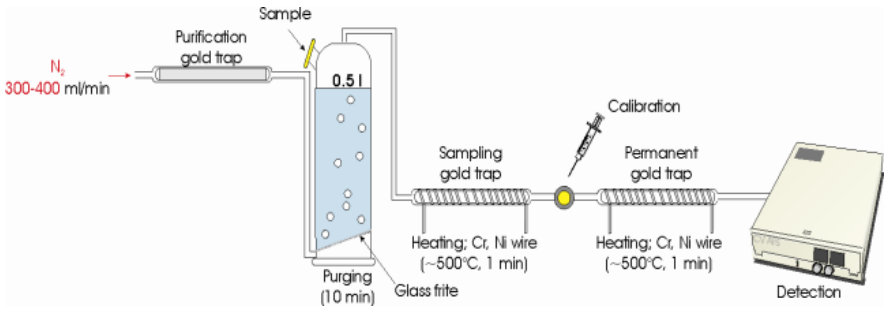


**Figure 1**: Presentation of system used for DGM determination [1, 16]

A soda lime trap was used between the bubbler system and the collection trap (installed upstream the bubbler) to avoid water vapours generated by the bubbling of the sample to go onto the gold trap causing in this way interferences with our measurements and also the so called passivation of gold traps.

## 2.2 Automated method description

Automated method used for DGM measurements, uses an opposite flow bubbler (gas/liquid separator or extractor). The working principle of the mentioned device consists in an opposite flow system, where a constant flow of mercury-free air is purged via a glass frit through the bubbler. The system consists of a smaller plexi glass cylinder attached inside a larger one. A constant flow of water sample is entering the top of the inner cylinder and leaving on the top of the outer one. Through the glass frit in the bottom of the inner cylinder, a constant flow of Hg-free air is entering the system and purges the sample in the opposite direction [12]. An equilibrium concentration of the $Hg^0$ concentration in the outgoing sample water is established and is represented as the $Hg^0$ equilibrium concentration in the outgoing air in the top of the inner cylinder according to Henry's law equilibrium [13].

The contact time between the air and the water is important to establish the equilibrium air-water. The contact time can be adjusted by regulating the flow rate of water and the air flow rate. The concentration of $Hg^0$ in the outlet of the inner cylinder, was measured with the Hg instrument, Lumex and UT 3000. A soda lime trap was used between the bubbler system and the inlet of the detector used. For the measurements, 2 different types of detector were tested: Lumex which is based on a atomic absorption (AAS) principle with a Zeeman background correction and UT

3000 which is based on a single gold amalgamation step with a AAS detection. The DGM concentration is calculated using the following equation (1) [12, 13, 14]:

$$— \quad (C_a - C_a^0)\frac{r_a}{} \tag{1}$$

Where $C_w^0$ is the concentration of the $Hg^0$ in the outgoing sample water; $C_a$ is the concentration in the outgoing air in the top of the inner cylinder; $r_a$ is the flow of air and $r_w$ is the flow of water.

A simplified picture of the automated device is given in the Figure 2:

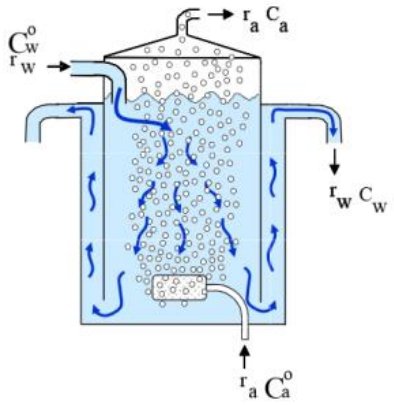


**Figure 2**: Automated system working principle [15]

Tap water was used to conduct the experiment. The purpose of the experiment was to monitor DGM concentration close to natural conditions. For this reason, different volumes of artificial saturated Hg water were introduced to the system constantly by using a peristaltic pump. A 5 litre bottle was saturated with $Hg^0$. Appropriate dilutions were to match concentrations of DGM in the range between 20 and 1500 pg/L. In parallel, aliquots of water samples were taken in the inlet of the bubbling system and measured in the manual method for comparison purpose. In the automated system, the detectors are measuring the concentrations of DGM in the outlet gas of the bubbler in ng/m$^3$. The latter is further converted in pg/L using Equation 1.

## 3 Results and discussion

The data collected from the comparison of both methods is presented below and the degree of agreement between measurements is evaluated.

In the automated method, different air: water rations were used, different sampling time, different Hg amounts were introduced to the system (this is why we were able to make an evaluation of the correlation between the methods), and different detectors were used. While, for the manual method, the standards procedure was followed (as described in the section 1.1.1). Both methods showed high precision of the data obtained, good reproducibility and repeatability. Also, the blanks of the manual system were always under control and constantly very low with low limit of detection ($LOD_{manual}$ = 3 pg)

The Figures 3, 4, 5 and 6, show the comparison between the results obtained with the manual and automated method by using 2 different detectors, different Hg concentrations measured in different days. In general, a good correlation between the methods was observed, except for the results present in Figure 3, where Lumex was used as a detector. At higher concentrations the agreement of the results was relatively poor. Moreover, the results obtained by the manual method are systematically higher in most cases. We should keep in mind that the equation 1 is quite complicated since it takes in account a lot of parameters and small changes can lead to differences. We suspect that the systematic error can be due to unaccountable factors in equation 1.

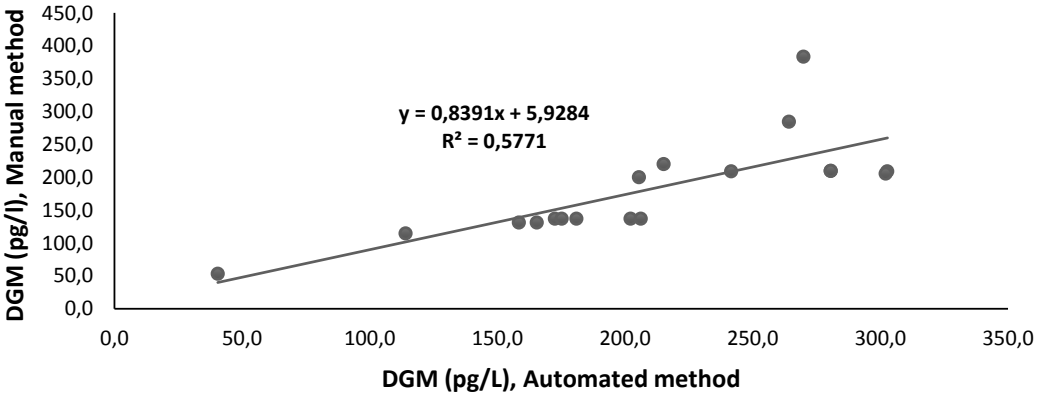


**Figure 3**: Comparison of the results when ***Lumex*** detector is used (air: water ratio is 2.1/2.7)

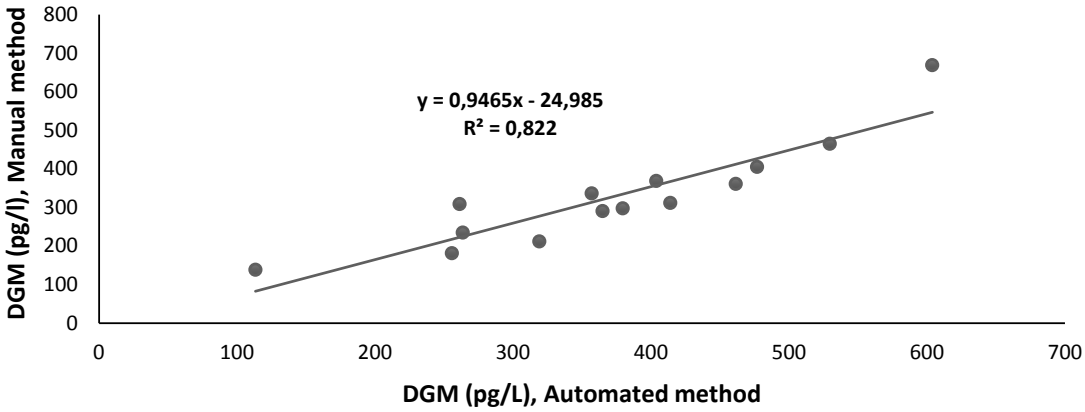


**Figure 4**: Comparison of the results when ***UT 3000*** detector is used (air: water ratio is 2.8/2.8)

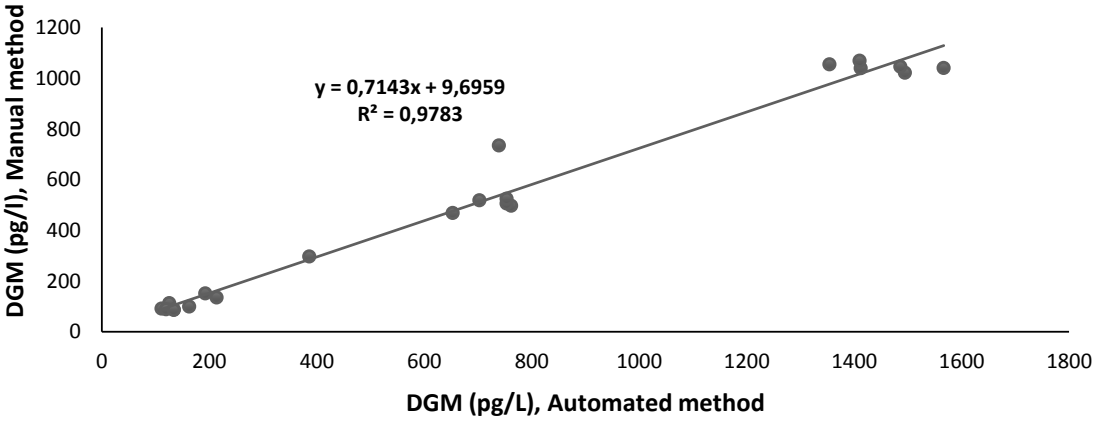


**Figure 5**: Comparison of the results when ***UT 3000*** detector is used (air: water ratio is 3.9/2.9)

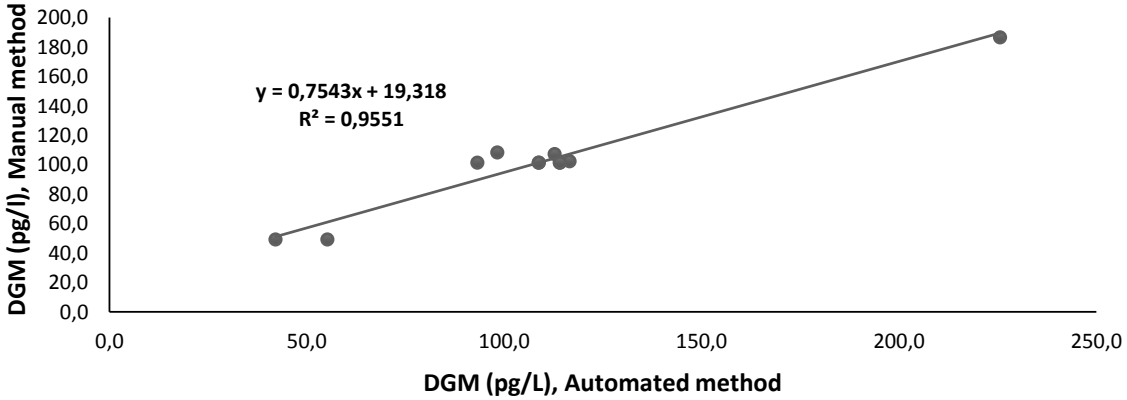


**Figure 6**: Comparison of the results when ***UT 3000*** detector is used (air: water ratio is 2.7/1.8

A comparison of DGM concentrations obtained by manual and automated methods and the stability of the two methods within the working day (8 hours) are presented in Figure 7. Each couple of bars shows the comparison of DGM concentration for the same sample, measured in the same day, at certain time frequency along the day, under the same conditions using both methods.

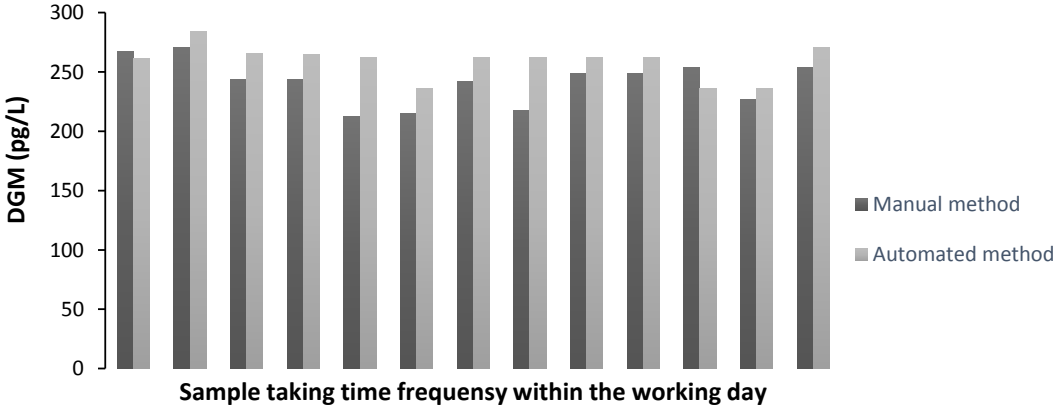


Figure 7: Comparison of the results when ***Lumex*** is used (air: water ratio is 2.3/2.7)

The concentration of the DGM is rather stable and the comparison between the automated and manual method are good.

The repeatability of the measurements for the manual method expressed as repeatability standard deviation, resulted to be 19 (with a relative standard deviation of 8%) while for the automated method, about 14 (with a relative standard deviation of 5%).
The work is still in progress.

## 4 Conclusions

The main parameter affecting the automated method performance is the air: water flow ratio of the gas liquid separator. This is the ratio which determines the necessary time for the equilibrium to be reached. Having a ratio close to 1, assures comparable results between the detectors for different concentrations introduced in the system. However, the results obtained from the manual system for the same sample, are systematically higher for 10 to 30 %, which might be due to unaccounted factors in Eq. 1. Further development of a method is planned.

# References:


[1] Horvat M., Kotnik J., Logara M., Fajon V., Zvonaric T., Pirrone N.: Speciation of mercuryin surface and deep-sea waters in the Mediterranean Sea, *Atmospheric Environment, 2003*

[2] Wangberg I., Schmolke S., Schager P., Munthe J., Ebinghaus R., Iverfeldt A.: Estimates of air-sea exchange of mercury in the Baltic Sea, *Atmospheric Environment, 2001*

[3] Rolfhus K. R. and Fitzgerald W. F.: The evasion and spatial/temporal distribution of mercury species in Long Island Sound, CT-NY. *Geochimica et Cosmochimica Acta, 2001*

[4] Amyot M., Mierle G., Lean D. R. S., McQueen D. J.: Sunlight induced formation of dissolved gaseous mercury in lake waters, *Environ. Sci. Technol. 1994*

[5] Qureshi A., O'Driscoll N., Macleod M., Neuhold M., Hungerbuhler K.: Photoreactions of Mercury in Surface Ocean Water: Gross Reaction Kinetics and Possible Pathways, *Environ. Sci. Technol., 2009*

[6] Fantozzi L., Ferrara R., Frontini F.P., Dini F.: Dissolved gaseous mercury production in the dark: Evidence for the fundamental role of bacteria in different types of Mediterranean water bodies, *Science of the total environment, 2009*

[7] Costa M., Liss P.S.: Photoreduction of mercury in sea water and its possible implications for Hg0 air–sea fluxes, *Marine Chemistry, 1999*

[8] Gardfeldt K., Sommar J., Ferrara R., Ceccarini C., Lanzillotta E., Munthe J., Wangberg I., Lindqvist O., Pirrone N., Sprovieri F., Pesenti E., Stromberg D.: Evasion of mercury from coastal and open waters of the Atlantic Ocean and the Mediterranean Sea, *Atmospheric Environment, 2003*

[9] O'Driscoll N., Siciliano S.D., Lean D.R.S.: Continuous analysis of dissolved gaseous mercury in freshwater lakes, *The Science of the Total Environment, 2003*

[10] Lindberg S.E., Vette A.F., Miles C., Schaedlich F.: Mercury speciation in natural waters: Measurement of dissolved gaseous mercury with a field analyzer, *Biogeochemistry, 2000*

[11] Brown R. and Brown A.: Accurate calibration of mercury vapour measurements, *The Analyst, 2008*

[12] Andersson M. E., Gardfeldt K., Wangberg I.: A description of an automatic continuous equilibrium system for the measurement of dissolved gaseous mercury, *Anal Bioanal Chem, 2008*

[13] Andersson M. E., Gardfeldt K., Wangberg I., Stromberg D.: Determination of Henry's law constant for elemental mercury, *Chemosphere, 2008*

[14] Nerentorp M., Gardfeldt K., Wangberg I.: Comparison of two measurement methods of dissolved gaseous mercury concentrations and estimations of supersaturation grade and mercury fluxes during a research campaign at the Mediterranean Sea, *EDP Sciences, 2013*

[15] Wangberg I., Gardfeldt K.: Measurement technique allowing continuous automatic determination of DGM in oceanic surface water, *International Workshop on Mercury in the marine environment: A global metrology challenge, 2011*

[16] Gardfeldt K., Horvat M., Sommar J., Kotnik J., Fajon V., Wangberg I., Lindqvist O.: Comparison of procedures for measurements of dissolved gaseous mercury in seawater performed on a Mediterranean cruise, *Anal Bioanal Chem., 2002*

## For wider interest

Mercury is a global pollutant. The global cycle of mercury includes the interactions of mercury between sediments-water-air. In natural aqueous environments it is found in very low concentration. However, the evasion of elemental mercury from surface ocean water to the atmosphere represents an important source of Hg in the environment, after the industrial settings which are so far the biggest source. Its availability in aqueous samples is affected by a lot of factors such as light, temperature, bacteria and tectonic activity. Although the manual methods have shown to give reliable data, in order to follow the daily variations of mercury oxidation/reduction reactions which leads to mercury loss/production from such systems, automated systems are needed which provide continuously data.

The presented automatic system can be applied in the industry, especially in thermo power plants which use a wet flue gas desulfurization technology (wet FGD) for removal of Hg from the flue gases. Having the detailed knowledge of oxidation/reduction reactions of DGM occurring in the wet FGD, would be of great help in improving the capturing of Hg in these systems, and thus reducing in the emission in the atmosphere.

# First worldwide interlaboratory study on cytostatic compounds in aqueous samples

**Marjeta Česen**[1,2], **Tina Kosjek**[1,2], **Ester Heath**[1,2]

[1] Department of Environmental Sciences, Jožef Stefan Institute, Jamova 39, 1000 Ljubljana, Slovenia

[2] Jožef Stefan International Postgraduate School, Jamova 39, 1000 Ljubljana, Slovenia

marjeta.cesen@ijs.si

**Abstract.** Increasing consumption and toxicity of cytostatic drugs raises concerns about their presence in the environment. In the absence of certified reference materials, interlaboratory comparisons are necessary if laboratories are to have confidence in their analytical abilities. The objective of this study was to perform an interlaboratory comparison to determine cyclophosphamide, ifosfamide, methotrexate and etoposide in surface water, wastewater and hospital wastewater. Laboratory performances were evaluated using z-score values, mean and median values, standard deviations (σ), repeatability and reproducibility. Overall, sample preparation was satisfactory. The smallest absolute differences between spiked values and participant's results were observed in surface waters. Repeatability was highest for methotrexate in all matrices and for three laboratories using LC-MS/MS (CV ≤ 12 %). Overall reproducibility was poor (CV: 27 % - 143 %) with the exception of MTX in sample C (CV: 8 %). This may be justified by the low number of participating laboratories.

**Keywords**: interlaboratory study, cyclophosphamide, ifosfamide, etoposide, methotrexate, surface water, wastewater, hospital effluent

## 1 Introduction

Cytostatic compounds are a group of pharmaceuticals used to treat cancer patients (chemotherapy) by either inhibiting or preventing the proliferation of cancer cells. Once administered and further excreted, they can enter the environment *via* municipal wastewater and surface waters. Cytostatics are highly hazardous

compounds and for that reason deserve special attention since they have the potential to exhibit adverse effects on non-target organisms including cytotoxicity, genotoxicity, mutagenicity and teratogenicity. This means that accurate and precise analysis of these compounds in the environment is necessary if they are to be monitored and controlled. Currently, only a limited number of laboratories are analysing these compounds [5].

Laboratories usually check the accuracy and precison of their methods by analysing certified reference materials (CRMs). In the absence of CRMs, an interlaboratory exercise can be performed in which participating laboratories determine some characteristic, e.g. the concentration of analyte in one or various homogeneous samples under documented conditions [1]. The results from such laboratory performance studies are of crucial interest for laboratories as these provide clear information of their measurement capabilities with respect to other laboratories and leads to improved quality of analytical results. Several interlaboratory studies of pharmaceutical residues in the environment have been published [2,3,4], but none regarding cytostatic compounds. The aim of this study was to perform an interlaboratory exercise for determining four commonly prescribed cytostatic drugs: cyclophosphamide (CP), ifosfamide (IF), etoposide (ETO) and methotrexate (MTX) in natural and wastewaters.

# 2 Experimental

## 2.1. Experimental design, sample collection and preparation

The participating laboratories were from Czech Republic, The Netherlands, Singapore, Slovenia, Spain (2 laboratories) and the UK. Each laboratory was assigned a unique code number: 1, 2, 3, 4, 6, 8 and 9. Three different types of matrices were sampled including the following: i) surface river water at a location downstream from a wastewater effluent outflow (A); ii) wastewater effluent from a wastewater treatment plant (D) and iii) effluent from a hospital (oncological ward) wastewater (B: non-spiked sample, C: spiked sample). Samples were collected in polyethylene containers, filtered (0.5 μm glass-fibre filters) and homogenized. Compounds of interest included cyclophosphamide (CP), ifosfamide (IF), etoposide (ETO) and methotrexate (MTX). All samples, except B, were spiked with selected

compounds at expected environmental and wastewater levels (Table 1) [5]. Frozen samples were then shipped on dry ice to the participating laboratories.

**Table 1: Spiking levels of CP, IF, ETO and MTX (ng $L^{-1}$) in various matrices.**

| Sample/Compound | CP | IF | ETO | MTX |
|---|---|---|---|---|
| **A** | 53 | 33 | 52 | 31 |
| **B** | * | * | * | * |
| **C** | 5239 | 394 | 3420 | 1141 |
| **D** | 23 | 55 | 127 | 432 |

**Note 1: *Non-spiked samples.**

Each participant received four 0.8 L samples (A, B, C and D). The laboratories were asked to filter the samples (0.45 μm) and extract them using solid phase extraction (SPE) within one week after the sample receipt. They were also requested to perform at least two independent analyses and submit the results within two months. Homogeneity of samples was checked for CP, IF and MTX by means of the Chi-square test using Equation 1:

$$\Sigma \text{———} \quad \text{(Equation 1)}$$

Where *Oi* represents the mean concentration of two parallels in each sample and *Ei* is the mean concentration of each batch containing 10 samples. Null hypothesis ($H_0$) says that homogeneity of samples is achieved and alternative hypothesis ($H_1$) says that homogeneity of samples is not achieved. When $\chi^2_{tab}$ ($\alpha$=0.05) is higher than $\chi^2_{exp}$, then $H_1$ is rejected or $H_0$ is accepted and *vice versa.* For the Chi-square test, 10 samples of each sample type (A, B, C and D) were sampled randomly and were analysed in two parallels. Stability of the compounds of interest (CP, IF, MTX and ETO) in aqueous samples has been studied by Negreira et al. [6]. Their results show that the selected compounds are stable for at least 1 month at - 20 °C even in complex matrices like wastewaters.

## 2.1 Chemicals and sample preparation

CP and IF were obtained from Sigma Aldrich (Steinheim, Germany), MTX was obtained from TOCRIS Biosciences (Ellisville, USA) and ETO from Santa Cruz Biotechnology (Heidelberg, Germany). The solvent DMSO was obtained from Sigma Aldrich (St. Luis, USA).

Chemical analysis was performed by either liquid or gas chromatography (LC or GC) coupled to mass (MS) or tandem mass (MS/MS) spectrometry. Table 2 shows the different analytical techniques and compounds analysed. In total 3, 4, 6 and 7 laboratories submitted results for MTX, ETO, IF and CF, respectively. All analytical methods included SPE for sample preconcentration. Laboratory 9 derivatizated their sample extracts prior to chemical analysis by GC-MS.

**Table 2: Applied analytical methods of participants for their selected compounds.**

| LAB CODE | 1 | 2 | 3 | 4 | 6 | 8 | 9 |
|---|---|---|---|---|---|---|---|
| TECHNIQUE | LC/ MS-MS | LC/ MS-MS | LC/ MS-MS | UPLC/ MS-MS | LC/ MS-MS | LC/ MS-MS | GC/ MS |
| COMPOUNDS | CP, IF, ETO MTX | CP | CP, IF, ETO | CP, IF, MTX, ETO | CP, IF, MTX, ETO | CP, IF | CP, IF |

## 2.2 Statistical parameters

Statistical evaluation was performed using MedCalc Software and Excel 2010. Outlier detection was performed by calculation of z-score values for each data received according to Equation 2, where $x_{lab}$ is the corresponding laboratory mean, $x_o$ is the known spiked concentration or, if unknown (as in sample B), the average concentration measured by the participating laboratories, and $\sigma_0$ is the corresponding standard deviation:

——— (Equation 2)

Results with calculated z-values higher than 3 would be directly excluded from further statistical analysis. For suspect outliers (z-score values were between $2.0 \leq |z| \leq 3$), a further Q test was applied (Equation 3):

—— (Equation 3)

Where gap is the absolute difference between the suspected outlier value and the closest number to it when arranged in increasing order and range is the difference between maximal and minimal values. When $Q_{exp}$ is higher than $Q_{tab}$, ($\alpha$=0.05), then this value is referred as an outlier.

After excluding any outliers the following statistical parameters were calculated for each series of samples and each selected compound: the mean and the median values, standard deviations ($\sigma$), repeatability and reproducibility. Repeatability was individually determined for each laboratory separately as the CV (Coefficient of

Variation, in %), which corresponds to the ratio between the standard deviation of the laboratory's measurement and its mean concentration (Equation 4):

$$CV\ (\%)\ = 100\ \times\ \frac{\sigma lab}{x lab} \quad \text{(Equation 4)}$$

Reproducibility was determined as the CV corresponding to the ratio between the standard deviation of the mean values reported by the various participating laboratories and the corresponding mean concentration for each compound and for each sample.

## 3 Results and discussion

Homogeneity was proved for all samples (A, B, C and D) using the Chi-square test on selected compounds (CP, IF and MTX). In total 219 data were received including parallels, outliers and <LOD values. The obtained results of z-score values and Q test gave 3 outliers (outliers are circled in Figure 1). These outliers all belong to the three parallel measurements performed by laboratory 3 on sample B.

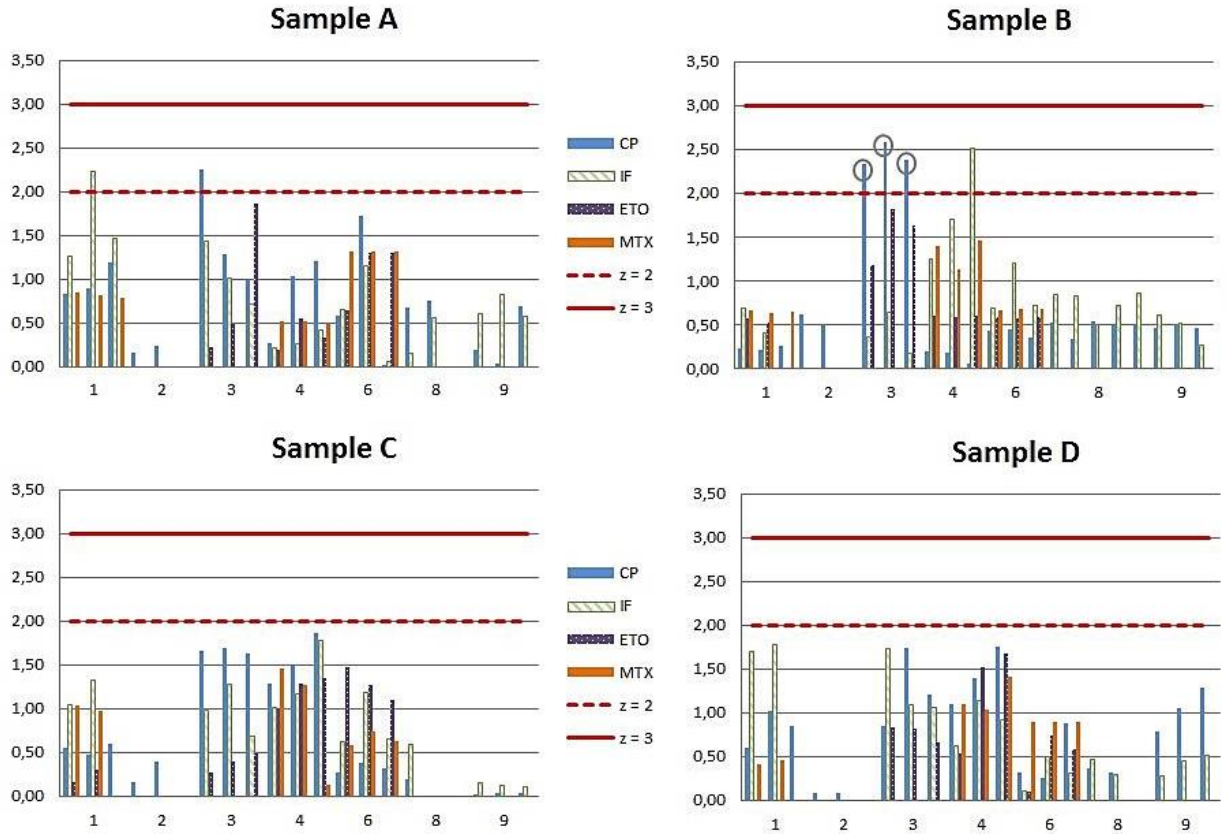


**Figure 1: z-score values for the tested compounds in the different samples.**

Amongst all received results, 210 were applied in statistical evaluation after outlier exclusion. The following statistical parameters including mean values, median values and standard deviations (σ) were determined (Table 3).

**Table 3: Data evaluation for CP, IF, ETO and MTX in samples A, B, C and D.**

| | Spiked value | Mean | Median | σ | | Spiked value | Mean | Median | σ |
|---|---|---|---|---|---|---|---|---|---|
| CP | | | | | IF | | | | |
| A | 53.00 | 60.17 | 60.00 | 17.40 | A | 33.00 | 40.94 | 37.50 | 16.70 |
| B | / | 912.5 | 790.0 | 281.3 | B | / | 2399 | 2010 | 778.5 |
| C | 5239 | 5909 | 5958 | 3004 | C | 394.0 | 2582 | 2485 | 686.2 |
| D | 23.00 | 45.55 | 47.00 | 17.66 | D | 55.00 | 72.41 | 65.40 | 25.09 |
| ETO | | | | | MTX | | | | |
| A | 52.00 | 49.73 | 53.00 | 15.15 | A | 31.00 | 123.66 | 74.30 | 95.64 |
| B | / | 5523 | 980.0 | 7893 | B | / | 58.2 | 1338 | 6859 |
| C | 3420 | 8452 | 8917 | 3010 | C | 1141 | 2271 | 2228 | 192.5 |
| D | 127.0 | 125.9 | 90.00 | 62.48 | D | 432.0 | 631.3 | 447.5 | 427.6 |

The smallest absolute differences between mean or median values and spiked values are observed in samples A for all compounds. One reason could be because this sample had the least complex matrix i.e., surface water. As expected, the highest absolute differences between mean or median values and spiked values are observed in case of sample C (hospital wastewater).

Repeatability i.e., the variation in measurements taken by a single person and instrument on the same sample and under the same conditions is shown for each sample and compound in Figure 2. Due to the lack of data, some CV values are absent. The lowest CVs were observed in the case of MTX (≤ 12 % for laboratory 4, sample C). The CVs for IF were ≤ 35 % (laboratory 6, sample A), while for ETO calculated CVs were < 25 % for all samples and all laboratories. The highest CVs were observed in the case of CP (≤ 72 % for laboratory 3, sample D). These results indicate good repeatability for laboratories 1, 4 and 6 when analysing MTX in all samples, while the CVs for CP, IF and ETO strongly depended on matrix type (i.e. laboratory 3 for CP in samples A, C and D).

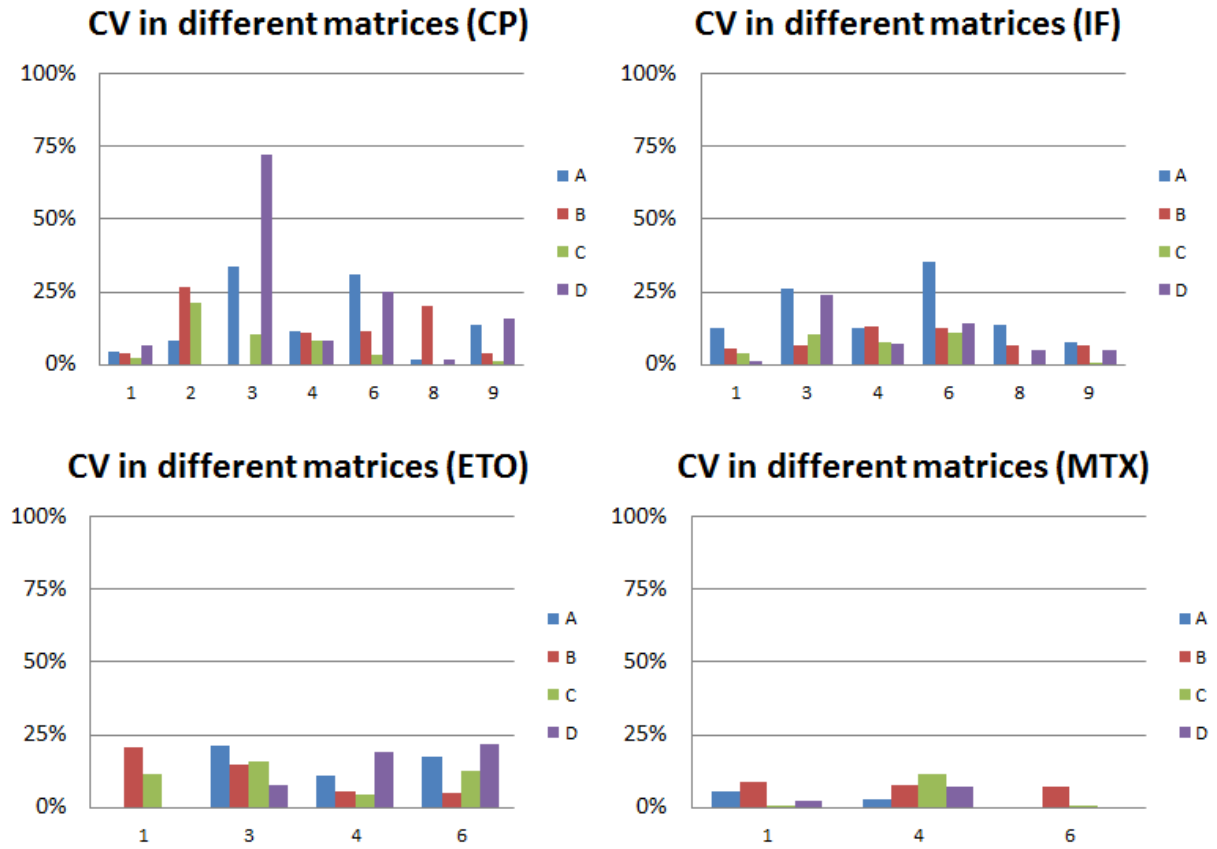


**Figure 2: Repeatability as CV for each sample and compound.**

Reproducibility is the ability of an entire experiment or study to be reproduced with the same method on identical test items in different laboratories with different operators using different equipment [1]. Reproducibility (CV) for each sample and compound is shown in Figure 3. Most CV values, except for MTX in sample C, are relatively high (27 % ≤ CV ≤ 143 %). High CV values and the observed large differences amongst samples, especially for ETO and MTX, can be explained by the low number of participating laboratories (3 and 4 for ETO and MTX, respectively).

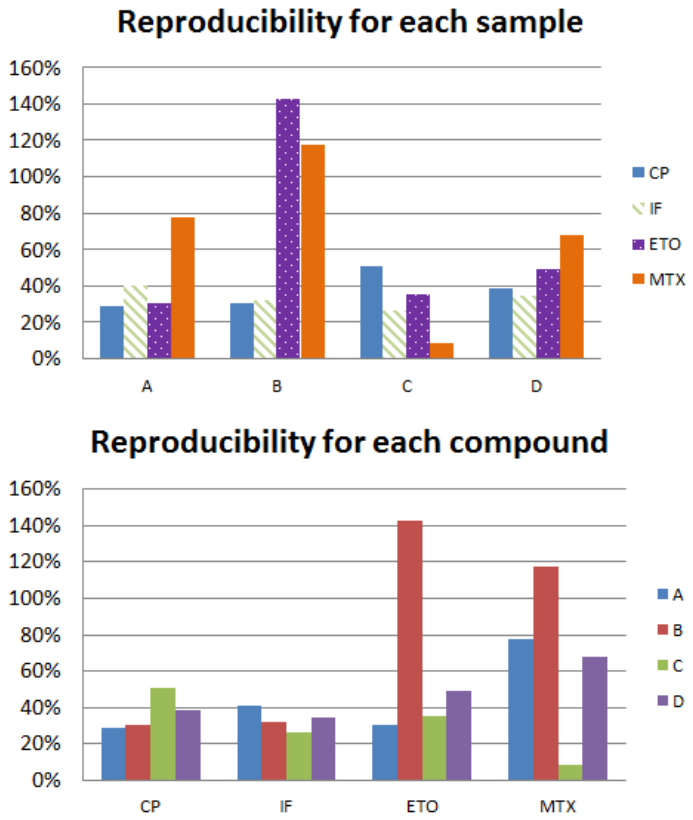


**Figure 3: Reproducibility as CV for each sample and compound.**

In conclusion, preparation of interlaboratory samples was satisfactory. The smallest absolute differences between spiked values and average values for all selected compounds were observed for sample A (surface water), which has the least complex matrix. Laboratories 1, 4 and 6 gave the highest repeatability for MTX in all samples, whereas for other compounds repeatability depended on matrix type. The reproducibility was relatively poor for all compounds and samples (27 % - 143 %) except for MTX in sample C. Further, it was shown that poor reproducibility and large differences in the case of MTX and ETO could originate from the low number of participating laboratories.

# References:


[1] E. Hund, D. Luc Massart, J. Smeyers-Verbeke. Inter-laboratory studies in analytical chemistry. *Analytica Chimica Acta,* 423:145-165, 2000

[2] E. Heath, T. Kosjek, H.R. Andersen, H.-C. Holten Lutzhoft, A. Adolfson Erici, M. Coquery, R.-A. During, O. Gnas, C. Guignard, P. Karlsson, F. Manciot, Z. Moldovan, D. Patureau, L. Cruceru, F. Sacher, A. Ledin. Inter-laboratory exercise on steroid estrogens in aqueous samples. *Environmental pollution*, 158(3):658-662, 2010

[3] E. Heath, T. Kosjek, M. Farre, J.B. Quintana, L.F. de Alencastro, S. Castiglioni, O. Gans, K. Langford, R. Loos,J. Radjenović, L. Mainero Rocca, H. Budzinski, D. Tsipi. M. Petrovic, D. Barcelo. Second interlaboratory exercise on non-steroidal anti-inflammatory drug analysis in environmental aqueous samples. *Talanta*, 81(4-5):1189-1196, 2010

[4] M. Farre, M. Petrovic, M. Gros, T. Kosjek, E. Martinez, E. Heath, P. Osvald, R. Loos, K. LeMenach, H. Budzinski, F. De Alencastro, J. Muller, T. Knepper, G. Fink, T.A. Ternes, E. Zuccato, P. Kormali, O. Gans, R. Rodil, J.B. Quintana, F. Pastori, A. Gentili, D. Barcelo. First interlaboratory exercise on non-stroidal anti-inflammatory drugs analysis in environmental samples. *Talanta*, 76:580-590, 2008

[5] T. Kosjek, E. Heath. Occurrence, fate and determination of cytostatic pharmaceuticals in the environment. *TrAC Trends in Analytical Chemistry*, 30:1065-1087, 2011

[6] Noelia Negreira, Nicola Mastroianni, Miren López de Alda, Damià Barceló. Multianalyte determination of 24 cytostatics and metabolites by liquid chromatography–electrospray–tandem mass spectrometry and study of their stability and optimum storage conditions in aqueous solution. *Talanta*, 116:290-299, 2013

## For wider interest

Cytostatics are a group of pharmaceuticals used extensively for treating cancer. With modern analytical instrumentation it is now becoming possible to measure their residues in environmental samples raising awareness about potential detrimental effects: cytotoxicity, genotoxicity, mutagenicity and teratogenicity, on non-target organisms at environmental concentrations.

Only a limited number of laboratories are currently analysing these compounds in environmental samples and the different methods used are yet to be evaluated. The aim of this study is to carry out an interlaboratory comparison. The exercise involved laboratories from Czech Republic, The Netherlands, Singapore, Slovenia, Spain and UK. Participants received four samples of surface water and wastewaters, which contained various concentrations of cyclophosphamide, ifosfamide, etoposide and methotrexate, all of which are commonly used cytostatics. Each laboratory was then asked to analyse the samples. Results were statistically evaluated. Overall, it was determined, that the performance of participating laboratories is adequate. The absolute differences between added compounds to samples and participant's obtained results were the smallest in case of surface water samples. Further, good repeatability was observed for methotrexate in all samples for all participating laboratories, whereas for other compounds repeatability depended on sample type. Finally, reproducibility was determined as weak for all compounds in all samples, except for MTX in hospital wastewater. These results revealed the need for a higher number of participating laboratories determining selected compounds in order to confirm the obtained results and conclusions.

# Occurrence and fate of benzophenone-type UV filters in the aqueous environment

**Kristina Kotnik**[1,2,3], **Tina Kosjek**[1], **Uroš Kranjc**[3], **Ester Heath**[1,2]

[1] Department of Environmental Sciences, Jožef Stefan Institute, Ljubljana, Slovenia

[2] Jožef Stefan International Postgraduate School, Ljubljana, Slovenia

[3] Ecological Engineering Institute Ltd, Maribor, Slovenia

kristina.pestotnik@ijs.si

**Abstract.** This study evaluates the occurrence of five benzophenone-type UV filters in the aqueous environment and their behaviour under the influence of artificial and natural light. Analysis of fourteen water and sediment samples from lakes, rivers and sea revealed the presence of UV filters in the majority of the surface waters ≤ 820 ng $L^{-1}$ (2-hydroxy-4-methoxybenzophenone) and up to 650 ng $g^{-1}$ of benzophenone in sediment samples. The results of photodegradation studies were consistent with previous studies, indicating a high photostability of UV filters during 7 h of irradiation using either a monochromatic low pressure or medium pressure mercury lamp. Solar irradiation experiments also showed UV filters are photostable compounds, since no significant degradation was observed after 2 weeks of exposure to natural sunlight. However, 4 weeks of irradiation did result in elimination of ≤ 80 % of studied compounds.

**Keywords**: UV filter, benzophenone, occurrence, environment, photodegradation

## 1 Introduction

UV filters are common ingredients in sunscreens, protecting skin from the deleterious effects of sunlight. They also serve as photostabilizers in other cosmetic products (e.g. moisturizers, hair sprays, shampoos, lipsticks and fragrances), fabrics, coatings, adhesives, plastic packaging and optical products [1-3]. Studies have reported the detrimental effects of benzophenone-type UV filters on aquatic organisms, since they exhibit estrogenic activity and genotoxic effects [1, 3]. The

increasing use of UV filters leads to their widespread occurrence in the environment, where they are recognised as emerging organic pollutants.

UV filters enter the aquatic environment through various pathways, which include domestic discharges containing UV filter residues from showering and laundering, excreted compounds after dermal application, and industrial wastewater discharges from production facilities. Nevertheless, the most critical source of UV filters is the direct input into surface waters, when they are released into lakes, rivers and seas by wash-off from the skin during bathing. There exists only limited data on the occurrence of UV filters in surface waters, but a few do report concentrations as high as several hundred ng $L^{-1}$ [1,3]. The physico-chemical properties of these compounds including their log $K_{ow}$ (2.9–3.9) indicate their moderate tendency to adsorb to organic particulate matter. Although sediment, as opposed to water, is less sensitive to factors such as seasonal variations, rainfall and industrial production and enables the study of long-term pollution, the presence of UV filters in sediments has received less attention, but reported concentrations are in the low ng $g^{-1}$ levels [1,3].

Photodegradation is one of the most important natural abiotic elimination processes determining the fate of organic compounds in the environment, yet published data concerning photolytic behaviour of UV filters are scarce. Environmental fate has been addressed only recently, where studies show high photostability of UV filters [2,3].

The focus of this study is to evaluate the occurrence of five benzophenone-type UV filters (benzophenone, 4-hydroxybenzophenone, 2-hydroxy-4-methoxybenzophenone, 2,4-dihydroxybenzophenone and 2,2'-dihydroxy-4-methoxybenzophenone) in the aqueous environment and to investigate their behaviour and fate under the influence of artificial UV light and natural sunlight. The chemical structures and important physico-chemical properties of the investigated compounds are presented in Table 1.

**Table 1 :** Chemical structures and physico-chemical properties of the target benzophenone derivatives

| IUPAC name, INCI name | Abbreviation | Chemical structure | Mw | Log $K_{ow}$ |
|---|---|---|---|---|
| Benzophenone | BP | 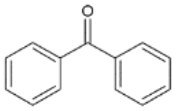 | 182.22 | 3.18 |
| 4-hydroxybenzophenone | H-BP | 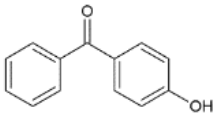 | 198.22 | 2.87 |
| 2,4-dihydroxybenzophenone Benzophenone-1 | DH-BP | 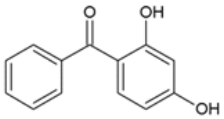 | 214.22 | 3.17 |
| 2-hydroxy-4-methoxybenzophenone Benzophenone-3 | HM-BP | 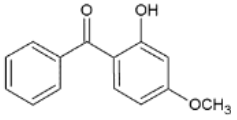 | 228.24 | 3.64 |
| 2,2'-dihydroxy-4-methoxybenzophenone Benzophenone-8 | DHM-BP | 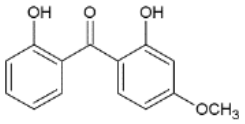 | 244.24 | 3.93 |

Abbreviations: IUPAC: International Union of Pure and Applied Chemistry, INCI: International Nomenclature of Cosmetic Ingredients, Mw: molecular weight (g/mol), $K_{ow}$: octanol-water partition coefficient

# 2 Materials and methods

## 2.1 Sample collection

Grab water and sediment samples were collected during the summer months from different locations in Slovenia and Croatia. In total 5 lakes, 3 river sites and 3 coastal sites on the North Adriatic Sea were selected since at these locations swimming, bathing and other recreational activities take place. Further, 3 rivers were sampled in the vicinity of wastewater treatment plant (WWTP) effluent outflows.

## 2.2 Analytical method

Aqueous samples were extracted and compounds of interest pre-concentrated with solid phase extraction (SPE) using an Oasis™ HLB reversed phase sorbent (Waters Corporation, MA, USA). Sample preparation for sediment samples involved microwave-assisted extraction (MAE) using a Microwave Accelerated Reaction System (MARS) 5 (CEM corporation, Matthews, NC, USA) and further clean-up by

SPE. To increase their volatility, the compounds were derivatized prior to GC-MS analysis. Derivatization of BP was performed at 60°C for 15 h using O-(2,3,4,5,6-pentafluorobenzyl)hydroxylamine hydrochloride (PFBHA) as derivatization agent, while the remainder (H-BP, DH-BP, HM-BP, DHM-BP) were derivatized by N-methyl-N-[trimethylsilyl]trifluoroacetamide (MSTFA) at 60°C for 1 h. Separation and identification were achieved using an HP 6890 (Hewlett-Packard, Waldbronn, Germany) gas chromatograph with a single quadrupole mass selective detector (GC-MSD).

### 2.3 UV and solar irradiation

Lab-scale UV degradation experiments were carried out in a cylindrical glass reactor by exposing aqueous solutions of each individual compound (1 μg $L^{-1}$) to UV irradiation. Monochromatic low pressure (LP) mercury UV lamp and a medium pressure (MP) mercury lamp were used as a source of radiation. The LP lamp emits predominately at 254 nm, while the MP lamp radiates over a broader range (200 - 600 nm). To determine elimination efficiency of UV treatment, different irradiation times (0 – 420 min) were studied.

Solar degradation studies were carried out by exposing aqueous solutions of each compound (1 μg $L^{-1}$) to sunlight. Samples in quartz Erlenmeyer flasks were exposed to irradiation in Ljubljana, Slovenia (latitude 46.1, longitude 14.5) in August 2012 for a period of 4 weeks under clear sky conditions with daily air temperature between 12 and 36°C, 15 h of sunshine per day and maximum local sunlight irradiation intensity of 932 W $m^{-2}$. Samples were collected after 1, 2, 3 and 4 weeks, when the elimination efficiency was evaluated.

## 3 Results and discussion

Fourteen water and sediment samples were collected from sites, affected either by recreational activities or WWTP discharges, and analysed according to the described procedure. Tables 2 and 3 show the frequency and concentration range of UV filters found in these samples. The most frequently detected compounds in both water and sediment samples were BP and HM-BP, which are also among the most commonly used UV filters. They were also the most abundant. In addition, DH-BP was found in most of the water samples and in several sediments. Since DH-BP is a major

metabolite formed from HM-BP and is also used as a personal care product, its occurrence may originate from different sources and this could account for the high frequency of its detection. Compounds H-BP and DHM-BP were less common in aqueous samples and were not detected in sediments. The occurrence of the investigated UV filters in surface waters and sediments is clearly more affected by recreational activities such as swimming and bathing than by WWTP discharges.

**Table 2 :** Concentration range (ng $L^{-1}$) of benzophenone-type UV filters in surface water samples

| **UV filter** | **Water** (ng $L^{-1}$) | | | | |
|---|---|---|---|---|---|
| | Frequency | **Lake** | **River** | **Sea** | **River (WWTP)** |
| **BP** | 14/14 | 33-120 | 30-88 | 51-56 | 54-190 |
| **H-BP** | 5/14 | 7.2-8.4 | <LOD | 4.1-5.1 | <LOD |
| **HM-BP** | 14/14 | 38-820 | 9.4-120 | 96-380 | 5.9-24 |
| **DH-BP** | 10/14 | 2.9-130 | 1.9-11 | 5.6-11 | 2.9-3.2 |
| **DHM-BP** | 6/14 | 2.6-6.5 | <LOD | 2.4-5.3 | <LOD |

**Table 3 :** Concentrations (ng $g^{-1}$) of target UV filters in sediment samples

| **UV filter** | **Sediment** (ng $g^{-1}$) | | | | |
|---|---|---|---|---|---|
| | Frequency | **Lake** | **River** | **Sea** | **River (WWTP)** |
| **BP** | 14/14 | 220-360 | 610-650 | 270-280 | 38-190 |
| **H-BP** | 0/14 | <LOD | <LOD | <LOD | <LOD |
| **HM-BP** | 14/14 | 10-17 | 23-32 | 10-13 | 2.5-7.4 |
| **DH-BP** | 7/14 | 2.5-3.7 | 2.6-3.5 | 2.0 | 3.1 |
| **DHM-BP** | 0/14 | <LOD | <LOD | <LOD | <LOD |

The results of UV treatment were consistent with previous studies [2,3] indicating the high photostability of UV filters during 7 h of irradiation using either the LP or MP lamp. The study also demonstrates that in case of the investigated compounds, the LP lamp is more efficient, making the degradation process faster and leading to reduced half-lives (Figure 1).

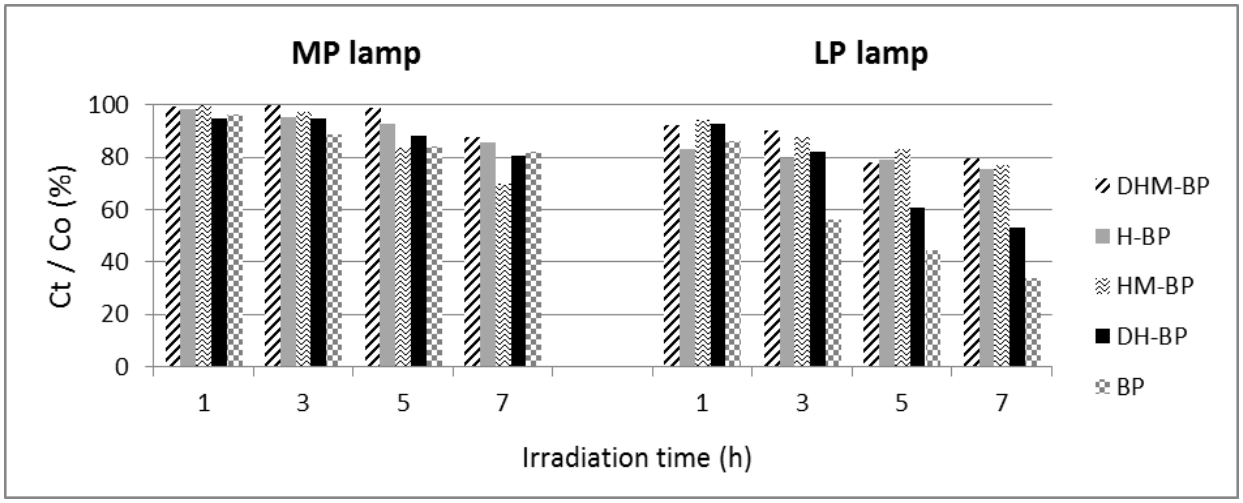


**Figure 1 :** Photodegradation of investigated UV filters during UV treatment using MP and LP lamp

Solar irradiation experiments showed high stability of H-BP, HM-BP and DHM-BP with removal of approximately 40 % after 4 weeks of irradiation. In contrast, photodegradation of BP and DH-BP followed a pseudo-first-order kinetics and resulted in approximately 80 % removal after 4 weeks of irradiation. Similar half-lives of 13.3 and 12.4 days were determined for BP and DH-BP, respectively.

## 4 Conclusion

Results show that benzophenone-type UV filters are present in the aquatic environment, both in water and sediments. Photodegradation studies show that they exhibit high photostability indicating the potential of being persistent in the environment. Due to increasing consumption and possible toxic effects of UV filters on aquatic ecosystems, it is crucial to further investigate their presence in different environmental compartments and to better understand their environmental behaviour, cycling and fate.

## References:

[1] H.K. Jeon, Y. Chung, J.C. Ryu. Simultaneous determination of benzophenone-type UV filters in water and soil by gas chromatography-mass spectrometry. *Journal of Chromatography A*, 1131:192-202, 2006

[2] R. Rodil, M. Moeder, R. Altenburger, M. Schmitt-Jansen. Photostability and phytotoxicity of selected sunscreen agents and their degradation mixture in water. *Analytical and Bioanalytical Chemistry*, 395: 1513-1524, 2009

[3] D.L. Giokas, A. Salvador, A. Chisvert. UV filter: From sunscreens to human body and the environment. *Trends in Analytical Chemistry*, 26: 360-374, 2007

## For wider interest

The increasing use of UV filters is leading to their widespread occurrence in the environment, where they are recognised as emerging organic pollutants. However, actual data regarding their presence, effects and fate in the environment is still limited. UV filters are common ingredients in sunscreens, protecting human skin from deleterious effects of sunlight. They also serve as photostabilizers in other cosmetic products (e.g. moisturizers, hair sprays, shampoos, lipsticks and fragrances), fabrics, coatings, adhesives, plastic packaging and optical products. They are produced in large quantities throughout the world and their consumption continues to rise. Consequently, these compounds enter the environment globally. In recent years there has been an increasing concern regarding the presence and effects of UV filters residues in the environment as studies have reported their toxic effects on aquatic organisms.

Among numerous UV filters this study is focused on benzophenone based compounds and their occurrence and fate in the aquatic environment. For this purpose, fourteen water and sediment samples were collected from lakes, rivers and sea, and analysed. Results revealed the presence of benzophenone-type UV filters in the majority of the surface waters in the concentration as high as 820 ng $L^{-1}$ (2-hydroxy-4-methoxybenzophenone) and up to 650 ng $g^{-1}$ of benzophenone in sediment samples. Since photodegradation is an important natural elimination process, behaviour of the target UV filters was evaluated when exposed to artificial and natural sunlight. Results confirmed high photostability of the investigated UV filters, which is in agreement with their use in sunscreens and other products. The results of photodegradation will provide a better understanding of the cycling and fate of these compounds in the environment.

# Dynamics of cave air ventilation in a dead-end passage of Postojna Cave (Pisani rov-Colourful gallery)

**Bor Krajnc[1], Sonja Lojen[2], Janja Vaupotič[2], David Dominguez-Villar[3], Nives Ogrinc[2]**

[1] Jožef Stefan International Postgraduate School, Ljubljana, Slovenia

[2] Department of Environmental Sciences, Jožef Stefan Institute, Ljubljana, Slovenia

[3] Centro Nacional de Investigación sobre la Evolución Humana, Burgos, Spain

bor.krajnc@ijs.si

**Abstract.** The dynamics of cave ventilation is interesting for different fields of science e.g. speleology, paleoclimatology, ecosystem carbon dynamics research etc. This work is a preliminary research of a bigger project where the influences of subterranean $CO_2$ storage to the adjacent soil $CO_2$ effluxes will be studied. We studied the patterns and possible causes of cave ventilation in Pisani rov, a dead-end passage of the Postojna Cave. We used $CO_2$ concentrations and $^{222}Rn$ activity concentrations in cave air as indirect indicators of cave ventilation. To gain more information on the origin of cave air $CO_2$, stable carbon isotope analyses of cave air were performed. First results show that $CO_2$ and $^{222}Rn$ concentrations correspond to the temperature differences between cave and outside air. Further, the increase in cave $CO_2$ concentrations is related to the $CO_2$ derived from remineralized organic carbon.

**Keywords**: Caves, ventilation, carbon dioxide, radon, $^{13}C$, stable isotopes

## 1 Introduction

Cave ventilation is an interesting process from both, aboveground (atmospheric) and belowground (speleological) point of view. From the aboveground point of view it is especially interesting for the studies of ecosystem $CO_2$ effluxes. Ecosystem fluxes are usually considered only as biological flux defined by the difference between the gross photosynthetic flux and ecosystem respiration [1]-[3]. However, recent studies of soil and ecosystem $CO_2$ fluxes on calcareous areas have shown that also other processes such as carbonate weathering and ventilation of subterranean caves and cavities can contribute to soil fluxes [4]-[10]. Therefore, the $CO_2$ efflux investigations at such

areas must also take into account the subterranean storage of $CO_2$, which can be positive in the case of stocking and/or negative in the case of degassing or ventilation [10]. Stocking into subterranean cavities happens mainly by water transport of dissolved soil $CO_2$ and diffusion [11]. $CO_2$ stored in subterranean reservoirs reaches the outside atmosphere by the means of ventilation processes. Those processes can in certain cases even surpass the biogenic $CO_2$ fluxes in carbonaceous regions [7], [12].

The drivers for ventilation can be dynamic (moving fluids - water or wind), or static (variation of pressure, temperature or air composition). Although every cave or even passage has its own specific characteristics, we can roughly separate two main groups of caves where different drivers for cave ventilation have to be taken in to account. In caves with more than one entrance at different elevations the convective air circulation prevails. That happens because of the difference between external and internal air densities [13]-[17]. Temperature can explain about 99% of the variation of the cave air density. However, when $pCO_2$ of the cave air exceeds the atmospheric values by an order of magnitude or more, also the influence of air $pCO_2$ has to be taken into account [18], [19]. In the caves with large volumes connected by small passages, with one entrance or with very small entrances, the barometric circulation can also take place. In these cases the ventilation is driven by pressure difference between the cave and outside atmosphere [13], [17], [20]. Cave ventilation rates can be measured directly or through variations of cave air density, pressure or trace gas composition such as $CO_2$ concentrations or $^{222}Rn$ activity concentrations. Beside the $CO_2$ concentration also the isotopic composition of $CO_2$, especially the stable isotope composition of C is interesting, because it can give us further information about processes and sources of this gas in the cave atmosphere.

The presented article is a result of preliminary studies of a bigger project, where influences of abiotic $CO_2$ sources to the karstic forest soil $CO_2$ fluxes will be studied. Understanding forest soil $CO_2$ fluxes in such regions is important because 44% of Slovenian territory can be classified as karst area and 60-70% of that area is covered by forest. Herein our research focused on the patterns and possible causes of cave ventilation in Pisani rov, a dead-end passage from the Postojna Cave. $CO_2$ concentrations and $^{222}Rn$ activity concentrations were measured in cave air as

indirect indicators of cave ventilation, while stable isotope composition of $CO_2$ was used to determine its possible sources.

## 2 Materials and methods

**Study area.** Pisani rov (Colourful Gallery) is a dead-end passage of Postojna Cave. It is a 920 m long horizontal passage, which deviates from the main Postojna Cave passage to the north and terminates below the slopes of the Velika Jeršanova dolina (Fig. 1). The collapse of Velika Jeršanova dolina disconnected the continuation of Pisani rov towards north [21]. Pisani rov is developed in Turonian limestone and its direction and shape is given by bedding planes and joints whose main direction follows N-S [22]. At the end of Pisani rov the thickness of the cave celling is estimated to be around 30 m [23]. In Pisani rov we can find some redeposited flish and dropstone argil, which is believed to be brought there by Pivka River in the past when it was flowing through this tunnel and later with occasional flood event [22].

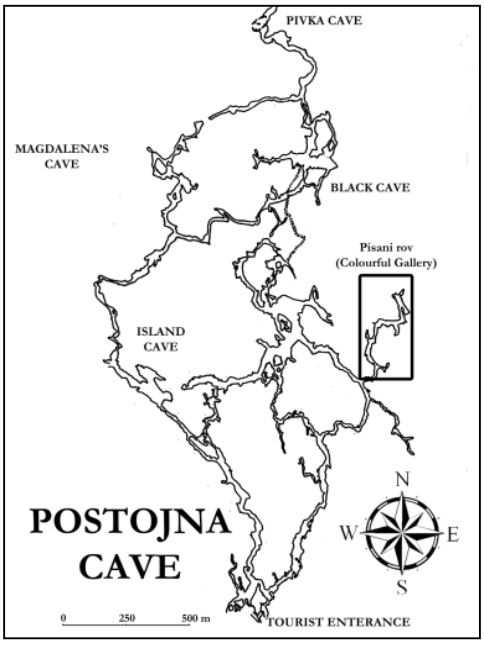


**Figure 1**: Postojna Cave with marked location of Pisani rov (Colourful gallery) (adopted from [24])

Pisani rov is interesting for our investigation, because it has limited ventilation compared to the rest of the cave and the temperature at the end of the gallery is almost stable at 8.4 $^{o}$C, with seasonal cycle < 0.015 $^{o}$C [25]. Here some of the highest concentrations of $CO_2$ and $^{222}$Rn in Postojna Cave were recorded. Maximum values

of $^{222}$Rn activity concentrations were around 45 000 Bq m$^{-3}$, while maximum $CO_2$ concentrations reached up to 7000 ppm [26]. Our maximum observed values were 26900 ±180 Bq/m$^{-3}$ for Rn activity concentration (3.8.2009) and 6780 ppm for $CO_2$ concentration (17.6.2010).

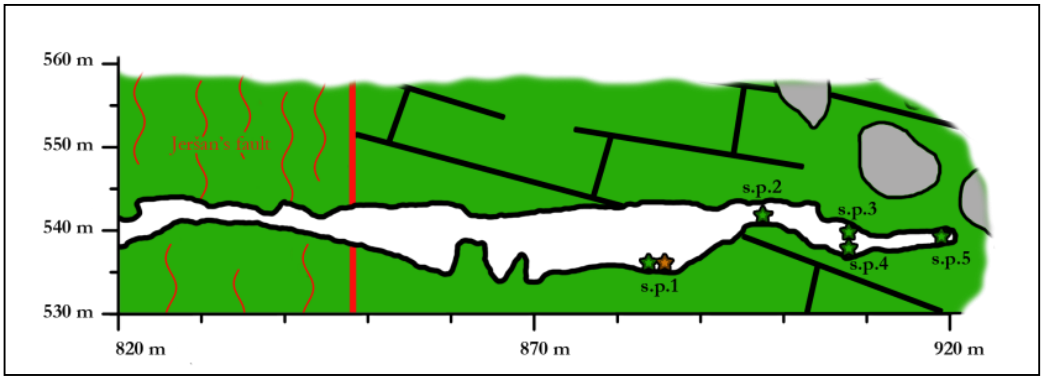


**Figure 2**: Cross section of the end of Pisani rov with marked sampling points (s.p.) (adopted from [21])

**Sampling and Measurement.** All sampling was performed during cave visits twice a month. The measurements comprise the data from 2009 and 2010 and the data obtained from October 2013. At the end of Pisani rov we have five locations where the air was sampled and at the first of those locations the active concentration of $^{222}$Rn was monitored (Fig. 2)

$CO_2$ concentration was measured with TESTO 435 multi-functional measurement instrument for Indoor Air Quality with installed IAQ probe. [27].

Samples for stable isotope analysis of $CO_2$ from cave air were taken in five replicates at each location using a 50 ml syringe. Sample was taken directly from the cave air and injected into closed, pre-evacuated 12 ml vials. Stable isotope composition of cave air $CO_2$ was determined with EUROPA 20-20 continuous flow isotope ratio mass spectrometer (CF-IRMS) coupled with ANCA-TG preparation module for trace gases. The accuracy of the measurements was ±0.2‰. Results are reported in usual $\delta$-notation against the international Vienna Pee Dee Belemnite (VPDB) standard in per mil (‰).

Air samples for measurements of $^{222}Rn$ activity concentrations at the sampling point 1 (Fig. 1) were taken directly into alpha-scintillation cells, manufactured at the Jožef Stefan Institute [28], [29]. Three hours after air sampling, when secular equilibrium between radon and its decay products has been reached, the activity in the cell was measured in an alpha counter PRM 145 (AMES, Slovenia).
Outside temperatures data were gathered from the nearby meteorological station in Postojna [30].

## 3 Results and discussion

It is seen from Figure 3 that the increase in outside temperature corresponds to the $CO_2$ concentration ($C_{CO2}$) increase in the cave atmosphere ($CO_2$ stocking). On the other hand, the decrease of the outside temperature causes a ventilation effect in the cave, which was also reflected in the decrease of $CO_2$ concentrations. This pattern is typical for a convective air circulation created by the difference in air density between cave and inside air where air temperature is the driving parameter controlling these differences. As already mentioned, this pattern is characteristic for caves with more than one entrance at different elevations [13]-[17]. This suggests that during the winter periods the cold air transported into the gallery raise the warmer cave air, which exhales through unknown fissures and cracks to the outside atmosphere. In some cases (red arrows in Figure 3), when the outside temperature was below $0^oC$, we observed that the $C_{CO2}$ concentrations began to increase. The elevated $C_{CO2}$ values suggest that the connection with outside atmosphere is closed due to frozen water in adjacent soils or possible snow cover. According to data obtained from the meteorological station in Postojna, the snow cower was present in those days (6-19 cm).

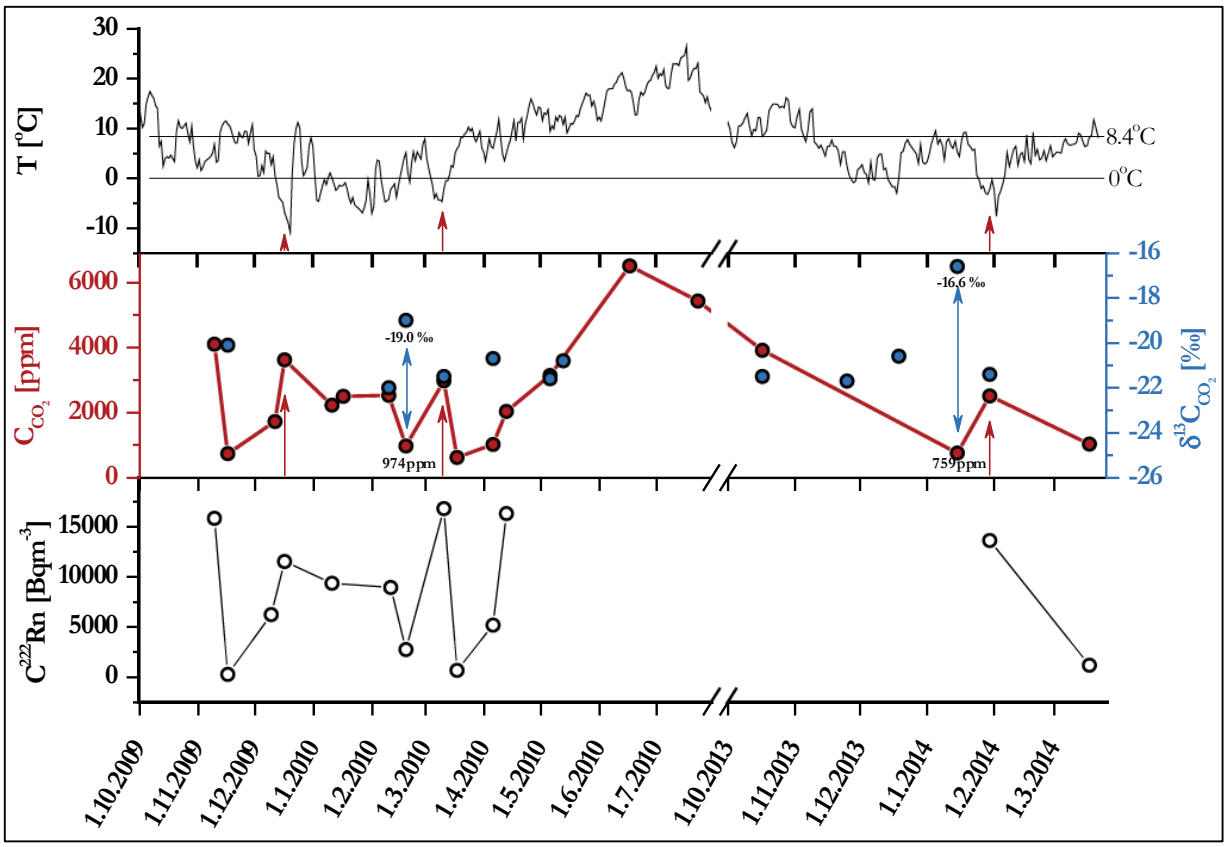


**Figure 3:** Average daily temperatures, cave air $CO_2$ concentrations ($C_{CO2}$), stable carbon isotope composition of cave $CO_2$ ($\delta^{13}C_{CO2}$) and radon activity concentrations ($C^{222}Rn$) during the sampling periods in 2009, 2010 and 2013.

A positive correlation ($R^2$ = 0.62) between $C_{CO2}$ and radon activity concentration ($C^{222}Rn$) was observed during the sampling periods in 2010 (Fig. 3). Concentrations of both gases increase during "stocking" period and decrease towards atmospheric values (≈380 ppm for $C_{CO2}$ and ≈10-30 Bq m$^{-3}$ for $C^{222}Rn$ ) during ventilation periods. These results suggest that during ventilation periods the fresh air was transported from the outside atmosphere through the main cave passage to the gallery and, in accordance with results previously discussed, the warm cave air from the gallery could be lost through unknown cracks and fissures out from the cave. Similar behaviour was also observed in previous studies performed by Gregorič et al. [26].

Results from C stable isotope analysis of cave air $CO_2$ reveal that higher $C_{CO2}$ corresponds to more negative $\delta^{13}C_{CO2}$ values. This indicates more pronounced influence of remineralized organic carbon to $CO_2$, which could come to the cave

from the adjacent soil air, via diffusion or via percolating water rich in dissolved $CO_2$ from the soil air. Water rich but not saturated with $CO_2$ runs through fissures of carbonate rocks (dissolution of carbonates). When reaching the subterranean cavity, the degassing of $CO_2$ from water takes place until the equilibrium of $CO_2$ partial pressures between water and cave air is obtained (degassing of $CO_2$ and carbonate precipitation).

When low $CO_2$ concentrations in the cave air were observed, the $\delta^{13}C_{CO2}$ values were more positive (marked with blue colour arrows in Figure 3) suggesting the mixing of cave air with fresh outside air ($\delta^{13}C_{CO2} \approx$ -8‰) that was transported to the gallery from different possible ways e.g. some smaller entrances or even the main tourist entrance. Another possible mechanism influencing $\delta^{13}C_{CO2}$ values in cave air could be the enchased outgassing of $CO_2$ from the drip waters. This was possible when $CO_2$ concentrations in cave were low causing less fractionation. In the case of more pronounced outgassing higher proportion of $^{13}CO_2$ influences $\delta^{13}C$ values in cave air $CO_2$. The prove of this mechanism in Pisani rov was shown in the work of Dominguez-Villar et al. [25]. They compared $\delta^{13}C$ values of dissolved inorganic carbon in drip water ($\delta^{13}C_{DIC}$ ) against $C_{CO2}$ in the cave air. It was shown that $\delta^{13}C_{DIC}$ values exponentially decay with increasing $C_{CO2}$.

## 4 Conclusion

Although Pisani rov is considered a part of Postojna Cave with limited ventilation, the fluctuations in $CO_2$ concentrations and $^{222}Rn$ activity concentrations are relatively high. In fact the time series of those trace gas concentrations indicate typical ventilation pattern with winter ventilation and summer stagnation periods. We can conclude that the main factor controlling the ventilation in Pisani rov is the difference in inside and outside air densities causing convective flow of the cave air. Further it was found that during ventilation periods the warm cave air was pressed to the outside atmosphere through unknown fissures and cracks. Stable isotope analysis of $CO_2$ suggested that during high $CO_2$ concentrations there is a pronounced influence of remineralized organic carbon to cave $CO_2$. It should be mentioned that these results are only preliminary results and further investigation is

needed in order to define more precisely the cave ventilation and its possible influence to the soil $CO_2$ effluxes.

Although concentrations of $CO_2$ and $^{222}Rn$ and $CO_2$ stable isotope composition suggest the fresh air inflow, the high stability of the cave temperature is not in favour of such explanation. To resolve this problem further research is required concerning the following issues: measuring of the same cave air parameters in the main cave passage in front of the entrance to the Pisani rov, studying possible sources of $CO_2$ in the cave atmosphere (including a detailed study of DIC in the drip waters) and monitoring the fluxes and concentrations of $CO_2$ in the soil above the cave.

## References:


[1] G. Lasslop, M. Reichstein, D. Papale, A.D. Richardson, A. Arneth, A. Barr, P. Stoy, G. Wohlfahrt. Separation of net ecosystem exchange into assimilation and respiration using a light response curve approach: critical issues and global evaluation. *Global Change Biology*, 16 (1): 187–208, 2010.

[2] M. Reichstein, E. Falge, D. Baldocchi, D. Papale, M. Aubinet, P. Berbigier, C. Bernhofer, N. Buchmann, T. Gilmanov, A. Granier, T. Grunwald, K. Havrankova, H. Ilvesniemi, D. Janous, A. Knohl, T. Laurila, A. Lohila, D. Loustau, G. Matteucci, T. Meyers, F. Miglietta, J.-M. Ourcival, J. Pumpanen, S. Rambal, E. Rotenberg, M. Sanz, J. Tenhunen, G. Seufert, F. Vaccari, T. Vesala, D. Yakir, R. Valentini. On the separation of net ecosystem exchange into assimilation and ecosystem respiration: review and improved algorithm. *Global Change Biology*, 11 (9): 1424–1439, 2005.

[3] P.C. Stoy, G.G. Katul, M.B. Siqueira, J.-Y. Juang, K.A. Novick, J.M. Uebelherr, R. Oren. An evaluation of models for partitioning eddy covariance-measured net ecosystem exchange into photosynthesis and respiration. *Agricultural and Forest Meteorology*, 141 (1): 2–18, 2006.

[4] M. Ferlan, G. Alberti, K. Eler, F. Batič, A. Peressotti, F. Miglietta, A. Zaldei, P. Simončič, D. Vodnik. Comparing carbon fluxes between different stages of secondary succession of a karst grassland. *Agriculture, Ecosystems & Environment*, 140 (1-2): 199–207, 2011.

[5] G. Plestenjak, K. Eler, D. Vodnik, M. Ferlan, M. Čater, T. Kanduč, P. Simončič, N. Ogrinc. Sources of soil CO2 in calcareous grassland with woody plant encroachment. *Journal of Soils and Sediments*, 12 (9): 1327–1338, 2012.

[6] M. Čater and N. Ogrinc. Soil respiration rates and δ13C(CO2) in natural beech forest (Fagus sylvatica L.) in relation to stand structure. *Isotopes in environmental and health studies*, 47 (2): 221–237, 2011.

[7] A.S. Kowalski, P. Serrano-Ortiz, I.A. Janssens, S. Sánchez-Moral, S. Cuezva, F. Domingo, A. Were, L. Alados-Arboledas. Can flux tower research neglect geochemical CO2 exchange? *Agricultural and Forest Meteorology*, 148 (6–7): 1045–1054, 2008.

[8] S. Cuezva, A. Fernandez-Cortes, D. Benavente, P. Serrano-Ortiz, A.S. Kowalski, S. Sanchez-Moral. Short-term CO2(g) exchange between a shallow karstic cavity and the external atmosphere during summer: Role of the surface soil layer. *Atmospheric Environment*, 45 (7): 1418–1427, 2011.

[9] P. Serrano Ortiz, S. Cuezva Robleño, A.S. Kowalski, S. Sánchez Moral. Cuantificación y procedencia de los intercambios de CO2 en un ecosistema carbonatado mediante la técnica de

eddy covariance y el análisis de los isótopos estables de carbono. *Ecosistemas*, 19 (3): 41–46, 2010.

[10]O. Pérez-Priego, P. Serrano-Ortiz, E.P. Sánchez-Cañete, F. Domingo, A.S. Kowalski. Isolating the effect of subterranean ventilation on CO2 emissions from drylands to the atmosphere. *Agricultural and Forest Meteorology*, 180 (0): 194–202, 2013.

[11]W. W. Wood. Origin of caves and other solution openings in the unsaturated (vadose) zone of carbonate rocks: A model for CO2 generation. *Geology*, 13 (11): 822–824, 1985.

[12]M. Roland, P. Serrano-Ortiz, A.S. Kowalski, Y. Goddéris, E.P. Sánchez-Cañete, P. Ciais, F. Domingo, S. Cuezva, S. Sanchez-Moral, B. Longdoz, D. Yakir, R. van Grieken, J. Schott, C. Cardell, I.A. Janssens. Atmospheric turbulence triggers pronounced diel pattern in karst carbonate geochemistry. *Biogeosciences*, 10 (7): 5009–5017, 2013.

[13]G. Badino. Underground meteorology - "What's the weather underground?". *Acta carsologica*, 39 (3): 427–448, 2010.

[14]A. Cigna. An analytical study of air circulation in caves. *International Journal of Speleology*, 3 (1/2): 41–54, 1968.

[15]J. Hakl, I. Csige, I. Hunyadi, A. Várhegyi, G. Géczy. Radon transport in fractured porous media — Experimental study in caves. *Environment International,* 22 (1): 433–437, 1996.

[16]A.J. Kowalczk and P.N. Froelich. Cave air ventilation and CO2 outgassing by radon-222 modeling: How fast do caves breathe? *Earth and Planetary Science Letters*, 289 (1–2): 209–219, 2010.

[17]T. M. L. Wigley. Non-steady flow through a porous medium and cave breathing. *Journal of Geophysical Research*, 72 (12): 3199–3205, 1967.

[18]A.S. Kowalski and E.P. Sánchez-Cañete. A New Definition of the Virtual Temperature, Valid for the Atmosphere and the CO 2 -Rich Air of the Vadose Zone. *Journal of Applied Meteorology and Climatology*, 49 (8): 1692–1695, 2010.

[19]E.P. Sánchez-Cañete, A.S. Kowalski, P. Serrano-Ortiz, O. Pérez-Priego, F. Domingo. Deep CO2 soil inhalation / exhalation induced by synoptic pressure changes and atmospheric tides in a carbonated semiarid steppe. *Biogeosciences*, 10 (10): 6591–6600, 2013.

[20]M. Leutscher and P.-Y. Jeannin. The role of winter air circulations for the presence of subsurface ice accumulations: an example from Monlési ice cave (Switzerland). *Theoretical and Applied Karstology* (17): 19–25, 2004.

[21]S. Šebela and J. Čar. Velika Jeršanova doline - a former collapse doline = Velika Jeršanova dolina - nekdanja udornica. *Acta carsologica*, 29 (2): 201–212, 2000.

[22]R. Gospodarič. K poznavanju Postojnske jame - Pisani rov. Naše jame, 4 (1-2): 9–16, 1962.

[23]S. Šebela. Accesses from the surface to the Postojna Cave system. *Annales. Series historia naturalis*, 20 (1): 55–64, 2010.

[24]T.R. Shaw. *Names from the past in Postojnska jama (Postojna cave)*. ZRC Publishing, 2006.

[25]D. Domínguez-Villar, S. Lojen, K. Krklec, A. Baker, I.J. Fairchild. Is global warming affecting cave temperatures? Experimental and model data. (Submitted to *Climate Dynamics*)

[26]A. Gregorič, J. Vaupotič, F. Gabrovšek. Reasons for large fluctuation of radon and CO2 levels in a dead-end passage of a karst cave (Postojna Cave, Slovenia). *Natural Hazards and Earth System Science*, 13 (2): 287–297, 2013.

[27]TESTO. http://www.testo.de/, 2014.

[28]J. Kristan, I. Kobal. A modified scintillation cell for the determination of radon in uranium mine atmosphere. *Health physics*, 24 (1): 103–104, 1973.

[29]J. Vaupotič, M. Ančik, M. Škofijanec, I. Kobal. Alpha scintillation cell for direct measurement of indoor radon. *Journal of Environmental Science and Health*, 27 (6): 1535–1540, 1992.

[30]ARSO. http://www.arso.gov.si/, 2014.

## For wider interest

Cave ventilation is an interesting process from both, aboveground (atmospheric) and belowground (speleological) point of view. From the aboveground point of view it is especially interesting for the study of ecosystem $CO_2$ sinks, sources and temporal storage of atmospheric $CO_2$ in the karstic areas. Long-term studies related to cave ventilation and their influence on soil $CO_2$ fluxes will help us to understand the mechanisms in the ecosystem C budget and its relation to global environmental changes.

# Determination of elements in river sediments at some selected Slovenian streams

**Ana Kroflič**[1,2], **Mateja Germ**[3], **Vekoslava Stibilj**[1]

[1] Department of Environmental Sciences, Jožef Stefan Institute, Ljubljana, Slovenia

[2] Jožef Stefan International Postgraduate School, Ljubljana, Slovenia

[3] Biotechnical Faculty, University of Ljubljana, Ljubljana, Slovenia

ana.kroflic@ijs.si

**Abstract.** Industry, traffic and agriculture are main sources of environmental pollution. Pollutants are released into river and are eventually accumulated into sediments. Investigation of elements Cr, Cu, Zn, As, Se, Cd and Pb in sediments was the main goal of our study.

Before the determination, the samples need to be digested, which in not an easy task. Optimization of acid digestion in microwave oven, using HF, HCl and $HNO_3$ was made. For the determination of elements in sediments from selected streams in Notranjska and Central regions of Slovenia, optimized method has been used. Recorded concentration ranges were: 25 - 77 mg Cr $kg^{-1}$, 6 - 48 mg Cu $kg^{-1}$, <LOD - 1102 mg Zn $kg^{-1}$, 2 - 13 mg As $kg^{-1}$, <LOD - 0.4 mg Se $kg^{-1}$, <LOD - 1.2 mg Cd $kg^{-1}$ and 14 - 23 mg Pb $kg^{-1}$. Investigated areas are mainly agricultural. Compared to rivers flowing through agricultural areas higher concentrations of some elements (Cr, Zn and Pb) were noticed in rivers that flow through industrial area.

**Keywords**: river sediments, elements, agricultural area, Slovenian streams

## 1 Introduction

Growing human population and related human activities have caused higher emission of various pollutants into the environment. Research of pollutants in different aquatic system is one of the major activities in environmental science [1]. Pollutants are released into aquatic system and they are eventually accumulated into sediments. They can realise back (change in conditions) and may have an impact on water organisms [2]. Contaminations of sediments with heavy metals are a

consequence of anthropogenic pollution due to atmospheric deposition, industrial and agricultural activities. Studies had shown that agriculture is also a source of metals pollution in environment [3]. This pollution has different sources associated with rainfall and snowmelt runoff, moving over and through the ground, carrying natural and human-made pollutants into lakes, rivers, streams, wetlands, estuaries and underground drinking water [4].

Sediments are persistent materials, so the digestion of sediments to determine the concentration of elements is not an easy task. In literature the mostly used method for digestion of sediment is acid digestion with various ratio and combination of acid such as HCl, $HNO_3$, HF and $HClO_4$, where hydrofluoric acid (HF) is needed for silicate compounds dissolution [1-3;5-10].

Commonly determined elements in sediments are: As, Cd, Co, Cr, Cu, Hg, Mn, Ni, Pb and Zn in different concentration ranges depending on research area [1-3;5-7]. For their detection in sediments often used analytical techniques are electrothermal atomic absorption spectrometry (ETAAS), inductively coupled plasma atomic emission spectrometry (ICP-AES), and inductively coupled plasma mass spectrometry (ICP-MS) [1-3;4-9].

During our research, a modification of the method published by Ščančar et. al., 2007 was made. The digestion in microwave oven with $HCl/HNO_3/HF$ was used in the first step and with $H_3BO_3$ in the second step. After optimization of selected parameters (time of digestion, volume of $H_3BO_3$ and temperature in first and second step of digestion) determination of elements in sediments, sampled in selected Slovenia streams in agricultural areas, was conducted.

## 2 Methods and materials

Sampling sites: The investigation of sediments was conducted on three streams in Slovenia (Pšata, Lipsenjščica and Žerovniščica). Sampling was performed in different months in 2009, 2010 and 2011.

Pšata stream is 28.4 kilometres long river in Central region of Slovenia. It is the right tributary of Kamniška Bistrica River. In 139 $km^2$ large catchments two medium-size

cities Mengeš and Trzin are located. Lipsenjščica and Žerovniščica are streams in Cerkniško field (Notranjska region). They are tributaries of Stržen River.

On Pšata stream two different sampling sites were selected where temperature was 0.0 – 21.6 °C and discharge 0.04 – 0.12 $m^3 s^{-1}$ (2011). In Lipsenjščica stream one sampling side was selected with 1.3 – 13.2 °C and discharge 0.05 – 1.05 $m^3 s^{-1}$, while in Žerovniščica stream five different sampling sites with temperature 6.2 – 12.0 °C and discharge 0.04 - 0.12 $m^3 s^{-1}$ were selected [11].

Sample preparation: At sampling sites around 2 kg of sediments were collected, which were dried in the air till constant mass. Samples were than sieved through 1 mm sieve and the particles smaller than 1 mm were grounded into fine powder by milling in agate bowls (Fritsch planetary mill Pulverisette 7) at 2500 rps for 7 minutes. The mass of particles < 250 μm was 70-90 % of grounded mass.

Analytical procedure: Around 0.25 g of milled sediments was weighed into Teflon vessels. Into each vessel 4 ml of $HNO_3$ (s.p.), 2 ml of HF (s.p.) and 1 ml of HCl (s.p.) were added. Solution was carefully mixed. For first part of digestion with microwave oven (Ethos One, Millstone, USA) the following program was used: 30 minute ramp to temperature 210°C, 60 minute hold with power of 1200 W and then cooling process was performed. When the vessels were cooled to room temperature, 15 ml 4 % aqueous solution of $H_3BO_3$ (s.p.) were added in each vessel and the following program was used for digestion: 15 min ramp to temperature 220 °C, 30 minute hold with power of 1200W and then cooling process to room temperature. The solutions without insoluble residue were obtained. The solutions were quantitatively transferred to 40 ml polypropylene tubes and filled with water. Digested solution was appropriate diluted (1:100) and detection of elements in sediments with ICP-MS (7500ce Agilent Technologies, Tokyo, Japan) was applied. On ICP-MS following parameters were used: power 1500 W, sample flow 0.1 rps, carrier gas (Ar) 0.9 L $min^{-1}$, make up gas (Ar) 0.1 L $min^{-1}$, integration time hydrogen 0.2 s (Se) and helium 0.1 s (other elements) and for sample introduction Babington nebulizer was needed. For calibration curve ICP multi-elemental standard solution XVI (Merck) was used.

The accuracy and precision was checked with standard reference material CRM 320R (Trace elements in river sediment) in every series.

# 3 Results and discussion

## 3.1. Optimization of digestion

The procedure (Ščančar et. al., 2007) prepared for marine sediments was modified. Time of digestion, volume of $H_3BO_3$ and temperature in first and second step were optimized (Table 1). $H_3BO_3$ was added to react with the excess of HF. The results obtained with various procedures using CRM 320R are present in Table 2. The good agreements between certified and obtained values were found with digestion procedure 6. In the first step 4 ml of $HNO_3$, 2 ml of HF and 1 ml of HCl were added to samples, samples were heated in digestion procedure 6 (30 min to 210 °C, 60 min on 210 °C, 1200 W) and 15 ml of 4% $H_3BO_3$ was added in the second step of digestion (15 min to 220 °C and 30 min on 220 °C). This digestion procedure was the best choice due to obtained solution without insoluble residue. 15 ml of 4 % $H_3BO_3$ was added because results were better than in the case where 12.5 ml of 4 % $H_3BO_3$ was added to the samples. Other procedure (1-5) did not give good results for CRM.

In literature, various sediment preparation and digestion procedures are reported. Authors sieved sediments through different screens (from 63 to 73 μm) [1,2,6,7]. Martinez et. al., 2011 reported, that samples were further homogenized using mortar and pestle and sieved also through 5 μm screen [6]. For digestion they used aqua regia ($HNO_3$:HCl=3:1), Akcey et. al., 2013 used mixture of four acids (HF:$HNO_3$:$HClO_4$:HCl=4:1:1:1) and Sun, et. al., 2012 used the same acid mixture as we did in our study ($HNO_3$, HCl and HF). Digestions of sediment samples from the Sava River were also conducted with the same acid mixtures and similar procedure to ours. Detection of selected elements in digested solution was made with ICP-MS [1,2,6] and ETAAS [7]. Lower limits of detection for Zn were obtained with ETAAS (0.1 mg $kg^{-1}$) [7]. In above cited literature limits of detection for other elements were not given.

**Table 1**: Temperature programmes for digestion optimization

| Digestion procedure | First step of digestion | | Second step of digestion | |
|---|---|---|---|---|
| | Chemicals | Temp. programme | Chemicals | Temp. programme |
| 1 | 4 ml $HNO_3$<br>2 ml HF<br>1 ml HCl | 30 min to 200 °C<br>45 min on 200 °C<br>1200 W | 12.5 ml 4 % $H_3BO_3$ | 15 min to 200 °C<br>30 min on 200 °C<br>1200 W |
| 2 | | 30 min to 200 °C<br>60 min on 200 °C | | |
| 3 | | 30 min to 220 °C<br>60 min on 220 °C | 15 ml 4 % $H_3BO_3$ | 15 min to 220 °C<br>30 min on 220 °C |
| 4 | | 30 min to 230 °C<br>60 min on 230 °C | | 15 min to 230 °C<br>30 min on 230 °C |
| 5 | | 30 min to 200 °C<br>60 min on 200 °C | | 15 min to 220 °C<br>30 min on 220 °C |
| 6 | | 30 min to 210 °C<br>60 min on 210 °C | | |

### 3.2. Elements in river sediments

Content of elements in sediment through the period 2009 - 2011 is presented in Table 3.

**Table 2**: Comparison of found and certified values (mg $kg^{-1}$) of CRM 320R

| | | Cr | Cu | Zn | As | Se | Cd | Pb |
|---|---|---|---|---|---|---|---|---|
| | | Certified value[a] | | | | | | |
| | | 59.0 ± 4.0 | 46.3 ± 2.9 | 319 ± 20 | 21.7 ± 2.0 | 0.96 ± 0.18[b] | 2.64 ± 0.18 | 85.0 ± 5.0 |
| Digestion[c] | # | Determined value[d] | | | | | | |
| 1 | 2 | 47.7 ± 10.6 | 40.7 ± 9.9 | 285 ± 60 | 19.3 ± 4.1 | / | 2.33 ± 0.79 | 76.8 ± 14.8 |
| 2 | 4 | 60.5 ± 5.1 | 48.5 ± 4.3 | 349 ± 24 | 23.2 ± 1.7 | 0.93 ± 0.18 | 2.85 ± 0.20 | 91.7 ± 7.8 |
| 3 | 2 | 60.2 ± 0.6 | 49.8 ± 0.3 | 353 ± 2 | 23.6 ± 0.4 | 0.97 ± 0.11 | 3.12 ± 0.16 | 92.5 ± 0.8 |
| 4 | 4 | 60.5 ± 1.8 | 46.4 ± 1.1 | 363± 73 | 21.7 ± 1.2 | 1.07 ± 0.32 | 2.86 ± 0.25 | 84.4 ± 10.9 |
| 5 | 2 | 64.7 ± 11.7 | 52.1 ± 8.1 | 348 ± 53 | 23.9 ± 3.7 | 0.82 ± 0.21 | 2.89 ± 0.31 | 91.7 ± 11.8 |
| **6** | **9** | **55.1 ± 4.8** | **48.1 ± 6.5** | **317 ± 26** | **21.5 ± 1.9** | **0.97 ± 0.19** | **2.72 ± 0.26** | **88.1 ± 8.7** |

# - number of determination

[a]Results are given as certified values with uncertainty

[b]Result is given as indicative value with uncertainty

[c] Digestions 1-6 are described in Table 1

[d] Results are given as determined values with standard deviation or absolute error (n=2)

**Table 3**: Determination of elements in river sediments (mg $kg^{-1}$)

| | | # | Cr | Cu | Zn | As | Se | Cd | Pb |
|---|---|---|---|---|---|---|---|---|---|
| Limits of detection | | | 3.15 | 4.81 | 66.9 | 0.19 | 0.36 | 0.25 | 1.01 |
| Stream | Year | | | | | | | | |
| Pšata | 2009 | 4 | 60.4 ± 11.9 | 11.8 ± 1.7 | 80.8 ± 10.7 | 4.00 ± 0.88 | <LOD | 0.29 ± 0.06 | 19.4 ± 3.9 |
| | 2010 | 2 | 77.5 ± 5.6 | 31.4 ± 11.1 | <LOD | 5.29 ± 0.34 | <LOD | <LOD | 14.4 ± 1,0 |
| | 2011 | 4 | 51.3 ± 17.3 | 10.5 ± 2.2 | <LOD | 4.57 ± 0.34 | <LOD | <LOD | 18.9 ± 7.7 |
| Lipsenjščica | 2009 | 2 | 64.4 ± 3.9 | 8.82 ± 1.32 | <LOD | 12.2 ± 0.4 | <LOD | 0.32 ± 0.08 | 23.4 ± 1.1 |
| | 2010 | 2 | 67.0 ± 3.0 | 13.9 ± 1.0 | <LOD | 12.6 ± 0.6 | <LOD | 0.39 ± 0.01 | 18.8 ± 1.1 |
| | 2011 | 2 | 65.4 ± 0.5 | 31.4 ± 0.2 | 1101 ± 58 | 11.0 ± 0.8 | 0.44 ± 0.17 | 1.18 ± 0.08 | 51.2 ± 0.9 |
| Žerovniščica | 2009 | 4 | 25.0 ± 13.8 | 12.3 ± 1.7 | <LOD | 2.37 ± 1.00 | <LOD | 0.27 ± 0.11 | 14.2 ± 5.6 |
| | 2010 | 4 | 31.3 ± 2.3 | 48.2 ± 9.8 | 72.2 ± 5.3 | 3.58 ± 0.82 | <LOD | 0.63 ± 0.49 | 16.6 ± 10.6 |
| | 2011 | 4 | 39.0 ± 28.2 | 4.51 ± 1.53 | <LOD | 4.07 ± 1.67 | <LOD | 0.37 ± 0.14 | 21.8 ± 20.7 |

#-number of determination

Results are given as average values with standard deviation or absolute error (n=2)

Concentrations of elements in Pšata stream have not changed much between consecutive years (2009 - 2011). The only exception was Zn, where its concentration is under limit of detection. Concentration of selected elements in Lipsenjščica sediments in general did not change much. Concentrations of Cu, Zn, Cd and Pb were higher in 2011 than in previous years. Concentration of Zn in 2011 was high in comparison to previous years (1101 mg $kg^{-1}$). Sampling in Žerovniščica stream was conducted at five sampling sites (less than 1 km distance). Comparison between concentrations in different years showed no significant difference with exception of Cu. Concentrations of Cu varied between 4.51 and 48.2 mg $kg^{-1}$. Large concentration range was possible due to different conditions at every sampling site. Concentrations of Cr and As were the highest at Lipsenjščica sediments comparing to other three river sediments. In Slovenia the addition of 0.5 mg of Se per kg in feedstuff is allowed (Slovenian legislation and European Union) and it can be released into environment by liquid and slurry manure [10]. In our case, almost in all sediment samples, concentrations of Se were under limit of detection.

A comparison between obtained and literature data was made. Concentrations of elements in steams on Notranjska and Central regions of Slovenia were lower than any other compared literature data (Table 4). In the area, where literature investigations were made, there are no industries and big cities. Near Pšata stream, a cattle farm and fields are located, near Lipsenjščica stream meadows and minor human impact can be seen and near Žerovniščica stream there are a village, nearly fields and daily farms with cattle [11].

Concentrations of selected elements in Sava River sediments were investigated by Milačič et. al., 2010 [1]. Sampling was made at twenty locations along Sava River where different anthropogenic sources (industry, traffic, agricultural and urban activities). Concentrations of Cr, Zn and Pb in their study are higher than obtained values of selected elements in our (concentration of Zn was high only in one sample). Similar concentration ranges (exceptions are Cd and Pb) were also found in the study performed by Martinez el. al. [6]. Investigated locations on Gillians River have minor human impact (recreational, seasonal cattle grazing, willows). High concentrations are a result of sampling below City's wastewater treatment plants. Another research was performed in Gediz and Buyak Menderes, two rivers in Turkey [7]. Industrial sources, sewage and agricultural sources have made consequences in higher concentrations of selected elements. Comparison to obtained values reviled that these two rivers in Turkey are probably contaminated with industrial sources. The river Xiangjiang in China has the highest concentrations of investigated elements comparing to other studies. River flows through two heavily polluted areas (metallurgical and chemical plants), which may cause high concentrations of selected elements. Exception is Cr, which was classified as geogenic components [2]. Concentrations of Se in sediments were not determined in none of the used literature.

Table 4: Concentration ranges of selected elements (mg $kg^{-1}$)

| | Cr | Cu | Zn | As | Se | Cd | Pb |
|---|---|---|---|---|---|---|---|
| our study | 25-77 | 6-48 | <LOD-1102 | 2-13 | <LOD-0.4 | <LOD-1.2 | 14-23 |
| Sava River (Milačič et. al., 2010) | 23-381 | 11-50 | 55-361 | 3-25 | / | 0.2-1.4 | 12-122 |
| Gallians River, USA (Martinez et. al., 2011) | / | 16-50 | 72-683 | 2-9 | / | 0.3-6.7 | 17-63 |
| Rivers in Turkey (Akcay et. al., 2013) | 160-220 | 108-152 | 85-185 | / | / | / | 35-140 |
| Xiangjiang, China (Sun et. al., 2012) | 34-130 | 19-162 | 53-1099 | 1-47 | / | 1-56 | 40-431 |

# 4 Conclusion

Good agreement between certificated and obtained values of CRM 320R was obtained, when 4 ml of $HNO_3$, 2 ml of HF and 1 ml of HF was heated with sample in microwave oven in the following temperature programme: 30 min to 210 °C, 60 min on 210 °C with power of 1200 W and then cooled to room temperature. In the second step 15 ml of 4% $H_3BO_3$ was added and the following temperature programme was used: 15 min to 220 °C, 30 min on 220 °C with power of 1200 W and then the samples were cooled down. Obtained solutions had no insoluble residue.

Concentrations of investigated elements in sediments in selected streams are similar in all three years of investigation. In Pšata sediments the only exception was Zn (under limit of detection). On the other hand, in Lipsenjščica stream high concentration of Zn (1102 mg $kg^{-1}$) in sediments in 2011 and in Žerovniščica sediments various Cu concentrations were obtained.

Lower concentrations of Cr, Zn and Pb were determined in sediments of selected Slovenian streams in comparison to the Sava River sediments [1]. Sava River flows through industrial areas where higher concentrations of selected elements could be released into the environment.

## References:


[1] R. Milačič, et. al. A complex investigation of the extant pollution in sediments of the Sava River. Part 1: Selected elements. *Environ. Monit. Assess.*, 163:263-275, 2010

[2] W. Sun, et. al.. Trace metals in sediments and aquatic plants from the Xiangjiang River, China. *J. Soils Sediments*, 12:1649-1657, 2012

[3] W. Tang et. al.. Heavy metal sources and associated risk in response to agricultural intensification in the estuarine sediments if Chaohu Lake Valley, East China. *J. Hazard. Mater.*, 176:945-951, 2010

[4] K. Farrell-Poe. Nonpoint Source Pollution. *All Achived Publications*. Paper 982, 1995

[5] J. Ščančar, et. al..Organotin compounds and selected metals in the marine environment of Northern Adriatic Sea. *Envior. Monit. Assess*, 127:271-282, 2007

[6] E. A. Martinez, et. al.. Determination of selected heavy metal concentrations and distribution in a southwestern stream using macrophytes. *Ecotox. Environ. Safe.,* 74:1504-1511, 2011

[7] H. Akcay, et. al.. Study of heavy metal pollution and speciation in Buyak Menderes and Gediz river sediments. *Water Res.,* 37:813-822, 2003

[8] S. Pajević, et. al.. Heavy metal accumulation of Danube river aquatic plants – indication of chemical contamination. *Cent. Eur. J. Biol.,* 3(3):285-294, 2008

[9] F. Duman, et. al.. Seasonal Variability of Heavy Metals in Surface Sediment of Lake Sapanca, Turkey. *Envir. Monit. Assess.*, 133:277-283, 2007

[10] W. E. Kline, et. al. Dissolution of Silicate Minerals by Hydrofluoric Acid. *Ind. Eng. Chem. Fundam.*, 20:155-161, 1981

[11] Š. Mechora, et al.. Monitoring of selenium in macrophytes - the case of Slovenia. *submitted to Chemosphere*

## For wider interest

The main aim of this study was to determine concentrations of elements in river sediments in selected streams on Notranjska and Central regions of Slovenia. In these areas there are no industries and big cities present. Near selected samplings sites mainly cattle farms, fields and small villages are located. The main goal of this study is to investigate the impact of agriculture on the concentrations of the selected elements Cr, Cu, Zn, As, Se, Cd and Pb on river sediments.

First task was to modify the digestion procedure, which was used for marine sediments. With optimized digestion, selected elements in sediment samples from selected streams were determined during the three consecutive years. Our results were in a good agreement with the data obtained in sediments not influenced by industry. The contents of Cr, Zn and Pb were higher in the Sava River compared to our study. Sava River flows through industrial area, where larger amounts of selected elements could be released into the environment.

According to our knowledge, investigated areas were not researched before. In this study basic data was obtained, which could be used for further research of pollution in agricultural areas. In the future work the selected elements will be also determined at the same sampling sites in water and macrophytes as well. With the obtained data bioaccumulation factor for selected elements in macrophytes could be calculated.

# Geochemical investigation of molecular and isotopic composition and origin of coal seam gas in Velenje Basin

**Jerneja Lazar**[1,2], **Tjaša Kanduč**[3], **Sergej Jamnikar**[1, 2], **Fausto Grassa**[4] **Simon Zavšek**[1]

[1] Velenje Coal Mine, Velenje, Slovenia

[2] Jožef Stefan International Postgraduate School, Ljubljana, Slovenia

[3] Department of Environmental Sciences, Jožef Stefan Institute, Ljubljana, Slovenia

[4] Instituto Nazionale di Geofisica e Vulcanologia Sezione di Palermo, Italy

jerneja.lazar@rlv.si

**Abstract.** The concentration of methane and carbon dioxide of coal seam gas, molecular and stable carbon isotope composition of methane and carbon dioxide, and stable hydrogen isotope composition of methane was investigated in the Velenje Basin. The aim was to obtain a better understanding of its origin and behaviour in advancement of the longwall face due to the high risk of $CO_2$ gas outbursts, and to obtain knowledge on the distributional behaviour of coal seam gases with advance of the longwall face. The average coal seam gas composition in the Velenje Basin is approximately $CO_2$:$CH_4 \geq 2$:1. The study revealed that at a distance of around 100 m from the working face, the influence of face dynamics causes gas to migrate. Stable carbon isotope composition of methane and $CO_2$ indicates that methane was generated via acetate fermentation and reduction of $CO_2$. Secondary processes were induced by active mining causing the enrichment of residual methane with $^{13}C$ isotope.

**Keywords**: Velenje Basin, coal seam gas composition, stable isotopes, coal seam gas origin

## 1 Introduction

Velenje Coal Basin is one of the basins with the thickest coal seam (up to 160 m) in the world and represents a large reservoir for coal seam gas with a mixture of carbon dioxide ($CO_2$) and methane ($CH_4$) in addition to nitrogen and higher hydrocarbons in minority. High coal seam gas content can cause coal gas outbursts (especially $CO_2$), which present a high risk in mining throughout the world coal mines.

Outburst of gas is a dynamic phenomenon occurring when gas is suddenly released through fissures and cavities or from tectonic fault zones when uncovered by boreholes or mining processes. Active mining causes dynamic changes in the coal seam especially in stress distribution and coal seam gas pressure around longwall coal faces. Lignite at the Velenje Coal Mine has an average coal gas mixture of approximately $CO_2$:$CH_4 \geq 2:1$ [1], where a high proportion of $CO_2$ is adsorbed on the lignite structure or is captured in the coal matrix, while $CH_4$ is mostly present free in coal fractures.

An improved understanding of the geochemical processes that control the occurrence and composition of coal seam gas is an important contribution not only to remediation of potential environmental or mining hazards, but also for exploration and development strategies for utilizing coal seam gas as an energy resource [2]. The stable carbon isotopes of coal bed methane are usually applied for the identification of its genesis [3]. Set of geochemical monitoring of coal seam gas was established in Velenje Coal Mine at different active mine areas (Mine Pesje, Mine South Preloge and Mine North Preloge) with the aim to determine coal seam gas distribution in advancement of the working face, to determine the isotopic composition and origin of coal seam gas and to compare the results with other coal basins.

The isotopic composition of $CO_2$ ($\delta^{13}C_{CO2}$) in conjunction with the carbon dioxide – methane index (CDMI = $[CO_2/(CO_2+CH_4)]\bullet 100$ (%)) is often used to infer the origin of $CO_2$ in coal gases [4]-[6], therefore this index was introduced to decipher the origin of $CO_2$ in the Velenje Basin, as in the Bowen and Sydney Basins, Australia [7],[8]. Four different types of $CO_2$ origin are known: endogenic $CO_2$, $CO_2$ originating from carbonates, $CO_2$ of microbial origin and $CO_2$ originating from headwaters recharging the basin [9]. Since production gases from many coal bed methane (CBM) and some shale gas fields are relatively dry, the ratio of $CH_4$ to the sum of ethane and propane (C1/(C2+C3)) is widely used to distinguish between microbial and thermogenic gases. Ratios greater than 1000 and less than 100 are considered to be typical for microbial and thermogenic gas, respectively, when used in combination with methane carbon isotope composition [6], [10]-[12].

## 2 Materials and methods

Coal seam gas was sampled from 25 m long boreholes drilled in the longwall panel or in the goaf of the previously excavated longwall panel (Figure 1). Determination of the concentrations of $CH_4$, $CO_2$, $N_2$, $O_2$ and Ar was performed by using a custom-made NIER type mass spectrometer [9] at Jožef Stefan Institute, Ljubljana. The method of singular decomposition of matrix was used, to obtain the simultaneous analyses of the gases. The precision of the method was ±3%.

The isotopic composition of $CH_4$ ($\delta^{13}C_{CH4}$) and $CO_2$ was determined using an Europa 20-20 continuous flow isotope ratio mass spectrometer (CF-IRMS) with an ANCA-TG preparation module [13]. Working standards calibrated to VPDB (Vienna Pee Dee Belemnite) were used during measurements with a defined value of -3.2‰ for $CO_2$ and -47.5‰ for methane [14]. The analytical precision for analyses of carbon isotope composition was ±0.2‰ for $CO_2$ and ±0.6‰ for $CH_4$. Determinations of the $^2H/^1H$ ratio of $CH_4$ were performed on a Thermo Delta XP GC-TC/CF-IRMS coupled to a TRACEGC analyser at Istituto Nazionale di Geofisica e Vulcanologia Sezione di Palermo in Italy. The accuracy and external precision were better than 0.5‰ and 2.5‰, respectively.

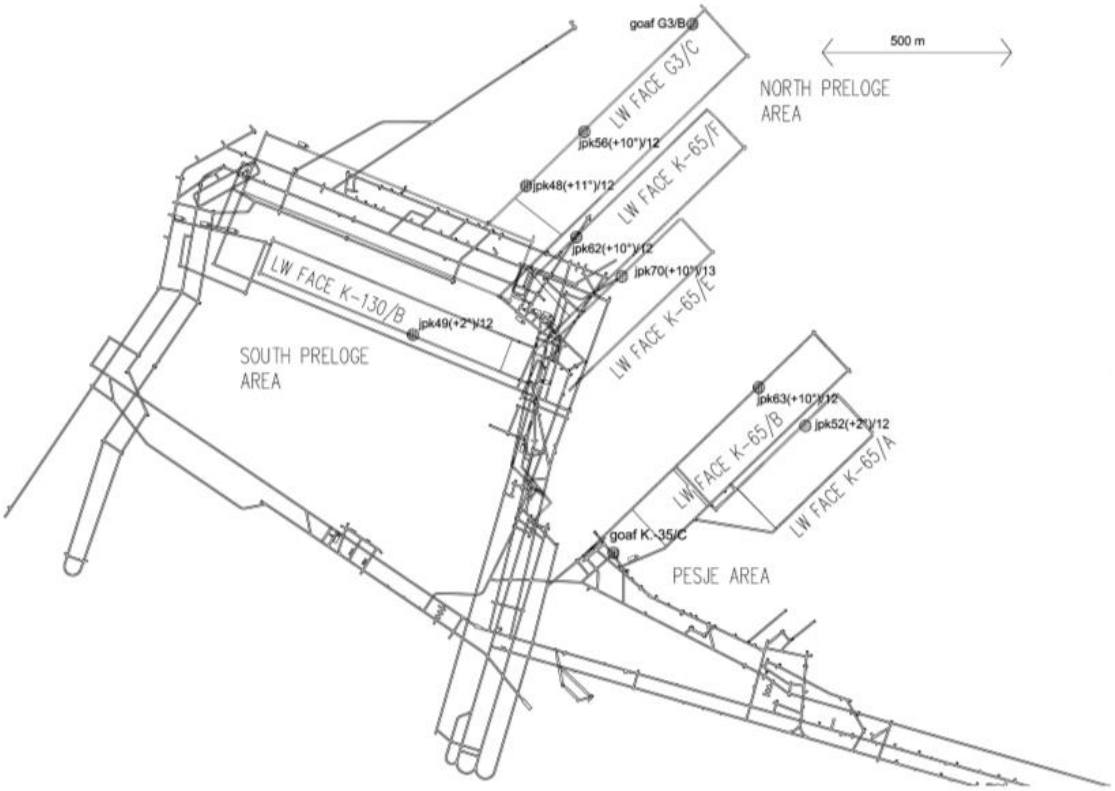


**Figure 1**: Sampling locations in the Coal Mine Velenje.

Higher hydrocarbons were analysed with a Shimadzu 2010 gas chromatographic system with He as carrier gas and equipped with a Poraplot Qcolumn and FID detector. Detection limit is 10 ppm for ethane, 4 ppm for propane, 3 ppm for n- and i-buthane and 1 ppm for penthane and exane. These analyses were also conducted at Istituto Nazionale di Geofisica e Vulcanologia Sezione di Palermo in Italy.

## 3 Results

The results for $CO_2$ and $CH_4$ concentrations and $\delta^{13}C_{CO2}$ and $\delta^{13}C_{CH4}$ from the investigated longwall panels (G3/C-North Preloge area, K.-65/B, K.-65/E, K.-65/F Pesje area, and K.-130/B, South Preloge area) and two goaf areas (K.-35/C in Pesje area and G3/B in North Preloge area) showed heterogeneity in gas and isotopic composition. Due to possible air contamination of samples, the results were recalculated on an air-free basis [9].

$CH_4$ and $CO_2$ concentrations at longwall panel G3/C (North Preloge area) varied from 22.2 to 63.9 vol. % and from 36.1 to 77.8 vol. %, respectively. The stable carbon isotope composition of $CH_4$ and $CO_2$ varied at longwall panel G3/C from -65.1 to -51.2‰ and from -2.4 to -1.8‰, respectively. At the longwall panel K.-65/B the concentration of $CH_4$ varied from 1.8 to 7.5 vol. % and concentration of $CO_2$ varied from 92.3 to 98.2 vol. %. $\delta^{13}C_{CH4}$ at K.-65/B varied from -65.9 to -51.2‰ and $\delta^{13}C_{CO2}$ ranged from -2.4 to -1.8‰. At longwall face K.-65/E in the Pesje Mine, the gas concentrations of $CH_4$ and $CO_2$ varied from 6.8 to 59.9 vol. % and from 38.9 to 93.2 vol. %, respectively. $\delta^{13}C_{CH4}$ at K. -65/E varied from -53.3 to -50.8‰ and $\delta^{13}C_{CO2}$ from –9.0 to -7.9‰. The concentration of $CH_4$ and $CO_2$ at the longwall panel K.-65/F varied from 13.6 to 53.0 vol. % and from 47.0 to 86.4 vol. %, respectively. $\delta^{13}C_{CH4}$ at longwall panel K. -65/F showed variation between -54.3 to -43.3‰ while $\delta^{13}C_{CO2}$ varied from -9.0 to -6.5‰. Stable hydrogen composition of $CH_4$ showed variable values, ranging from -298.8 to -291.4‰ at longwall face K.-65/F. At longwall face K.-65/B it varies from -301.7 to -223.1‰. Values of $\delta^{2}H_{CH4}$ at G3/C longwall face range from -343.5 to -292.5‰, which shows the highest difference between the maximum and minimum values in the mine. $\delta^{2}H_{CH4}$ at the longwall face K.-65/E varies from -319.8 to -297.9‰.

Calculated gas dryness index (C1/(C2+C3)) range from 340 to 23273 ppm. Investigated concentrations of higher hydrocarbons in Velenje Basin range as follows: ethane concentrations range from 0 to 122 ppm, propane concentrations range from 0 to 158 ppm, iso-butane concentrations range from 0-15.3 ppm, n-butane concentrations range from 0 to 7.6 ppm, iso-pentane concentrations range from 0 to 12.2 ppm, n-pentane concentrations range from 0 to 5 ppm, and hexane concentrations range from 0 to 21 ppm.

# 4 Discussion

Dynamic approach of the working longwall face influences on stress situation in front of the longwall face and consequently influences on coal seam gas migration in the excavated coal panel. This temporal variation of the coal seam gas content is shown in Figure 2, where the gas concentration at longwall panel K.-65/F was plotted as a function of the distance from the longwall face. Rate of advancement affects on the coal seam gas desorption. In previous studies concentrations in advance of the working face were investigated at -120 B Preloge South, G2/B Preloge North, and -50/B Pesje and it was concluded that at a distance of 92 m from the working face (rate of advancement of the working face 2.5 m/d), the highest concentration of $CH_4$ and the lowest concentration of $CO_2$ were detected. If the working face advance rate was slow, lower fluctuations in coal seam gases were observed [13]. Results at the longwall panel K.-65/F showed that de-stressing of the coal started to affect the coal gas mixing at a distance of around 70 m in front of the borehole location. $CH_4$ migrates first due to its smaller molecular size compared to $CO_2$ and the fact that it is present free in fractures [2]. Also, $CO_2$ in comparison to $CH_4$ is the most preferred to be adsorbed in the coal structure [15], therefore it can migrate in the coal structure under stress release changes. At a distance of the longwall face from 30 to 50 m from geotechnical measurement points the vertical stresses are so high that the lignite structure collapses [16].

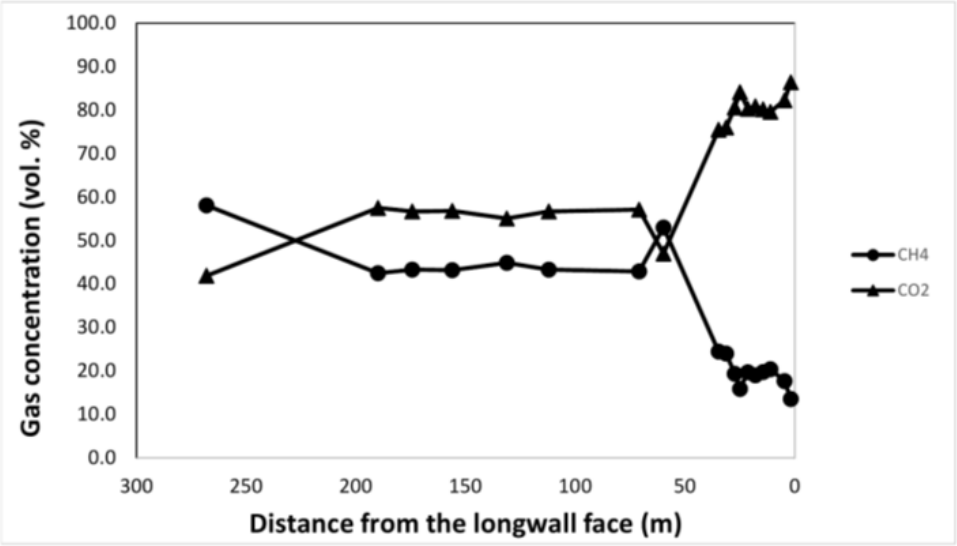


**Figure 2**: Distribution of gas concentration in advancement of the longwall face K.-65/F in Pesje Mine.

The likely sources of $CO_2$ in coal depend on its burial and uplift history and may include dissolved $CO_2$ from the atmosphere and soil gas, microbial degradation of organic substrates, thermal maturation of kerogen, thermal decomposition of carbonates and magmatic/mantle degassing [17]-[19]. For determination of the $CO_2$ origin in the Velenje Basin, CDMI index versus $\delta^{13}C_{CO2}$ chart was used (Figure 3). $CO_2$ of microbial degradation is associated with a relatively low CDMI index ($CO_2$ content less than about 5.0%). Typical $\delta^{13}C_{CO2}$ values of endogenic $CO_2$ are about -7.0‰ with a high CDMI index (>90%). $\delta^{13}C_{CO2}$ derived from carbonates is dependent on the $\delta^{13}C$ value of the carbonates and the temperature of their degradation [20], where values of $\delta^{13}C_{CO2}$ range from -10.0 to -6.0‰. At all four fields the high values of the CDMI index and $\delta^{13}C_{CO2}$ values between -7.0 to -1.8‰ indicate endogenic $CO_2$ and microbial $CO_2$. Area of North Preloge Mine (longwall face G3/C) lies on the carbonate floor strata and the isotopic values of $\delta^{13}C_{CO2}$ indicate $CO_2$ origin from thermal decomposition of dolomites. High CDMI index (up to 98.2 %) and $\delta^{13}C_{CO2}$ values between -2.4 and -1.8‰ show that the origin of $CO_2$ in the longwall panel K.-65/B in Pesje area is endogenic mixed with microbial $CO_2$.

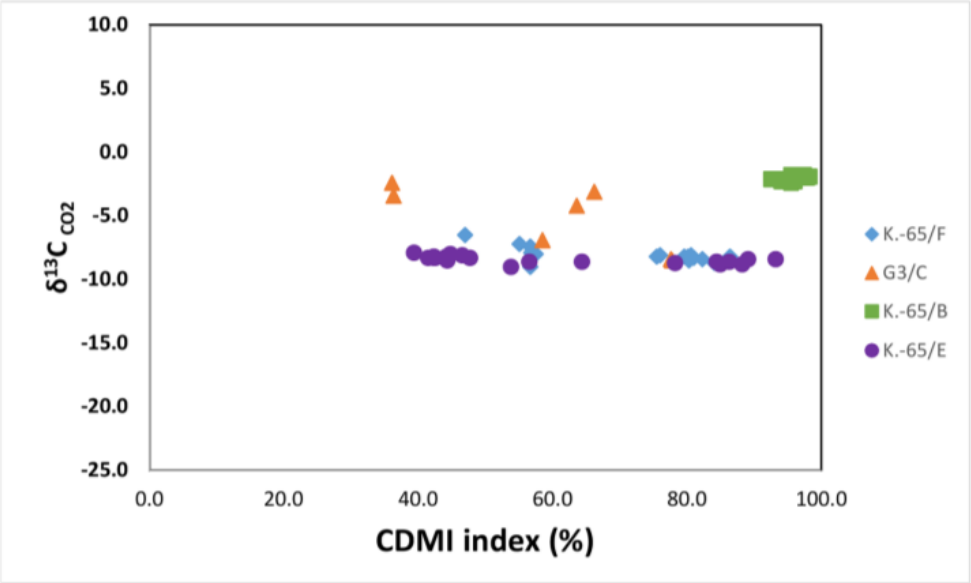


**Figure 3**: Interpretation of the origin of $CO_2$ from the analysed coal seam gas samples from the Velenje Basin using the $\delta^{13}C_{CO2}$ versus CDMI index in the lignite seam ahead of the working face at the longwall faces K.-65/F, G3/C, K.-65/B and K.-65/E.

In most cases $CH_4$ is the dominant component of coalbed gas in high-volatile bituminous and higher rank coals, with secondary amounts of higher molecular weight hydrocarbons and $CO_2$ [21]; on the other hand in the Velenje Basin the dominant component in coal seam gas is $CO_2$. Microbial $CH_4$ has a wide range of C and H isotope ratios, varying in $\delta^{13}C_{CH4}$ from -110‰ to -50‰, and in $\delta^{2}H_{CH4}$ from -400 to -150‰ [22]. Typical $\delta^{13}C_{CH4}$ values of thermogenic $CH_4$ range from -50 to -20‰, whereas biogenic $CH_4$ from microbial acetate fermentation ranges from ~-65 to -45‰. $CH_4$ from microbial $CO_2$ – reduction is even more depleted ranging from ~-110 to -60‰ [23]-[25], while values of $\delta^{13}C_{CO2}$ in the case of microbial methane from $CO_2$ reduction range from ~ 0 to 20‰. Thermogenic $CH_4$ ($\delta^{13}C_{CH4}$ between -50 and -20‰) in Velenje Basin could be generated in the Oligocene marine clays containing high concentrations of organic matter, which were overheated at a depth of over 2000 m and afterwards might have migrated through the main faults Smrekovec, Velenje Fault and fractures in the lignite strata at the time of formation of the Basin [14]. The second explanation of thermogenic $CH_4$ is likely to be connected with secondary chemical processes, which are the results of mining activities in the Velenje Basin. It seems that in the Velenje Basin the reservoir of $CO_2$ was not depleted by methanogens (recently formed $CH_4$) since contact with the

headwaters recharging the Basin is prevented by impermeable strata [14]. Results of $\delta^{13}C_{CH4}$ and $\delta^{2}H_{CH4}$ for coal seam gases in the Velenje Basin reveal that the $\delta^{13}C$ signal in the Velenje Basin has mixed origin (microbial, thermogenic and mixed). Considering gas dryness versus $\delta^{13}C_{CH4}$ in comparison to other coal basins (Bowen Basin, Powder River Basin, Michigan Basin, Illinois basins, northern Appalachian Basin) Velenje Basin fall within 100 % of biogenic and thermogenic gas (Figure 4).

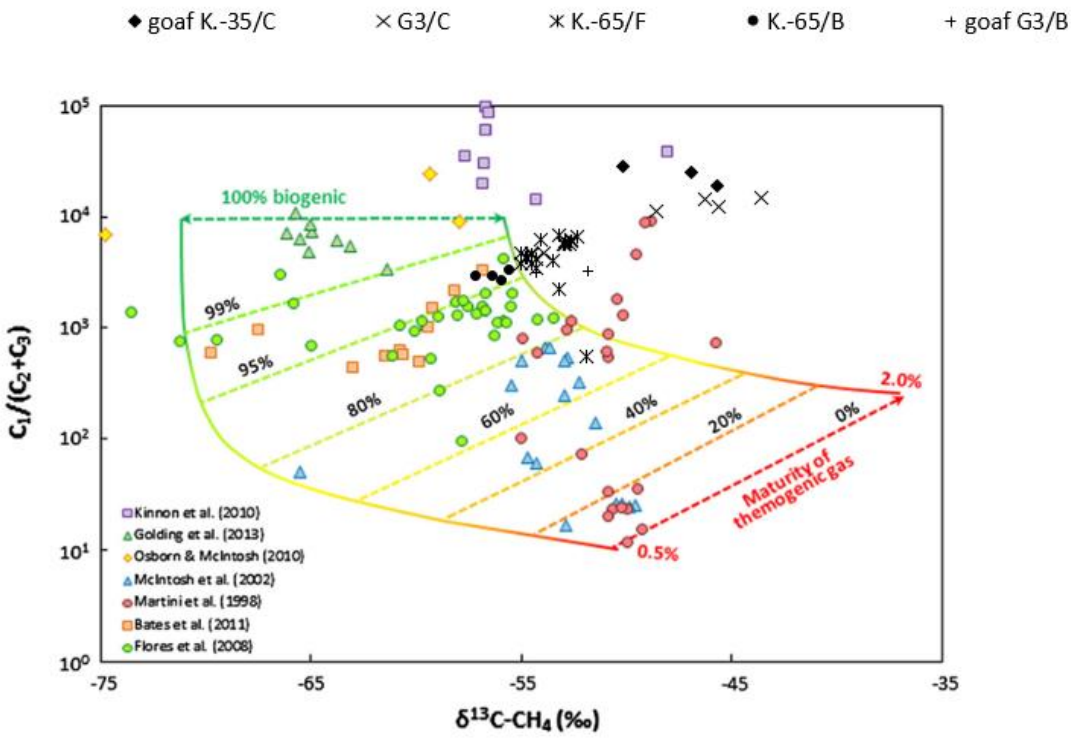


**Figure 4**: Gas dryness (C1/(C2+C3)) versus $\delta^{13}C_{CH4}$ in coal seam gases in Velenje Basin. Gas origin in comparison with the Bowen Basin [19], [26] and the Powder River Basin [27], [10] after [12]

## 5 Conclusion

The study of the Velenje Basin showed that $CH_4$ desorbs more quickly than $CO_2$ as can be observed in the gas composition distribution in advance of the longwall faces from the excavation fields. Interpretation of the $CH_4$ origin in the Velenje Basin is much more complicated (secondary processes) due to excavation of coal and migration of gas, which could lead to additional isotopic fractionation, especially of $CH_4$. Characterization of $CH_4$ from the Velenje Basin is similar to $CH_4$ from low rank coal basins such as the Powder River Basin and the San Juan Basin, USA, while completely different from the Lower and Upper Silesian Basins, Poland. When

interpreting the origin of coal seam gas, especially $CH_4$ in a dynamic system such as the Velenje lignite Basin, all aspects should be taken into account (distance from the longwall, advancement rate of the longwall, location of the excavation fields with depth, pre-mining area and stress state) besides the gas isotopic content ($\delta^{13}C_{CH4}$, $\delta^{13}C_{CO2}$, $\delta^{2}H_{CH4}$) and gas dryness values. Further research is required to determine the origin of coal seam gases and higher hydrocarbons in the Velenje Basin, which should be correlated with the hydrogeochemical characteristics of the Basin.

## References:


[1] S. Zavšek. *Model for research of structural and petrographical changes of the Velenje lignite depending on various stress states and presence of gases.* PhD thesis. University of Ljubljana. Faculty of Natural Sciences and Engineering, Department of Geology, 2004

[2] J.L., Clayton. Geochemistry of coalbed gas – A review. *International Journal of Coal Geology 35, 159-173*, 1998

[3] H. Guoyi, L. Jin, M. Chenghua, L. Zhisheng, Min, Zgang, Z. Qiang. Characteristics and Implications of the Carbon Isotope Fractionation of Desorbed Coalbed Methane in Qinshui Coalbed Methane Field, China. *Earth Science Frontiers 14 (6), 267 – 272,* 2007.

[4] M.J. Kotarba. Composition and origin of coalbed gases in the upper Silesian and Lublin basins, Poland. *Organic geochemistry, 163-180,* 2001

[5] M.J. Kotarba, D.D. Rice. Composition and origin of coalbed gases in the Lower Silesian Basin, northwestern Poland. *Applied Geochemistry, 16, 895-910*, 2001

[6] J.W. Smith, R.J. Pallasser. Microbial origin of Australian coalbed methane. *AAPG Bull. 80, 891 – 897,* 1996

[7] J.W. Smith and K.W. Gould. An isotopic study of the role of carbon dioxide in outbursts in coal mines. *Geochemical Journal 14, 27 – 32*, 1980

[8] M.M. Faiz, A. Saghafi, S.A. Barclay, L. Stalker, N.R. Sherwood, D.J. Whitford. Evaluating geological sequestration of CO2 in bituminous coals. The Southern Sydney Basin, Australia as a natural analogue. *International Journal of Greenhouse Gas Control 1, 223– 235*, 2007

[9] T. Kanduč, J. Pezdič. Origin and distribution of coalbed gases from the Velenje Basin, Slovenia. *Geochemical Journal 39, 397 – 409*, 2005

[10] R.M. Flores, C.A., Rice, G.D. Stricker, A. Warden, M.S. Ellis. Methanogenic pathways of coalbed gas in the Powder River basin, United States: the geological factor. *International Journal of Coal Geology 76, 52– 75,* 2008

[11] S.G. Osborn, J.C. McIntosh. Chemical and isotopic tracers of the contribution of microbial gas in Devenian organic-rich shales and reservoir sandstones, northern Appalachian Basin. *Applied geochemistry 25, 456-471*, 2010

[12] D. Strapoć, M. Mastalerz, K. Dawson, J. Macalady, A.V. Callaghan, B. Wawrik, C. Turich, M. Ashby. Biogeochemistry of microbial coal-bed methane. *Ann. Rev. Earth Planet. Sci. 39, 617-656,* 2011

[13] T. Kanduč, J. Žula, S. Zavšek. Tracing coalbed gas dynamics and origin of gases in advancement of the working faces at mining areas Preloge and Pesje, Velenje Basin. *RMZ – Materials and Geoenvironment 58, 273 – 288,* 2011

[14] T. Kanduč, M. Markič, S. Zavšek, J. McIntosh. Carbon cycling in the Pliocene Velenje Coal Basin, Slovenia, inferred from stable carbon isotopes. *International Journal of Coal Geology 89, 70 – 83,* 2012

[15] S. Mazumder, P. van Hemert, A. Busch, K.-H.A.A. Wolf, P Tejera-Cuesta. Flue gas and pure CO2 sorption properties of coal: A comparative study. *International Journal of Coal Geology, 67, 267-279,* 2006.

[16] S. Zavšek. *Projekt raziskovalne proge na k. +75 v jami Škale, projektna študija, rudarski projekt, REK Velenje,* DO Rudnik Lignita Velenje, Premogovnik Velenje, Hidrogeološki oddelek, 30 pp. (in Slovene), 1990

[17] J.X. Dai, Y. Song, C.S. Dai, D.R. Wand. Geochemistry and accumulations of carbon dioxide gases in China. *American Association of Petroleum Geologists Bulletin 80, 1615 – 1626,* 1996

[18] H. Wycherley, A. Fleet, H. Shaw. Some observations on the origins of large volumes of carbon dioxide accumulation in sedimentary basins. *Marine and Petroleum Geology 16. 489 – 494,* 1999

[19] S.D. Golding, C.J. Boreham, J.S. Esterle. Stable isotope geochemistry of coal bed and shale gas and related production waters: A review. *International Journal of Coal Geology 120, 24 – 40,* 2013

[20] T., Kanduč, J. Pezdič, S. Lojen, S. Zavšek. Study of the gas composition ahead of the working face in a lignite seam from the Velenje Basin. *RMZ- Materials and Geoenviroment 50, 503– 511,* 2003

[21] D.D. Rice, B.E. Law, J.L. Clayton. Coalbed gas – an undeveloped resource. The Future of Energy Gases, *U.S. Geological Survey Professional Paper 1570, 389 – 404*, 1993

[22] M.J., Whiticar. Carbon and hydrogen isotope systematics of bacterial formation and oxidation of methane. *Chemical Geology 161, 291 – 314*, 1999

[23] A.R., Scott, W.R. Kaiser, W.D. Ayers Jr. Thermogenic and secondary biogenic gases, San Juan Basin, Colorado and New Mexico – implication for coalbed gas production. *American Association of Petroleum Geologists Bulletin, 78, 1186 – 1209*, 1994.

[24] M.O. Jedrysek. Carbon isotope evidence for diurnal variations in methanogenesis in freshwater lake sediments. *Geochimica et Cosmochimica Acta 59, 557 – 561,* 1995.

[25] M.J. Whiticar. Stable isotope geochemistry of coals, humic kerogens and related natural gases. *International Journal of Coal Geology 32, 191 – 215*, 1996.

[26] E.C.P. Kinnon, S.D. Golding, C.J. Boreham, K.A. Baublys, J.S. Esterle. Stable isotope and water quality analysis of coal bed methane production waters and gases from the Bowen Basin, Australia. *International Journal of Coal geology 82, 219-231,* 2010.

[27] B.L. Bates, J.C. McIntosh, K.A. Lohse, P.D. Brooks. Influence of groundwater flowpaths, residence times and nutrients on the extent of microbial methanogenesis in coal beds: Powder River Basin, USA. *Chemical Geology 284, 45-61*, 2011.

## For wider interest

In underground coal mines high coal seam gas content can present a potential risk for miners. The aim of this study was to determine coal seam gas composition and its origin, which is one of the tasks of Clean Coal Technologies research group at Velenje Coal Mine. The results were analysed and compared with other coal basins from the world. Knowing the composition and origin of coal seam gas we can predict and prevent coal seam gas outburst. Also understanding of the geochemical processes occurring in the coal seam in addition to the geotechnical characteristics of the coal can help to establish the coal seam gas drainage system. The drainage system in the Velenje Coal Mine will reduce ventilation costs and improve safety in the working place for the miners.

# Determination of PBDEs in environmental water samples by GC-ICP-MS

**Petra Novak**[1,2], **Tea Zuliani**[1], **Radmila Milačič**[1,2], **Janez Ščančar**[1,2]

[1] Department of Environmental Sciences, Jožef Stefan Institute, Ljubljana, Slovenia

[2] Jožef Stefan International Postgraduate School, Ljubljana, Slovenia

petra.novak@ijs.si

**Abstract.** Polybrominated diphenyl ethers (PBDEs) belong to the group of brominated flame retardants, which are added to different industrial products such as plastics, textiles, electronic equipment and building materials. Due to their widespread use PBDEs are frequently present as pollutants in all parts of the environment. They belong to lipophilic poorly degradable persistent organic pollutants (POPs) that are via food chain bioaccumulated or biomagnified in living organisms. In human, PBDEs may disrupt thyroid hormones and reproductive organs.

In the EU Water Framework Directive (WFD) six PBDE congeners (BDE 28, BDE 47, BDE 99, BDE 100, BDE 153 and BDE 154) are listed as priority substances. To prevent pollution of the aquatic environment, WFD recommends their regular monitoring. To meet the WFD requirements, highly sensitive analytical procedure for the determination of six PBDEs in environmental water samples by gas chromatography – inductively coupled plasma mass spectrometry (GC-ICP-MS) was developed. To demonstrate the applicability of the newly developed GC-ICP-MS procedure, PBDEs were determined in river and sea water samples.

**Keywords**: polybrominated diphenyl ethers; environmental waters; gas chromatography-inductively coupled plasma mass spectrometry; water framework directive

## 1 Introduction

Polybrominated diphenyl ethers (PBDEs) belong to the group of brominated flame retardants, which are added to different industrial products such as plastics, textiles, electronic equipment and building materials [1]. After use such products are

disposed of to landfills. PBDEs can be easily released from these materials, to which they are not chemically bonded, into the terrestrial or aquatic environment and, to a lesser extent, to the air [2]. PBDEs belong to a class of lipophilic poorly degradable persistent organic pollutants (POPs) that are bioaccumulated via the food chain or biomagnified in living organisms. Increasing concentrations of PBDEs in human tissues have caused worldwide health concerns due to their tendency to disrupt the functioning of thyroid hormones and reproductive organs [3].

The European Union (EU) banned the use of their commercially available mixtures in 2004 and 2008). Despite the bans PBDEs will continue to be released from existing products into the environment for many years and will remain environmental problem for the foreseeable future.

The European Union Water Framework Directive (WFD) included six BDE congeners (BDE 28, BDE 47, BDE 99, BDE 100, BDE 153 and BDE 154) in the group of priority hazardous substances [4]. For their determination highly sensitive, selective and accurate analytical methods should be used that can meet the required limit of quantification (LOQ) set by the WFD. To prevent pollution of the aquatic environment, WFD recommends regular monitoring of the six PBDE congeners.

The aim of our study was to develop an analytical procedure that would meet the requirements set by the WFD for very sensitive and reliable determination of the six PBDE congeners in environmental water samples by GC-ICP-MS. For this purpose the parameters influencing GC-ICP-MS detection and the extraction procedure were optimised. To improve the extraction efficiency of PBDEs from water into iso-octane by liquid – liquid extraction, the use of sodium acetate – acetic acid or Tris – citrate buffer was tested. The accuracy of the analytical procedure was checked by spike recovery tests and by applying species-specific isotope-dilution (ID) GC-ICP-MS quantification. The stability of PBDEs in acidified and non-acidified spiked surface water samples was checked over a time span of more than 30 days. To demonstrate the applicability of the GC-ICP-MS analytical procedure developed, PBDEs were determined in river and sea water samples.

# 2 Materials and methods

## 2. 1 Instrumentation

The analysis of PBDEs was carried out on an Agilent 6890 gas chromatograph (GC) (Agilent Technologies, Santa Clara, CA, USA) equipped with an Agilent 6890 Series Autosampler Injector. The GC was coupled to an Agilent 7700x ICP-MS via a heated transfer line and fitted with a 15 m x 0.25 mm DB-5MS capillary column (film thickness 0.25 μm) coated with 5 % phenylmethylpolysiloxane (Agilent J&W Scientific, Palo Alto, CA, USA). Control and operation of the coupled system was performed using Agilent MassHunter software.

For the separation of PBDEs on a 15 m column, the following GC temperature program was applied: at the start the column temperature was raised from 120 °C to 300 °C at a heating rate of 30 °C $min^{-1}$ and held there for 5 min. The inlet temperature and transfer - line was held at 280 °C. Helium at a flow rate of 1.5 mL $min^{-1}$ was used as carrier gas, the injection mode was split-less and the injection volume 2 μL. The operating parameters of the GC-ICP-MS system are presented in Table 1.

**Table 1:** ICP-MS and GC operating parameters

| *ICP-MS* | Unit |
|---|---|
| RF power | 1300 W |
| Sample depth | 7.0 mm |
| Carrier gas (Ar) | 1.50 L $min^{-1}$ |
| Optional gas (20 % $^{v}/_{v}$ $O_2$ in Ar) | 10 % |
| Integration time per isotope | 0.1 s |
| Isotopes measured | $^{79}Br$, $^{81}Br$ |
| Tune gas | 100 ppm Xe in Ar |
| Total acquisition time | 666 s |
| *GC* | Unit |
| Injection volume | 2 μL |
| Mode | Splitless |
| Carrier gas (He) | 1.50 mL $min^{-1}$ |
| Inlet temperature | 280 °C |
| Transfer line temperature | 280 °C |

## 2. 2 Analytical procedure

Liquid – liquid extraction of PBDEs from water samples was used prior to their determination by GC-ICP-MS. Briefly, a 300 mL sample aliquot, acidified with nitric

acid to pH 2 (1 mL $HNO_3$ per 1 L of water), was transferred to a 1 L glass reactor vessel. As internal standard BDE 77 was added, followed by the addition of 300 mL Tris – citrate buffer solution (pH 6). Then 2 mL of iso-octane was added as extracting agent. Samples were mechanically shaken for 6 h. After that the organic phase was collected and concentrated under a gentle nitrogen flow to a final volume of approximately 25 μL. Finally the organic phase was collected in a 2 mL amber vial by a Pasteur pipette and 2 μL injected into the GC. Analysis was made by GC-ICP-MS and the concentrations of PBDEs calculated by both the standard addition calibration method and isotope dilution GC-ICP-MS procedure. Blank samples were determined under the same analytical protocol.

# 3 Results and discussion

## 3.1 Optimization of the GC-ICP-MS operating parameters

By applying a 15 m chromatographic column, the GC temperature programme and GC operating parameters described under *2.1. Instrumentation*, all PBDEs were efficiently separated. In order to obtain the best signal intensities for the determination of the separated PBDEs, ICP-MS operating parameters were further optimized by modifying the ICP RF power, the flow rate of carrier gas and by addition of oxygen as optional gas. The results are presented in Figure 1.

The highest signal intensities for all the PBDEs investigated were obtained at an ICP RF power of 1300 W (Figure 1A). At this RF power, the flow rate of carrier gas was then optimized. As can be further seen from Figure 1B the most intensive signals were obtained at a carrier gas flow rate of 1.5 L $min^{-1}$. Finally, the influence of the addition of optional gas was examined. The data in Figure 1C demonstrate that addition of oxygen in optional gas substantially improved the signal sensitivity. This phenomenon is related to carbon removal, which was the most efficient on addition of 10 % of optional gas containing 20 % $^{v}/_{v}$ $O_2$ in Ar.

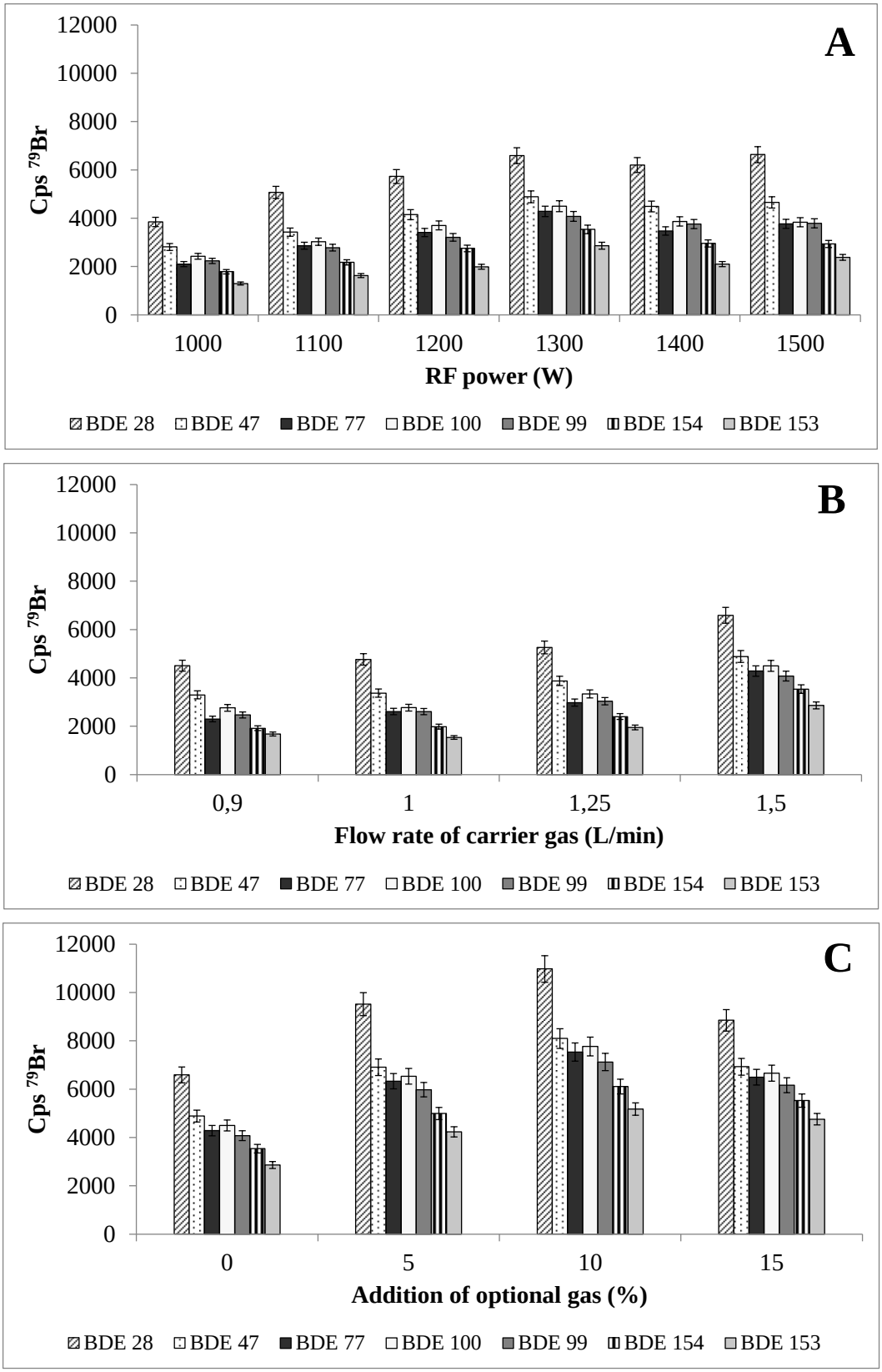


**Figure 1 :** Influence of ICP RF power (A), the flow rate of carrier gas (B) and addition of optional gas (20 % $^{v}/_{v}$ $O_2$ in Ar) (C) on signal intensities of PBDEs (400 ng $L^{-1}$).

## 3.2 Optimization of the extraction procedure

### Influence of different sample treatments on extraction efficiency

Signal intensities of PBDEs for different sample treatments are presented in Fig. 2.

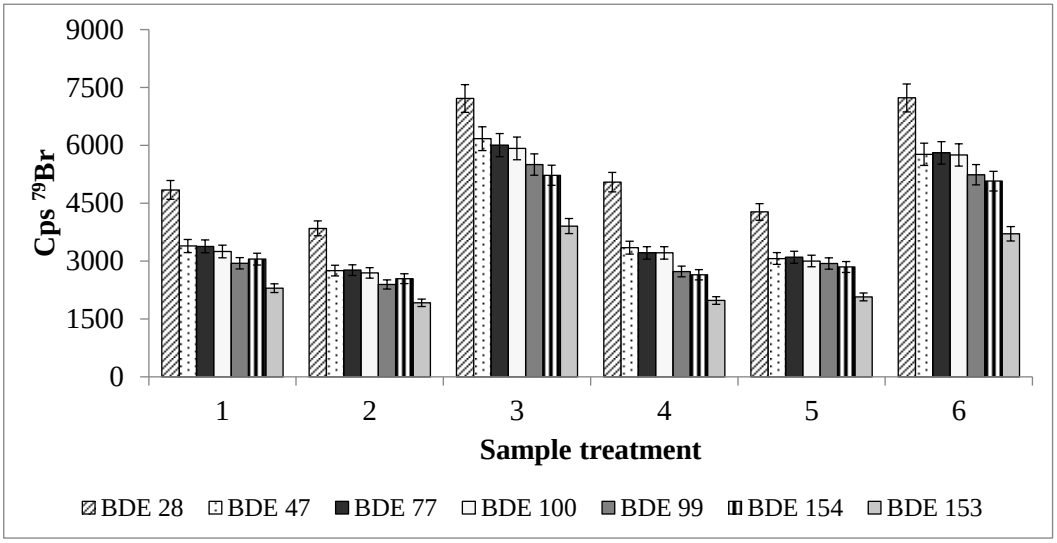


**Figure 2 :** Influence of different sample treatments on signal intensities of spiked river water sample containing PBDEs (400 ng $L^{-1}$). 1: Non-acidified sample. 2: Non-acidified sample followed by the addition of acetate buffer (pH 4.8). 3: Non-acidified sample followed by addition of Tris-citrate buffer (pH 6). 4: Sample acidified with $HNO_3$ (pH 2). 5: Sample acidified with $HNO_3$ to pH 2, followed by addition of acetate buffer (pH 4.8). 6: Sample acidified with $HNO_3$ to pH 2, followed by addition of Tris-citrate buffer (pH 6).

From the experimental results, it is evident that the use of Tris-citrate buffer facilitates the extraction of PBDEs from the matrix of the water sample analysed, as it almost doubles the signal intensities for both non-acidified and acidified samples in comparison to those samples where no Tris-citrate buffer or acetate buffer was used. Hence, in further experiments the stability of PBDEs over a time span of 30 days was followed in non-acidified and acidified water samples using Tris-citrate buffer in the liquid – liquid extraction stage.

Data from Figure 3 clearly demonstrate that non-acidified samples are stable only for one day, while samples acidified prior to Tris-citrate buffer addition are stable for at least 20 days. Acidification of the sample prevents adsorption of PBDEs on the surface of the glass bottles, while citric acid enables efficient desorption of PBDEs

from SPM. For that reason, acidified samples, buffered to pH 6 with Tris-citrate buffer, were used in all the following experiments.

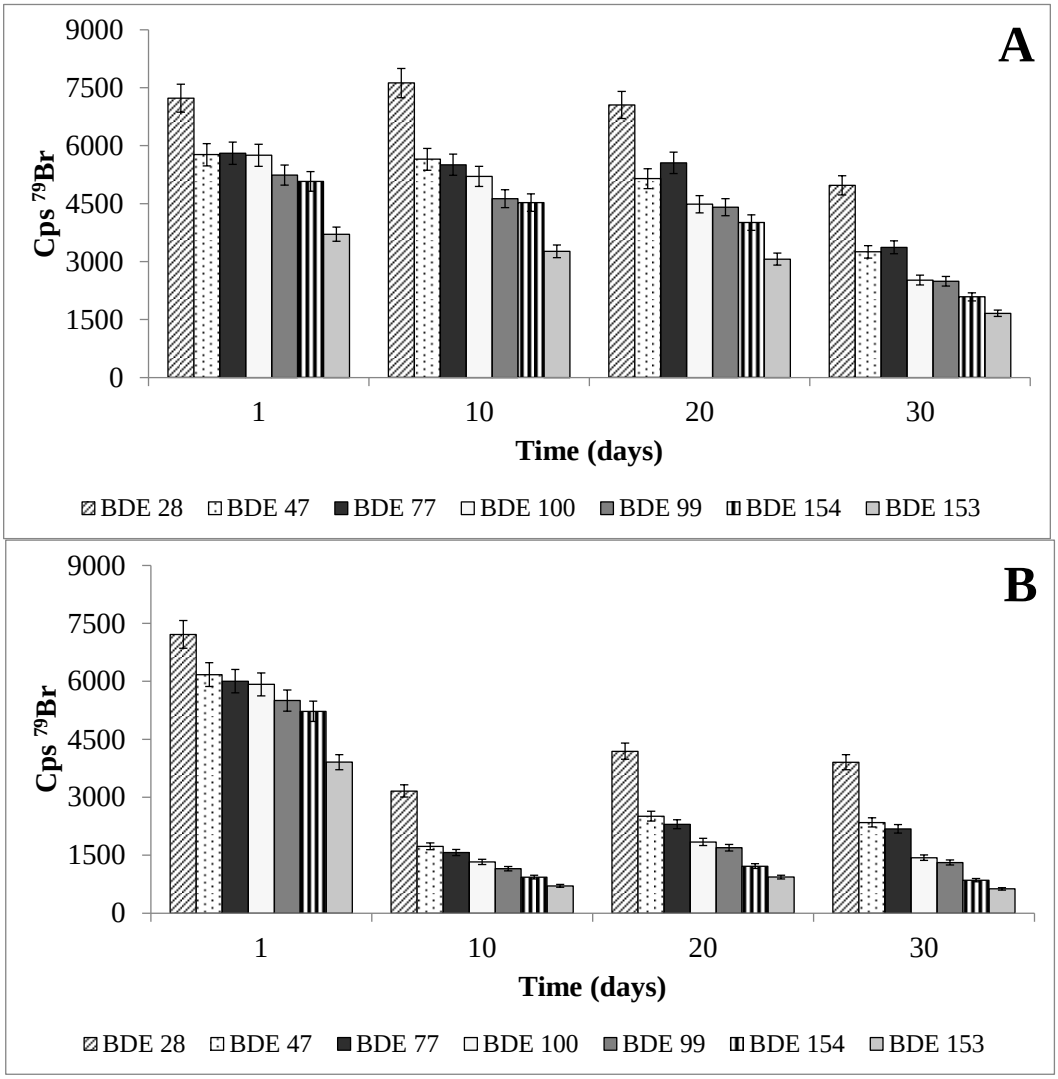


**Figure 3 :** Stability of acidified (A) and non-acidified (B) river water samples spiked with PBDEs (400 ng $L^{-1}$).

## 3.3 Limits of detection and quantification

Samples of Milli Q water and saline water (3.8 % NaCl) containing 35 mg $L^{-1}$ of suspended particulate matter (SPM) and 5 mg $L^{-1}$ of humic acids (HA) were prepared. The corresponding LODs and LOQs are presented in Table 2. They are below 0.15 ng $L^{-1}$, the LOQ for the ∑PBDEs required by the WFD [4].

**Table 2:** LODs and LOQs of analytical method for the determination of PBDEs in water and saline water (3.8 % NaCl) samples containing 35 mg $L^{-1}$of SPM and 5 mg $L^{-1}$of HA.

| BDE congener | Water | | Saline water | |
|---|---|---|---|---|
| | LOD (ng $L^{-1}$) | LOQ (ng $L^{-1}$) | LOD (ng $L^{-1}$) | LOQ (ng $L^{-1}$) |
| BDE 28 | 0.0054 | 0.018 | 0.0052 | 0.017 |
| BDE 47 | 0.0048 | 0.016 | 0.0054 | 0.018 |
| BDE 100 | 0.0052 | 0.017 | 0.0047 | 0.016 |
| BDE 99 | 0.0059 | 0.020 | 0.0051 | 0.017 |
| BDE 154 | 0.0051 | 0.017 | 0.0054 | 0.018 |
| BDE 153 | 0.0064 | 0.021 | 0.0051 | 0.017 |
| ΣPBDEs | / | 0.109 | / | 0.103 |
| ΣPBDEs set by WFD | / | 0.15 | / | 0.15 |

### 3.4 Analysis of PBDEs in environmental water samples

The newly developed GC-ICP-MS analytical procedure was applied for the determination of PBDEs in several Slovenian river water samples. For the water samples from the river Drava sampled at Brezno, the river Krka at Otočec, the Gradaščica at Šujica and the Hruševnik rivulet at Hruševo, the concentrations of the six BDE congeners were below the LODs. In addition, sea water samples from the Northern Adriatic were also analysed. A chromatogram of sea water from the Izola Marina is presented in Fig. 4, while the results of the analyses of sea water samples are presented in Table 3.

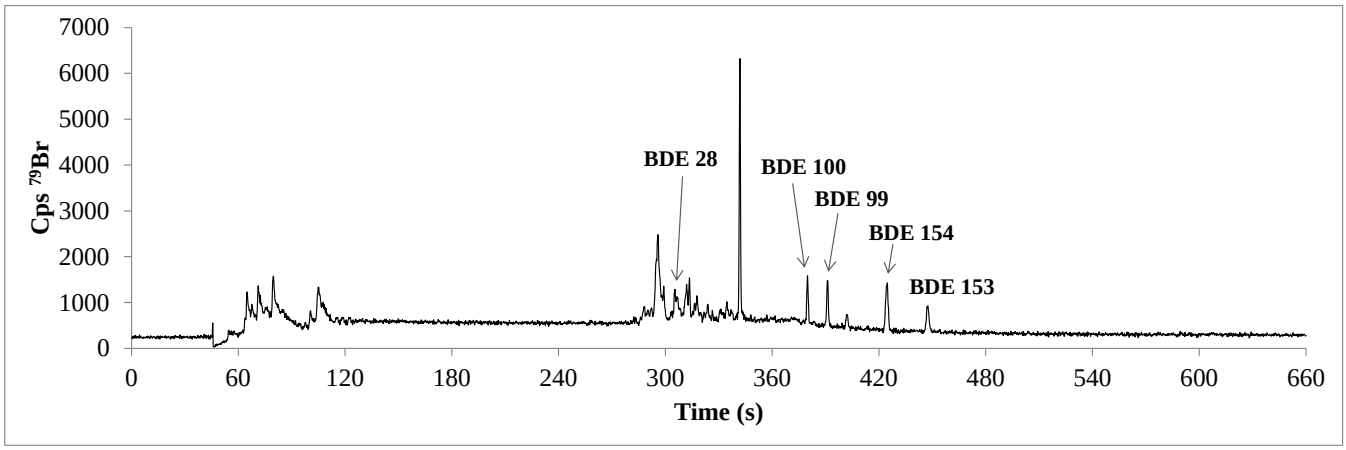


**Figure 4 :** Chromatogram of PBDEs in marine water sample from Izola Marina (sample volume 300 mL)

**Table 3 :** Concentrations of PBDEs found in sea water samples from the Northern Adriatic (Slovenia)

| PBDE listed by WFD (ng $L^{-1}$) | Bele skale beach | Strunjan Nature Reserve | Izola Marina | Port of Koper |
|---|---|---|---|---|
| BDE 28 | 1.14±0.03 | <0.0052 | 0.053±0,004 | 0.540±0.016 |
| BDE 47 | <0.0054 | <0.0054 | <0.0054 | <0.0054 |
| BDE 99 | <0.0051 | <0.0051 | 0.094±0.003 | 0.125±0.004 |
| BDE 100 | 0.160±0.005 | <0.0047 | 0.074±0.002 | 0.178±0.006 |
| BDE 153 | <0.0051 | 0.213±0.006 | 0.051±0.002 | <0.0051 |
| BDE 154 | <0.0054 | 0.153±0.006 | 0.085±0.003 | 0.108±0.004 |
| ∑PBDEs | 1.3 | 0.366 | 0.357 | 0.951 |

## 4 Conclusions

A new analytical procedure was developed for the determination of PBDEs in environmental water samples by GC-ICP-MS. The instrumental parameters were optimized for efficient separation and sensitive detection of six PBDEs from the list of priority substances of the WFD, and the parameters that influence the extraction efficiency and sample stability investigated. When a 300 mL sample was analysed, and the organic phase concentrated to 25 μL, the LOQ for ∑PBDEs in river water was 0.109 ng $L^{-1}$ and was below the 0.15 ng $L^{-1}$ limit value required by the WFD. The analytical procedure developed was successfully applied for reliable determination of the six PBDEs congeners in environmental water samples.

## References:


[1] S. Król, B. Zabiegała and J. Namieśnik. PBDEs in environmental samples: sampling and analysis. *Talanta*, 93:1-17, 2012

[2] C.A. De Witt. An overview of brominated flame retardants in the environment. *Chemosphere*, 46:583-624, 2002

[3] A.P. Vonderheide, K.E. Mueller, J. Meija and G.L. Welsh. Polybrominated diphenyl ethers: causes for concern and knowledge gaps regarding environmental distribution, fate and toxicity. *Sci. Tot. Environ.*, 400:425-436, 2008.

[4] Directive 2008/105/EC of the European Parliament and of the Council of 16 December 2008 on environmental quality standard in the field of water policy. *Official Journal Of the European Union*. 348:84-97, 24.12.2008

## For wider interest

Polybrominated diphenyl ethers (PBDEs) belong to the group of brominated flame retardants. They are lipophilic persistent organic pollutants that are via food chain bioaccumulated or biomagnified in living organisms. Increasing concentrations of PBDEs in human tissues have caused health concern since they disrupt functioning of thyroid hormones and reproductive organs. The EU Water Framework Directive (WFD) listed six PBDE congeners (BDE 28, BDE 47, BDE 99, BDE 100, BDE 153 and BDE 154) to a group of priority pollutants. In the present work selective, sensitive and reliable analytical procedure was developed for determination of PBDEs in environmental water samples by GC-ICP-MS. With limit of quantification < 0.15 ng $L^{-1}$ for the sum of the six PBDE congeners, the procedure developed fulfils the requirements of the WFD for their regular monitoring in surface waters.

# Isotopically enriched tin tracers: a powerful tool to study the transformation of organotin compounds in landfill leachate

**Kelly Peeters**[1,2], **Tea Zuliani**[1], **Janez Ščančar**[1,2], **Radmila Milačič**[1,2]

[1] Department of Environmental Sciences, Jožef Stefan Institute, Jamova 39, 1000 Ljubljana, Slovenia
[2] Jožef Stefan International Postgraduate School, Ljubljana, Slovenia
kelly.peeters@ijs.si

**Abstract.** The present study is an evaluation of the process of biomethylation and degradation of OTC by microorganisms within leachates. Leachates were each spiked with another Sn-enriched isotopic tracer: $^{117}$Sn-enriched tributyltin, $^{117}$Sn-enriched $SnCl_2$ and $^{117}$Sn-enriched $SnCl_4$. This allowed simultaneous observation of the transformation of OTC in the leachate itself and of the added spike. Based on the analysis of OTC by GC-ICP-MS, The transformation processes in the spiked leachates were followed for 6 months or 10 days. To discriminate between biotic and abiotic transformations, data from sterilized leachates was compared with non-sterilized samples. During the course of the experiment the biotic degradation of TBT to inorganic tin was clearly observed. Methyltin products were only formed when the leachate was spiked with concentrations of $SnCl_2$ or $SnCl_4$, close to that found for total tin in landfill leachates. Hydrolysis of $Sn^{2+}$ and $Sn^{4+}$ species was found to control the extent of methyltin formation.

**Key words:** landfill leachate, organotin compounds, Sn-enriched isotopic tracers, gas chromatography - inductively coupled plasma mass spectrometry.

## 1 Introduction

Organotin compounds (OTC) are chemicals that possess a tetravalent tin atom, which is covalently bound to 1-4 alkyl or aryl groups [1]. Organotin compounds (OTC) have a wide spectrum of physical, chemical and biological properties. That is why a larger number of organometallic derivatives of tin are commercially used in comparison to any other element. The most important applications of OTC are as biocides in agriculture, textiles, antifouling paints and in timber treatment, or as heat and light stabilizers in PVC. Because of the enormous growth in its industrial production and applications, considerable amounts of OTC have entered various ecosystems [2]. OTC are among the most hazardous pollutants known so far to be ever introduced in aquatic ecosystems by men. They are highly toxic,

even at ng $L^{-1}$ concentration levels, with high bioacummulation potential into different organisms. In the marine environment imposex in dogwhelk populations was observed, while in mammals including humans, OTC are neurotoxic and endocrine disrupters [3].

In addition to different environmental samples, OTC are also present in plastic materials and manufactured household products, while tin metal is used mostly in cans for food packing. [4]. The collection of this products as municipal waste on landfill sites is one of the most commonly employed waste management systems over the world. In this way, a landfill can be considered to be an important pool of OTC. Inorganic tin and OTC can be easily mobilised and likely released in the environment by the percolation of water through the garbage pile. To prevent that leached water comes in contact with surface or groundwater, a pond that collects leachates is constructed. The environments in landfills are generating conditions to transform inorganic tin and OTC by hydridation, methylation, ethylation, dealkylation or transalkylation reactions [5].

In our previous work the occurrence of OTC in leachates from the landfill Barje, Slovenia, was investigated [6]. The data revealed that the prevailing OTC found in leachates were methyltin and butyltin species. To better understand the processes that OTC undergo in leachates the emphasis in present work was to follow the degradation and biomethylation processes of OTC in leachate. For this purpose, the leachates were spiked with a different Sn-enriched isotopic tracers, namely $^{117}$Sn-enriched $SnCl_2$, $^{117}$Sn-enriched $SnCl_4$ and $^{117}$Sn-enriched TBT. The transformation processes were followed over a period of 10 days for the ionic tin species or six months for TBT. Quantification of OTC was performed by GC-ICP-MS.

# 2 Materials/ Methods

## 2.1 Instrumentation

The analysis of organotin compounds was carried out on an Agilent 6890 gas chromatograph (GC) (Agilent Technologies, Santa Clara, CA, USA) equipped with Agilent 6890 Series Autosampler Injector that was coupled to an Agilent 7700x ICPMS via a heated transfer line and fitted with a 15m x 0.25 mm DB-5MS capillary column (film thickness 0.25 μm) coated with 5 % phenylmethylpolysiloxane (Agilent J&W Scientific, Palo Alto, CA, USA). Control and operation of the coupled system was performed by using Agilent MassHunter software.

For the separation of OTC on a 15 m column, the following GC temperature program was applied: at the start, the column temperature was held at 50 °C for 0.8 min, then raised to

200 °C at a heating rate of 20 °C $min^{-1}$ and held there for 2 min, then raised to 220 °C at a heating rate of 40 °C $min^{-1}$ and held there for 0.5 min and, in a final step, raised to 280 °C at a heating rate of 50 °C $min^{-1}$ and held at this temperature for 2 minutes. Inlet temperature was held at 240 °C and transfer - line at 280 °C. Helium at a flow rate of 1 mL $min^{-1}$ was used as a carrier gas, the injection mode was split-less and the injection volume 2 μL.

Mechanical shaking of samples during the extraction was performed on orbital shaker Vibromix 40 (Tehtnica).

## 2.2 Reagents

The in house synthesized enriched spikes of TBT, $SnCl_2$ and $SnCl_4$ were prepared, starting from a $^{117}$Sn-enriched metal plate ($^{117}$Sn, 97 %) (Cambridge Isotope Laboratories Inc., MA, USA).

To synthesize the ionic tin spikes, suprapur hydrochloric and nitric acid ($HNO_3$) purchased from Merck (Darmstadt, Germany) were used.

For the sample preparation prior to ICP-MS analysis, citric acid monohydrate (p.a.) and Tris (hydroxymethyl)aminomethane (Tris) (p.a.) were obtained from Merck (Darmstadt, Germany). Hexane and methanol were from J.T. Baker (Deventer, Holland). Sodium tetraethyl borate ($NaBEt_4$, 98 %) was obtained from Strem Chemicals (Newburyport, MA, USA). The aqueous solution of $NaBEt_4$ (2 % (w/v)) was prepared just before derivatization. The Tris-citrate buffer was prepared weekly. Milli-Q water (18.2 MΩ) (Milipore, Bedford, MA, USA) was used for the preparation of all aqueous solutions.

The standards for quantification, monobutyltintrichloride ($MBTCl_3$, 95%) and tributyltinchloride (TBTCl, 96 %) were purchased from Aldrich (Milwaukee, WI, USA). Monomethyltin trichloride ($MMETCl_3$, 98 %), dimethyltin dichloride ($DMeTCl_2$, 95 %) and trimethyltin chloride (TMeTCl, 99 %) were purchased from Acros Organics (New Jersey, NY, USA). Dibutyltindichloride ($DBTCl_2$, 98 %) and tripropyltin chloride (TPrTCl, 98 %) were obtained from Merck. OTC standard stock solutions containing 1000 mg (expressed as Sn $L^{-1}$) were prepared in methanol and stored in the dark at 4 °C. Working OTC standard solutions were prepared daily.

## 2.3 Preparation of the Sn-enriched spikes

Tin(IV) chloride ($SnCl_4$) was prepared by adding 1 mL of aqua regia to 5 mg of an enriched $^{117}$Sn-enriched metal plate. Tin(II) chloride ($SnCl_2$) was prepared by adding 1 mL of

concentrated HCl to 5 mg of an enriched $^{117}$Sn-enriched metal plate and warm it to 160 °C on a hot plate.

The in-house synthesis of $^{117}$TBTCl was performed starting from a $^{117}$Sn-enriched metal plate, which is first brominated to form $SnBr_4$. This process is immediately followed by butylation to get tetrabutyltin ($^{117}$TeBT) and the final addition of HCl gives $^{117}$TBTCl. The reaction mixture was stored at 4 °C in the dark in 10 mL of methanol. [7]

### 2.4 Sampling

Sampling of the leachates was performed in the non-hazardous municipal waste landfill Barje, Ljubljana, Slovenia. 15 L of sample was taken from a leachate control well of the active landfill basin by an aluminium bucket from the bottom of the well, poured into 15 L polyethylene bottle and directly transported to the laboratory. There 2 L of leachates were then transferred in 3 L amber glass bottles and immediately spiked with Sn-enriched standards.

### 2.5 Experimental set-up

The experimental set-up consisted out of three duplicates of 3 L amber bottles, each filled with 2 L of landfill leachate sample, 6 overall. Spiking was performed with $^{117}$Sn-enriched TBT, $^{117}SnCl_2$ or $^{117}SnCl_4$. $^{117}$TBT was added in a concentration of 920 ng Sn $L^{-1}$, containing 190 ng Sn $L^{-1}$ of $^{117}$Sn-enriched dibutyltin ($^{117}$DBT), while $^{117}SnCl_2$ and $^{117}SnCl_4$ were added in a concentration of 100 μg Sn $L^{-1}$. All bottles were tightly closed with aluminium covered caps, shaken to get homogeneous samples and/or equilibration of spikes and held at conditions similar to that on the active landfill basin. The transformations of the Sn-enriched OTC spikes in the leachates were followed over a time span of six months.

### 2.6 Speciation analysis

Speciation analysis was carried out under a previously optimised procedure [6]. For derivatization $NaBEt_4$ was used. Ethylated OTC were extracted into 2 mL of hexane and speciation analysis performed by GC-ICP-MS. Calculation of OTC concentrations were done by the standard addition calibration method.

## 3 Results and discussion

Concentrations of $^{117}Sn^{2+}$ and $^{117}Sn^{4+}$ (100 μg Sn $L^{-1}$), which were close to the total Sn concentrations found in the investigated landfill leachate and those reported in the literature [5], were added. The concentrations of methyltin species were determined 3 and 10 days after spiking.

As can be seen in Fig. 1, after 3 days, only $^{117}$MMeT was formed from both, $^{117}Sn^{2+}$ and $^{117}Sn^{4+}$. During longer incubation time $^{117}$DMeT and $^{117}$TMeT were also formed, most probably from $^{117}$MMeT, which was the methyltin species first observed. The results of our experiments demonstrate that methylation processes in the leachate are carried out from both, $Sn^{2+}$ and $Sn^{4+}$. Ridley et al. [8] proposed a mechanism in which $Sn^{2+}$ is oxidised to a stanyl radical in the presence of Fe(III) and Mn(IV) in the leachate, while $Sn^{4+}$ can be reduced by the available organic matter, also forming a stanyl radical. Homolytic cleavage of methylcobalamin by this stanyl radical gives MMeT. By stepwise methylation DMeT and TMeT species are formed. The transfer of a methyl group from methylcobalamin to tin is also possible as a carbonium or carbanion [9]. From Fig. 1 it may be further seen that due to higher of hydrolysis for $Sn^{4+}$, which is a stronger Lewis acid [10], lower concentration of monomethyltin is formed.

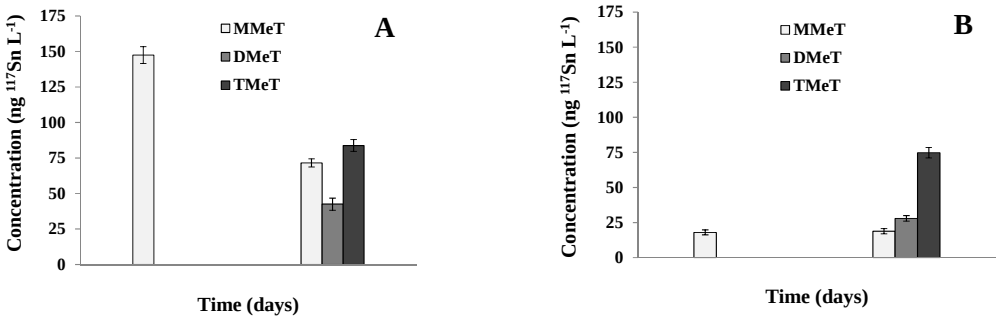


**Figure 1:** Transformation of methyltin compounds in landfill leachates over a time span of 10 days. Landfill leachate was spiked with (A) 100 μg Sn $L^{-1}$ of $^{117}$Sn-enriched $SnCl_2$ or (B) 100 μg Sn $L^{-1}$ of $^{117}$Sn-enriched $SnCl_4$. The concentrations were determined at m/z 117.

From Fig. 2A it may be seen that in house prepared $^{117}$TBT contained also about 20 % of $^{117}$DBT. Nevertheless, it was possible to follow the transformation processes of $^{117}$TBT. Extensive biodegradation of $^{117}$TBT through a stepwise debutylation process is observed during the course of the experiment. Since at the end of the experiment the sum of concentrations of $^{117}$Sn-enriched butyltins was lower than the starting concentration of the spike, it means that $^{117}$MBT was, next to its formation, also progressively degraded to ionic tin. Methyltins were not formed from the added Sn-enriched butyltin spikes, most probably due to the fact that in aqueous solutions $Sn^{2+}$ and $Sn^{4+}$ have a strong tendency to hydrolyze. Reaction with water yields sparingly soluble tin hydroxides [10]. So the TBT concentration was far too low to produce by degradation a sufficient concentration of inorganic tin, which could be further methylated by bacteria.

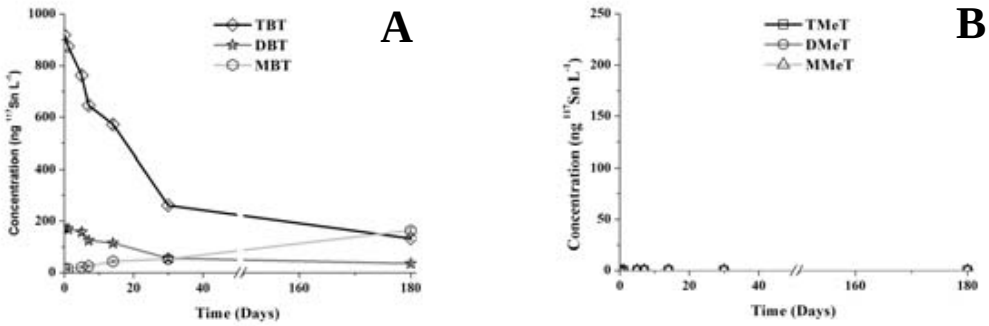


**Figure 2:** Transformation of OTC in landfill leachates over a time span of 6 months. Landfill leachate was spiked with $^{117}$Sn-enriched TBT (920 ng Sn $L^{-1}$) and the concentrations determined at m/z 117 for (A) butyltin compounds and (B) methyltin compounds.

To discriminate the biotic and abiotic transformations of $^{117}$TBT and inorganic tin species, sterilization of leachate was also performed and data compared to non-sterilized samples. During the course of the experiment no degradation of $^{117}$TBT is observed in sterilized spiked samples, while in non-sterilized samples about 40% of $^{117}$TBT added was degraded within 10 days. Based on these observations it may be concluded that degradation of TBT in non-sterilized samples is governed by microorganisms activity. After the addition of $^{117}$Sn-enriched $Sn^{2+}$ or $Sn^{4+}$ species to non-sterilized samples of landfill leachate, only $^{117}$MMeT species was formed, while in sterilized samples $^{117}$MMeT was not formed from the added $^{117}$Sn-enriched $Sn^{2+}$ or $Sn^{4+}$ species. These data revealed that also methylation in the landfill leachate is governed by microbial activity.

# 4 Conclusions

- Transformation of OTC in the landfill leachate was followed over the time span of six months or 10 days, under simulated landfill conditions by the use of Sn-enriched isotopic tracers, which provide new insights into the mechanisms of methylation and degradation of OTC in landfill leachates by bacterial strains.
- Biomethylation processes result in toxic methyltins formation, while biodegradation of butyltins leads to less toxic tin species.
- Under landfill conditions methyltin formation occurred only from inorganic tin. Butyltin concentration was far too low to produce by degradation sufficient concentration of inorganic tin, which could be further methylated by bacteria.
- Methylation processes were observed from both, $Sn^{2+}$ and $Sn^{4+}$ ionic tin species.
- Hydrolysis of $Sn^{2+}$ and $Sn^{4+}$ species is a limiting factor, which controls the extent of methyltin formation.

- Knowledge about the pathways of biomethylation and biodegradation of OTC in landfill leachates is of significant importance for the managers of the landfills to assure adequate clean-up before the leachates are released into the environment.
- Degradation of TBT and formation of methyltins were both biotic transformations.

## References:


[1] E. Rosenberg. Speciation of Tin, *Handbook of Elemental Speciation II – Species in the Environment, Food, Medicine and Occupational Health. Eds. R. Cornelis, J. Caruso, H. Crews and K. Heumann. John Wiley & Sons, Ltd, Chichester*: 422-464, 2005

[2] M. Hoch. Organotin compounds in the environment – an overview, *Applied Geochemistry,* 16: 719-743, 2001

[3] K. Fent. Ecotoxicological effects at contaminated sites, *Toxicology,* 205: 223-240, 2004

[4] Greenpeace Research Laboratories. Hazardous chemical in consumer products, *Technical Note 01/2003, GRL-TN-01-2003*

[5] P. Pinel-Raffaitin, D. Amouroux, I. LeHécho, P. Rodríguez-Gonzalez and M. Potin-Gautier. Occurrence and distribution of organotin compounds in leachates and biogases from municipal landfills, *Water Research*, 42 (4-5): 987-996, 2008

[6] M. Vahčič, , R. Milačič, and J. Ščančar. Development of analytical procedure for the determination of methyltin,butyltin, phenyltin and octyltin compounds in landfill leachates by gas chromatography–inductively coupled plasma mass spectrometry, *Analytica Chemica Acta,* 694: 21-30, 2011

[7] K. Peeters, J. Iskra, T. Zuliani, J. Ščančar and R. Milačič. The micro-scale synthesis of 117Sn-enriched tributyltin chloride and its characterization by GC-ICP-MS and NMR techniques, *Chemosphere, http://dx.doi.org/10.1016/j.chemosphere.2014.01.003* (In Press)

[8] W.P. Ridley, L.J. Dizikes and J.M. Wood. Biomethylation of toxic elements in the environment, *Science*, 197: 329-332, 1977

[9] B.Chen, Q. Zhou, J. Liu, D. Cao, T. Wang and G. Jiang. Methylation mechanism of tin(II) by methylcobalamin in aquatic systems, *Chemosphere*, 68: 414-419, 2007

[10] G.G. Graf. *An Ullmann's Encyclopedia. Industrial Inorganic Chemicals and Products, Sodium Chloride to Zirconium Compounds. Tin Compounds. Speciation of Tin. Wiley-VCH Verlag GmbH,* 6: 4955-4967, 1998

## For wider interest

The release of organotin compounds (OTCs) from landfill leachates into the aquatic ecosystem or atmosphere is still scarcely documented. In order to prevent environmental pollution, there is a need for estimation of the ecological impact of OTCs, since tin was found as one of the main leachate contaminants among the metals and metalloids. Microorganisms may significantly influence the transformation processes of OTCs in landfill leachates, so it is important to study the pathways of their degradation and/or the formation of newly formed OTCs. Data of the present investigation importantly contribute to better understanding of the processes that OTCs undergo in leachates. This information helps to prevent the release of toxic methyltin species into the nearby environmental compartments.

The study also shows that the use of enriched isotopes can provide comprehensive information in investigations of the transformation of OTCs in environmental samples.

# The influence of climate change on the quality of some Italian wine products: chemical characterization and environmental impacts

**Fabio Paolo Polo**[1], **Giulio Cozzi**[2], **Nives Ogrinc**[3,4]

[1] Department of Economics, Calle Larga Santa Marta, 2137, 30123 Venice, Italy;

[2] IDPA – CNR, Institute for the Dynamics of Environmental Processes, Calle Larga Santa Marta, 2137, I-30123 Venice, Italy;

[3] Department of Environmental Sciences Jožef Stefan Institute, Ljubljana, Slovenia.

[4] Jožef Stefan International Postgraduate School , Ljubljana, Slovenia.

fabio.polo@unive.it

**Abstract.** This study wants to focus on the chemical, environmental and economic consequences of climate change on wine products. Some important vintages of varieties of wine from the North and from the South of Italy are being analyzed for a specific chemical description. The addition analyses of wine's parent musts, rain waters and soils from the grape fields during some specific vintages will give more information on the effects of climatic conditions. Stable isotopes of C and O are commonly used to understand the geographical origin of the wines or to detect illegal sugar additions, but they are also strictly related to temperature and climate change, which is the main target of this work. The stable isotope analysis (IRMS), the single elements analysis (ICP-MS) of metals and Rare Earth Elements in all the set matrices, together with the organoleptic analysis are going to give a complete description of the samples. This paper shows some preliminary results.

**Keywords**: Wine, Climate Change, Stable Isotope ratios, IRMS, ICP-MS, REE.

## 1 Introduction

The average climate is changing in the Earth, and these changes in global and local temperatures are already modifying weather patterns, causing a number of impacts

and increasing the vulnerability of regions, economic sectors and communities. As we know from a discrete number of prevision models [1], climate change is going to affect and modify Earth's environmental conditions. Due to green house gases (GHGs) emission, temperature is going to increase and in the best scenario the predictions are talking of a 2°C increase in the next century (Fig. 1).

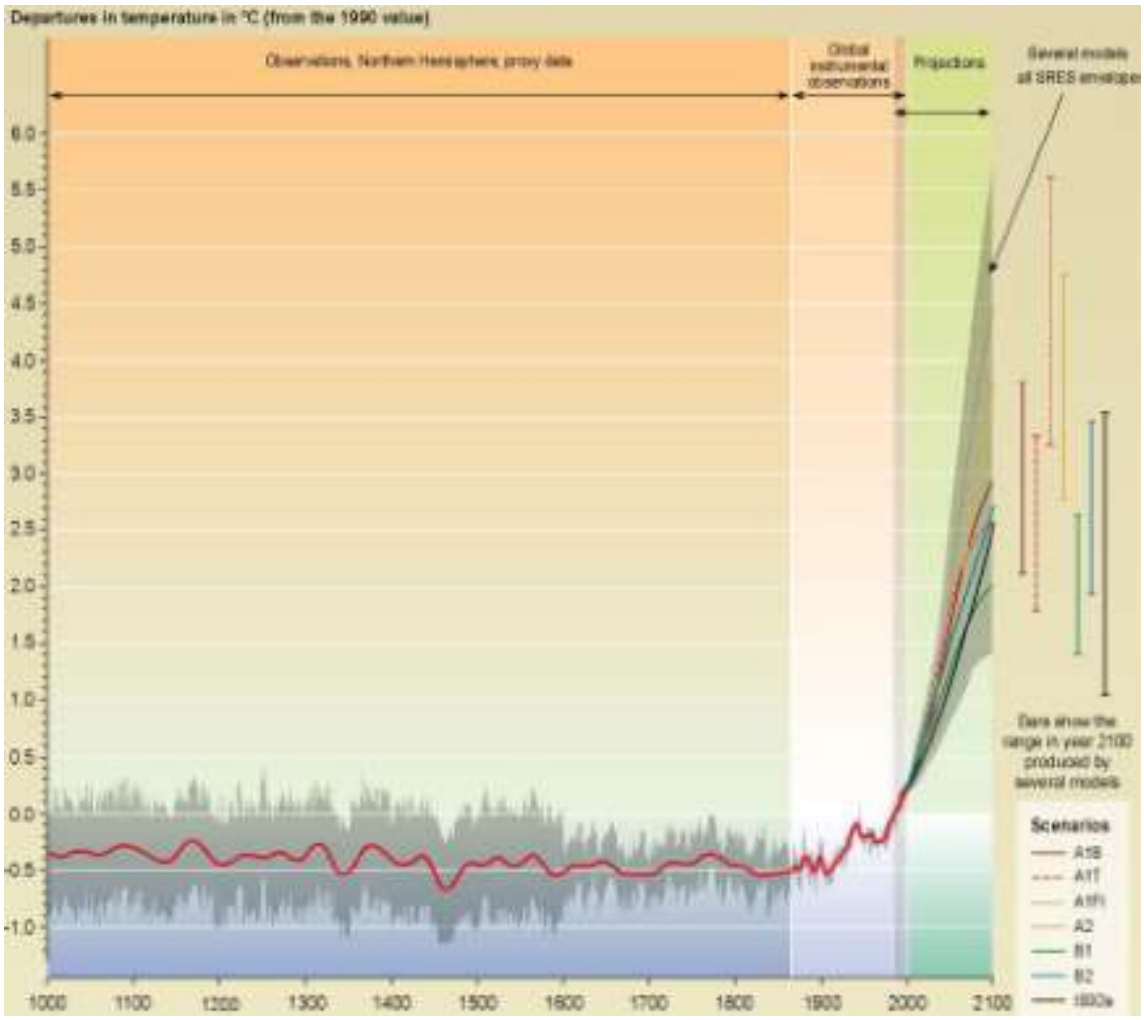


**Figure 1:** Some models of temperature increasing, [1].

Agriculture is highly exposed and extremely vulnerable to climate change, as farming activities directly depend on climatic conditions.

Stable isotope ratios of bio-elements have been used for over twenty years for the authentication of different foodstuffs and derivates. Environmental factors, like temperature and rain that influence the physiology of the plants contribute to modify its overall $^{13}C$ content [2]. This behavior may be important for plants like the grape vine, which have very large foliar surfaces and evaporate a great quantity of water by transpiration. It has been shown that a large range of $\delta^{13}C$ values may be observed for ethanol from grapes harvested in typical soil and climatic conditions [3].

The trace element diffusion in the food chain is one of the most important indicators of environmental conditions. In fact, ground composition influences the presence of oligoelements in vegetables and directly the organisms in the food chain. The relationships between environment and food chain are tightly correlated to both geologic factors such as rock mineralogy, landscape and climate, as well as to factors specifically correlated to soil chemistry. This argument is also interesting for its relevance to nutritional quality evaluation of the foodstuff and for the possible verification of adulteration. For this reason in recent years different works have been carried out to study trace element content and stable isotope ratios as indicators of food industry product origin [4], [5].

**Study area**: Grape fields in the North and South of Italy are respectively located in different climatic zones, and wine products are generally very different. Three vintage years of Negroamaro wine (2011-2013) from the Salento areas (Puglia, Italy) and 4 years (2009-2012) of Valpolicella wine from the Veneto areas (Veneto, Italy) are under investigation in our study. For each field also musts, soils, irrigation and precipitation will be analyzed.

## 2 Materials and methods

**Sampling:** The grapes from Valpolicella are Corvina species cultived in a Guyot system. The musts were sampled and produced by the CRA (Italian Research Center on Agriculture) choosing grapes at two different steps of maturation: 15 day before the harvest and during the harvest. Wines were also produced by the CRA. Samples of rain water were sampled during the same years of harvest, while samples of soil were taken directly in the fields. The Negroamaro wine and must from Salento were also sampled by CRA.

**Analysis.** The methods adopted for all the analysis are the official ones suggested by OIV (International Organisation of Vine and Wine). Stable isotope analysis of C, O and H were performed at the Jožef Stefan Institute (JSI) laboratories: musts were centrifuged to separate the pulp from the juice water. $^{18}O/^{16}O$ ratios were measured in water, while $^{13}C/^{12}C$ ratios were determined in the must pulp. Wine will be distilled at the Agricultural Institute of Slovenia (AIS) laboratories to obtain the ethanol at the alcohol grade higher than 96‰.

The following stable isotope analysis will be performed:
- $^{2}H/^{1}H$ ratios will be measured in the water of the musts.
- $^{18}O/^{16}O$ ratios will be measured in must, wine and in distillation residue.
- $^{13}C/^{12}C$ ratios will be measured from the ethanol obtained by wine distillation and in the sugar of the must. The measurements will be performed by IRMS (Isoprime Multiflow Bio and Europa 20-20 with preparation module for solid and liquid samples ANCA-SL).
- SNIF-NMR analysis will be performed in the ethanol obtained after wine distillation at the Slovenian Institute of Chemistry (SIC).

Stable isotope measurements will be expressed in δ-notation against a suitable standard in per mil (‰). For C V-PDB is used, while for H and O V-SMOW is used. The precision of measurements was estimated to be ±0.2‰, ±0.1‰ and ±1.0‰ for C, O and H, respectively.

The experimental part concerning organic compounds will be based on analytical protocols developed in the laboratory of the Ca' Foscari University of Venice (CNR-IDPA) and in the laboratories of CRA. Specifically, determination will be carried out by HRGC-LRMS and HRGC-HRMS. The analysis of trace elements will be carried out by ICP-MS through validated and new methods.

## 3 Results and discussion

Some preliminary results of the analyses of musts are shown in Figure 2. Each point in the figures shows a sample, the first sample has been harvested in the 2011, the other 6 samples are from 2012. The all samples have been harvest at the Valpolicella area.

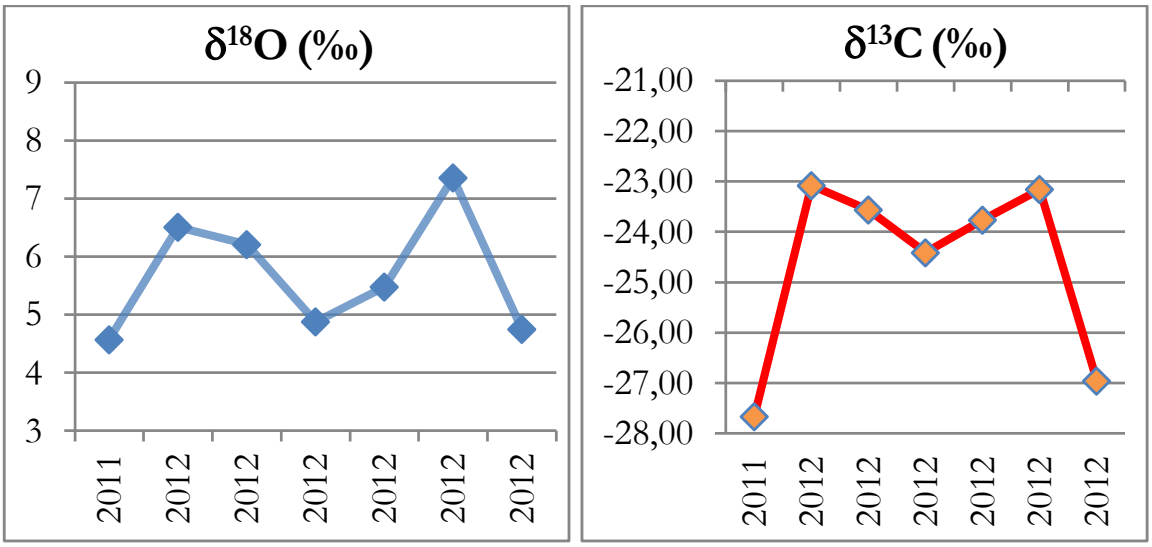


**Figure 2:** Isotope composition of Oxygen and Carbon in must samples from the field num. 5 at Valpolicella area (Italy).

Preliminary results from musts show that there should be some correlation between the trends of the two isotopic ratios. The first sample from 2011 has lower $\delta^{13}C$ and $\delta^{18}O$ values. These differences could be related to the metrological conditions, which were different in 2011 comparing to 2012. The amount of precipitation was higher in 2011 and in addition there were more sunny days in 2012, which could lead to a higher $\delta^{13}C$ values observed in 2012. However it should be mentioned that these are only preliminary results that has to be further evaluated in order to obtain more clear picture on the changes and distribution of stable isotopes in wine and must samples in relation to year and region of harvest.

## 4 Conclusions

A statistical approach (Principal Component Analysis) will be used to correlate the complete set of results to the rain, temperature, and some basic organoleptic analyses of the wine (made by CRA). The extreme dependency of the wine products to the climatic situation will allow us to detect the effects of wine quality in these recent years. We will try to focus on this quality working on prediction models for the future years. Moreover, our intention is to inform the producer and the consumer in order to achieve robustness of these important products. This type of research is considered to be a starting point for the study of climate change in terms of food in wine sector, in fact there are no particular historical precedents or information in this study area.

# References:

[1] Intergovernmental Panel on Climate Change (2007). IPCC Fourth Assessment Report: Climate Change 2007, IPCC, Geneva.

[2] Martin G. J. and Thibault J-N, Spatial and temporal dependence of the 13c and 14c isotopes of wine ethanols. Laboratoire de RMN-RC, URA-CNRS 472, Universite de Nantes, 2 rue de la Houssiniere, F- 44072 Nantes cedex 03, France. RADIOCARBON, VOL. 37, No. 3, 1995, P. 943-954.

[3] Day, M., Zhang, B. L., Martin, G. J., Asselin, C. and Morlat, R., 1995 Essai de caracterisation du millesime et de la zone de production des vins a 1'aide de traceurs metalliques et isotopiques. Journal International des Sciences de la Vigne et du Vin 29: 75-87.

[4] Suhaj M., Koreňovska M., "Application of elemental analysis for identification of wine origin", Acta Alimentaria 2005, 34 (4), 393-401.

[5] Arvanitoyanis I.S., . Katsota M.N, Psarra E.P., Soufleros E.H., Kallithraka S., "Application of quality control methods for assessing wine authenticity: use of multivariate analysis (chemometrics)", Trends Food Sci. Technol. 1999, 10, 321-336.

[6] Antle M. John. Food System, adaptation to Climate Change. Resources for the future. 2009. Intergovernmental Panel on Climate Change (2007). IPCC Fourth Assessment Report: Climate Change 2007, IPCC, Geneva.

[7] Giaccio M., Vicentini A., Determination of the geographical origin of wines by means of the mineral content and the stable isotope ratios: a review. J. COMMODITY SCI. TECHNOL. QUALITY 2008, 47 (I-IV), 267-284

[8] Jones, G.V., White, M.A., Cooper, O.R., and Storchmann, K-H., Climate and Wine: Quality Issues in a Warmer World. Proceedings of the Vineyard Data Quantification Society's 10th Œonometrics Meeting. Dijon, France, May 2004.

[9] OIV, International Organisation of Vine and Wine. www.oiv.int

## For wider interest

Environmental changes are currently the subject of important scientific research, as well as broader political and economic interest, as they can significantly affect the quality of life and human activities, which adversely may affect the climate in general. Higher temperatures eventually reduce yields of desirable crops while encouraging weed and pest proliferation. Changes in precipitation patterns increase the likelihood of short-run crop failures and long-run production declines. Although there will be gains in some crops in some regions of the world, the overall impacts of climate change on agriculture are expected to be negative, threatening global food security.

This study wants to focus on the chemical, environmental and economic consequences of climate change on wine products. Future prospects for the cultivation and production in terms of economic and environmental conditions will be constructed in order to help companies and local authorities to protect wine production in Italy.

# Fatty acid composition as a tool for determination of adulteration of milk and dairy products

**Doris Potočnik**[1,2]**, Nives Ogrinc**[1,2]

[1] Department of Environmental Sciences, Jožef Stefan Institute, Ljubljana, Slovenia

[2] Jožef Stefan International Postgraduate School, Ljubljana, Slovenia

doris.potocnik@ijs.si

**Abstract.** Milk and dairy products are in considerable demand and relatively expensive, therefore, the authenticity and determination of geographical origin of these products are becoming important issues for providers and consumers. In this study fatty acid (FA) composition is used to obtain information about the provenience of milk and dairy products and to detect possible adulteration. Milk samples from different geographical regions (Mediterranean, Pannonia, Dinaric and Alpine) in Slovenia were collected and used to determine the content and isotopic composition of individual FA. FA composition was analyzed using the *in-situ* trans-esterification method and characterized by gas chromatography with FID detector (GC-FID), while isotopic composition was determined with compound specific isotope ratio mass spectrometry (CS-IRMS). In order to verify authenticity of cheese, 26 samples of high price cheeses in Slovenian market were analyzed. It was found that 20% of them do not correspond to the declaration. In addition the adulteration of raw milk with vegetable palm tallow could be detected at 1.1%.

**Keywords:** dairy products, fatty acids, isotopes, adulteration, geographical origin, GC-FID, GC-IRMS

## 1. Introduction

Milk and dairy products are an important everyday nutrition, since they are a source for many key nutrients including proteins, energy and many essential minerals and vitamins. In the human diet, milk and dairy products contribute between 18% – 24% total fat, 30% – 40% total saturated fatty acids (SFA) and 20% – 25% total *trans* fatty acids intake. The largest contribution of SFA intake is in cheese consumption [1].

Quality of milk varies with the diet of dairy cows, which is further reflected in FA composition. Increasing the proportion of fresh forages compared with conserved forages or cereal concentrates, enhances the concentration of certain unsaturated FA and reduces SFA content. Thus, the total SFA concentrations of milk fat are usually lower in summer comparing to winter [2]. In addition, grassing generally increases 18:3n-3 (α-linolenic acid, ω-3 fatty acid) and CLA (conjugated linoleic acid) concentrations, but at the same time the increase in *trans* fatty acids content may occur due to incomplete biohydrogenation of dietary unsaturated FA in the rumen [1]. Several studies have already shown that milk products from mountain areas are reputed to have specific nutritional qualities, so the tracing of milk production sites is essential for the prevention of fraud. Different effects of feeding, pasture or maize silage can be also track using stable isotope composition. C3 plants have lower $\delta^{13}C$ values ranging from −30 and −23‰, while C4 plants such as maize have higher $\delta^{13}C$ values ranging from −11 to −14‰ [2 – 4]. These differences could be also observed in the isotopic composition of FA.

Milk and dairy products are used extensively and therefore vulnerable to economic adulterations. Food adulteration and fraud profit has been practiced since ancient times, but nowadays they become increasingly more sophisticated. Therefore there is a high risk of intentionally mislabeled products especially when price is a factor. In the production of high quality cheese, the price depends on the type of milk (goat, sheep, cow's milk), therefore the correct declaration is very important [5]. FA composition could be used to detect cow milk in goat and sheep cheese. Goat and sheep milk cheese exhibited a characteristically different lower chain length fatty acid pattern than did the cow milk cheeses. The most abundant fatty acids are C6:0, C8:0 and C14:0 comprising around 20% of all fatty acids in goat milk, while C14:0, C16:0 and C18:1 are the most abundant fatty acids in sheep milk. Another important adulteration of dairy products appearing on the market is admixture of vegetable tallow with raw milk. Detection of fraud is based on non-milk fat. Palm fat does not contain butyric acid (C4:0) and contains higher amount of lauric acid (C12:0) comparing to milk, thus any addition of palm fat to milk would result in the decrease in concentration of butyric acid (C4:0) and increase in the concentration of lauric acid (C12:0). Likewise, by addition of palm fat the content of palmitic acid (C16:0) decreases. At the same time, the concentration of C18:1n9 (oleic acid) decreases,

while the concentration of stearic acid (C18:0) slightly increases. Based on the FA composition it is possible to determine very low concentrations, such as 1.2% [6].

The aim of this work is to determine FA composition of milk that has been mixed with different amount of vegetable tallow and to verify the authenticity of cheese from cow, sheep and goat milk available on Slovenian market. Another important part of this research is to examine the effect of season and geographical location on proportional changes in milk fat content in relation to the diet composition.

## 2. Materials and methods

*Collection and storage of samples*

**Milk samples**. The sampling of cow's milk was performed four times per year covering different geographical regions (Mediterranean, Pannonia, Dinaric and Alpine) in Slovenia. Forty samples were obtained from five Slovenian diary producers at each sampling period. The samples were stored in a plastic containers and frozen at −20°C before analysis. For the identification of adulteration cow's milk with vegetable palm fat, mixtures of milk of different adulteration percentage were produced in a laboratory experiment; adulteration of cow milk with 1%, 2%, 4%, 7%, 9%, 11%, 13%, 16%, 18% and 20% of palm tallow were analyzed. Each sample was analyzed in triplicates.

**Cheese samples.** Various types of cheese (goat, sheep, cow) of different geographical origin from different European countries available on Slovenian market were collected. All 26 samples of cheese were of higher price ranges. Samples were grated and stored in a freezer at −20°C before analysis.

*Analytical methods*

For identification and quantification of FA the *in-situ* trans-esterification method was used. Total lipids from milk and cheese samples were extracted with dichloromethane and sodium hydroxide in methanol, than purged with nitrogen and heated for 10 minutes at 90°C. Afterwards samples were cooled. To complete the reaction fatty acids methyl esters (FAMEs) were formed by addition of 14% $BF_3$-methanol solution and heated again for 10 minutes at 90°C. After fast cooling, the fatty acids methyl esters (FAMEs) were extracted into hexane phase. The

characterization of FAMEs was performed by gas chromatography with FID detector (GC-FID), equipped with a capillary column (Omegawax 320, 30 m × 0.32 mm, × 0.25 μm), with split ratio of 100:1. The temperature program started at 50°C (2 min) and increased by 4°C/min to 220°C (20 min). The carrier gas was helium at a flow rate of 1mL/min, makeup gas nitrogen at 45 mL/min, hydrogen at 40 mL/min and air flow rate at 450 mL/min. Total running time was 74.5 min. The individual fatty acids were identified and quantified by comparing their retention times with those of standard (Supleco 37 component FAME Mix) and expressed as weight percent of total fatty acids.

To support the quality of the data, procedural blank were performed with each set of samples. Standard (Supleco 37 component FAME mix) was analyzed after every 10 samples to verify the stability of the analytical system. Precision of the method, based on replicate of real samples, was up to 5%.

Isotopic compositions of FA were determined using Isoprime GV GC-C-IRMS system. Carbon isotope measurements were reported in delta notation ( δ ) relative to the Vienna-Pee Dee Belemnite (V-PDB) standard and expressed in per mile (‰). The precision of measurements ranged between 0.3 and 0.5‰.

*QA/QC for stable isotope analysis*

At the moment there are no standards available with known isotopic composition, so the following approach was used. FA C19:0 standard (methyl nanodecanoate, RESTEK Corporation) was first analysed using elemental analyser coupled to IRMS (EA-IRMS.). The isotope value of EA-IRMS was taken as "true values" of the standard and was compared with GC-C-IRMS measurements. In order to validate integrity of analytical system and to monitor the conditions of the chromatographic and detection system for GC-C-IRMS analysis, a solution containing C20:0 standard enriched in $^{13}C$ (icosanioc acid methyl ester, Indiana University, USA), with the known isotopic composition, was analysed prior to any sequence of samples. Since the nonlinearity causes shifts in the isotopic values, evaluation of the potential occurrence of nonlinearity of the system was performed with C19:0 standard. The isotopic shift due to the carbon introduced in the fatty acid methylation was then corrected by mass balance.

## 3. Results and discussion

### *Adulteration of milk with palm fat*

For identification of adulteration milk with vegetable palm fat the total concentrations of individual FA are important, since as little as 1% palm tallow in milk fat can be detected (Fig. 1). The content of total SFAs in pristine homogenized milk is 72.9 weight % (wt%), while the content of SFAs in falsified milk with palm fat is 77.2 wt%. In the sample with the addition of 20% of palm fat SFAs content reached up to 94.7 wt%. It can be observed, that the total content of MUFAs (monounsaturated fatty acids) decreased in unadulterated milk from 23.9 w% to 7.8 wt% in the 20% adulterated milk. Thus, the total content of MUFAs can be another indicator for identification of adulterated milk with vegetable palm fat. The total MUFAs content in unadulterated milk are 23.9 wt%, while in 1% adulterated milk content is 19.6 wt%. With the addition of vegetable palm fat, the content of n-3 and n-6 PUFAs (polyunsaturated fatty acids) decreased.

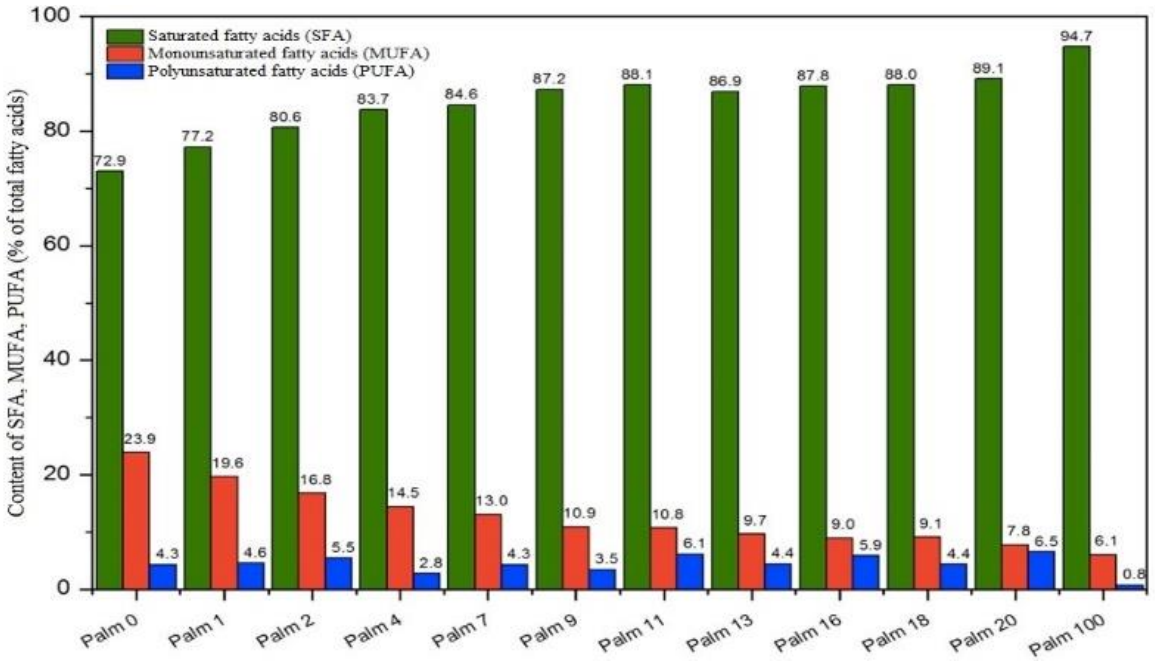


Palm 0 – unadulterated homogenized milk
Palm 1 – adulterated milk with 1% palm fat
Palm 2 – adulterated milk with 2% palm fat
Palm 4 – adulterated milk with 4% palm fat
Palm 7 – adulterated milk with 7% palm fat
Palm 9 – adulterated milk with 9% palm fat
Palm 11 – adulterated milk with 11% palm fat
Palm 13 – adulterated milk with 13% palm fat
Palm 16 – adulterated milk with 16% palm fat
Palm 18 – adulterated milk with 18% palm fat
Palm 20 – adulterated milk with 20% palm fat
Palm100 – 100% palm fat

**Figure 1:** Content of fatty acids in addition of different amount of palm fat.

### *Adulteration of cheese available on Slovenian market*

Authenticity and declaration of individual cheese based products was determined using fatty acid composition of cheese. Our main focus was related to identification of milk present in cheese and whether this figure corresponds to that data on the declaration. The obtained results were compared with results from the literature [1, 7 – 9]. The content of palmitic acid (C16:0) in cow's milk ranges between 27.9 – 32.4 wt% and it is higher that the range in goats and sheep's milk which ranges between 25 – 26 wt%. The difference between goat, sheep and cow's milk can be also identified by total content of caproic (C6:0), caprylic (C8:0) and capric (C10:0) acids. The total content of aforementioned acids in cow's milk varies between 5 and 7 wt%, for sheep about 12 wt% and for goats about 14 wt% and higher. Furthermore, appreciably higher content of capric acid (C10:0) concentration can be detected in goat milk. Due to inconsistency between measured FA content and data on the declaration, we can suspected that at least 20% of high-price cheeses are adulterated. Results are collected in Table 1. Results indicated that we have sufficient reason to believe that at least 4 samples are adulterated (shaded in yellow, Fig. 1). The most significant difference between cow and sheep cheese is that the sum of caproic (C6:0), caprylic (C8:0) and capric (C10:0) fatty acids is lower in cow's cheese, while the content of palmitic acid (C16:0) increases. We can claim with certainty that one of the tested sheep cheese samples is adulterated (shaded in orange Fig.1), since its FA composition fells under the range of cow's cheese. For the remaining sheep cheeses samples we can only suspect adulteration, due to the sum of caproic (C6:0), caprylic (C8:0) and capric (C10:0) fatty acids being lower than reference values from literature data and palmitic acid (C16:0) being higher.

**Table 1**: Fatty acid composition (% of total fatty acid methyl esters) of goat, cow and sheep cheeses, which could be used to determine the correct labelling of the cheeses.

| Samples [a] | | Fatty acid (%) | | | | |
|---|---|---|---|---|---|---|
| | | **C6:0** | **C8:0** | **C10:0** | **Σ (C6:0, C8:0, C10:0)** | **C16:0** |
| **Reference values from the literature** | cow's milk | 2.11 | 1.21 | 2.69 | 6.01 | 32.39 |
| | cow's milk | 2.50 | 1.50 | 3.20 | 7.20 | 27.90 |
| | sheep milk | 2.60 | 2.50 | 7.50 | 12.60 | 25.20 |
| | sheep milk | 2.80 | 2.70 | 9.00 | 14.50 | 25.40 |
| | goat milk | 2.90 | 2.70 | 8.40 | 14.00 | 24.60 |
| | goat milk | 3.17 | 3.50 | 10.78 | 17.45 | 25.90 |

| | | | | | |
|---|---|---|---|---|---|
| cow's milk | 2.04 | 1.54 | 3.52 | 7.10 | 32.64 |
| cow's milk | 3.16 | 2.00 | 3.93 | 9.09 | 29.58 |
| cow's milk | 2.94 | 1.93 | 4.23 | 9.10 | 30.57 |
| cow's milk | 2.64 | 1.68 | 3.56 | 7.88 | 32.72 |
| cow's milk | 2.22 | 1.48 | 3.29 | 6.99 | 32.25 |
| cow's milk | 1.50 | 1.17 | 2.95 | 5.61 | 32.48 |
| sheep milk | 2.81 | 2.86 | 8.81 | 14.48 | 25.08 |
| sheep milk | 2.98 | 2.78 | 7.70 | 13.47 | 25.46 |
| sheep milk | 2.16 | 2.41 | 7.42 | 11.98 | 27.00 |
| sheep milk | 2.13 | 2.53 | 8.11 | 12.78 | 25.63 |
| sheep milk | 2.74 | 2.55 | 6.84 | 12.13 | 26.60 |
| sheep milk | 2.52 | 3.19 | 9.44 | 15.15 | 24.87 |
| sheep milk | 3.20 | 3.34 | 9.52 | 16.06 | 25.61 |
| sheep milk | 3.93 | 4.65 | 14.58 | 23.17 | 21.45 |
| sheep milk | 2.04 | 2.42 | 7.89 | 12.35 | 28.60 |
| sheep milk | 2.16 | 1.31 | 2.36 | 5.82 | 34.07 |
| sheep milk | 2.94 | 3.33 | 10.00 | 16.27 | 24.22 |
| sheep milk | 1.69 | 2.20 | 7.68 | 11.56 | 28.08 |
| sheep milk | 2.47 | 1.58 | 3.25 | 7.30 | 33.41 |
| sheep milk | 2.15 | 2.99 | 10.64 | 15.79 | 27.14 |
| cow and sheep milk | 2.41 | 1.73 | 4.10 | 8.23 | 33.33 |
| goat milk | 2.30 | 3.50 | 12.88 | 18.68 | 26.42 |
| goat milk | 2.85 | 3.32 | 10.45 | 16.62 | 26.93 |
| goat milk | 2.12 | 3.12 | 10.71 | 15.95 | 25.52 |
| goat milk | 3.20 | 3.64 | 11.56 | 18.41 | 25.61 |
| goat milk | 2.31 | 2.72 | 8.42 | 13.45 | 25.10 |

[a] samples of higher price cheese in Slovenia market
suspected adulterated milk
adulterated milk

### *Geographical Origin*

Further it was possible to differentiate between milk from different geographical origin based on the content and isotopic composition of FA. FA composition in milk varies according to the environmental factor such geographical origin which is correlated with the diet. Due to a small amount of unsaturated FA present in corn silage, diet modification from pasture to a meal dominated on corn silage, results in increased content of SFA and decreased content of C18:3n3 FA. Where dairy cows are associated with grazing, high concentration of n-3 and lower concentration of SFA may be observed as well as increased amount of CLA content [10].

The stable isotope composition in milk reflects the isotopic composition of ingested food and drinking water. $\delta^{13}C$ values in FAs from Mediterranean were −24.0‰ or

lower and were statistically different from $\delta^{13}C$ values in FAs from Pannonia (> −20.1‰) indicating an increased use of corn in the diet (evidenced in Fig 2).

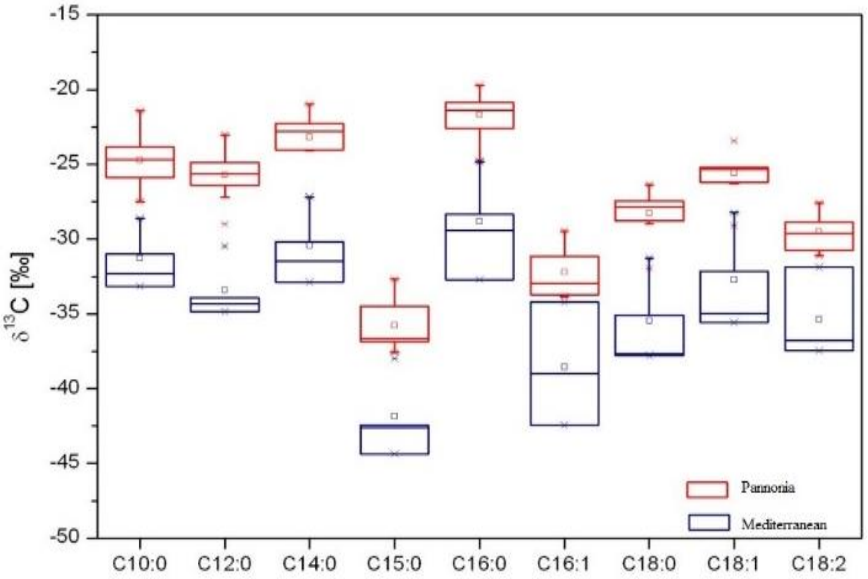


**Figure 2:** Stable carbon isotope composition of individual fatty acids for Mediterranean and Pannonia region.

## 4. Conclusion

The present study indicates that FA composition could be used to detect adulteration of milk and dairy products and to determine geographical origin. Adulteration of raw milk with vegetable palm tallow is easily observed using *in situ* trans-esterification method, due to the difference in fatty acids composition. If cow's milk is adulterated with as little as 1% palm tallow, the content of SFAs observably increases and MUFAs detectably decreases. Introducing palm tallow in cow's milk also decreases n-3 and n-6 PUFAs. Research concluded on high-price cheese present in Slovenian market indicated that at least 20% of them do not correspond to declaration. The geographical origin of milk can be also differentiate based on FA composition. The content as well as isotopic composition of FA is influenced by diet in dairy cows. Milk originating from Mediterranean region has increased amount of n-3 FA and CLA content and lower $\delta^{13}C$ values in FAs, since the food in this area is based on grass silage. Gras silage in the diet of dairy cows reflected decrease level of SFA.

The performed analyses of FA composition serve as a preliminary research, which could be used in the future to detect possible adulteration. The results indicated that

FA composition is suitable for qualitative determination of cow's milk presence in goat's and sheep's milk or cheeses. In addition the presence of palm tallow in pristine milk and dairy products could be detected. Even though method showed that is suitable for qualitative and possible quantitative analyzes, further research is still needed to evaluate its real potential.

**Acknowledgement**

The work was performed within the project V4-1108 entitled "The use of specific methods for determination and prevention of adulteration of milk and dairy products" financially supported by Slovenian Research Agency and Ministry of Agriculture and the Environment.

## References:

[1] K. E. Kliem, K. J. Shingfield, K. M. Livingstone, D. I. Givens. Seasonal variation in the fatty acid composition of milk available at retail in the United Kingdom and implications for dietary intake. *Food Chemistry*, 141: 274 – 281, 2013.

[2] J. Molikentin and A. Giesemann. Differentiation of organically and conventionally produced milk by stable isotope and fatty acid analysis. *Analytical and Bioanalytical Chemistry*, 388: 297 – 305, 2007.

[3] J. Renou, C. Deponge, P. Gachon, J. Bonnefoy, J. Coulon, J. Gerel, R. Verite, P. Ritz. Characterization of animal products according to geographic origin and feeding diet using nuclear magnetic resonance and isotopic ratio mass spectrometry: cow milk. *Food Chemistry*, 85: 63 – 66, 2004.

[4] F. Camin, K. Wietzerbin, A. B. Cortes, G. Haberhauer, M. Lees, G. Versini. Application of Multielement Stable Isotope Ratio Analysis to the Characterization on French, Italian, and Spanish Cheeses. *Journal of Agricultural and Food Chemistry*. 52: 6592 – 6601, 2004.

[5] R. Karoui, J. De Daerdemaeker. A review of the analytical methods coupled with chemometric tools for determination of the quality and identity of dairy products. *Food Chemistry*, 102: 621 – 640, 2007

[6] J. Dennis. Recent developments in food authentication. *Analyst*; 123: 151R – 156R, 1998.

[7] M. R. S. Sampelayo, L. Perez, J. J. M. Alonso, L. Amigo, J. Boza. Effects of concentrates with different contents of protected fat rich in PUFAs on the performance lactating Granadian goats Part II. Milk production and composition. *Small Ruminant Research*, 43: 141 – 148, 2002.

[8] J. M. Jandal. Comparative aspects of goat and sheep milk. *Small Ruminant Research*, 22: 177 – 185, 1996.

[9] P. F. Fox and P. L. H. McSweeney. *Advanced Dairy Chemistry Volume 2 Lipids, 3rd edition*. Springer, 2006.

[10] M. Collomb, W. Bisig, U. Butikofer, R. Sieber, M. Bregy, L. Etter. Seasonal variation in the fatty acid composition of milk supplied to dairies in the mountain region of Switzarland. *Dairy Science and Technology*, 88: 631 – 647, 2008.

## For wider interest

Milk and dairy products are known in diet as a complete nutrient, since they are a source for many key nutrients, including proteins, energy and many essential minerals and vitamins. Thus the quality of this products is very important for consumer. Due to the high prices on the market, they are vulnerable to adulteration or false denomination. For this reason, the need to monitor the authenticity and quality of dairy products has led to increase in the demand for methods to provide the geographical origin and adulteration. Information obtained during this research could be used to protect consumers and high-quality Slovenian dairy products.

# Nitrate origin and distribution in the Sava River Basin

**Janja Vrzel**[1,3], **Nives Ogrinc**[2,3]

[1]Ecological engineering institute d.o.o., Maribor, Slovenia

[2] Department of Environmental Sciences, Jožef Stefan Institute, Ljubljana, Slovenia

[2] Jožef Stefan International Postgraduate School, Ljubljana, Slovenia

janja.vrzel@ijs.si

**Abstract.** Environmental stressors such as climate change, change in land use and anthropogenic pollutants have a great impact on freshwater ecosystems. Nitrate ($NO_3^-$) is one of the special concerns since large amounts in the environment leads to several problems such as reduction of the water quality, eutrophication and creation of overall imbalance in the ecosystem. In this presentation we investigated the distribution and origin $NO_3^-$ at selected locations in the Sava River Basin in Slovenia. Basic statistical analyses $NO_3^-$ concentrations and $\delta^{15}N$ values according to the year, season, water temperature and discharge have shown that the Sava River is not polluted by anthropogenic $NO_3^-$. Its concentrations are yearly depended. Intra-annual changes of the concentrations and isotopic composition of $NO_3^-$ was observed as well. These data extend our knowledge in understanding the hydrological cycle of the Sava River, which would be helpful to evaluate its future changes.

**Keywords**: stressors on aquatic systems, nitrate, Sava River Basin.

## 1 Introduction

Environmental stressors can be divided into two categories: those that act globally but with varying intensity; and those that act at a local to regional level but occur globally [1]. Impacts on freshwater are shaped by interactions between both of them. These may lead to complex, irreversible changes in ecological structure, functioning and the delivery of ecosystem services [2]. At the top of all stressors is climate change that influences shifts in temperature, precipitation, run-off patterns, and in nitrogen deposition. Numerous other anthropogenic stressors impact on water quantity and quality, including acidification, pollution (e.g. by nitrates), land use and land cover change (Fig. 1) [3].

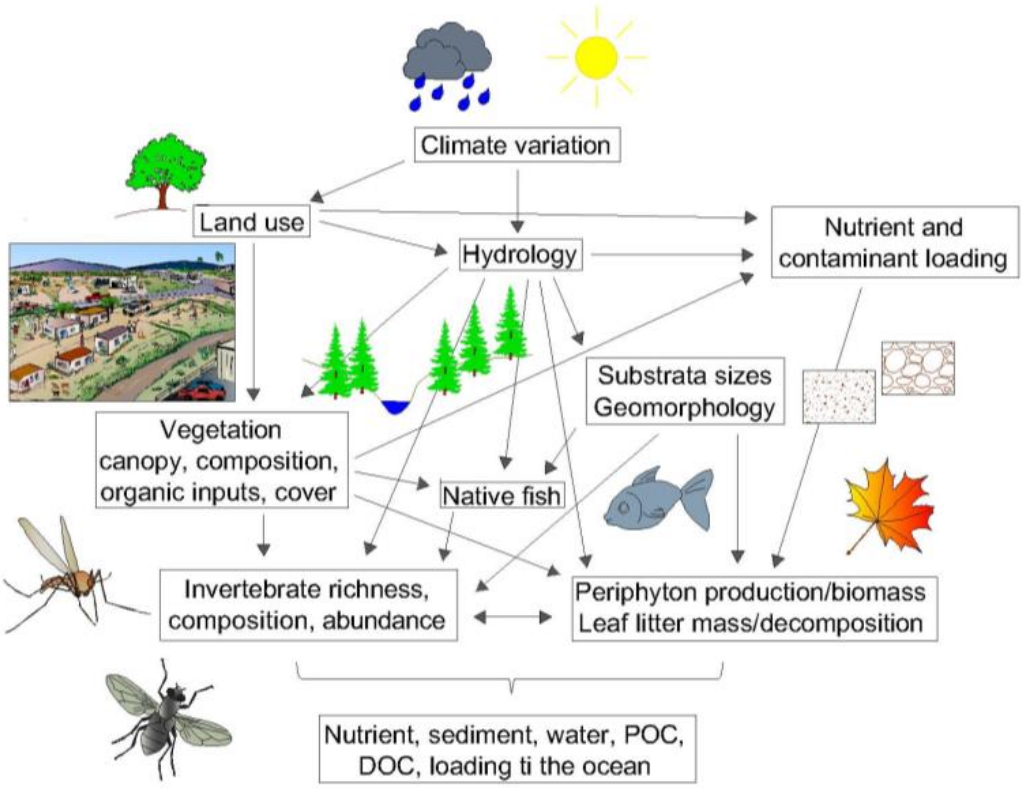


**Figure 1:** Effect of multiple stressors in freshwater ecosystems under strong pressure for water resources in Slovenia (adapted from Cooper et al., 2013) [4].

Anthropogenic stressors derive from domestic, agricultural and industrial activities. They, compromise the quality of water resources, particularly from microbial [5, 6, 7], sediment [8, 9], nutrient [10, 11] pollution, and contamination with especially pesticides and heavy metals [12]. After the evaluation of Falkowsky et al. (2000) significant human activities impacts on global nutrient cycles have occurred [13]. Yet human activities have enhanced global cycles of global nitrogen by on average 100%. Increases in river nutrient loads generally lead to increases in the production of algae and aquatic plants, loss of biodiversity and are at the same time associated to water quality problems [14].

Nutrient sources operate through both point and diffuse pathways linking land to water. Diffuse pollutants pose a particular problem because they are hard to detect and their fluxes are highly variable in time [15, 16, 17]. Understanding human driver of changes to biogeochemical cycles, particularly nutrient cycles, and tackling the multiple stressors that lead to diffuse pollution are important for sustaining the long-term quality and hence availability of water from rivers and groundwater. Recent

studies have shown that stable isotopes are useful tools in identifying nitrate sources in water systems [18, 19, 20, 21, 22, 23].

The aim of our work is to evaluate the changes of nitrate in the Sava River at selective locations in Slovenia. This research represents the start of the international European project GLOBAQUA – Managing the effects of multiple stressors on aquatic ecosystem under water scarcity (EU Project 7 OP). The study area of the project is full Sava River Basin (SRB) and represents one of the steps to the better understand multiple stressors effects on freshwater ecosystem and thus to better predict their responses to future changes.

## 2 Data analyses

$NO_3^-$ concentrations were investigated at two locations Litija and Jesenice na Dolenjskem in the period from 2006 to 2012. Therefore daily averaged flow rates ($m^3$ $s^{-1}$), river's water temperature (°C) and concentrations of $NO_3^-$ at these two locations were provided by the Environmental Agency of the Republic of Slovenia (ARSO) [24]. The locations are shown in the Figure 2.

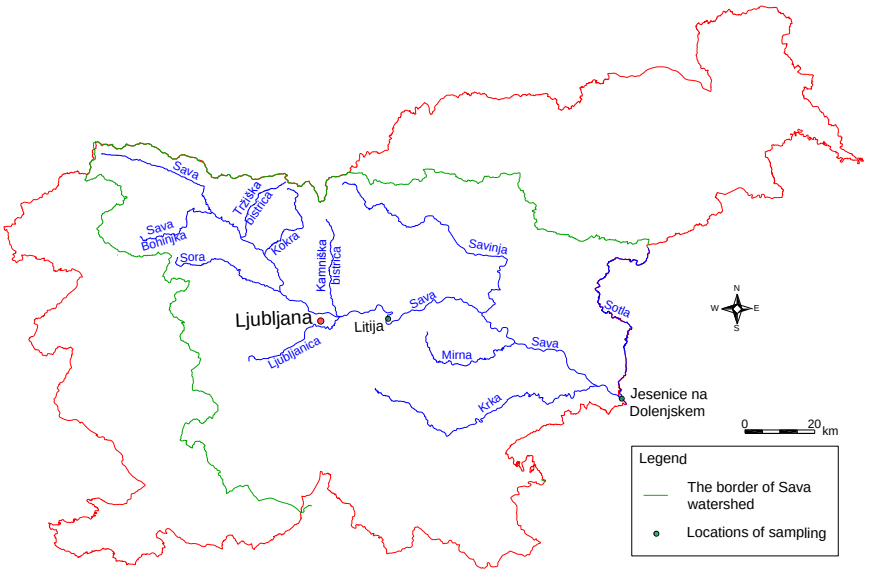


**Figure 2:** Map of sampling locations in the SRB.

Samples for $\delta^{15}N_{NO3}$ analyses were taken only in Litija in the period from June 2010 to April 2011. The $\delta^{15}N_{NO3}$ values were measured by continuous flow isotope ratio mass spectrometer (CF-IRMS). The detailed procedures of field sampling and

analyses are described in related studies, in which $\delta^{15}N_{NO3}$ values were used to describe $NO_3^-$ sources in the Sava River Basin in Slovenia [25–27].

Data were analysed by ANOVA to test for the differences in $NO_3^-$ concentrations and $\delta^{15}N$ values according to the year, season, water temperature and discharge. Both the one-way ANOVA and two-way ANOVA were performed on ranked data. The F-statistic or F-value is a random variable that has an F distribution [28]. A probability (P) value is determined by F-statistic value. In all statistical test P-values of less than 0.05 were used to indicate the significance level. All statistical analyses were run using OriginPro software package 8.5 (OriginLab Corporation, Northampton, USA).

## 3 Sava River Basin

The study key of the topic of the effects of multiple stressors on aquatic ecosystem is the Sava River Basin (SRB). Sava River is the largest river in Slovenia, including Sava Dolinka with headwater in Zelenci. Sava is also a major tributary of Danube River.

SRB has a very heterogeneous climate and exceptional diversity in terms of morphology, geology, pedology and vegetation. The area is influenced by four different climates: Continental, sub-Alpine, Alpine and Mediterranean climate. Sava watershed is composed of Permo-Carbonian clastic sediments, Triassic carbonates, Miocene sandstones, clay and gravels, and Pleistocene sediments [29]. After all, land is diverse and complex, reflecting the difference in relief, climate and stream flow [30]. Therefore land use changes along Sava River. Steep river banks are covered by forest in the northwestern and central part of Sava's watershed, where Sava flows through Alps and Posavje hills. On the other hand agriculture plays a dominant role in the southeastern part of the watershed, where the topography is lower and flat. Some industrial towns were built along Sava: Jesenice, Kranj, Brežice and Krško, even the capital Ljubljana.

## 4 Results and discussion

Figure 3 shows that there are differences between $NO_3^-$ concentrations in both locations. There are substantial intra-annual variations in $NO_3^-$ concentrations, which could be described by the fitting of simple harmonic curves in Jesenice na

Dolenjskem. A very strong seasonal pattern ($P = 2.71 \cdot 10^{-6}$, $F = 9.09$) was noted with the maximum occurring in the winter months from December to March. The timing of this maximum reflects factors such as the leaching of nitrate, which accumulated in the soil in the summer and autumn, by high rates of soil water movement in the winter months and the absence of nitrogen uptake by plants due to low temperatures in winter period. In contrast, diminished soil water movement, increased plant uptake of nitrogen and the occurrence of denitrification during low flow conditions cause $NO_3^-$ concentrations to decrease to a minimum in July and August [30]. Differences of $NO_3^-$ concentrations in different seasons were not observed in Litija ($P = 0.82$, $F = 0.38$). The reason might be in land use. Forest predominates in Litija, on the other hand much more agricultural areas and artificial surfaces are present around Jesenice na Dolenjskem.

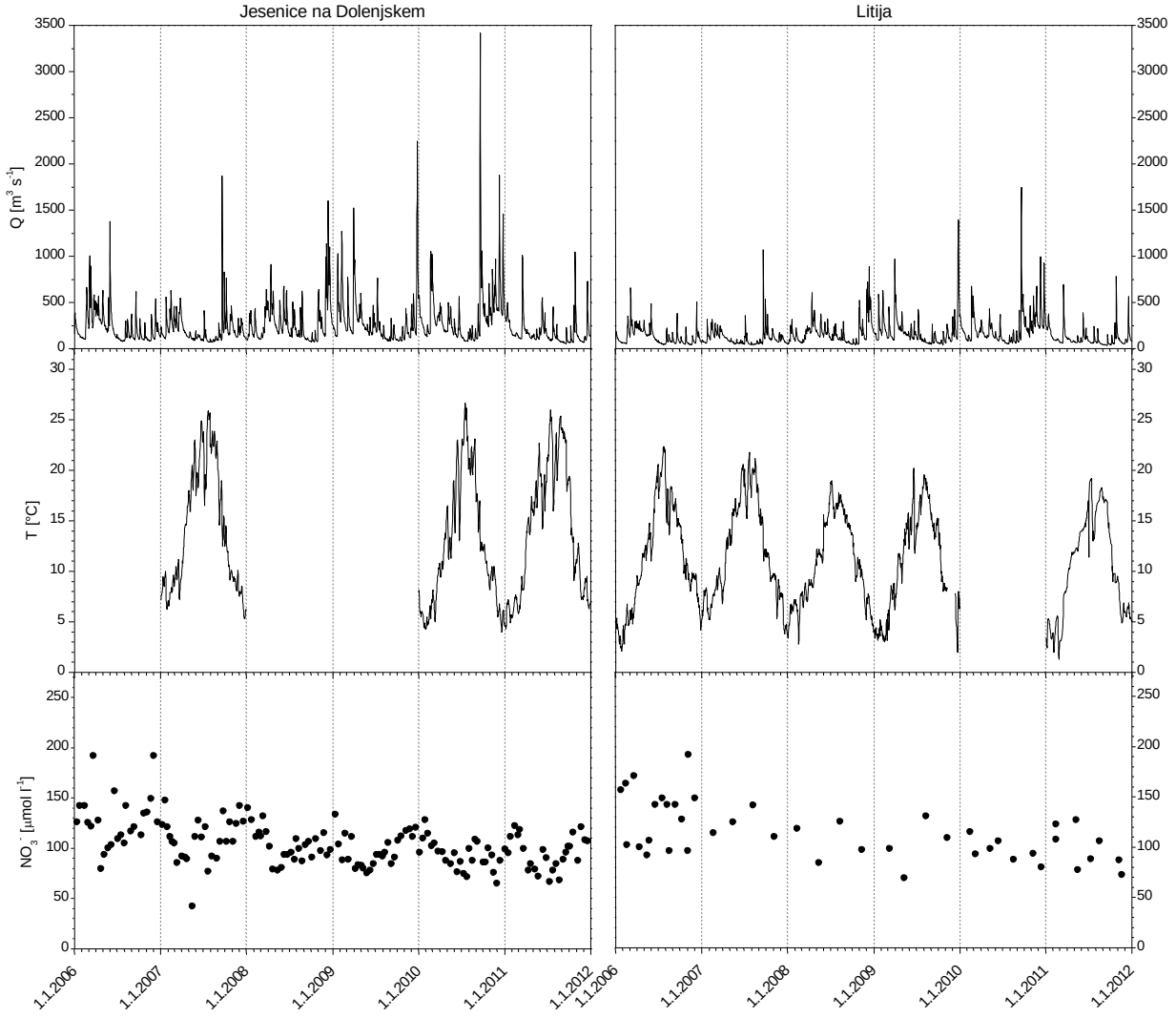


**Figure 3:** The annual mean discharge, temperature and nitrate concentrations since 2006 at Litija and Jesenice na Dolenjskem.

A significant difference was observed between the year and $NO_3^-$ concentrations at Jesenice na Dolenjskem ($P = 1.87 \cdot 10^{-8}$, $F = 9.09$) and Litija ($P = 0.03$, $F = 2.54$). Further, it was found that $NO_3^-$ concentrations decrease linearly with time (Fig. 3). The temperature does not play a significant role in the distribution of the $NO_3^-$ concentrations at both locations.

Higher $NO_3^-$ concentrations were observed during low river discharges in autumn than in spring at both locations [30]. Larger effect of dilution is present at Litija comparing to Jesenice na Dolenjskem (Fig. 4), although much higher discharge of Sava is present.

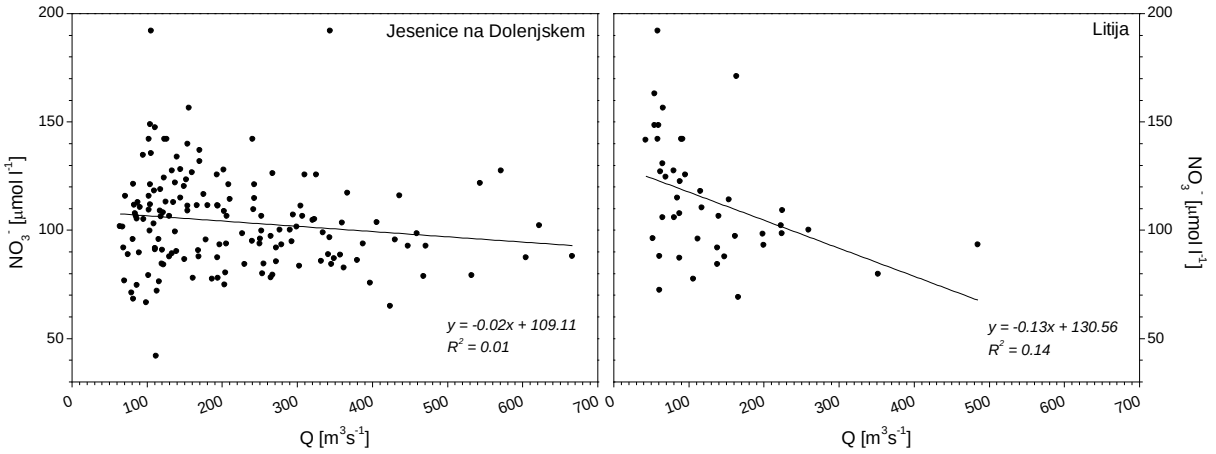


**Figure 4:** The relationship between discharge and $NO_3^-$ at Jesenice na Dolenjskem and Litija. The diagrams shows that dilution effect is presen at both locations.

$\delta^{15}N_{NO3}$ analyses show that at Litija predominant source of the $NO_3^-$ is not seasonally dependent ($P = 0.98$, $F = 1.58$). However, the mean $\delta^{15}N_{NO3}$ value of 5.6‰ indicates that $NO_3^-$ dynamics of the Sava's ecosystem is influenced manly by natural inputs and only by negligible anthropogenic inputs. It can be concluded that the main stream of the Sava in Slovenia is not affected by pollution with anthropogenic nitrogen. Some problems were mainly related to its triburtary Kamniška Bistrica. Higher concentrations of up to 0.69 mmol $l^{-1}$, in parallel with higher $\delta^{15}N_{NO3}$ values (up to +16.7‰) determined at the month of the river, indicate an organic fertilizer source of N or the influence of N derived from animal manure from the large pig farm (Ihan) [30]. Problems with eutrophication were also not observed in the SRB, but this situation could change, since in the future new hydroelectric power plants are under construction.

# 5 Conclusion

Aquatic systems are increasingly at risk due to land-use changes, population growth, pollution discharges and excessive groundwater pumping. Our research focused on the sources and distribution of $NO_3^-$ concentrations at selected locations in the Sava River Basin in Slovenia during 2006-2012.

Based on the basic statistical analyses it can be concluded that $NO_3^-$ concentrations and $\delta^{15}N_{NO3}$ values depend on the season and year selected locations Litija and Jesenice na Dolenjskem. The dilution effect is also present indicating that within SRB the risk of $NO_3^-$ pollution is low. $\delta^{15}N_{NO3}$ data indicated that nitrate in the river is originating mainly from soil.

The plane of our future work is to define how the $NO_3^-$ concentrations and other parameters influence the life of different organisms in the Sava River. This would be possible by analysing the environmental data by machine learning methods.

# References:


[1] K. Noone, R. Sumaila, R. J. Díaz. The Impacts of Multiple Stressprs, A complex web of challenges. *Stockholm Environment Institute*. URL: http://www.sei-international.org/mediamanager/documents/Publications/SEI-Preview-TheImpactsOfMultipleStressors-AComplexWebOfChallenges.pdf (accessed March 2014).

[2] UNESCO. *World Water Assessment Programme (2009). Water in a Changing World.* The United Nations World Water Development Report 3, 2009.

[3] C. J. Vörösmarty, P. B. McIntyre, M. O. Gessner, D. Dudgeon, A. Prusevich, P. Green, S. Glidden, S. E. Bunn, C. A. Sullivan, C. R. Liermann, P. M. Davies. Global threats to human water security and river biodiversity. *Nature,* 467: 555–561, 2010.

[4] S. D. Cooper, P. S. Lake, S. Sabater, J. M. Melack, J. L. Sabo. The effects of land use changes in streams and rivers in Mediterranean climates. *Hydrobiologia,* 719: 383–425, 2013.

[5] D. Kay, M. D. Wyer, J. Crowther, L. Fewtrell. Faecal indicator impacts on recreational waters: budget studies and diffuse source modelling. *Journal of Applied Microbiology,* 85: 70S–82S, 1999

[6] D. Kay, R. Falconer. Hydro-epidemiology: the emergence of a research agenda. *Environmental Fluid Mechanics,* 8: 451–459, 2008

[7] D. M. Oliver, P. M. Haygarth, C. Clegg, A. L. Heathwaite. Differential *E. coli* die-off patterns associated with agricultural matrices. Environmental Science & Technology, 40(18): 5710–5716, 2006

[8] D. E. Walling. The sediment delivery problem. *Journal of Hydrology*, 65: 203–207, 1983

[9] E. M. Bennett, S. R. Carpenter, N. F. Caraco. Human impact on erodible phosphorous and eutrophication: a global perspective. *Bioscience,* 51: 227–234, 2001

[10] H. W. Pearl. Controlling eutrophication along the freshwater-marine continuum. *Estuaries and Coasts*, 35: 593–601, 2009

[11] V. H. Smith, D. W. Schindler. Eutrophication science: where do we go from here? *Trend in Ecology and Evolution*, 24(4): 201–201, 2009

[12] U. Foerster, G. T. W. Wittmann. *Metal Pollution in the Aquatic Environment, 2nd Edition*. Springer, 1981.

[13] P. Falkowski, R. J. Scholes, E. Boyle, J. Canadell, D. Canfield, J. Elser, N. Gruber, K. Hibbard, P. Högberg, S. Linder, F. T. Mackenzie, B. Moore, T. Pedersen, Y. Rosenthal, S. Seitzinger, V. Smetacek, W. Steffen. The global carbon cycle: a test of our knowledge of Earth as a system. *Science,* 290: 291–296, 2000

[14] P. M. Vitoušek, R. Naylor, T. Crews, M. B. David, L. E. Drinkwater, E. Holland, P. J. Johanes, J. Katzenberger, L. A. Martinelli, P. A. Matson, G. Nziguheba, D. Ojima, C. A. Palm, G. P. Robertson, P. A. Sanchez, A. R. Townsend, F. S. Zhang. Nutrient imbalances in agricultural development. *Science,* 324: 1519–1520, 2009

[15] J. A. Thornton, W. Rast, M. M. Holland, G. Jolankai, S. O. Ryding [Eds]. *Assessment and Control of Non-Point Pollution of Aquatic Ecosystems*. Man and the Biosphere Series, Parthenon Publishing Group, Reading, 1999.

[16] P. Cullen, E. M. O'Loughlin. Non-point sources of pollution. In *Prediction of Water Quality*, Australian Academy of Science, Canberra, Australia, 1982.

[17] R. Carpenter, N. F. Caraco, D. L. Correl, R. W. Howarth, A. N. Sharpley, V. H. Smith. Nonpoint pollution of surface waters with phosphorus and nitrogen. *Ecological Applications,* 8: 559–568, 1998

[18] A. Johannsen, K. Dähnke, K. Emeis. Isotopic composition of nitrate in five German rivers discharging into the North Sea. *Organic Geochemistry,* 39(12): 1678–1689, 2008

[19] B. Mayer, E. W. Boyer, C. Goodale, N. A. Jaworski, N. Van Breemen, R. W. Howarth, S. Seitzinger, G. Billen, K. Lajtha, K. Nadelhoffer, D. Van Dam, L. J. Hetling, M. Nosal, K. Paustan. Sources of nitrate in rivers draining sixteen watersheds in the northeastern U.S.: Isotopic constraints. *Biogeochemistry,* 57/58: 171–192, 2002

[20] G. Hebert, L. I. Wassenaar. Stable nitrogen isotopes in waterfowl feathers reflect agricultural land use in western Canada. *Environ Science & Technology,* 35(17): 3482–3487, 2001

[21] M. Voss M, B. Deutsch, R. Elmgren, C. Humborg, P. Kuuppo, M. Pastuszak, C. Rolff, U. Schulter. Source identification of nitrate by means of isotopic tracers in the Baltic Sea catchments. *Biogeosciences,* 3: 663–676, 2006

[22] R. Harrington, B. P. Kennedy, C. P. Chamberlain, J. D. Blum, C. L. Folt. $^{15}N$ enrichment in agricultural catchments: field patterns and applications to tracking Atlantic salmon (Salmo salar). *Chemical Geology,* 147(3): 281–294, 1998

[23] Y. Chang, C. Kendall, S. R. Silva, W. W. Battaglin, D. H. Cambell. Nitrate stable isotopes: tools for determining nitrate sources among different land uses in the Mississippi River Basin. *Canadian Journal of Fisheries and Aquatic Sciences*, 59(12): 1874–1885, 2002

[24] Agency of the Republic of Slovenia (ARSO). URL : http://www.arso.gov.si/en/ (accessed March 2014).

[25] T. Kanduč, K. Szramek, N. Ogrinc, L. M. Walter. Origin and cycling of riverine inorganic carbon in the Sava River watershed (Slovenia) inferred from major solutes and stable carbon isotopes. *Biogeochemistry,* 86: 137–154, 2007a

[26] T. Kanduč, M. Burnik Šturm, J. McIntosh. Chemical dynamics and evaluation of biogeochemical processes in alpine river Kamniška Bistrica, North Slovenia. *Aquat Geochem* 19 : 323–346, 2013

[27] T. Kanduč, N. Ogrinc, T. Mrak. Characteristics of suspended matter in the River Sava watershed, Slovenia. *Isotope Environmental and Health Studies* 43(4): 369–386, 2007b

[28] Stat Trek. *Statistics and Probability Dictionary*. URL : http://stattrek.com/statistics/dictionary.aspx?definition=f_statistic (accessed April 2014).

[29] N. Ogrinc, T. Kanduč, W. Stichler, P. Vreča. Spatial and seasonal variations in $\delta^{18}O$ and $\delta D$ values in the River Sava in Slovenia. *Journal od Hydrology,* 359: 303–359, 2008

[30] N. Ogrinc, T. Kanduč, D. Kocman. Integrated approach to the evaluation of chemical dynamics and anthropogenic pollution sources in the Sava River Basin, Sava River Basin book in press.

## For wider interest

This research was performed within on going EU project GLOBAQUA dealing with multiple stressors in the Sava River Basin. One of the main objectives is to improve our knowledge on relationships between multiple stressors and how these interactions might determine changes in the chemical and ecological status in studied ecosystem. Such studies are needed in order to improve water protection and sustainable development.

The plane of our future work is to define how the $NO_3^-$ concentrations and other parameters influence the life of different organisms in the Sava River. This would be possible by analysing the environmental data by machine learning methods.

# Informacijske in komunikacijske tehnologije (Information and Communication Technologies)

# Analysis of the open advertising data set

**Martin Frešer**[1,2], **Domen Košir**[3]

[1] Department of Intelligent Systems, Jožef Stefan Institute, Ljubljana, Slovenia

[2] Faculty of Mathematics and Physics, Faculty of Computer and Information science, Ljubljana, Slovenia

[3] Faculty of Computer and Information science, Ljubljana, Slovenia

martin.freser@gmail.com

**Abstract.** A crucial task of world's biggest search engines, which want to make revenue out of advertising (ads), is to predict impressions of ads, clicks on ads and Click-Through-Rate(CTR) for ads, so that they could show ads to the interested users, according to their search queries. So it is not surprising, that companies like Google and Microsoft invest a lot of money in researches for this field. This paper analyses, how values of impressions, clicks and CTR vary over time. The analysis is done on the open advertisement data set, retrieved from the University College London (UCL). Those three values are also the main focus of this work. We will test, if markets of US and UK are correlated. At the end, we will try to predict CTR value of US-market learned from UK-market, using various machine learning techniques.

**Keywords**: CTR, impressions, clicks, advertising, predicting, machine learning

## 1 Introduction

Advertising is one of the most important fields of study for big companies, e.g. Google, since it highly contributes to their revenue. For example, in 2012 Google made almost 95% out of its 46.039 billion of dollars revenue out of web advertising [6]. That is 43.686 billion just from advertising. Interesting finding is that the most expensive keyword at the time of writing is "Insurance", which costs the advertiser around 54 dollars per click. One of the most expensive sites for advertising is the American website Hulu, which charges around 35 dollars for 1000 impressions. Number of impressions is number of times the ad was shown. Google has two systems, AdSense [13] and AdWords [12], which charge advertisers mostly with two techniques. Those are cost-per-click (CPC) and cost per 1000 impressions, which is

also known as cost-per-mile (CPM). Therefore we see that predicting a number of impressions and clicks could be vital information for improving those systems. Problem lies in the fact, that big companies will not give their studies and information to the public, so there does not exist a lot of data to study. Still, related work exists and will be presented in Section 2. Researchers from the University College London created a freely available computational advertising data set [5] called "Open Advertising Data set" from publicly available sources, which we will use in this work and it will be presented in Section 3. One of the most important values for predicting, how likely the user will click on ad is CTR. CTR is an abbreviation for Click-through-rate and it is derived as:

$$CTR = \frac{\#clicks}{\#impressions} \tag{1}$$

Predicting CTR is very important for AdWords and other similar systems. Those systems show ads to the users according to their search queries. When user starts a search query, system launch an auction, where every advertiser can make only one entry. Advertiser's ad is then ranked as the product of highest CPC bid and quality score. Quality score is the relevance and usefulness of an ad to the user, where the crucial component is the prediction of CTR. In the data set we only have information about ad title and 3 observed values, so we will focus on markets as whole and we will try to predict CTR for the whole market. Section 4.1 presents 3 supervised machine learning techniques that are used for predicting CTR and 3 correlation tests that are used for testing, if two markets are correlated. Results of experimental work with data is presented in Section 4.2, where we also show some interesting trends of advertisers and users and also some correlations between two very differently sized markets.

## 2 Related work

A various researches in this field were already made. Dembczynski et al. [1] presented an approach to this problem using decision rules. Interesting part is that Microsoft provided a big set of data, under their program Beyond Search, which is rather rare for big search companies.

A Microsoft research department published their model in [2]. They claimed that their model is able to improve accuracy at predicting CTR, which also improve search system revenue and user satisfaction.
Google researchers published their research in [3], where they optimize their existing models and experiment on them.

# 3 Data set

Data set was obtained from UCL [5] and is divided into 3 parts, but we use data sets number 2 and 3, because they have a new format, which includes all data we need. Data set 2 contains information about ads from 24th of May 2012 to 14th of February 2013, while data set 3 contains information from 25th of July 2012 to 14th of February 2013. Each data set covers US and UK market. Data set 2 contains 546 ads for both markets; data set 3 contains 747 ads for both markets. In each file, which represent one day, the first line sums up all values (impressions and clicks) and also derives CTR value according to those sums. Following lines represent a keyword, number of impressions, number of clicks, CTR and cost per click. Because of very truncated information about the ads (the keyword is the only information about the ad's content) we will only use the first line of a file, which is a generalization of a day.

# 4 Experimental setup and results

## 4.1 Experimental setup

Focus of the paper is on 3 most important values, which are impressions, clicks and CTR. First, we looked how the number of impressions and clicks vary throughout the year. This was done to detect the variation of numbers and analyse the best and worst timing to advertise according to the time of the year. We analyse UK and US markets separately on both data sets, so we get 2 graphs with 2 curves for each observed value, where time is independent variable and observed value is dependant variable. We grouped data in 7 consecutive days, so that the graph is more readable.

Because of the very interesting visual results of CTR in the US and UK markets, we set the hypothesis that those two markets are correlated. We measured their correlation with 3 different correlation tests: Pearson product-moment correlation

coefficient, Spearman's rank correlation coefficient (Spearman's ϱ) and Kendall tau rank correlation coefficient (Kendall's τ) [11], which are all implemented in R library stats [10]. They measure the correlation between two variables, meaning they test null-hypothesis if two variables are independent. We tested null-hypothesis, that US and UK market are independent, with confidence interval of 0.05. We reject the null hypothesis, if p-value [14] is less than 0.05. Furthermore, we tried to predict CTR value on the US market, using CTR values of the UK market. Note that this is conceptually wrong, because data is obtained at the same time. For training the data we omitted unknown values. We used 3 supervised machine-learning techniques. We worked with the statistical programming language R and respective libraries that were needed for executing algorithms. Regression methods were used since we had to predict continuous class. We used linear regression, regression decision tree and random forest with regression values [9].

We trained a model and evaluated it on every data set separately, using UK market as training set and US market as test set. As we could see from the graph on figures 5 and 6, a month has a rather big influence on CTR, so we decided that a month should always be treated as an attribute. At first we tried only with one attribute. Then we also added a day of week. Here the problem becomes more complex so it would be interesting to see, if random forest predicts better than the two other models.

## 4.2 Results

### 4.2.1 Graphs and overview

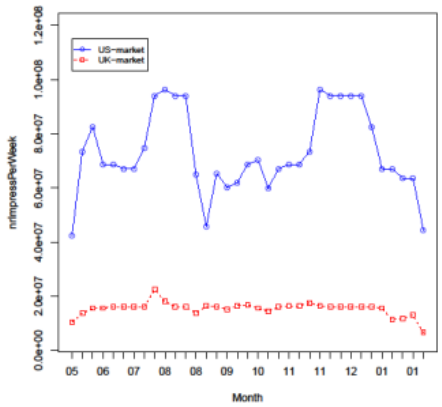


**Figure 1**: Number of impressions of ads per week for data set 2 on both markets

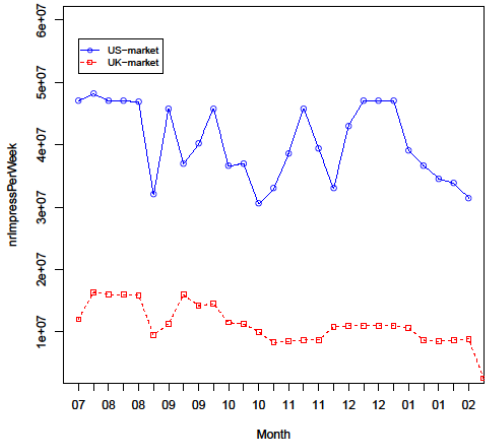


**Figure 2**: Number of impressions of ads per week for data set 3 on both markets

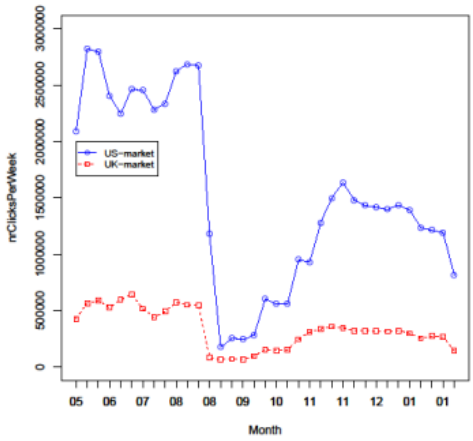


**Figure 3**: Number of clicks on ads per week for data set 2 on both markets

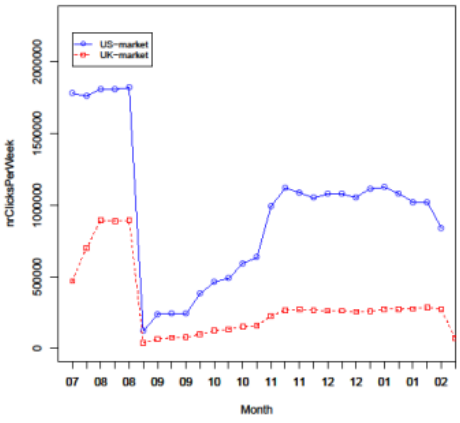


**Figure 4**: Number of clicks on ads per week for data set 3 on both markets

Number of impressions for both markets is presented on figures 1 and 2. Number of clicks for both markets is presented on figures 3 and 4. On figures 1, 2, 3 and 4 we can see, that in the US-market there is more data and therefore higher values for

number of impressions and number of clicks. We labeled x-axis with the number of months for better understanding, though units on axis represent weeks. As for data set 2, on figure 1 we can see that the number of impressions is rather steady for the UK market. On the other hand, we can see that in the US market, there is a growth of impressions in July and August, and towards the end of the summer, there is a visible fall. That could be because advertisers end their advertising campaigns and are preparing for December, where we can again see the growth of impressions. If we look at the figure 3, there is about the same trend for the US market, which is rather logical, if number of impressions fall, then also the number of clicks should fall. Although what we could see is, even if the number of impressions in the UK is constant, the number of clicks falls at the end of the summer and then slightly increases until December. Number of impressions on data set 3 on figure 2 is much noisier for the US market, but still, we could see, that number of clicks on figure 4 is acting very similar as on data set 2. For the UK market we can see on figure 2 that number of impressions has almost the same trend as clicks on figure 4, only with a little delay, so we can see that advertisers have to quickly adapt to new circumstances, to avoid spending money for impressions, which do not bring success.

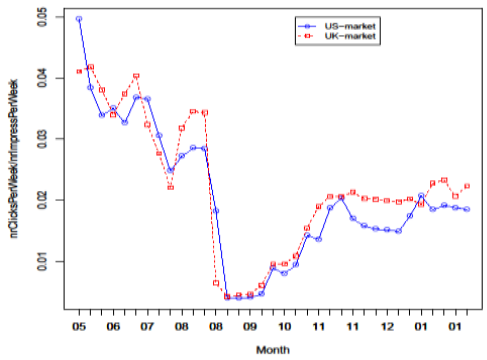


**Figure 5**: CTR of ads per week for data set 2

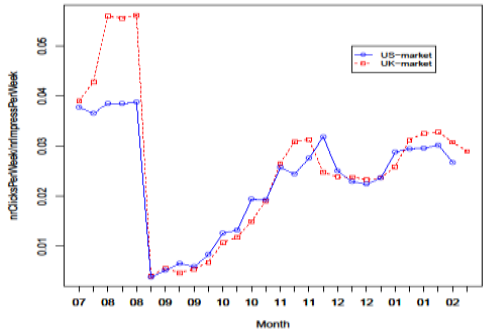


**Figure 6**: CTR of ads per week for data set 3

Only reliable way to somehow compare the two observed markets are seen on figures 5 and 6. Firstly we see that curves on both graphs are rather similar, at least they have same ups and downs on similar time. Sometimes, CTR of the UK is much higher than the US but in general the curves are pretty much the same. This is potentially a very good result, because of the next example. Let's take a look at graph on figure 1, showing just impressions. We can see, that the US-market has much bigger numbers of impressions, at one point the difference is 8e+07, calculated over the thumb. So only for our data set, we looked at around 9 months, which is around 36 weeks, which means that we had to monitor around $36 \cdot 8e+07$ impressions more than on the UK-market. So if we could study only the UK-market, it would save us time, money and work. And those figures of CTRs per week are showing us exactly that we could study the smaller UK-market and people here are acting very similar opposing to the US-market.

Value CTR is probably the most important to advertisers, since it combines impressions and clicks and it is a great indicator that tells us, when is best to invest our money to advertise. From this two graphs we can see, that the most appropriate time to advertise according to our data is in the summer months and the least appropriate between the end of the summer and start of the fall. Of course we lack data between January and at least May.

### 4.2.2 Models for predicting changes of observed values according to the day of the week

**Table 2**: Correlation coefficients performed on data set 3

| Test | p-value | correlation coefficient |
|---|---|---|
| Pearson's coefficient | 1.6e-13 | 0.94 |
| Spearman's $\varrho$ | 2.5e-07 | 0.96 |
| Kendall's $\tau$ | 3.3e-15 | 0.87 |

On table 2, we can see that all tests have p-value lower than 0.05, so we reject every single null-hypothesis (which means that two variables are independent) and accept alternate hypothesis that observed two variables are dependent. All correlation coefficients are near to 1 and over 0.5, which means that the two variables are

strongly connected. That result allows us to try to predict the US-market's CTR with models, learned with the UK-market's CTR.

**Table 3**: Predicting CTR for US-market learned from UK market, data set 3, Attributes: Month

| Algorithm | SE | MSE |
|---|---|---|
| Regression tree | 90.99 | 0.48 |
| Linear regression | 223.97 | 1.19 |
| Random Forest | 89.53 | 0.47 |

**Table 4**: Predicting CTR for US-market learned from UK market, data set 3, Attributes: Month, Day of week

| Algorithm | SE | MSE |
|---|---|---|
| Regression tree | 90.99 | 0.48 |
| Linear regression | 223.75 | 1.19 |
| Random Forest | 64.40 | 0.34 |

We will only take a look at data set 3, while results on data set 2 are very similar. If we take a look at table 3, we can see that linear regression is very poor, producing a high error. On the other hand we see that random forest and regression decision tree performed well, and produced quite a small error. If we continue and include the day of week along with the month, results are shown on table 4, we see that regression decision tree did not even consider this attribute useful and produced the same model, on the other hand, random forest made a progress and produced a model with much smaller mistake.

## 5 Conclusion

Just analysing and visualizing data from our data set showed us some very interesting trends and correlations. We saw, that advertising is the most active in summer days until the end of August and after that, it starts to rise again in December. We also acknowledged that the behaviour of CTR in the US-market is very similar to the CTR behaviour in the UK-market, which is useful since the UK-market is much smaller, and it is consequently easier to obtain interesting data. We confirmed that with various correlation tests. So we learned a model learned from the UK-market and applied it to the US-market. Random forest gave best and also good results. This

could be a useful finding for future attempts to predict single ad CTR, since we could find a similar ads in other markets and try to predict CTR according to those ads. But probably future researches should be done to discover such dependencies. We also predicted change of impressions, clicks and CTR according to the day of the week with various algorithms. In the future, we could try to predict CTR for single ads and could also try to learn more complex models but for that we would need more information about ads.

## References:


[1] Dembczynski, Krzysztof, W. Kotlowski, and Dawid Weiss. "Predicting ads click- through rate with decision rules." Workshop on Targeting and Ranking in Online Advertising. Vol. 2008. 2008.
[2] Richardson, Matthew, Ewa Dominowska, and Robert Ragno. "Predicting clicks: estimating the click-through rate for new ads." Proceedings of the 16th international conference on World Wide Web. ACM, 2007.
[3] McMahan, H. Brendan, et al. "Ad click prediction: a view from the trenches." Proceedings of the 19th ACM SIGKDD international conference on Knowledge discovery and data mining. ACM, 2013.
[4] Shuai Yuan, Jun Wang, "Sequential Selection of Correlated Ads by POMDPs", CIKM, 2012
[5] (2014, January) Open advertising dataset [Online] https://code.google.com/p/openadvertising-dataset/
[6] (2014, January) 2013 financial tables. [Online] http://investor.google.com/financial/tables.html
[7] Breiman, Leo. "Random forests." Machine learning 45.1 (2001): 5-32.
[8] Bonett, Douglas G., and Thomas A. Wright. "Sample size requirements for estimating Pearson, Kendall and Spearman correlations." Psychometrika 65.1 (2000): 23-28.
[9] Liaw, Andy, and Matthew Wiener. "Classification and Regression by randomForest." R news 2.3 (2002): 18-22.
[10] (2014, January) The R Stats Package [Online] http://stat.ethz.ch/R-manual/R-patched/library/stats/html/00Index.html
[11] Chok, Nian Shong. "Pearson's Versus Spearman's and Kendall's Correlation Coefficients for Continuous Data. " Master's Thesis, University of Pittsburgh. (2010)
[12] (2014, January) AdWords [Online] adword.google.com
[13] (2014, January) AdSense [Online] adsense.google.com
[14] Schervish, M. J. "P Values: What They Are and What They Are Not" The American Statistician 50 (1996).

## For wider interest

Big search engines companies e.g. Google and Microsoft provide most of their revenue from showing ads (Google for example earned 43 billon out of 46 billon $ of their revenue out of showing ads in 2012). So it is no surprise that they have to show ads, which are interesting for users according to their search queries. Very important value for algorithms that determine, if an ad will be shown, is Click through rate (CTR). CTR tells us the rate of how many times ad was clicked according to how many times was shown. In this work we predict CTR on an average week basis. We discover some interesting correlations between US and UK market. We use this knowledge, to learn from much smaller UK market and try to predict average CTR for much larger US market. We also discover, that users likes to click on ads much more in summer months and around Christmas, while in the fall, there are less clicks.

# Recognizing Human Activities and Detecting Falls in Real-time

**Hristijan Gjoreski**[1,2], **Simon Kozina**[1,2], **Mitja Luštrek**[1,2], **Matjaž Gams**[1,2]
[1] Department of Intelligent Systems, Jožef Stefan Institute, Ljubljana, Slovenia
[2] Jožef Stefan International Postgraduate School, Ljubljana, Slovenia
hristijan.gjoreski@ijs.si

**Abstract.** The paper presents a system that recognizes human activities and detects falls in real-time. It consists of two wearable accelerometers placed on the user's torso and thigh. The system is tuned for robustness and real-time performance by combining domain-specific rules and classifiers trained with machine learning. The offline evaluation of the system's performance was conducted on a dataset containing a wide range of activities and different types of falls. The F-measure of the activity recognition and fall detection were 96% and 78%, respectively. Additionally, the system was evaluated at the EvAAL-2013 activity recognition competition and awarded the first place, achieving the score of 83.6%, which was for 14.2 percentage points better than the second-place system. The competition's evaluation was performed in a living lab using several criteria: recognition performance, user-acceptance, recognition delay, system installation complexity and interoperability with other systems.

**Keywords**: Activity recognition; Fall detection; Ambient assisted living; Machine learning; Rules; Accelerometers.

## 1 Introduction

The world's population is aging rapidly, threatening to overwhelm the society's capacity to take care of its elderly members. The percentage of persons aged 65 or over in developed countries is projected to rise from 7.5% in 2009 to 16% in 2050 [1]. This is driving the development of innovative ambient assisted living (AAL) technologies to help the elderly live independently for longer and with minimal support from the working-age population [2][3]. To provide timely and appropriate assistance, AAL systems must understand the user's situation and context, making activity recognition (AR) an essential component [4][5][6]. Fall detection (FD) is an

important component of many AAL systems because approximately half of the hospitalizations of the elderly are caused by falls [7]. Fear of falling is an important cause for nursing home admission [8], and "the long lie" (not being able to get up and call for help) is an important predictor of death within six months [9].

This paper presents the RAReFall system, which recognizes the user's activities and detects falls in real time. The architecture of the system combines rules to recognize postures (static activities), which ensure the behavior of the system is predictable and robust, and classifiers trained with machine learning (ML) algorithms, to recognize dynamic activities, for which the rules are not sufficiently accurate. For the FD, rules are used that take into account high accelerations associated with falls and the recognized horizontal orientation (e.g., falling is often followed by lying).

Initially, the RAReFall system was evaluated offline, on a dataset containing a wide range of activities and different types of falls. Its recognition performance was very high, encouraging us to take part in the EvAAL-2013 activity recognition competition [10], which evaluates AR systems in a living lab. The RAReFall system was evaluated best on a combination of criteria: recognition performance, user-acceptance, recognition delay, system installation complexity and interoperability with other systems.

## 2 Related Work

AR approaches can be divided into those using non-wearable sensors and those using the wearable type. The most common non-wearable approach is based on cameras [11]. Although this approach is physically less intrusive for the user compared to the wearable sensors, it suffers from problems such as low image resolution, target occlusion, time-consuming processing, and often the biggest issue is user privacy: the user has to accept the fact that a camera will record him/her. The most exploited and probably the most mature approach to AR is using wearable accelerometers, which are both inexpensive and effective [12][13]. This is also the reason why wearable accelerometers were used for our RAReFall system.

There are two common types of wearable-sensor approaches to AR that have proved to be successful: using domain knowledge encoded with rules, and using ML. The first approach uses rules applied to accelerometer's data in order to recognize an activity. This approach proved to be successful for static activities such as: standing, sitting and lying [12]. The second approach is based on known classification methods, e.g., decision trees, Random Forest, SVM, kNN, Naive Bayes, etc., which are applied on the accelerometer's data [13]. The problem with this approach is that the training data should include each activity of the user performed in all possible ways, e.g., lying backwards, lying sideway, lying on the back, etc. This makes the ML approach unpredictable and less-attractive for real-life usage. In our approach we overcome this issue by combining the two approaches, thus we use domain rules for some of the static activities and ML for the others. This way, we increase the understandability of the system and also making it more predictable and robust for situations that are not included in the training data.

## 3 System Implementation

The RAReFall system is shown in Fig. 1. It consists of two accelerometers, placed on the user's torso and the thigh. The accelerometers can be attached to the user's body in several ways, making the system more user-acceptable and also adjustable to the occasion (e.g., worn indoors or outdoors). Some examples of how and where the sensors can be worn include, but are not limited to:

- torso: worn on a cord around neck, elastic strap, pockets sewn into garment
- thigh: in the pocket, elastic strap, pocket sewn into garment

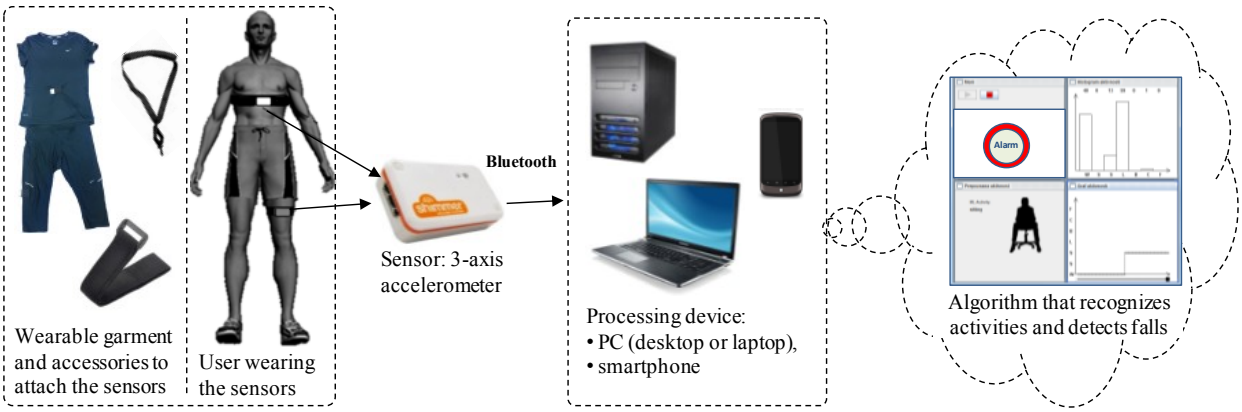


**Figure 1**: RAReFall system overview.

The placement of the sensors was chosen as a trade-off between the physical intrusiveness and the performance in preliminary tests [14][15]. The Shimmer accelerometer-sensor platform [16] was chosen because it has a reasonable battery life, compact size, 3-axis accelerometer and uses Bluetooth communication. In general, any sensor with 3-axis accelerometer and Bluetooth module can be used.

The sensors' data are received and processed on a Bluetooth-enabled processing device which processes the data in real time. The current implementation of the system is developed for indoor usage (a house, a flat, etc.); therefore a laptop/desktop PC is used for processing. Additionally, the PC is equipped with a long-range Bluetooth antenna in order to ensure the maximum reliability and signal strength (theoretically covering up to 300 meters radius, which is more than enough for indoors coverage). However a smartphone implementation is technologically possible and considered for future work.

## 4 Methods

The AR and FD pipeline is shown in Fig. 2. First, the sensors transmit the raw acceleration data over Bluetooth to the processing unit, i.e., PC. The data from both sensors are then preprocessed: synchronized, filtered and segmented. Then the pipeline splits in two. On one side, the segmented data are transformed into feature vectors for the AR module, which recognizes the user's activity. On the other side, the FD module checks the acceleration for falls. If a fall pattern is recognized, the user's orientation is checked. If the orientation corresponds to lying, a fall is detected. Both the AR and FD modules are evaluating the user’s situation every 250 milliseconds using the last 2 seconds of sensor data. For instance, if the current system time is denoted with t, the FD module evaluates fall events in the [t – 2 s, t – 1 s] interval, and the [t – 1 s, t] interval is used to check if the user's orientation corresponds to lying. If the fall event is detected and the orientation is correct, the reported activity is falling, otherwise the reported activity is computed with the AR module in the [t – 2 s, t] interval. The system thus reports the user’s activity and detects falls with a two-second delay. In the following sections, the AR and FD methods are briefly described. More technical details can be found in our previous work, [17] for AR, and [18] for FD.

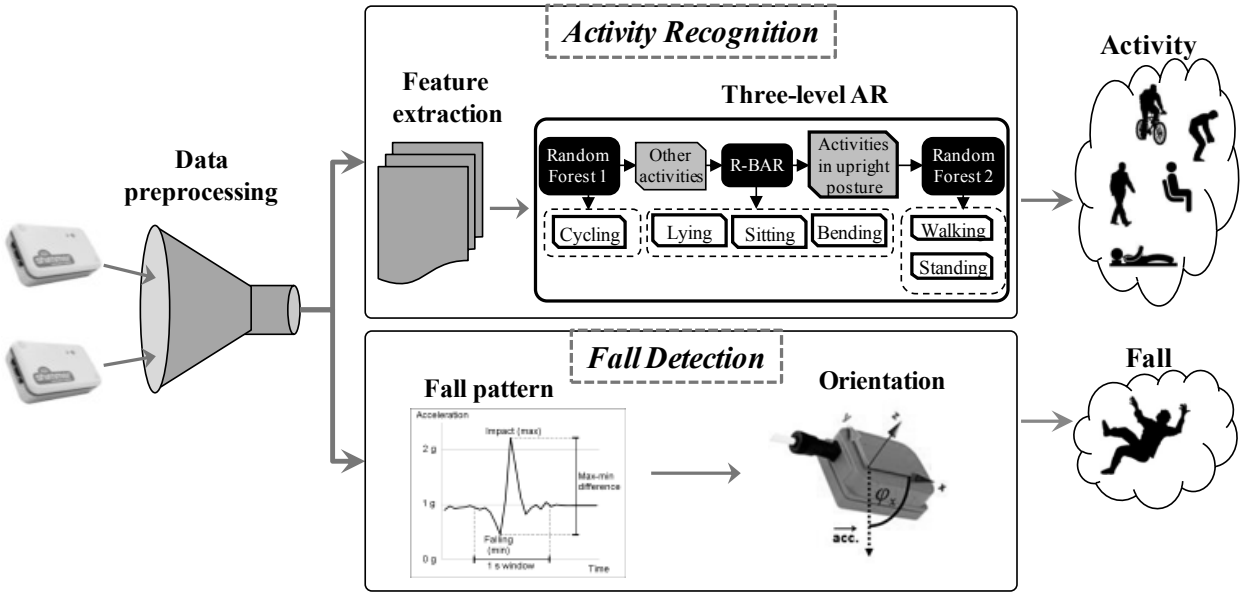


**Figure 2:** The data and recognition flow in the RAReFall system.

## 4.1 Activity Recognition

In the AR module, the activities are recognized by a three-level scheme [17]. The AR scheme was developed after empirical analysis of the data, which showed that some activities (such as cycling) are better recognized by a classifier trained only to distinguish that particular activity from the others. Therefore, on the first level the feature vector is fed into a Random Forest classifier, which is trained to distinguish cycling from the other activities. If the activity is not classified as cycling, the feature vector is passed to the second level, where the activities are recognized by rules. On this level, only the features that the best represent the sensor orientation are used (using component of the acceleration that corresponds to the gravity). The following activities are recognized at this level: sitting, lying, bending, and upright posture. If the recognized activity is the upright posture, the third level of AR is used to distinguish between standing and walking. The feature vector is again fed into a Random Forest classifier, which is trained to separate these two activities.

## 4.2 Fall Detection

A typical acceleration pattern during a fall, measured by an accelerometer placed on the abdomen, is a decrease in acceleration followed by an increase [18]. This is because an accelerometer, when stationary, registers 1 g (the Earth's gravity) and during free fall 0 g. When a person starts falling, the acceleration decreases from 1 g

to around 0.5 g (perfect free fall is never achieved). Upon the impact with the ground, a short strong increase in the acceleration is measured.

To detect acceleration fall patterns, we used the length of the acceleration vector to ignore the direction of the acceleration. The minimum and the maximum acceleration within a one-second window were measured. If the difference between them exceeded 1 g and the maximum came after the minimum, a fall pattern was found. We augmented the fall-pattern detection with the measurement of the user's orientation after a potential fall. We assumed that the orientation of the user's body after a fall cannot be upright. Therefore, a fall was detected if a fall pattern was detected and the orientation in the next second was not upright.

# 5 Evaluation

## 5.1 Offline Evaluation

The offline evaluation of the RAReFall system was performed in order to check the recognition performance of the methods, using a pre-recorded dataset (publicly available at: http://dis.ijs.si/ami-repository/). A 90-minute, test scenario was designed in cooperation with a medical expert to capture the real-life conditions of a person's behavior, although it was recorded in a laboratory. The scenario was performed by 10 volunteers. It included the following elementary activities: standing, sitting, lying, on all fours, bending (standing leaning), walking and cycling. These activities were selected as they are the most common elementary, everyday-life activities.

Table 1 shows the offline performance of the RAReFall system on the pre-recorded dataset. The performance of the AR is high, achieving 96.36% F-measure score averaged over all activities. The performance of the FD shows that 93.3% of the falls were detected (recall value), and 66.7% of all the fall detections were actually falls (precision value), giving the final F-measure of 77.8%. The detailed FD results (Table 2) show that the first event – tripping (quick uncontrolled fall) was detected each time (15 out of all 15 events). The next event, fainting, was detected 13 out of 15 times. The next two events were the non-fall events that are difficult to distinguish from the fast falls because of the high acceleration. Because the FD

module also checks the user's orientation after a potential fall, it was able to distinguish quickly sitting on the chair from the falls, since the user ended up in the upright posture. However, this was not the case for quickly lying in the bed (13 false detections). For correct recognition of this event, additional information about the user would be needed, e.g., user's location.

**Table 1.** RAReFall system - offline performance.

| Performance | Activity Recognition | Fall Detection |
|---|---|---|
| **Recall** | 96.19% | 93.33% |
| **Precision** | 96.53% | 66.67% |
| **F-measure** | 96.36% | 77.78% |

**Table 2.** RAReFall system - Fall detection detailed results.

| Events | Detected/All |
|---|---|
| **Tripping** | 15/15 |
| **Fainting** | 13/15 |
| **Quickly lying** | 13/15 |
| **Quickly sitting** | 1/15 |
| **Other** | 0 |

## 5.2 Online Evaluation - EvAAL Competition

The initial results were promising, but they were performed offline, on pre-recorded dataset and not in real-life situation. Therefore, we decided to participate in the EvAAL-2013 activity recognition competition [10], which evaluates AR systems intended to be used by the elderly using the following criteria:

- Recognition performance − how accurately the system recognizes the activities.
- Recognition delay – elapsed time between the time at which the user begins an activity and the time at which the system recognizes it.
- User acceptance − how invasive the AR system is in the user's daily life; this and the following two parameters were evaluated by an evaluation committee.
- Installation complexity – how much effort is required to install the AR system in the living lab.
- Interoperability with AAL systems – the metrics used are: the use of open-source solutions, availability of libraries for development, integration with standards.

EvAAL-AR is a live competition taking place in a living lab, where the competitors install and run their systems, recognizing the activities of an actor. An evaluation committee oversees the competition and evaluates the systems using the aforementioned set of usability criteria. The '12 and '13 competitions were held in the CIAmI Living Lab in Valencia, Spain.

Table 3 shows the scores on the scale of 0–10 for the five criteria (accuracy, delay, installation time, user acceptance and interoperability) for the '12 and '13 editions. Due to the change in the weights of the criteria for the ’13 edition, the final scores for the both years' rules are included. Our RAReFall system was evaluated as best, achieving the score of 83.6%, which was for 14.2 percentage points better than the second-place system (CNR-Italy). Moreover, our system obtained the highest final score for the both years, by achieving not only high accuracy, but also scoring very well on the other criteria.

**Table 3.** EvAAL-AR '12 and '13 teams and results (score: from 0 to 10).

| | Team | Accuracy | Delay | Installation complexity | User Acceptance | Interoper-ability | Overall score '12 | Overall score '13 |
|---|---|---|---|---|---|---|---|---|
| EvAAL-AR '13 | **RAReFall (Slovenia)** | **6.94** | **10** | **10** | **8.55** | **7.2** | **8.45** | **8.36** |
| | CNR (Italy) | 4.04 | 10 | 10 | 7.04 | 6.15 | 7.19 | 6.94 |
| | Seville'13 (Spain) | 4.68 | 9 | 10 | 6.99 | 5.54 | 7.05 | 6.89 |
| | Chiba'13 (Japan) | 4.43 | 10 | 0 | 5.44 | 2.24 | 4.8 | 4.86 |
| EvAAL-AR '12 | Seville'12 (Spain) | 4.33 | 9 | 10 | 7.47 | 7.63 | 7.39 | 7.07 |
| | CMU&Utah (USA) | 7.17 | 9 | 0 | 7.93 | 6.15 | 6.5 | 6.51 |
| | Chiba'12 (Japan) | 1.44 | 5 | 0 | 5.6 | 5.09 | 3.52 | 3.13 |
| | Dublin (Ireland) | 0 | 0 | 10 | 5.2 | 1.25 | 2.99 | 2.67 |

## 6 Discussion

This paper presented a system for real-time AR and FD, called RAReFall. It was designed for robust performance in real life, so it uses a combination of relatively mature but finely tuned methods. Similar implementations of our system are widely used in the observational studies (evaluated by hundreds of people) of two European projects: Confidence and Chiron. In the first one, the AR module is used to detect falls and daily behavior change of elderly. In the second the AR is used in order to estimate the energy expenditure of users which have heart-related problems.

The competition setting is closer to real life than most AR evaluations, so our result at the competition is evidence of RAReFall's practical applicability. Current implementation of the system is intended to be used indoors; however a smartphone implementation is considered for future development, which will make the system usable for outdoors as well. We are also working on a system that will have only one

wearable device comprising several sensors (accelerometer, ECG, body temperature, body humidity, etc.). Using these sensors' data, the system should not only recognize the activity of the user, but also should reason about the user's behavior and health in general.

## References:


[1] United Nations 2009, World population ageing, report.

[2] A. Bourouis, M. Feham, A. Bouchachia, "A new architecture of a ubiquitous health monitoring system: a prototype of cloud mobile health monitoring system," The Computing Research Repository, 2012.

[3] M. Luštrek, B. Kaluža, B. Cvetković, E. Dovgan, H. Gjoreski, V. Mirchevska, M. Gams, "Confidence: ubiquitous care system to support independent living" DEMO at European Conference on Artificial Intelligence, pp. 1013-1014, 2012.

[4] D.A. Gregory, K. D. Anind, J. B. Peter, D. Nigel, S. Mark, S. Pete, "Towards a better understanding of context and context-awareness," 1st International Symposium Handheld and Ubiquitous Computing, pp. 304-307, 1999.

[5] N. Vyas, J. Farringdon, D. Andre, J. I. Stivoric, "Machine learning and sensor fusion for estimating continuous energy expenditure". Innovative Applications of Artificial Intelligence Conference, pp. 1613-1620, 2012.

[6] H. Gjoreski, B. Kaluža, M. Gams, R. Milić, M. Luštrek. "Ensembles of multiple sensors for human energy expenditure estimation," Proceedings of the 2013 ACM international joint conference on Pervasive and Ubiquitous computing, Ubicomp, pp. 359-362, 2013.

[7] M. J. Hall, L. Fingerhut, M. Heinen, "National Trend Data on Hospitalization of the Elderly for Injuries, 1979-2001. American Public Health Association (APHA), 2004.

[8] M. E. Tinetti,C. S. Williams, "Falls, Injuries Due to Falls, and the Risk of Admission to a Nursing Home," The New England Journal of Medicine, vol. 337, pp. 1279–1284, 1997.

[9] D. Wild, U. S. Nayak, B. Isaacs, "How dangerous are falls in old people at home?," British Medical Journal (Clinical Research Edition), vol. 282, no. 6260, pp. 266–268, 1982.

[10] EvAAL competition. http://evaal.aaloa.org/ [Accessed: November, 2013]

[11] G. Sukthankar and K. Sycara, "A cost minimization approach to human behavior recognition," Proc. The Fourth International Joint Conference on Autonomous Agents and Multi-Agent Systems (AAMAS), 1067-1074, 2005.

[12] H. Wu, E. D. Lemaire and N. Baddour, "Activity Change-of-state Identification Using a Blackberry Smartphone," Journal of Medical and Biological Engineering, 32: 265-272, 2012.

[13] J. R. Kwapisz, G. M. Weiss and S. A. Moore, "Activity Recognition using Cell Phone Accelerometers," Human Factors, 12: 74-82, 2010.

[14] H. Gjoreski, M. Luštrek, M. Gams, "Accelerometer Placement for Posture Recognition and Fall Detection," International Conference on Intelligent Environments, pp. 47–54, 2011.

[15] S. Kozina, H. Gjoreski, M. Gams, M. Luštrek,"Three-layer Activity Recognition Combining Domain Knowledge and Meta-classification," JMBE, vol 33, no 4, 2013.

[16] Shimmer sensor platform. http://www.shimmer-research.com [Accessed: November, 2013]

[17] S. Kozina, H. Gjoreski, M. Gams, M. Luštrek, "Efficient Activity Recognition and Fall Detection Using Accelerometers," Evaluating AAL Systems Through Competitive Benchmarking Communications in Computer and Information Science, pp 13-23, 2013.

[18] H. Gjoreski, M. Luštrek, M. Gams.: Context-Based Fall Detection using Inertial and Location Sensors. In: International Joint Conference on Ambient Intelligence, Lecture notes in computer science, pp. 1-16, 2012.

## For wider interest

The world's population is aging rapidly, threatening to overwhelm the society's capacity to take care of its elderly members. This is driving the development of innovative ambient assisted living (AAL) technologies to help the elderly live independently for longer and with minimal support from the working-age population. To provide timely and appropriate assistance, AAL systems must understand the user's situation and context, making activity recognition (AR) task an essential component. Detection of falls is also another important component of many AAL systems because approximately half of the hospitalizations of the elderly are caused by falls.

This paper presents the RAReFall (**R**eal-time **A**ctivity **Re**cognition and **Fall** detection) system, which recognizes the user's activities and detects falls in real time. The RAReFall system consists of two wearable sensors (accelerometers), placed on the user's torso and the thigh, and a laptop that receives the data through Bluetooth and analyzes the data in real-time using artificial intelligence algorithms. The algorithm architecture combines domain-expert rules to recognize postures (static activities), which ensure the behavior of the system is predictable and robust, and classifiers trained with machine learning algorithms, to recognize dynamic activities, for which the rules are not sufficiently accurate. For the fall detection, rules are used that take into account high accelerations associated with falls and the recognized horizontal orientation (e.g., falling is often followed by lying).

Initially, the RAReFall system was evaluated offline, on a dataset containing a wide range of activities and different types of falls. The accuracy of the activity recognition and fall detection were 96% and 93%, respectively, encouraging us to take part in the international EvAAL-2013 activity recognition competition, which evaluates AR systems in a living lab. The RAReFall system was awarded the first place, achieving the score of 83.6% (over all criteria), which was for 14.2 percentage points better than the second-place system. The evaluation was performed in a living lab using several criteria: recognition performance, user-acceptance, recognition delay, system installation complexity and interoperability with other systems.

# Network-Coding-Based Retransmission Scheme for Real Time Streaming Applications in Wireless Broadcast Networks

**Melisa Junuzović**[1,2], **Kemal Alič**[1], **Aleš Švigelj**[1,2]

[1] Department of Communication Systems,Jožef Stefan Institute, Ljubljana, Slovenia

[2] Jožef Stefan International Postgraduate School, Ljubljana, Slovenia

melisa.junuzovic@ijs.si

**Abstract.** In this paper, the real-time streaming applications over wireless broadcast networks are considered. Deployment of real-time streaming applications into the wireless networks poses more challenges than deployment of non-real-time applications. Real-time streaming applications in wireless systems must cope with time-varying bandwidth, jitter, delay and must be resilient to packet loss. We propose a Network-Coding-Based Retransmission Scheme integrated into the application layer that maintains the required reliability and Quality of Service while posing lower bandwidth demands in comparison to the traditional approaches. In the proposed Retransmission Scheme, Network Coding is used to encode packets tended for retransmission.

**Keywords**: Network Coding, wireless network, broadcast, retransmission

## 1 Introduction

Real-time streaming applications such as Voice over IP (VoIP), video and voice conferencing, multimedia streaming etc. play an important role in today's world of Internet-based services. However, providing efficient and reliable communication in particular in wireless environments is challenging since these applications have requirements that differ from traditional data-oriented applications [1]. They must cope with the Quality of Service (QoS) parameters such as delay, bandwidth, packet loss, jitter, which all heavily influence the Quality of Experience (QoE). Moreover, lossy nature of wireless networks may result in violation of those parameters which cause degraded quality. For example, in the real-time video streaming applications packet loss results in a video with blocky, mosaic-like appearance. Furthermore, User Datagram Protocol (UDP) is preferred over the Transport Control Protocol (TCP)

in the transport layer for the real-time streaming applications because it favours time delivery over reliable delivery [2]. UDP is transport protocol without connection setup delays, flow control and retransmission providing applications more raw interface to the network. Therefore, UDP is often used in delay-sensitive real-time streaming applications. UDP has no mechanisms to deal with packet loss, delay and packet reordering which makes it an unreliable protocol. Thus, in order to be resilient to packet loss UDP needs appropriate retransmission mechanism. So in this paper an application layer retransmission scheme is proposed with packet loss detection at the end-user side and with the retransmission mechanism at the server side. Moreover, all retransmitted packets are potentially coded using Network Coding (NC) technique, thus improving efficiency by reducing the number of retransmissions.

The NC technique was originally proposed by Ahlswede et al. [3], to increase the capacity of a single-source communication, such as a multicast stream. In opposite to traditional networks where data packets are transmitted by store-and-forward mechanisms in which the intermediate nodes only repeat data packets that they have received, the NC source or intermediate node is allowed to code together several packets that it has generated or received into one or several outgoing packets. Those packets are then decoded by the receivers (in our case end-users). Hence, a typical NC mechanism is composed of two main operations: coding outgoing packets on the source node and decoding of incoming packets upon their reception on destination nodes. Coding and decoding can be performed via the simple algebraic coding functions such as XOR [4]. There are many different coding approaches used in NC but the XOR operation is simple and low demanding in terms of implementation and complexity.

The aim of this paper is to describe our approach to Network-Coding-Based Retransmission Scheme, to compare it to the related work and to show the value of the approach on an illustrative example. This paper is structured as follows. Related works are presented in Section 2 where similar existing architectures are presented with their respective advantages and disadvantages. Section 3 describes the network model used for the implementation of the experimental testbed. Section 4 describes our approach to the retransmission scheme in the synergy with NC. Section 5

describes preliminary results of the network model. Finally, Section 6 gives conclusion and directions to our future work.

## 2 Related Work

Since the pioneering work of Ahlswede et al. [3] numerous papers (e.g., [3]–[9]) have appeared on the subject of NC and significant progress has been made in applying NC to different wireless networks. The proposed works distinguish in network model used (single-hop or multi-hop), coding and decoding algorithms (Random NC, Linear NC etc.), retransmission schemes (ACK and/or NACK-based schemes), OSI layers in which NC is implemented (network layer, application layer), and applications in which NC can be applied: real-time streaming applications, [5] file distribution, security etc. Coding Opportunistically (COPE) [4] is the first practical NC implementation which demonstrates the practical gains obtained with NC. There are several studies that build on top of COPE such as Efficient Retransmission Scheme for Wireless LANs (ER) [6] but do not address the real-time streaming applications. Nguyen al.et. [7] propose an approach for broadcast, single-hop wireless networks with time-based retransmission scheme for real-time streaming applications. The Network Coding Wireless Broadcasting Retransmission (NCWBR) [8] extends the work from Nguyen et al. [7] to cover also multi-nodes situation with envision to focus on application with NCWBR in the future. In paper by Weiwei Fang et al. [9] they claimed that Nguyen et al. [7] paid little attention to the solution for packet selection algorithm for coding and decoding so they proposed novel vertex colouring-based heuristic algorithm. However, this approach does not consider delay constraints in real-time applications neither do they pay attention to the retransmission scheme. The possibility of maximizing throughput through retransmission scheme in dense WiFi spaces has been addressed recently in [10].

## 3 Network Model

NC has proven as a promising approach for increasing throughput by reducing the number of retransmissions. Combining the NC with the retransmission scheme the performance in terms of efficiency, quality and reliability can be improved. The

abstraction of the network model used in this paper is depicted in Figure 1 and is consisted of three main parts: server, wireless router and end-users. In a real-time system, application server transmits streamed data which is received by the end-users application. Stream is divided into data packets with fixed sizes. Packets are sent to the end-users in sequentially order with equal inter-arrival time using multicast technique. Multicast technique has been selected as it is more selective since only a group of end-users are receiving the stream [11].

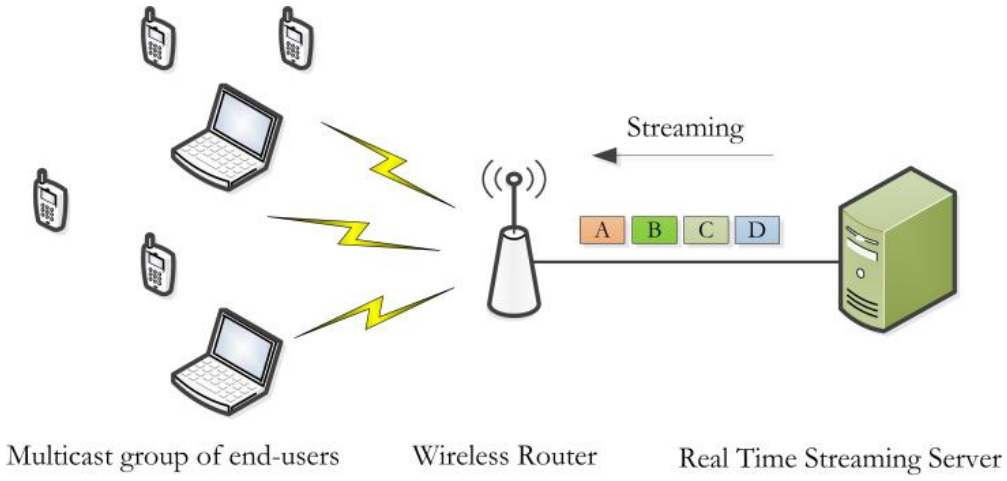


**Figure 1**. Network model

One of the solutions would be a unicast technique where every packet is unicasted to each end-user. Although the wireless medium is inherently broadcast in nature, there are a number of key differences between the handling of unicast and multicast/broadcast frames. In order to cope with the higher frame loss and collision rates in the wireless network as compared to a wired network, the 802.11 Medium Access (MAC) protocol mandates Acknowledgments (ACKs) of received unicast frames and retransmission of non-acknowledged frames. In contrast, the 802.11 MAC does not provide retransmission mechanism for multicast/broadcast traffic so that the packet delivery is not guaranteed. On the other hand multicast and broadcast techniques conserve bandwidth of a network because only the transmission of a single packet is necessary rather than sending packets individually addressed to each node as in unicast technique. This is especially important with wireless networks having limited throughput available. If a large group of wireless end-users need to receive a particular video stream then unicasting to each user individually would require many separate video streams, resulting in inefficient use of the available bandwidth. In contrast to the unicast, multicast and broadcast

approaches permit a much more efficient use of bandwidth by sending just one copy of the packet to all or a group of end-users. As we want to improve bandwidth to get more end-users per Access Point (AP) multicast scheme has been selected. Moreover, retransmission scheme is needed to guarantee reliability and desirable QoS and QoE. Negative Acknowledgement (NACK)-based retransmission approach has been selected over the Positive Acknowledgement (ACK) approach. In ACK approach each end-user has to send an ACK for each received packet which may lead to numerous ACK packets at the server side and to additional occupation of the wireless channel. Instead of acknowledging every successfully received packet, NACK is used to detected missing packet. NACK-based protocols generally require less frequent feedback to the server which improves protocol efficiency.

## 4 The proposal of Network-Coding-Based Retransmission Scheme

Proposed scheme that is considered has been depicted in Figure 2. Sequence diagram in Figure 3 describes the same concept. For simplicity reasons, only two end-users are shown in the presentation, though the concept can easily be extrapolated to multiple users. In the planned testbed the number of end-users will be increased to test the capacity limits of the system. Real-time server sequentially transmits packets to a multicast group of end-users as depicted in Figures 2 and 3. Stream is divided into packets A, B and C, respectively. Due to wireless link quality variations, End User 1 has not received packet B. In addition, End User 2 failed to receive packet C. Missing packet are identified at the End User side with the help of a sequence number. End-users request retransmission of lost packets with NACK packets. Thus, as depicted in our case on Figures 2 and 3, the End User 1 sends request for retransmission of packet-B, while the End User 2 requests the retransmission of packet-C.

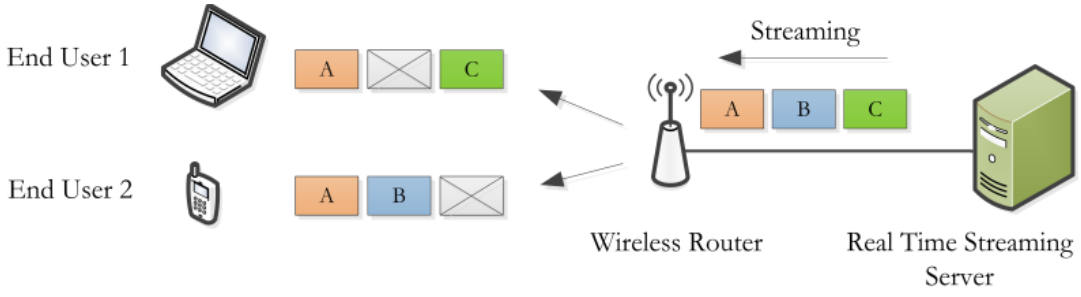


**Figure 2.** Streaming over lossy wireless network

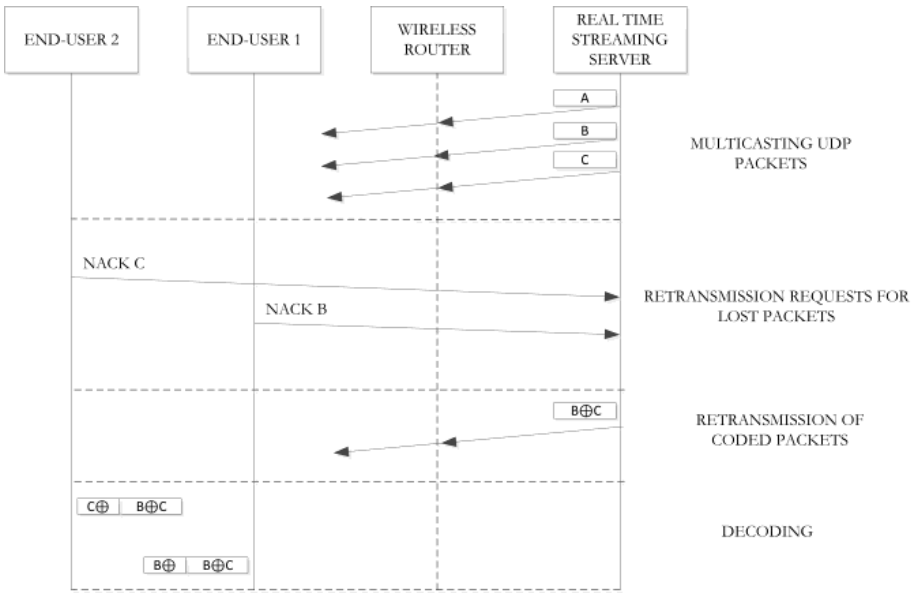


**Figure 3.** Sequence diagram for Network-Coding-Based Retransmission Scheme

When the server receives the retransmission requests it selects appropriate packets for coding as depicted in Figure 4. The goal of coding is that encoded packet can be decoded by as many end-users as possible. In our case the server codes packets B and C together into packet B⊕C and multicasts it to both users. Upon receiving the encoded packet end-users can decode it only if they have received and stored one of the original packets. Decoding is presented also in Figure 4. For example, End User 1 has stored packets A and C. When he receives encoded packet B⊕C he will take the original packet C from his buffer and perform decoding XOR operation C⊕(B⊕C) = B. As we can see, decoded packet is B, which is exactly the requested one. The same process is applied at End User 2 where content of packet C is received. In the case of traditional retransmission approach server would need two retransmissions to deliver the lost packets. By applying the NC principle and coding the two packets together bandwidth required by the retransmission mechanism is in our case reduced by 50%. By increasing the number of end-users also higher gains can be obtained.

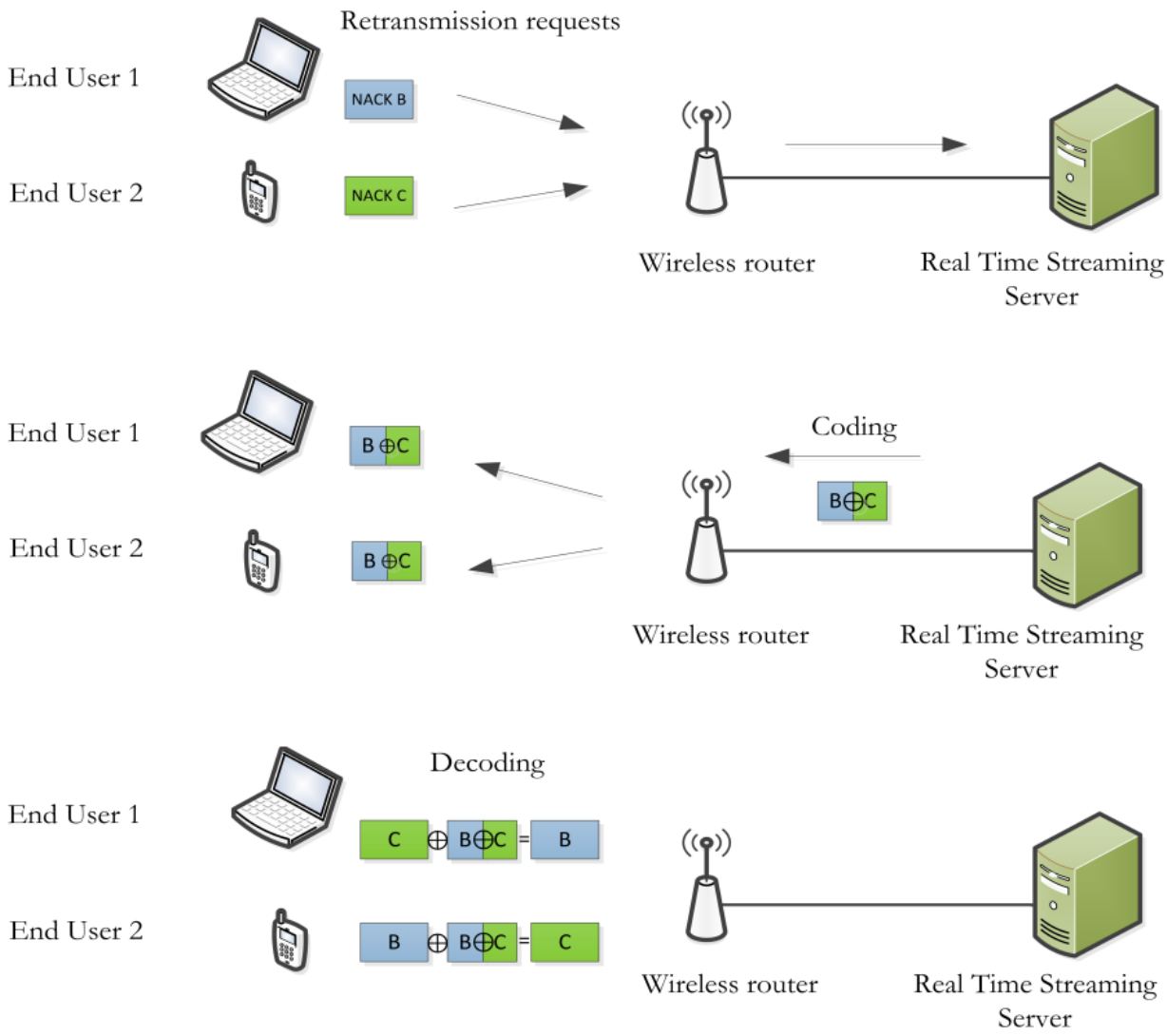


Figure 4. Retransmission request, coding and decoding procedures

By introducing NC the question of addition delay arises naturally. In comparison to unicast mechanism the confirmation messages cannot be synchronous, thus introducing additional delay. Furthermore, the coding and decoding process require processing time. Still, we expect that the additional delay introduced by NC will not affect the QoE on the end-user side as all the operations will be carried out within the buffer time of the stream.

## 5 Preliminary evaluation of the proposed wireless multicast network model

In this section we describe preliminary results that were collected on the experimental wireless multicast network consisting of server, wireless router and two

end-users. The environment is based on IEEE 802.11 Wireless Local Area Network (WLAN). Server is connected to the wireless router via Ethernet cable while end-users are connected via WLAN interfaces. Both applications for server and end-users were written in C programming language using UDP multicast sockets. Router must also support multicast traffic. Server was streaming a text file divided into packets of 512 bytes to the end-users which were part of the multicast group. End-users were storing the received text file packet by packet and detecting lost packets.
Preliminary results show that packet loss at end-users is unpredictable and highly varies, from 20% to 50%. Based on these measurements we conclude that wireless channel is lossy and prone to errors and thus very suitable for the proposed retransmission scheme. Moreover, performed experiment showed that packet loss is asymmetric which means that diversity of lost packets is represented across different users. This is a prerequisite for Network-Coding capable wireless network. Thus, applying Network-Coding-Based Retransmission Scheme to wireless packet networks seems a great way of achieving the appreciable efficiency gains.

## 6 Conclusions and Future Work

In this paper we presented our approach to improve quality in real-time streaming systems using NACK-based retransmissions scheme in the synergy with the NC. The proposed approach will be implemented for the real-time streaming application at both, the server and the end-users sides. Appropriate packet selection algorithm will be developed for coding and decoding purposes in order to take into account delay constraints in real-time streaming systems and to reduce the number of retransmissions. Thus, not only the network throughput will be improved, but also, more importantly, quality of real-time streams in wireless network.

# References:


[1] C. M. Aras, J. F. Kurose, D. S. Reeves, and H. Schulzrinne, "Real-Time Communication in Packet-Switched Networks," *Proceedings of the IEEE,* vol. 82, no. 1, 1994.

[2] Y. T. H. Dapeng Wu, Wenwu Zhu Ya-Qin Zhang,Jon M. Peha, "Streaming Video over the Internet: Approaches and Directions," *IEEE TRANSACTIONS ON CIRCUITS AND SYSTEMS FOR VIDEO TECHNOLOGY*, 2011.

[3] R. Ahlswede, N. Cai, S.-Y. R. Li, and R. W. Yeung, "Network information flow " *Information Theory, IEEE Transactions on* vol. 46, no. 4, 2000.

[4] S. Katti, H. Rahul, W. Hu, D. Katabi, M. M. ́edard, and J. Crowcroft, "XORs in the Air: Practical Wireless Network Coding," *IEEE/ACM Transactions on networking,* vol. 16, 2008.

[5] E. Pertovt, K. Ališ, A. Švigelj, and M. Mohorčič, "Voice over Internet Protocol in Wireless Mesh Networks with Opportunistic Network Coding " *International journal of communications*, 2007.

[6] E. Rozner, A. P. Iyer, Y. Mehta, L. Qiu, and M. Jafry, "ER: efficient retransmission scheme for wireless LANs," *CoNEXT '07 Proceedings of the 2007 ACM CoNEXT conference* 2007.

[7] D. Nguyen, T. Tran, T. Nguyen, and B. Bose, "Wireless Broadcast Using Network Coding," *IEEE TRANSACTIONS ON VEHICULAR TECHNOLOGY,* vol. 58, 2009.

[8] X. Xiao, Y. Lu-Ming, W. Wei-Ping, and Z. Shuai, "A Wireless Broadcasting Retransmission Approach Based on Network Coding," *Circuits and Systems for Communications, 2008. ICCSC 2008. 4th IEEE International Conference on* 2008.

[9] W. Fang, F. Liu, Z. Liu, L. Shu, and S. Nishio, "Reliable Broadcast Transmission in Wireless Networks Based on Network Coding," *Computer Communications Workshops (INFOCOM WKSHPS), 2011 IEEE Conference on* 2011.

[10] D. Ferreira, R. A. Costa, and J. Barros, "Real-Time Network Coding for Live Streaming in Hyper-Dense WiFi Spaces," *Selected Areas in Communications, IEEE Journal on,* vol. 32, no. 4, 2014.

[11] T.-L. Sheu, and S.-T. Lin, "A Multicast Retransmission Scheme Using Negative ACK in Wireless Networks " *2013 IEEE 27th International Conference on Advanced Information Networking and Applications*, 2013.

## For wider interest

Real-time streaming applications such as VoIP, video and voice conferencing, multimedia streaming etc. play an important role in today's world of Internet-based services. Those services have stringent requirements in terms of delay and quality which are sensitive to packet loss and delay. Due to the lossy nature of wireless networks it is challenging to deal with those requirements so two techniques are combined to overcome these problems. The first one is Retransmission Scheme and the second is Network Coding (NC).

Retransmission scheme is implemented because the majority of real-time streaming applications are based on the unreliable transport protocol which has no retransmission scheme to deal with the packet loss. Retransmission scheme on top of the transport protocol will be implemented to detect lost packets and retransmit them in order to provide better quality.

Moreover, NC is used to improve the throughput of the wireless network. NC combine different packets together and instead of retransmit them one by one, it codes them together and transmits them in one retransmission. However, the end-users must also have the support for decoding those packets.

The advantages of the proposed schemes over the traditional wireless broadcast are in the improved network performance in terms of reliability, quality and throughput.

# Performance evaluation of ITU-R P.1546 Propagation Model

**Arsim Kelmendi**[2], **Tomaž Javornik**[1,2], **Igor Ozimek**[1], **Andrej Vilhar**[1], **Andrej Hrovat**[1, 2], **Gorazd Kandus**[1, 2]

[1] Department of Communication Systems, Jožef Stefan Institute, Ljubljana,Slovenia

[2] Jožef Stefan International Postgraduate School, Ljubljana, Slovenia

arsimkelmendi@gmail.com

**Abstract.** This paper presents the performance evaluation of the ITU-R P.1546 propagation model implemented in an open source network planning tool GRASS RaPlaT. The ITU-R P.1546 propagation model is implemented as a separate path loss module r.ITUR1546. The path loss predictions obtained by the r.ITUR1546 module were compared with path loss predictions calculated by the WinProp propagation modelling tool and the r.hataDEM GRASS RaPlaT module. We noticed high agreement between the WinProp and r.ITUR1546 model results for distances up to 100 km and between the r.hataDEM and r.ITUR1546 model results for distances up to 10 km.

**Keywords**: Propagation prediction, path loss, field strength.

## 1 Introduction

Software tools for radio signal coverage prediction and network planning are essential for network design and maintenance. The prediction of signal levels at a particular location is based on path loss propagation models. The conventional propagation models for the UHF frequency band are the Hata and Okumura-Hata models for mobile networks, and the ITU-R Recommendation P.1546 for TV broadcasting. The ITU-R Recommendation P.1546 is implemented by several propagation tools and it is actually a standard model for radio coverage prediction for TV broadcasting.

Existing commercial radio propagation prediction tools use dedicated computer software for simulation of signal loss in conditions very similar to the real world environment, but they are intended for specific tasks and in general do not allow

users to add new propagation models or modify the existing ones. Since radio propagation depends on geographical data (e.g. terrain profile, vegetation data), a possible approach is to take an existing open-source modular GIS (Geographic Information System) tool and create additional specific modules for radio propagation calculations [1]. Our tool, GRASS-RaPlaT (Radio Planning Tool for GRASS), is based on the open-source Geographical Resources Analysis Support System (GRASS). It uses the GRASS support for geographic environment (terrain relief) and other functionalities (displaying, etc.) important for radio coverage computations and display [2].

The paper is organized as follows. In the next section we describe the ITU-R P.1546 model and its implementation. Our implementation of the model, i.e. the r.ITUR1546 module for the GRASS RaPlaT network planning tool, is described in Section 3. The performance evaluation of the implemented ITU-R P.1546 model is given in Section 4. The paper concludes with final remarks and future work.

## 2 ITU-R P.1546 Propagation Model

The ITU-R P.1546 propagation model describes point-to-area signal path loss for terrestrial services in the frequency range from 30 MHz to 3000 MHz over land and sea paths up to 1000 km length for effective transmitting antenna height less than 3000 m.

The Recommendation provides a method for point-to-area predictions for terrestrial services based on empirically determined field-strength curves, as functions of distance $d$ between the transmitter and the receiver and other parameters such as carrier frequency $f$, transmitting/base antenna height $h_1$, time percentage $t$ of the service availability at 50% locations, and the receiving antenna height $h_2$ at the representative clutter height. The field-strength curves in Figure 1 represent an example of land path field-strength values for 1 kW effective radiated power (e.r.p.), where $f = 600$ MHz, $t = 50\%$. For land paths, there are nine such collections of curves that define field strengths for different frequencies and percentage of time. The reliability of the model depends on the accuracy of the measurements and on the similarity between the environment considered in the model and the environment in which the measurements were actually carried out.

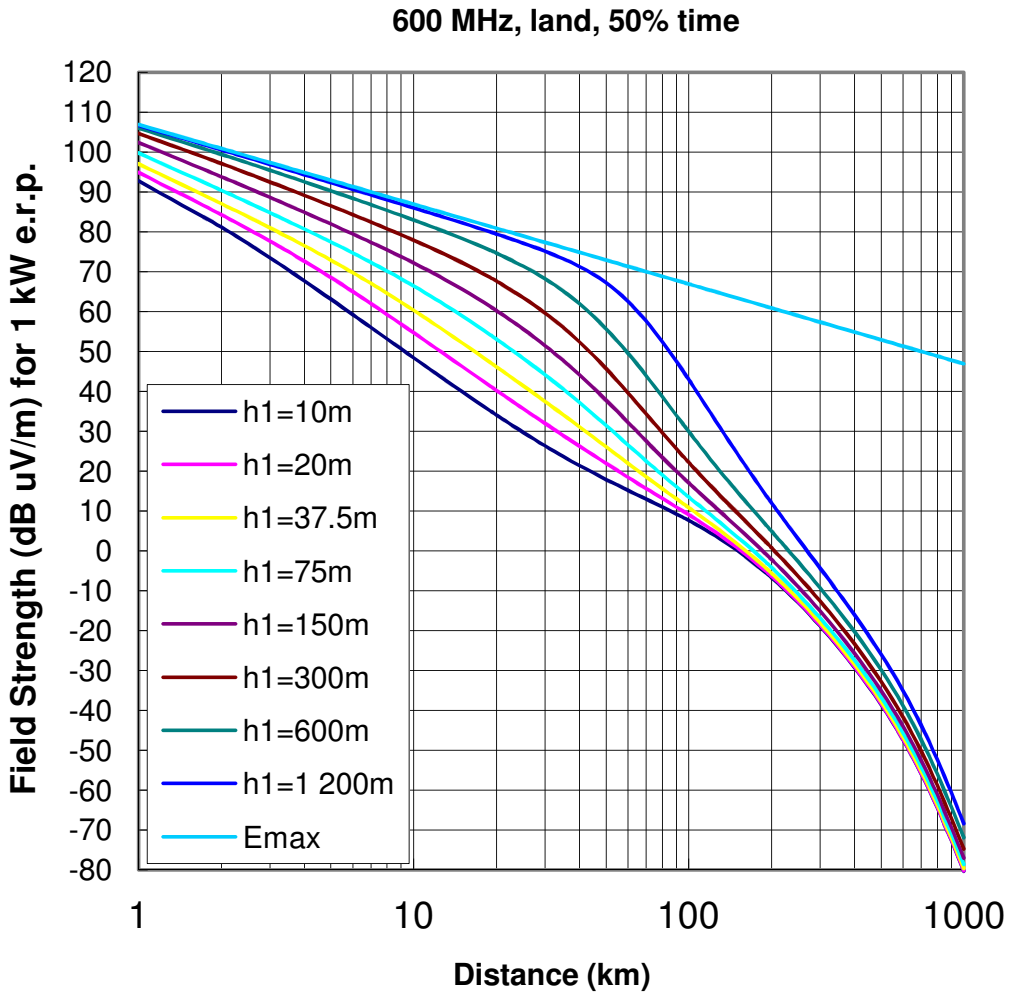


**Figure 1**: An example of ITU.R P.1546 electrical field strength curves

For the implementation of the method, we used tabulated field strengths available from Radiocommunication Bureau [3]. The actual field strengths values are obtained by interpolation or extrapolation of the tabulated values. The field strength calculation includes also corrections concerning terrain clearance and terminal clutter obstructions.

## 2.1 Interpolation/extrapolation of fields

If actual parameter values do not coincide with tabulated parameter values $t=\{1,10,50\}$, $f=\{100,600,2000\}$, $h_1=\{10,20,...,300,600,1200\}$, $d=\{1,2,3,...,975,1000\}$, the interpolation or extrapolation of the field strength is to be performed. The Recommendation specifies the interpolation/extrapolation procedures and limitations of parameter values. First, the distance $d$ between the transmitter (Tx)

and receiver (Rx) is calculated. Next, the average terrain height between Tx and Rx is estimated using the terrain digital elevation model. If $d < 15$ km, the terrain is averaged between *0.2*d* and distance *d*, while for distances larger than 15 km the terrain is averaged between 3 km and 15 km from the transmitter. The average terrain height is applied to determine the effective transmitter antenna height $h_1$, which is the difference between the antenna height above sea level and the average terrain height. Next, the inferior and superior values of the input *(t, f,* $h_1$*, d)* parameters are calculated: *Tinf, Tsup, Finf, Fsup, Hinf, Hsup, Dinf, Dsup*. Inferior and superior mean the nearest tabulation values smaller and greater, respectively, from the actual value. Knowing the distance *d* between Tx and Rx, height $h_1$, carrier frequency *f*, percentage of time *t*, and inferior and superior values, interpolation or extrapolation is performed according to the standard procedures and formulas [3].

## 2.2 Electrical field corrections

In order to improve the precision of the model, additional corrections to the calculated field strength *E* from the interpolation/extrapolation in section 2.1 are applied, namely, the terrain clearance angle correction, correction of the receiving/mobile antenna height, correction for short urban/suburban paths and correction based on tropospheric scattering.

The most important correction of the field strength is the terrain clearance angle correction, which improves the prediction accuracy by taking into account the obstacles near the receiver that are obstructing the direct line from the receiver to the transmitter. The terrain clearance angle is defined as an angle between two lines, namely (i) a horizontal line from the top of the receiver antenna and (ii) the line connecting the top of the receiving antenna with the point of the highest obstacle in the direction toward the transmitter but no further that 16 km from the receiver (if $d \geq 16$km). The angle must be limited to the range between 0.55 and 40 degrees. The electrical field correction that depends on this angle lies between 0 and -37 dB for small and large clearance angles, respectively.

Beside this correction, tropospheric scattering also contributes to the received signal. Additionally, correction for the receiving antenna height has to be added to the model if the receiving antenna height is below the height of the surrounding

obstacles *R*. For transmitters located in the urban and suburban areas, the correction over short urban and suburban paths must be added.

# 3 Implementation of the r.ITUR1546 module

The RaPlaT module r.ITUR1546, written in the C programming language, calculates radio signal path loss according to the ITU-R P.1546 propagation model. For its computation, the module needs DEM (Digital Elevation Map), i.e. a raster map describing the terrain profile (heights above sea level in [m]). The signal path loss in [dB] is calculated for each raster point, representing a possible receiver location. DEM data is used to calculate the transmitting/base antenna height, and (for each point) the receiver antenna height, terrain clearance angle, and other necessary variables including all the corrections. The result is a raster GRASS map (Figure 2) with circular surface with the transmitter in its center, with each point having the value of the signal fading in [dB] in that point relative to the transmitter (the situation corresponds to the isotropic radiation diagram with 0 dB gain). We limit our implementation of the module r.ITUR1546 only to propagation over land. The sea path propagation will be included in the future.

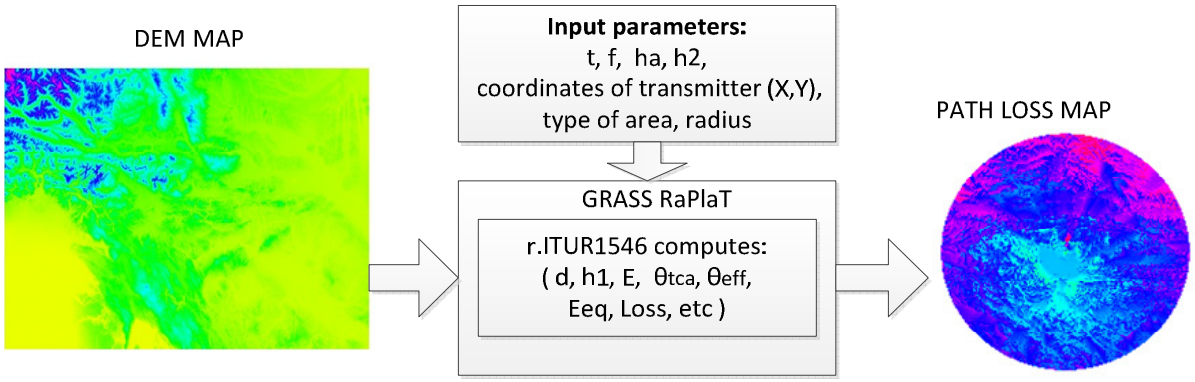


**Figure 2**: The principle of creating path loss map from module r.ITUR1546

# 4 Performance evaluation of the model ITU-R P.1546

## 4.1 Comparison between r.ITUR1546 and WinProp

Performance and accuracy of the developed module for the signal path loss prediction was investigated by comparing simulation results from the GRASS-RaPlaT module r.ITUR1546 and the WinProp simulation tool [4]. An example of a

path loss map obtained with r.ITUR1546 is shown in Figure 3 (a) for a transmitter located on the Krvavec mountain, Slovenia. Figure 3 (b) shows path loss computed with WinProp for the same transmitter and parameters: transmitter antenna height $ha$ = 70 m, frequency $f$ = 562 MHz, time percentage $t$ = 50%, receiving antenna height $h_2$ = 20 m, calculation radius 100 km [5].

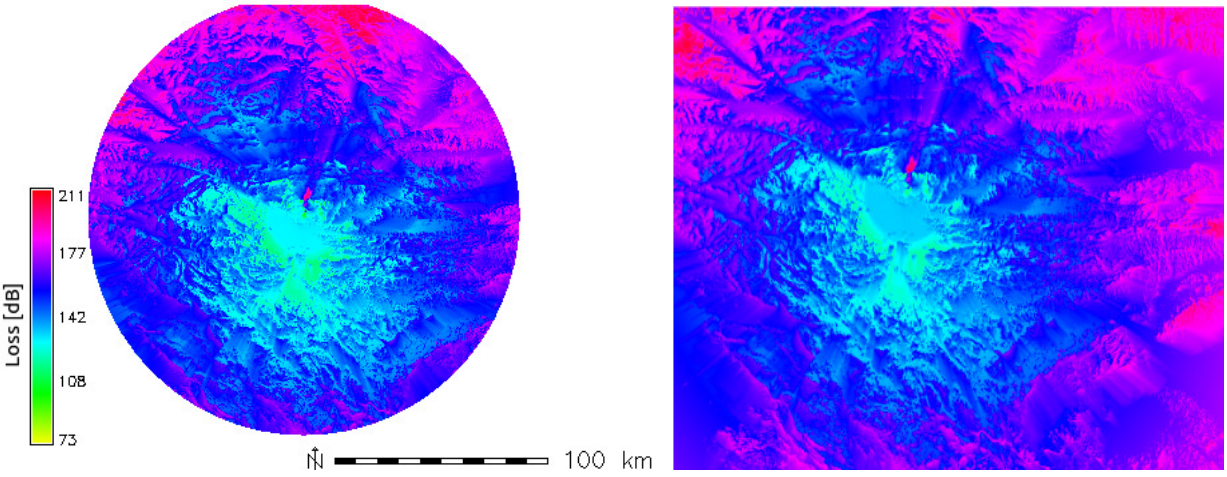


**(a)** **(b)**

**Figure 3**: Path loss at 562 MHz: (a) computed with r.ITUR1546 , (b) computed with WinProp

Table 1 shows the mean error and standard deviation of the difference between the path loss maps produced by r.ITUR1546 and WinProp. The comparison includes four TV transmitters in Slovenia located at Krvavec, Krim, Kum, and Trdinov vrh, with the same parameters: $f$ = 562 MHz, $t$ = 50%, $h_2$ = 20 m, radius of calculation 100 km. Since WinProp does not take into account the correction due to the receiving antenna height defined in section (2.2), all comparisons are done by neglecting this correction to the field strength also by the r.ITUR1546 module. For all transmitters, the path loss prediction results from both modules agree rather well. Good agreement is also confirmed by Figure 4 showing a path loss segment from loss maps from r.ITUR1546 and WinProp.

**Table 1:** Statistical error data of the difference between the path loss maps from r.ITUR1546 and WinProp

| Location | ha (m) | mean error (dB) | standard deviation (dB) |
|---|---|---|---|
| Krvavec | 70 | -0.685876 | 0.590472 |
| Krim | 50 | -0.562168 | 3.57949 |
| Kum | 50 | 0.342717 | 3.2903 |
| Trdinov vrh | 70 | 0.62162 | 2.24569 |

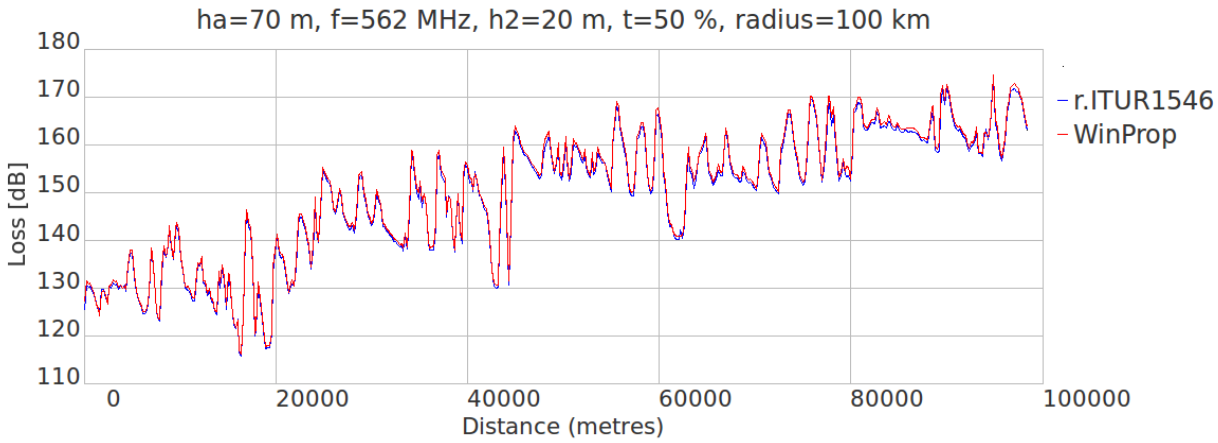


**Figure 4**: Path loss segment from r.ITUR1546 and WinProp at distance 0-100 km from transmitter at Krvavec

## 4.2 Comparison between r.ITUR1546 and r.hataDEM

According to Recommendation, ITU-R P.1546 produces results similar to the Okumura-Hata method for distances up to 10 km, $h_2 = 1.5$ m, $R = 15$ m [3]. For comparison with the Okumura-Hata method, we used the r.hataDEM module developed at Jozef Stefan Institute (JSI), which implements a modified/extended Okumura-Hata model that additionally takes into account the ground cover surrounding the receiving/mobile antenna. The comparison has been done for two locations, JSI in Ljubljana and Krvavec, with the same parameters: $ha = 70$ m, $f = 900$ MHz, $t = 50\%$, $h_2 = 1.5$ m, $radius = 10$ km. Statistical analysis of the difference between the maps created by both tools shows that the path loss prediction results from both tools agree rather well for the transmitter at the JSI location for short distances up to 10 km, but not for the transmitter at the Krvavec location, even for short distances below 10 km.

Figures 5 and 6 show path loss segments created by r.hataDEM and r.ITUR1546 for both locations. For the flat terrain around JSI with the transmitter at the JSI location, both models produce very similar results (Figure 5). In the case of a hilly terrain like the one at the location Krvavec (a mountain with the transmitter 1740 m above sea level), the differences between both models are much more pronounced (Figure 6).

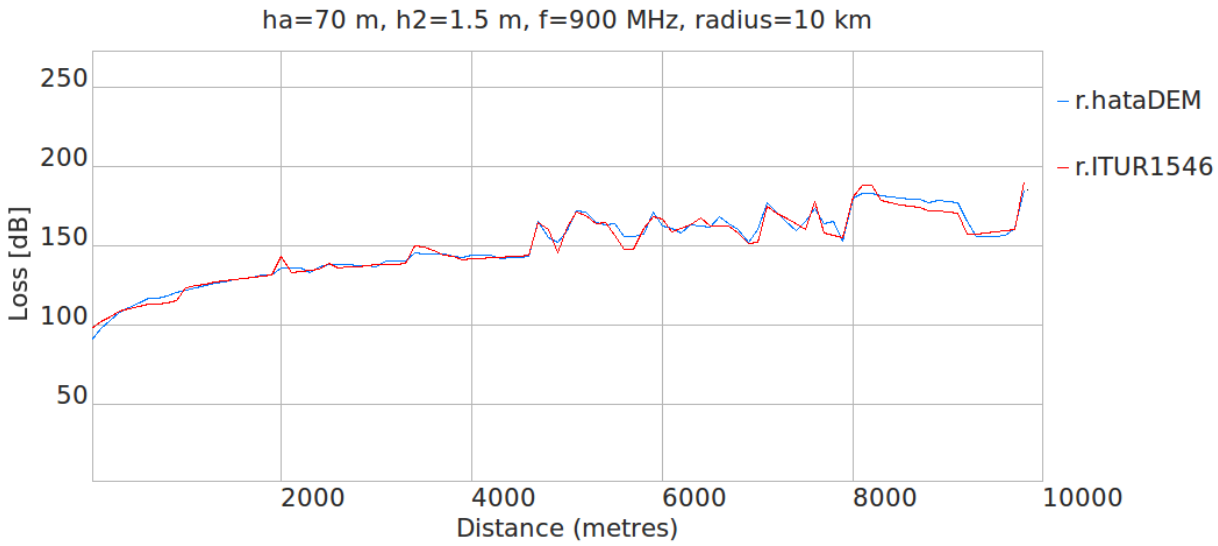


**Figure 5**: Path loss segment from r.ITUR1546 and r.hataDEM at distance 0-10 km from the transmitter at JSI

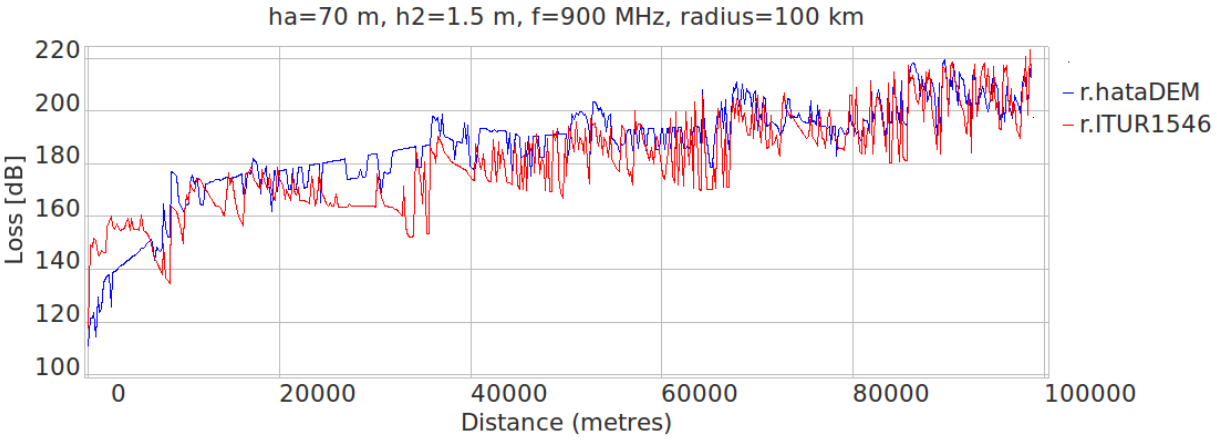


**Figure 6**: Path loss segment from r.ITUR1546 and r.hataDEM at distance 0-100 km from the transmitter at Krvavec

## 5 Final remarks and future work

The main purpose of creating the r.ITUR1546 module was to be able to use the RaPlaT tool also for TV broadcast propagation prediction. The correctness of our implementation has been verified by comparison of the results with the results of the commercial WinProp tool.

ITU-R P.1546 describes a method for point-to-area radio coverage prediction for land services in the frequency range 30 MHz up to 3000 MHz and as such it could also be used for umbrella cells in mobile networks. Comparison with the Okumura-Hata model (using the RaPlaT r.hataDEM module) for distances up to 10 km (as specified by ITU-R P.1546) confirmed that both models produce very similar results for a flat terrain, while for a hilly terrain the differences between both models are noticeable.

Currently, the r.ITUR1546 module computes only land path loss and does not support clutter maps, which would be used to specify various types of the terrain in the coverage area (urban, suburban, etc.). In the future, the module will be improved by adding computation over sea and support for clutter maps.

Another future improvement will be implementation of the Recommendation ITU-R P.1812, which complements ITU-R P.1546 and specifies a path-specific propagation prediction method for point-to-area terrestrial services in the VHF and UHF bands.

## References:


[1] I. Ozimek, A. Hrovat, A. Vilhar, T. Celcer, I. Saje, T. Javornik, GRASS-RaPlaT - an open-source tool for radio coverage calculations, Joint Workshop on Wireless Communications - JNCW 2011, 1-2 March 2011, Paris, France.

[2] Igor Ozimek, Andrej Hrovat, Andrej Vilhar, Tomaž Javornik, GRASS-RaPlaT Radio Planning Tool for GRASS, User Manual V1.0a, JSI, Ljubljana, September 2013.

[3] ITU-R Recommendation P.1546-4, "Method for point-to area predictions for terrestrial services in the frequency range 30 MHz to 3000 MHz" October 2009.

[4] WinProp, AWECommunications, http://www.awe-communications.com

[5] Arsim Kelmendi, GRASS Raplat Modul for Point-to-Area Propagation Prediction based on Rec. ITU-R P.1546-4, User Manual, JSI, Ljubljana, Slovenia, January 2014.

## For wider interest

Radio network planning and dimensioning have significant impact on wireless system performance and capacity. Various commercial network planning and dimensioning tools with different radio signal propagation models are implemented and available on the market. Their price and especially inflexibility led us to look for an open-source solution. At JSI we developed our own GRASS-RaPlaT tool, which is an open-source radio planning tool, especially designed for radio coverage calculation of GSM/UMTS systems, but can be applied also to other wireless systems. Its structure is modular and characterized by high level of flexibility and adaptability.

The paper describes the performance evaluation of the ITU-R P.1546 Recommendation method, implemented in a particular new module, suitable for modelling propagation path loss in broadcasting, land mobile and certain fixed services in the frequency range 30 to 3000 MHz and for the distance range 1 km to 1000 km. The propagation module is based on interpolation or extrapolation from empirically derived field strength curves as functions of distance, antenna height, frequency and percentage of time. The calculation procedures also include corrections for terrain clearance and terminal clutter obstructions.

The path loss predictions obtained by the r.ITUR1546 module were compared in the paper with the path loss predictions calculated by the professional WinProp propagation modelling tool, and the r.hataDEM GRASS RaPlaT module based on the well-known Okumura-Hata propagation model. The r.ITUR1546 model simulation results show considerable matching with the WinProp tool for distances up to 100 km and with the r.hataDEM module for distances up to 10 km.

# Model predictive control of bioreactor with Evolving Gaussian process model

**Martin Stepančič**[1,2], **Juš Kocijan**[2,3]

[1] Department of systems and control, Jožef Stefan Institute, Ljubljana, Slovenia

[2] Jožef Stefan International Postgraduate School, Ljubljana, Slovenia

[3] University of Nova Gorica, Nova Gorica, Slovenia

martin.stepancic@ijs.si

**Abstract.** The paper presents a case study on adaptive nonlinear model predictive control (MPC) based on a Gaussian process (GP) model. MPC requires a model of the controlled system. We identify a NARX GP model using only 15 measurements of inputs and outputs. The model prediction itself is a normally distributed random variable. The information from a normally distributed prediction is used for implementation of probabilistic model predictive control. Our goal is to illustrate the effects on the controlled system performance. By examining the empirical results under the specified requirements, we can infer that the control performance is acceptable.

**Keywords**: Adaptive model predictive control, Gaussian process model.

## 1 Introduction

Control systems are most often based on the principle of feedback, whereby the signal to be controlled is compared to a desired reference signal and the discrepancy used to compute corrective control action. The term named *closed-loop control* comes from the information path in the system: process inputs have an effect on the process outputs, which is measured with sensors and processed by the controller to form a control signal. This signal is "fed back" as input to the process, closing the loop. Methods such *model predictive control* (MPC) were developed to make control of nonlinear systems to perform as close as possible to optimality. The idea of MPC is that a control performance test is measured on a model by finding the optimal input signal. The control performance relies on a criterion to be minimized which is called

a *cost function*. When finding an optimal control performance according to the cost function, a part of this input signal is applied to the real process. We will focus specially on the variance obtained from the probabilistic model and we will use this information inside a cost function.

## 2 Model predictive control

Model predictive control (MPC) is an intuitive and advanced approach for the control of dynamical systems. It requires a model of the controlled process and this model can be as simple as a step response in time-domain or a first-principle one, described with partial differential equations. The model is used by an optimization algorithm which simulates the process output to find a suitable control input which is then partially applied to the process. The devotion to output response optimality is expressed in terms of cost function minimization under some feasibility constraints but it always depends on the model accuracy. A cost function takes three arguments in general: the reference point where the process is wanted to be driven, the simulated output from the model and input to the model.

The usual way of computer-aided control design restricts the process output sampling and input control action to be taken at discrete-time intervals[1]. In a similar way we are dealing with the discrete model. We can present the values of a simulated output signal for a given input as discrete-time values for a finite number of discrete-time steps as shown in Figure 1. $H_p$ is called the *predictive horizon* and is the number of total time steps we take into account for predicting the future signals. MPC control is called also *receding horizon* control because the optimal control input is recalculated by each new discrete-time instant. Another point of MPC is how an input signal is chosen. A possible simple design is to set a parameter for each step till the end of *control horizon* $H_u$ is reached and the sequent input signal is set to a constant value till the end of prediction horizon.

[1] We omit the discretization problem of continuous systems

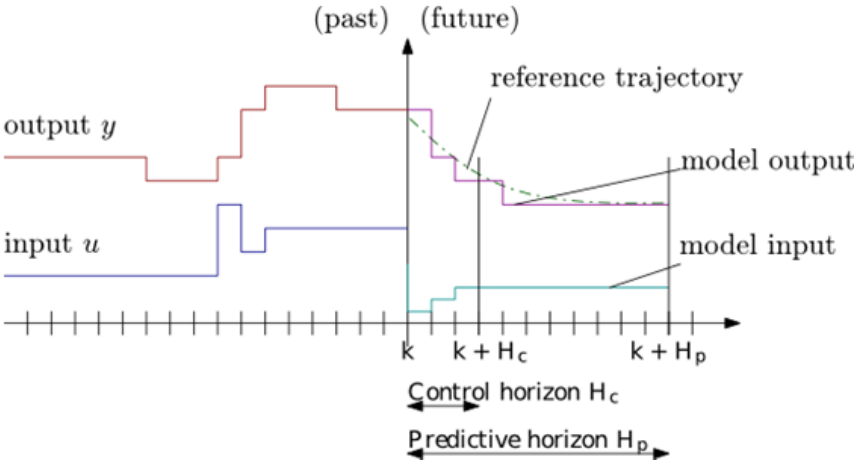


Figure 1 : Illustrative example of input optimization within the receding horizon context

From a practical point of view, the concept of receding horizon uses the predictive horizon as a moving frame inside which a sequence of future $H_p$ discrete input values is chosen to optimize the simulated (model) response with same initial state as the current state of the controlled process. By matching the current state of process with the model, we apply a feedback from the process state to the model and form a *closed-loop* control. The closed-loop concept occurs because using the state of process is a persistent observation of the system output and this information is fed back to the regulator part.

Adaptive controller is the controller that continuously adapts to some changing process. These are meant for the control of time-varying nonlinear systems or for time-invariant nonlinear systems that are modeled as parameter-varying simplified nonlinear models. The designed scheme used for adaptive MPC is shown in Figure 3. The optimizer uses a model to simulate, searching the desired response $r$ by finding a suitable input which will be then partially applied to the plant. Furthermore, the control algorithm is altered to an adaptive one which repeatedly updates the model online. This structure is shown as *model identification* block. The data for identification is made by taking the process input $u$ and output $y$. A problem occurs when such control system starts without any identification data to build a model. We override this by giving an initial model.

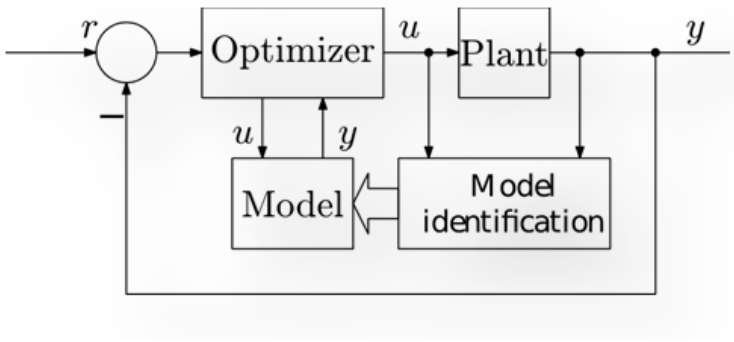


Figure 2 : Scheme of adaptive MPC algorithm

## 3 Model identification

The MPC control algorithm requires a model of the controlled system. We consider a black-box dynamic model in the NARX representation [1-2], where the output at time step $k$ depends on the delayed outputs $y$ and the exogenous control inputs $u$:

$$y(k) = f\big(y(k-1), \dots, y(k-L), u(k-1), \dots, u(k-L)\big) + \epsilon(k), \qquad (1)$$

where $f$ denotes a function, $\epsilon$ is white noise and the output $y(k)$ depends on the state vector $\boldsymbol{x}(k) = [y(k-1), \dots, y(k-L), u(k-1), \dots, u(k-L)]^T$ [1]. Assuming the signal is known up to $k$, we wish to predict the output of the system $l$ steps ahead, i.e., we need to find the predictive distribution of $y(k+1)$ corresponding to $x(k+1)$, if a probabilistic model is taken into account. Multi-step-ahead predictions of a system modelled by $(1)$ can be achieved by iteratively making repeated one-step-ahead predictions, up to the desired horizon [1]. One of possible implementations of a NARX model is the Gaussian process model which will be presented in subsection 3.1.

### 3.1 GP model

GP model is a probabilistic, non-parametric model based on the principles of Bayesian probability [3]. It is probabilistic because its prediction is normally distributed and it is non-parametric because it has no structural evidence of a modeled system. This kind of modeling is classified as supervised learning and during the building phase it depends on a learning set. In our case, the learning set can be percieved as the model itself. The learning set $\mathcal{U}$ of our model is composed from delayed input and output signal measurements of the process. This kind of

data is followed from the NARX model form. Each element $\{\boldsymbol{x}_i, y_i\} \in \mathcal{U}$ is split into an input vector $\boldsymbol{x}_i$ and its predictive target $y_i$ for $i = 1, \dots, N$ where $N$ is the size of learning set $\mathcal{U}$. The output values $y_i$ are assumed to be noisy measurements of an underlying function $f(\boldsymbol{x}_i)$ with conditional probability distribution $p(y_i|f_i) = \mathcal{N}(f_i, \sigma^2)$. Let $\boldsymbol{f} = [f(\boldsymbol{x}_1), \dots, f(\boldsymbol{x}_N)]^T$ and $\boldsymbol{f} = [y_1, \dots, y_N]^T$ , then the learning set $\mathcal{U}$ is used to form a joined Gaussian distribution of function values $\boldsymbol{f}$ [4]. This is a Gaussian process and it is defined as a collection of random variables with joined Gaussian distribution $p(y_i|\mathcal{U}) = \mathcal{N}(\mathbf{0}, \mathbf{K})$ where K is a (semi-positive definite) *covariance matrix* which inherits the input part of the learning set $\mathcal{U}$ by mapping its paired inputs $\boldsymbol{x}_i, \boldsymbol{x}_j$ with a *covariance function* $\boldsymbol{k}(\boldsymbol{x}_i, \boldsymbol{x}_j)$. Intuitively, the covariance function $\boldsymbol{k}$ returns a scalar value, representing how two inputs from $\mathcal{U}$ are related to each other. For now, we keep in mind just what covariance function does, but not how it is made. A common aim in regression is to predict the output $y^*$ from a new input $\boldsymbol{x}^*$ given the learning set $\mathcal{U}$ and a known covariance function $\boldsymbol{k}(\boldsymbol{x}_i, \boldsymbol{x}_j)$. It can be shown that the single posterior distribution $p(y^*|\mathcal{U}, \boldsymbol{x}^*)$ can be analytically solved [4], hence we get the form of GP model prediction:

$$p(y^*|\boldsymbol{x}^*, \mathcal{U}) = \mathcal{N}(y^*| \ \mathbf{k}^{*T}\mathbf{K}^{-1}\boldsymbol{y} \ \ , k(\boldsymbol{x}^*, \boldsymbol{x}^*) - \mathbf{k}^{*T}\mathbf{K}^{-1}\mathbf{k}^*) \qquad (2)$$

where $\mathbf{k}^* = [k(\boldsymbol{x}_1, \boldsymbol{x}^*), \dots, k(\boldsymbol{x}_N, \boldsymbol{x}^*)]^T$ is the vector of covariance function values between the inputs $\boldsymbol{x}_i \in \mathcal{U}, i = 1, \dots, N$ and the prediction input $\boldsymbol{x}^*$.

The *covariance function* design was omitted but it is essentially the main part of GP model structure along the learning set $\mathcal{U}$. Inference in GP firstly involves finding the form of covariance function $\boldsymbol{k}(\boldsymbol{x}_i, \boldsymbol{x}_j)$ to provide a Bayesian interpretation of *kernel methods* [2][3]. Its value expresses the correlation between the individual outputs $y_i$ and $y_j$ with respect to inputs $\boldsymbol{x}_i$ and $\boldsymbol{x}_j$[3]. Usually, the covariance function is used along with some parameters, i.e. *hyperparameters*. The use hyperparameters can highlight or neglect the regressors from an input vector $\boldsymbol{x}_i$. Assuming stationary data is contaminated with white noise, most commonly used covariance function is a composition of the square exponential (SE) covariance function with "automatic

[2] The theory of kernel methods will not be discussed here. For more information, some surveys into kernel methods are provided [4-6].

relevance determination" [7] (ARD) hyperparameters and an additional term $\delta_{ij}$ for the white noise assumption [3]:

$$k(\boldsymbol{x}_i, \boldsymbol{x}_j) = v_0 \exp\left(-\frac{1}{2}\sum_{d=1}^{D} \vartheta_d (x_{id} - x_{jd})^2\right) + v_1 \delta_{ij}, \quad (3)$$

where $\vartheta_d$ are the automatic relevance determination hyperparameters, $v_1$ and $v_0$ are hyperparameters of the covariance function, $D$ is the input dimension, and $\delta_{ij} = 1$ if $i = j$ and $\delta_{ij} = 0$ otherwise. The method of setting hyperparameters $\boldsymbol{\theta} = [v_0, v_1, \vartheta_1, \ldots, \vartheta_d]$ will not be discussed here, but can be further provided in [3-4][7].

### 3.2 Evolving GP model

This subsection is summarized from [3]. The Evolving GP model (EGP) is inspired by Evolving systems [8], which are self-developing systems, adapting on-line both, structure and parameter values of the model from incoming data [8]. We use the term Evolving GP models in sense of sequential adapting of both, the "structure" of GP model and hyperparameter values. This enables fast and efficient GP model adaptation to the time-varying system. In comparison with the learning set $\mathcal{U}$ of a GP model, the learning set of an EGP model $\mathcal{U}_A$ is said to be an *active set* with the property that only a subset $\mathcal{U}_A \subset \mathcal{U}$ of entire learning dataset $\mathcal{U}$ is used for modeling with EGP.

Similarly as in [9] we decided to use fixed squared exponential (SE) covariance function with ARD (3) because its functionality is able to find influential regressors. With the optimization of the hyperparameter values, uninfluential regressors have consequently smaller influence to the result. Therefore, all available regressors can be used and consequently, only the active set $\mathcal{U}_A$ and hyperparameter values $\boldsymbol{\theta}$ are to be adapted sequentially. In general the proposed method consists of three main steps to adapt the GP model sequentially: Update of active learning set, hyperparameter optimization, covariance matrix inverse calculation.

In our specific case we have an EGP of NARX form whose incoming data consists from an input vector $\boldsymbol{x}_i$ of delayed inputs and outputs and its target value $y_i$ of the current output. For every new incoming data, the novelty of the data according to the current GP model is verified. This is simply done by predicting the output mean value $E[y_i^*]$ of the incoming input vector $\boldsymbol{x}_i$ and comparing to the measured value

$y_i$. If the condition $|E[y_i^*] - y_i| > \zeta_{EGP}$ is true for a pre-set threshold $\zeta_{EGP}$, the element $\{\boldsymbol{x}_i, y_i\} \in \mathcal{U}$ is added to the active set $\mathcal{U}_A$. A method for excluding elements must be used if the active learning set has to be limited to a maximum size. This methodology will not be discussed here but more information about excluding elements from an active set is available from [3,9-10].

# 4 Case study

## 4.1 Bioreactor

The adaptive MPC-GP method will be examined with a simplified model of bioreactor [12]. It is an open-loop stable, nonlinear and second order system, desribed with difference equations:

$$x_1(k+1) = 0.5\,\frac{x_1(k)x_2(k)}{x_1(k)+x_2(k)} - 0.5\,u(k)\,x_1(k), \tag{4}$$

$$x_2(k+1) = 0.5\,\frac{x_1(k)x_2(k)}{x_1(k)+x_2(k)} - 0.5\,u(k)\,x_2(k) + 0.05\,u(k), \tag{5}$$

$$y(k) = x_1(k) + \epsilon(k), \tag{6}$$

where $u$ is system input, limited to $[0,0.7]$, $x_1$ and $x_2$ are system states, and the output $y$ is contaminated with a normally distributed noise $\epsilon$ with $p(\epsilon) = \mathcal{N}(0,0.001)$.

## 4.2 Control design

The cost function:

$$J = \sum_{i=1}^{H_p} (r(k+i) - E[y^*(k+i)])^2 + \gamma_v \,\mathrm{var}[y^*(k+i)] \tag{7}$$

is used to find the optimal control input $u$.

Because we need an initial GP model to perform effectively a simple proportional (P) regulator was used to train a GP model in closed-loop in the first $0 \leq k \leq 30$ time steps. At $k > 30$ the adaptive MPC-EGP regulator was activated and replaced the proportional one. The error threshold for EGP model update is set to $\zeta_{EGP} = 0.021$ and we restricted the EGP active learning set $\mathcal{U}_A$ to a maximum of 15 learning points.

Just a representative segment of the closed-loop performance is shown in Figure 3 for prediction horizon $H_p = 8$, control horizon $H_u = 1$ and cost function parameter $\gamma_v = 0.14$.

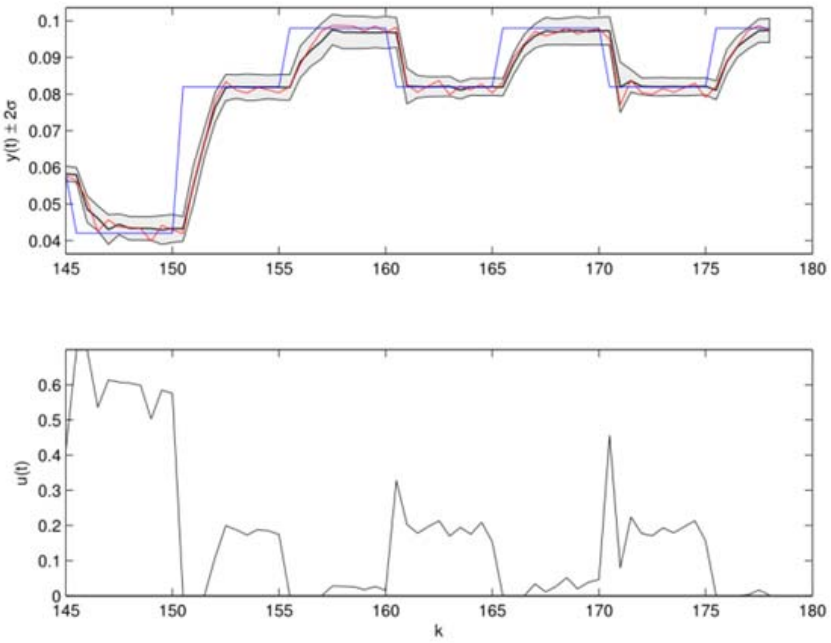


Figure 3: Closed-loop control of bioreactor. The upper window contains a reference signal (blue), process output (red) and one-step prediction mean with double std. deviation (black with gray gap). The lower window is control input.

## 5 Conclusion

Our goal was to illustrate the controlled system performance using an EGP model with a limited learning set to 15 data inputs. The results from Figure 3: Closed-loop control of bioreactor. The upper window contains a reference signal (blue), process output (red) and one-step prediction mean with double std. deviation (black with gray gap). The lower window is control input. show that the performance is acceptable. Using a larger prediction horizon is unnecessary for this specific case.
One should note that we implemented an adaptive control algorithm which adapts the GP model on-line and its prediction could predict a much smaller uncertainty compared to an offline GP model.

## References:


[1] J. Kocijan. Control Algorithms Based on Gaussian Process Models: A State-of-the-Art Survey. In *Special International Conference on Complex systems: synergy of control com-munications and computing*, September 16-20, 2011, Ohrid, Republic of Macedonia.

[2] R. Sałat, M. Awtoniuk, and K. Korpysz, "Black-Box system identification by means of Support Vector Regression and Imperialist Competitive Algorithm," in Przeglad Elektrotechniczny, 2013.

[3] D. Petelin and J. Kocijan: Evolving Gaussian process models for predicting chaotic timeseries. In *2014 IEEE Conference on Evolving and Adaptive Intelligent Systems (EAIS)*, 2014.

[4] C. Bishop, Pattern Recognition and Machine Learning. Springer, 2006.

[5] G. Pillonetto, F. Dinuzzo, T. Chen, G. D. Nicolao, and L. Ljung, Kernel methods in system identification, machine learning and function estimation: A survey. *Automatica*, vol. 50, no. 3, pp. 657–682, 2014.

[6] C. Campbell, Kernel methods: a survey of current techniques. *Neurocomputing*, vol. 48, pp. 63–84, 2002.

[7] C. E. Rasmussen and C. K. I. Williams, Gaussian Processes for Machine Learning. MIT Press, 2006.

[8] P. Angelov, D. P. Filev, and N. Kasabov: Evolving intelligent systems: Methodology and applications. In *IEEE Press Series on Computational Intelligence*, Wiley IEEE Press, April 2010.

[9] D. Petelin, A. Grancharova, and J. Kocijan: Evolving Gaussian process models for prediction of ozone concentration in the air. *Simulation Modelling Practice and Theory*, vol. 33, pp. 68 – 80, 2013.

[10] D. Petelin and J. Kocijan: Control system with evolving Gaussian process models. In *Evolving and Adaptive Intelligent Systems (EAIS), 2011 IEEE Workshop on*, pp. 178–184, 2011

[11] K. Ažman and J. Kocijan: Application of gaussian processes for black-box modelling of Biosystems, *ISA Transactions*, vol. 64, pp. 443–457, 2007

## For wider interest

Bioreactor processes are the core manufacturing process in the biotech industry. Delays and process upsets can result in the loss of money in revenue through lost product and downtime. Because the bioreactor is such a critical component, keeping it running is essential to the profitability of a biotech operation. For the efficient operation high-quality control is necessary. Processes demonstrating highly nonlinear behaviour such bioreactors can be operated in regimes closer to the process optimum, where simple controllers may fail. Unfortunately, the precise and appropriate model for MPC requires significant time and effort to construct and the proposed adaptive MPC using a probabilistic black-box model might be an efficient solution.

# Smart-Home Energy Management System: A Trade-off between Energy Consumption and Thermal Comfort Experience According to Occupant's Activity

**Domen Zupančič**[1,3] , **Božidara Cvetkovič**[2,3], **Matjaž Gams**[2,3]

[1] Robotina d.o.o., OIC-Hrpelje 38, SI-6240 Kozina, Slovenia

[2] Department of Inteligent Systems, Jožef Stefan Institute, Ljubljana, Slovenia

[3] Jožef Stefan International Postgraduate School, Ljubljana, Slovenia

domen.zupancic@ijs.si

**Abstract.** Energy consumption and occupant's comfort are key factors when evaluating smart home environments. The focus of this paper is on thermal comfort, which is highly affected by environmental factors (temperature, humidity, radiation of elements and air movement), as well as by occupant-related factors (occupants' level of activity and clothing insulation). To satisfy a thermal comfort objective, energy is needed for heating and cooling. However, the energy saving aspect should not be omitted. This paper's contribution is two-fold: (i) a proof-of-concept analysis of smart home control based on occupants' activity level, which was estimated using an activity monitoring method and (ii) a trade off analysis between the energy consumption and thermal comfort when the activity level is served as an input into an intelligent home energy management system.

**Keywords**: HVAC, energy saving, occupants' comfort, occupants' activity level.

## 1 Introduction

Research focused on regulation of the smart home environment has already been looked at from various perspectives, such as economic, ecological, assistive, etc. Common to each of them is that they all take into account the occupants' satisfaction and comfort, both depending on the environmental and personal factor.

The regulation of the temperature in a building environment is a complex problem. The room heating process is (i) slow due to room's thermal inertia, (ii) time delayed, since the effect of actions take time to feel the results (iii) multivariable, since indoor temperature is affected by various heating bodies, such as occupants, the sun shining

through the window, as well as mechanic heaters, and (iv) non linear, i.e. the rise time of indoor temperature varies at different outdoor temperatures [1]. In development of temperature control strategies it is highly important to have a good building model. The building model can be either a black box model, a pure machine-learning model in which the physical relations are result of a machine-learning process, a white box model in which the physical relations are given according to laws of physics, or a combination of both [2].

It is a well-known fact that the lack of time of active population has taken certain tasks from the dedicated facilities to our homes, one of such being the scheduled physical activity. Such task has an increased impact on the temperature and quality of air either in the dedicated facility or, as in our case, at home, change of which affects the comfort of the occupant. For example, if the occupant is resting and watching television, the temperature of the room should be higher than in the case when the occupant exercises. This indicates that smart home systems would positively benefit if a measure of occupant's activity level were one of the inputs to the system. Can we measure the activity level?

The term used to quantity physical activity is energy expenditure (EE) and is usually expressed in metabolic equivalents of task (MET), where 1 MET is considered as resting metabolic rate (RMR), defined as the energy expended at rest. MET values range from 0.9 (sleeping) to over 20 in extreme exertion. EE can be directly measured using approaches such as direct or indirect calorimetry, or doubly labelled water [3]. These methods are expensive and cumbersome for free-living applications. Commercial devices for estimation of EE come in a form of one- [4][5] or multi-sensor wrist or armbands [6] that can be used in every-day life. They are based on the concept of high correlation between movement of inertial sensors and activity level. Shortcomings of these devices are high price and low estimation accuracy when it comes to non-sport activities. Our research on activity monitoring has proved that similar or even better results can be obtained utilizing commercial inertial sensors. For example, smartphone inertial sensor [7], which can be easily integrated into the smart home architecture as a software agent. An example of multi-agent architecture for smart building control can be seen in literature [8], where the occupant chooses the strategy, either to minimize the energy consumption, energy costs or to maximize the comfort. The referenced system is adopted as an initial system in this paper.

## 2 The notation of thermal comfort experience

Thermal comfort experience is the notion of the thermal sensation of a person in a conditioned environment. The predicted mean vote (PMV) index expresses the thermal sensation on a 7-point scale ranging from -3 to +3, where negative values denote cold sensation and positive values denote warm sensation. The value 0 denotes neutral sensation, which is the target value for indoor air conditioning. The more distant from 0 the PMV is, the more cold (if negative) or hot (if positive) is the sensation.

The PMV calculation is based on environmental factors, such as temperature and humidity, and occupant-related factors, such as clothing insulation and activity level. In contrast to environmental factors, the occupant-related factors are harder to perceive in order to include them into a control system. The following subchapter presents the environmental and occupant-related factors, which are included in calculation of the PMV according to the standard ISO-7730 [13].

Several research papers can be found on PMV index regulation. Calvino et al. [12] developed fuzzy controller and Ciglar ert al. [14] and Liang et al. [15] used the model predictive controller for PMV regulation. Experiments were done either in simulated environment or in the real living environments, but all of them assume the clothing and activity of a person as a static, predefined value.

### 2.1 Parameters, used to compute PMV

According to ISO-7730, the PMV is calculated according to the following parameters: clothing insulation ($clo_{Rate}$ [clo]), activity ($met_{Rate}$ [MET]), air temperature ($T_{in}$ [°C]), relative air velocity ($v_{ar}$ [m/s]), relative humidity (RH [%]) and mean radiant temperature ($T_{mr}$ [°C]). The units important for this research are defined as follows: 1 clo=0.155 $m^2$°C/W and 1 MET =58.2 W/$m^2$. We analysed how the parameters influence the value of PMV. For this analysis, we fixed the value $clo_{Rate}$ at 0.5 clo and $v_{ar}$ at 0.1m/s. Figure 1 shows the PMV per $met_{Rate}$, where the $T_{in}$ is a parameter ranging from 14 to 28°C; $T_{mr}$ equals $T_{in}$; RH is fixed at 60%. Figure 2 shows the PMV per $met_{Rate}$, where RH is a parameter ranging from 10 to 90%; $T_{in}$ and $T_{mr}$ are fixed at 22°C. Comparing Figure 1 and Figure 2, we can observe that the $T_{in}$ has significantly stronger influence on the PMV than RH. Therefore we decided to regulate PMV using $T_{in}$.

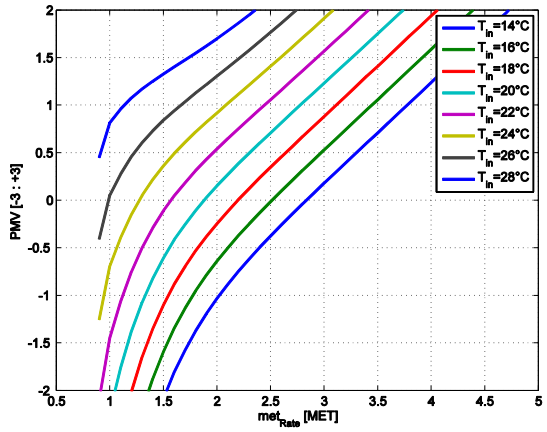


**Figure 1:** PMV according to metRate at different $t_{in}$, $t_{mr}=t_{in}$

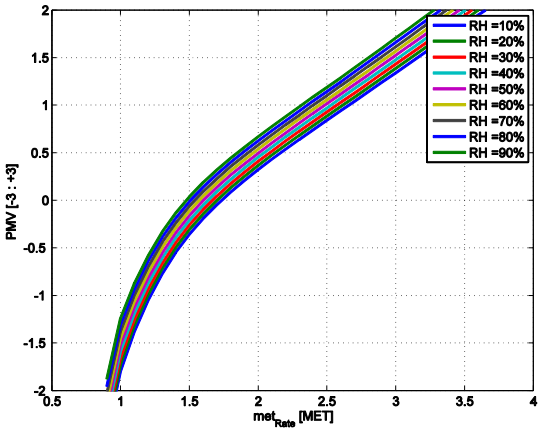


**Figure 2:** PMV according to metRate at different RH, $t_{mr}=t_{in}$

## 3 Control system

The control system is implemented in Java Agent Development Environment (JADE) [8] as a part of hierarchical agent architecture, based on our previous research [9] and is roughly presented in Figure 3. The right part of the figure presents a model of a building and its occupant. The weather and person dataset present the data used for simulation. The top side presents a sensor network, which performs environmental state sensing and estimation. The left side presents a heating controller, which controls the temperature in the building (Reg) by minimizing the difference between the reference temperature $T_{in}$ and the indoor temperature $t_{in}$ and operates only during occupancy. $T_{in}$ is delegated by a set-point delegation module (Setpt. deleg.) of the heating controller in a way to minimize the difference between the value of PMV and $PMV_{ref}$. The $PMV_{ref}$ is set according to the occupants' requirements for comfort and energy consumption. The value of

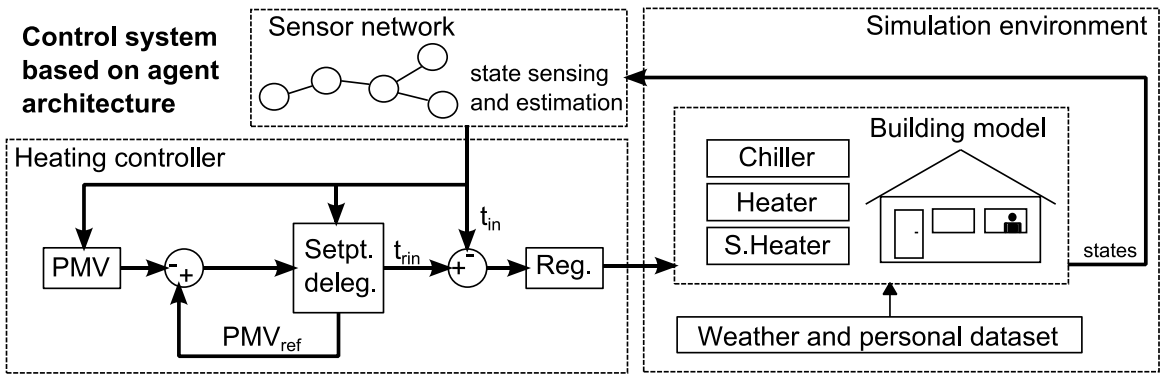


**Figure 3:** Control schema. The left side of the figure presents the control system and the right side the controlled environment.

$PMV_{ref}$ is an absolute threshold value for PMV regulation, which should be satisfied during room temperature control. For example, if the value of $PMV_{ref}$ is set to 0.5, than the comfort threshold is set to -0.5 for heating and +0.5 for cooling, and the desired interval of PMV is therefore [-0.5, +0.5].

# 4 Case study

The system was examined using a simulation model of a building, where the weather data and occupant clothing were prepared in advance. The data about occupant's activity was estimated by an activity monitoring method, which runs on the regular smartphone [7].

## 4.1 The thermal model of a building and the HVAC system

Thermal model was created using EnergyPlus [10] and simulated using BCVTB environment [11]. The building contains a heating, ventilation and air conditioning (HVAC) system, composed of a packaged terminal heat pump system with direct expansion heating coil, direct expansion cooling coil and supplementary heater, with capacities of 8kW, 5.5kW and 3 kW respectively.

## 4.2 Activity monitoring

The activity monitoring of the occupant was performed using an application on the occupants' smartphone. The application uses a regression model over the inertial sensor signal to estimate the EE. The stream of data is collected and split into 10 seconds windows, each window overlapping with the previous one by one half of its length. For each overlapping window a set of attributes is computed. The reader is referred to [7] for details on the computed features. The model was trained using SVR algorithm as implemented in Weka machine learning suite [16] and cross-validated using leave-one-person-out approach. The dataset used for training the model was collected in a laboratory environment where activities, such as walking, running and cycling, were performed under speed control for ten healthy volunteers. The scenario for the dataset was designed to contain activities of normal daily living. The activities range from resting, cooking, cleaning and office work to sports activities such as fast walking, running and cycling. In addition to smartphone, each person was also equipped with Cosmed indirect calorimeter for reference energy expenditure and a commercial device SenseWear for comparison of the results. The result is expressed using a typical performance measure, the mean absolute error (MAE), and it shows that our approach slightly outperforms the costly commercial

device and proves sufficient to be used in our simulation of a smart home. Our approach performed with MAE of 0.83 MET and SenseWear performed with MAE of 0.86 MET.

# 5 Demonstrative results

## 5.1 The dataset collection

The purpose of this paper is a proof-of-concept of smart home control based on thermal comfort experience. Occupant's perceived thermal comfort is highly affected by his/her activity level. To satisfy the thermal comfort goal we have collected a dataset comprised of two-day data of a single occupant (male). One day presents a normal week-day (Friday, February) and the second day presents a normal day over a weekend (Saturday, February). The occupant's timetable for the two collected days can be observed on last graph of Figure 4 and goes as follows. Friday is less active day; the occupant sleeps until 7:00; prepares for work and leaves at 8:00; returns at 17:00 and does some regular home chores before engaging in regular exercise comprised of stretching and running on treadmill for 45 minutes; the day ends with shower, meal and rest while watching TV. He goes to sleep at 22:00. Saturday is active day; the occupant sleeps until 8:00; has morning chores until 8:30; does exercise for one hour which includes stretching, running and cycling; regular chores as cleaning and some office work until 12.00; showers at 12:30 lives home; returns at 15.00; does regular home chores as cleaning until 15:10; rests for 40 minutes; office work is done until 17:00; 30 minutes of running on a treadmill until 17:30; normal evening activities until 22:00 when the occupant leaves home. The dataset was analysed by the activity monitoring method running on a smartphone (Section 4.2) to produce estimation of occupant's EE every 10 seconds. The showering activity was estimated according to the atomic activities performed during the task (standing walking, leaning), since it is impossible to use smartphone while showering. The aggregated one-minute values were presented as input to the heating control system.

## 5.2 Control System

The presented dataset served as an input for the control system simulator. The results of the control system demonstrate the heating control of a building with one occupant, which is presented on Figure 4. It presents the two days operation of heating, where the PMV, $T_{in}$, $met_{Rate}$, $clo_{Rate}$, occupancy and power of heater, chiller and supplementary heater operation are presented in time. The first graph presents

the PMV over the respective two days of the dataset. The threshold is set to 0.5, so if PMV is not in the range of the $PMV_{ref}$, the controller adapts $T_{rin}$ in order to achieve the range defined with $PMV_{ref}$. The system controls the PMV only in case when the occupant is at home, which is denoted as occupancy is 1. The $T_{in}$ can be seen on the second graph of Figure 4. The third graph presents occupancy and $clo_{Rate}$. The fourth graph presents the power rates of the heater, the supplementary heater and the chiller. The last graph presents the occupant's activity level ($met_{Rate}$).

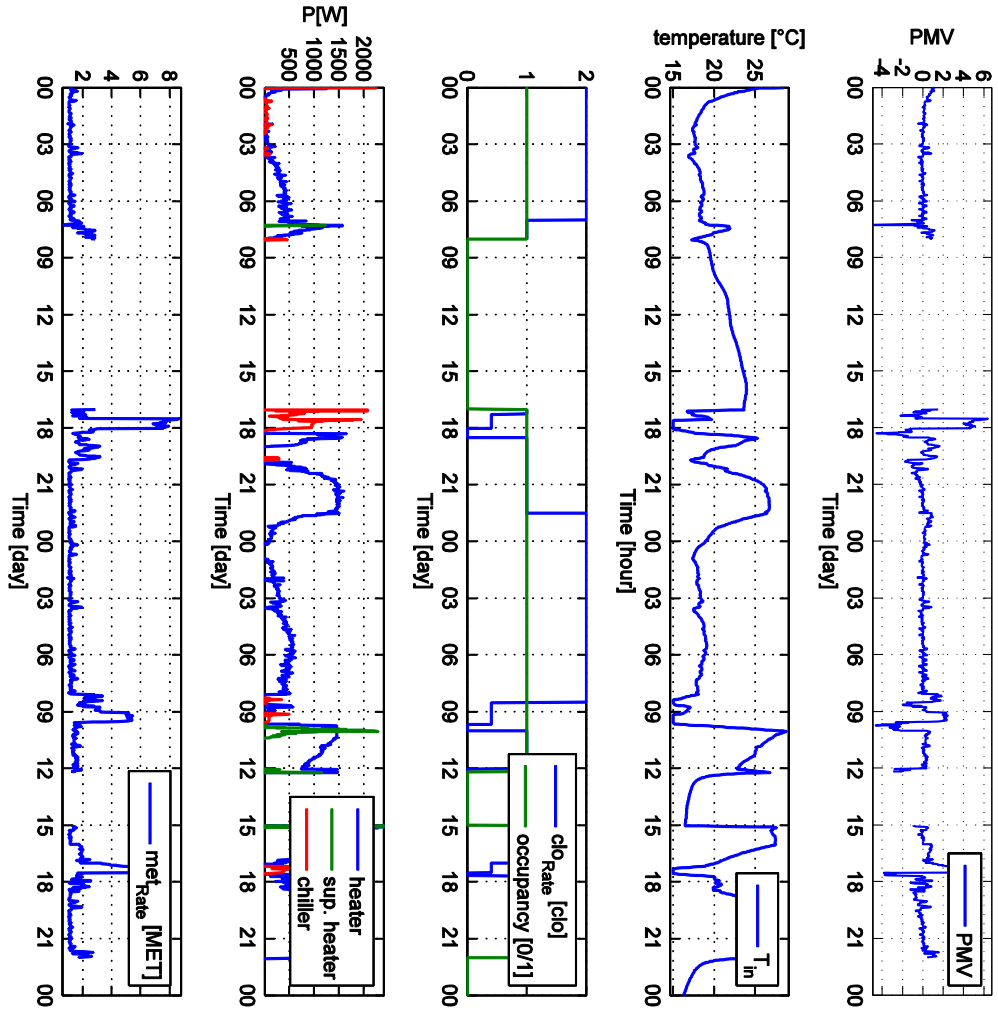


**Figure 4:** Simulation of two days control, environmental and person states presented in time.

We can observe that when the $met_{Rate}$ is low (1-2 met), $T_{in}$ does not fluctuate and the PMV is always in interval [-0.5, +0.5]. When the $met_{Rate}$ rises (over 3 MET, such as for example at 18:00 on first day) the PMV also rises and the controller starts to lower the $T_{rin}$. It can be seen, that the $T_{in}$ should be low, to achieve the PMV in interval [-0.5, +0.5], for example, when the occupant is running (high activity level), the control system has trouble compensating by decreasing $T_{in}$. The minimum value

for cooling is set to 15°C. Furthermore, we can observe the end of the first day, when the person goes to sleep; the $clo_{Rate}$ is set to sleeping (it changes from 1 to 2 clo). The controller decreases the $T_{in}$ from approximate 25°C to approximate 18°C and keeps PMV in the interval [-0.5, +0.5].

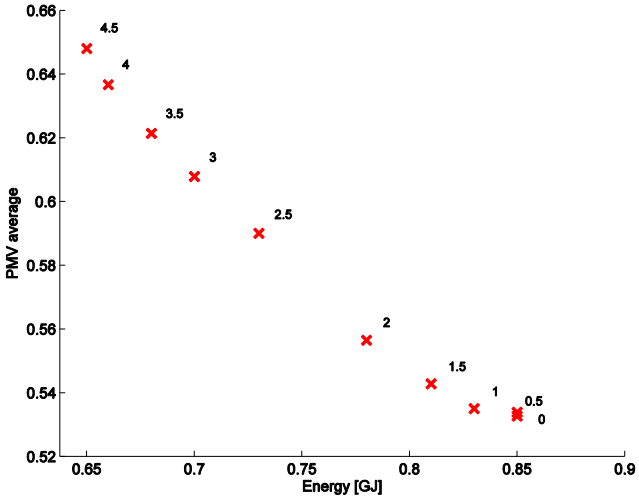


**Figure 5:** Energy consumption according to average PMV during occupancy at different PMVref threshold values

Figure 5 presents the simulations results, where the x axis represents energy consumption by the HVAC system in GJand y axis represents the average value of PMV, which is computed only for the moments, the person is present. Each point presents simulation result for $PMV_{ref}$, where $PMV_{ref}$ varies from 0 to 4.5 with 0.5 steps. The value next to the point denotes the $PMV_{ref}$ for the current simulation run. It is obvious, that lower the $PMV_{ref}$, higher the energy consumption and vice versa. According to the trade-off between the energy consumption and the comfort experience, the occupant can choose the strategy, which will satisfy his needs.

## 6 Discussions and conclusions

This paper presents a smart building control system, which regulates the PMV. The PMV is highly dependent on occupants' activity level in a controlled environment and is compensated with the indoor temperature. Our system estimates the activity level as energy expenditure expressed in MET, which is the important factor for computing the PMV. Our system is able to compensate the comfort experience, perceived by occupant, with the indoor temperature control, using the HVAC system.

We have demonstrated the advanced HVAC control system, which utilizes an integrated model for EE estimation. The comfort system allows the occupant to specify a desired trade off between the thermal comfort and energy consumption for HVAC operation. The results show (i) how the energy expenditure of a person influence the room temperature at which the person feels comfortable and (ii) demonstrates the feasibility of smart regulation of PMV to achieve the desired trade-off between energy consumption and thermal comfort experience.

## Acknowledgements

*Operation part financed by the European Union, European Social Fund. Operation implemented in the framework of the Operational Programme for Human Resources Development for the Period 2007- 2013, Priority axis 1: Promoting entrepreneurship and adaptability, Main type of activity 1.1.: Experts and researchers for competitive enterprises.*

## References:

[1] C. E. García, D. M. Prett, M. Morari. Model predictive control: Theory and practice—A survey. *Automatica*, 25(3), 335-348, 1989.

[2] P. Bacher, H. Madsen. Procedure for identifying models for the heat dynamics of buildings. *IMM-Technical Report-2010-04*, Technical University of Denmark.

[3] R. Brychta, E. Wohlers, J. Moon, K. Chen. Energy Expenditure: Measurement of Human Metabolism. *Engineering in Medicine and Biology Magazine*, 29(1), 42–47, 2010.

[4] Nike+ FuelBand, http://www.nike.com/us/en_us/c/nikeplus-fuelband

[5] Fitbit Flex, http://www.fitbit.com

[6] SenseWear, http://sensewear.bodymedia.com/

[7] B. Cvetković, B. Kaluža, R. Milić, M. Luštek. Towards human energy expenditure estimation using smart phone inertial sensors. *LNCS 8309*, 94-108, 2013.

[8] F. Bellifemine. JADE - a java agent development framework. *Multi-Agent Programming*, 2005.

[9] D. Zupančič, M. Luštrek, M. Gams. A Network of Sensor and Actuator Agents for Building Automation Systems. *HAI,* 121-132, 2013.

[10] D. B. et al. Energyplus: creating a new generation building energy simulation program. *Energy and Buildings*, 33, 319-331.

[11] M. Wetter. Co-simulation of building energy and control systems with the building controls virtual test bed. *Journal of Building Performance Simulation*, 4,185-203, 201.

[12] F. Calvino, M. La Gennusa, G. Rizzo, G. Scaccianoce. The control of indoor thermal comfort conditions: introducing a fuzzy adaptive controller. *Energy and Buildings*, 36(2), 97-102, 2004.

[13] ISO 7730:2005, Ergonomics of the thermal environment

[14] J. Cigler, S. Prívara, Z. Váňa, E. Žáčeková, L. Ferkl. Optimization of Predicted Mean Vote index within Model Predictive Control framework: Computationally tractable solution. *Energy and Buildings*, 52, 39-49, 2012.

[15] J. Liang, R. Du. Thermal comfort control based on neural network for HVAC application. *Control Applications*, 819,824, 2005.

[16] M. Hall, E. Frank, G. Holmes, B. Pfahringer, P. Reutemann, I. H. Witten. The WEKA Data Mining Software: An Update. *SIGKDD Explorations,* 11(1), 10–18, 2009.

## For wider interest

Energy consumption and occupant's comfort are key factors when evaluating smart home environment. The focus of this paper is the thermal comfort, which is highly affected by the environmental temperature, humidity, radiation of elements, air movement and nevertheless the occupants' level of activity and clothing insulation. To satisfy the thermal comfort objective, additional energy has to be used for heating and cooling, but the energy saving is an important factor from various aspects and is not to be omitted. This papers contribution is two-fold: (i) a proof-of-concept analysis of smart home regulation based on occupants' activity level, which was estimated using the activity monitoring method and (ii) a trade off analysis between the energy consumption and thermal comfort when the activity level is served as an input into the intelligent heating control system.

# Nanoznanosti in nanotehnologije (Nanosciences and Nanotechnologies)

# Transformations of alcohols with silanes under green reaction conditions

**Njomza Ajvazi**[1], **Stojan Stavber**[2,3]

[1] Jožef Stefan International Postgraduate School, Ljubljana, Slovenia

[2] Department of Organic and Bioorganic Chemistry, Jožef Stefan Institute, Ljubljana, Slovenia

[3] Centre of excellence for integrated approaches in chemistry and biology of proteins

njomzaajvazi@hotmail.com

**Abstract.** Different structure types of alcohols were proceeded with silanes, such as chlorotrimethylsilane (TMSCl), bromotrimethylsilane (TMSBr), azidotrimethylsilane ($TMSN_3$) and trimethylsilylcyanide (TMSCN) without the catalyst under solvent-free reaction conditions. Various primary, secondary and tertiary benzyl alcohols and tertiary alkyl alcohols were directly transformed to corresponding benzyl or alkyl halides using halogen atom bearing silanes (TMSCl and TMSBr) with quantitative conversion and high selectivity, while in the case with $TMSN_3$ and TMSCN under the same conditions we got silylation of hydroxyl substrates.

**Keywords:** green chemistry; trimethylsilanes; alcohols; halogenation; silylation

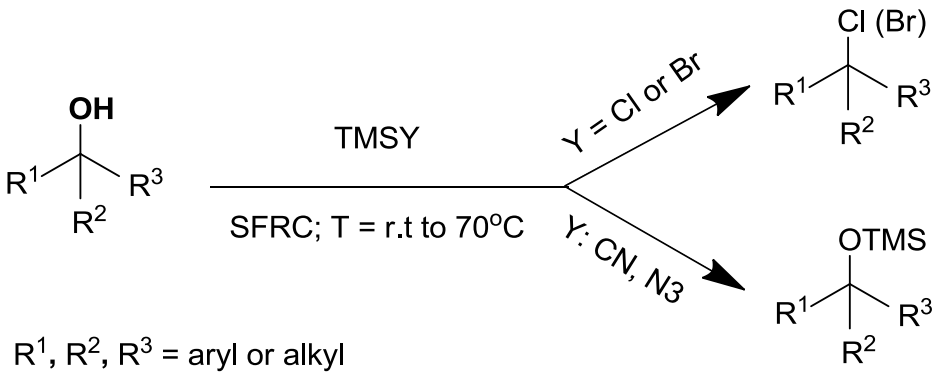

# 1 Introduction

The concept of green chemistry, based on twelve basic principles [1], represents one of the most important trends in chemical sciences, in organic chemistry particularly. In this view it is one of the major challenge in organic chemistry planning organic reactions and processes involving the principle of atom economy, efficient catalytic methodologies, suitability of a safer reaction media (water, ionic liquids, fluorous liquids…) or solvent-free reaction conditions (SFRC) in place of volatile organic solvents, low energy consumption and low waste leaving behind.

Hydroxy functional group is one of the most abundant functional groups in organic compounds, thus transformations of it under green reaction conditions represents considerable challenge and interest among organic chemists. Reactions of alcohols with silanes are widely used methodology for transformation of hydroxyl group in organic molecule. Many silanes such as chlorotrimethylsilane, 3,4-hexamethyldisiloxane, hexamethyldisilazane have been used for the transformation of oxygen-hydrogen bond in hydroxyl group to oxygen-silicon bond, i.e. for the silylation of OH group [2], while trimethylhalosilanes were found to be useful for halogen substitution of OH group in various alcohols [3]. Halogenation of alcohols, following nucleophilic substitution process, is an important transformation in organic chemistry and has attracted significant interest over the years. Due to the lower leaving ability the hydroxyl moieties are hardly substituted under mild conditions. So, it should be activated before the treatment with the nucleophiles. The most recent introduced methods for chlorination of alcohols using silanes utilize $HSiMe_2Cl/InCl_3$/benzyl as a selective and mild system [4], dichlorodiphenylcyclopropene [5], and chlorodimethylsilane catalysed by a gallium trichloride/tartrate system [6]. Some alternative reagents reported for bromination of alcohols are: hexamethyldisilane/pyridinium bromide perbromide and chloromethylsilane/lithium bromide [7]. However, these synthetic procedures for preparation have several disadvantages: such as multiple step synthesis, toxic and expensive reagents, problematic manipulation, and long reaction time.

The aim of this work is to achieve direct transformation of the hydroxyl group in alcohols using different substituted trimethylsilyl derivatives under reaction conditions which follow as much as possible the principles of green chemistry. We

now report the transformations of various structure types of alcohols following their reactions with trimethylhalosilanes, trimethylsilyl azide and trimethylsilyl cyanide under catalys-free and solvent-free reaction conditions.

## 2 Results and discussion

We chose phenyl(*p*-tolyl)methanol (1, Figure 1) as the basic model compounds for the investigation of reactions of alcohols with silanes and treated it with trimethylchlorosilane (TMS) under solvent free reaction conditions, and after 4 hours at room temperature found out that the reaction quantitatively resulted in the formation of 1-(chloro(phenyl)methyl)-4-methylbenzene (2) accompanied with the small amounts of the dimeric ether (3) of the starting alcohol.

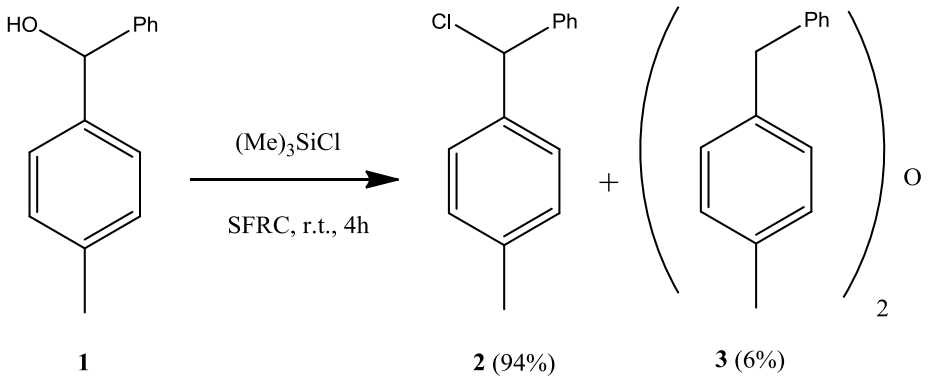


**Figure 1**: Chlorination of secondary benzyl alcohol with trimethylchlorosilane (TMSCl) under solvent-free reaction conditions

Encouraged with this result we checked the reaction of naphtalen-1-yl(phenyl)methanol (4, Figure 2) with TMSCl under SFRC and established the quantitative formation of the corresponding chloride 5, but in this case after 24 hours at 70-75 $^{o}$C.

We further investigated the corresponding reactions of primary benzyl alcohols with TMSCl and results are collected in Table 1. In the case of performing the reaction with benzyl alcohol (6a) we observed high conversion of starting material into corresponding chloride (7a) as the main product which also accompanied with a small amount of dimer (8a). In the case of p-methoxybenzyl alcohol (6c) the quantitative conversion of starting material to the corresponding chloride (5c) wasobserved, while in the case of 4-methylbenzyl alcohol (6b), 4-chlorobenzyl

alcohol (6d) and 4-fluorobenzyl alcohol (6e) we observed high conversion of starting materials resulting in the formation of the corresponding chlorides (7b, 7d and 7e) as the main products, accompanied with a small amounts of dimers (8b, 8d and 8e). In the case of 3-nitrobenzyl alcohol we did not observe any conversion of starting material. Electro donating substituents on the phenyl ring thus supported considerably the course of the reaction, while nitro group, as strong electron withdrawing group, supressed the transformation. The pathway of these reaction is thus connected with the stabilization of benzylic carbocation intermediates what represents a basic characteristic of nucleophilic substitution transformation following the $SN_1$ reaction course. In order to verify this assumption we chose 1-phenyl-1,2-ethanediol (9, Figure 3) as the additional testing compound. We established the quantitative formation of 2-chloro-2-phenylmethanole (10) when 9 was treated with TMSCl under SFRC thus proving the $SN_1$ reaction pathway of the substitution.

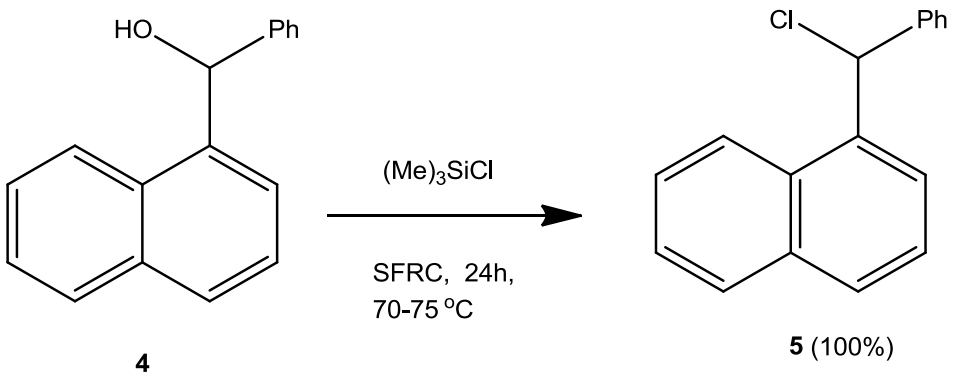


**Figure 2**: Chlorination of naphthalen-1-yl(phenyl)methanol (4) with TMSCl under SFRC

**Table 1***: Chlorination of various primary benzyl alcohols with TMSCl under SFRC*

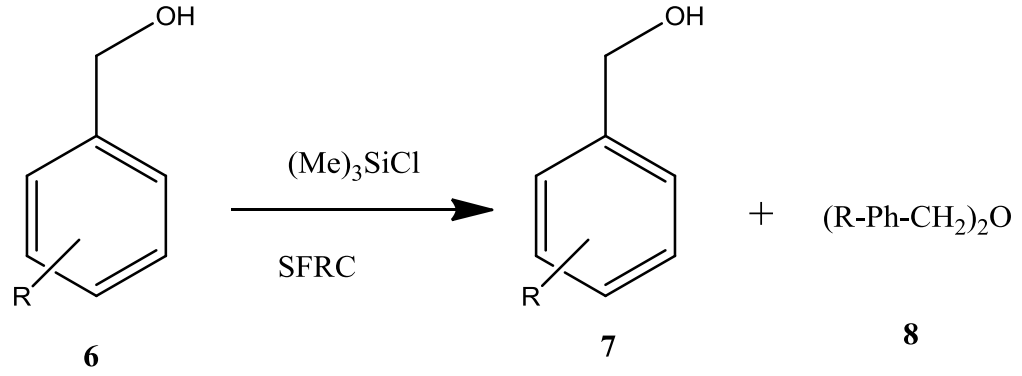


**6** **7** **8**

| Entry | R | Conv.(%)[b] of **6** | Relative distribution(%)[b] | |
|---|---|---|---|---|
| | | | **7** | **8** |
| 1 | H **(6a)** | 78 | 68 | 10 |
| 2 | 4-Me **(6b)** | 100 | 87 | 13 |
| 3[c] | 4-OMe **(6c)** | 100 | 100 | / |
| 4 | 4-F **(6d)** | 100 | 88 | 12 |
| 5 | 4-Cl **(6e)** | 84 | 75 | 9 |
| 6 | 3-$NO_2$ **(6f)** | / | / | / |

[a] Reaction conditions: Benzyl alcohol **1** (0.5 mmol), TMSCl (0.55 mmol), 70-75°C, 2-24 h.

[b] Determined from $^1$H NMR spectra of isolated crude reaction mixtures

[c] rt,

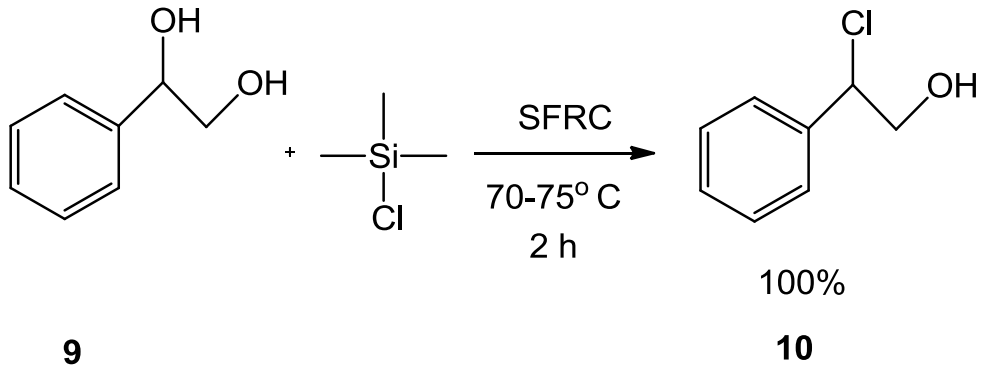


**9** **10**

**Figure 3**: Chlorination of 1-phenyl-1,2-ethanediol (9) with TMSCl under SFRC

Similarly to secondary and primary benzyl alcohols, effective transformation was observed in the reaction with tertiary alkyl alcohols under the same conditions. In the case of α,α-dimethylbenzenepropanol (11a, Figure 4) and triethylmethanol (11b) we observed quantitative conversion of starting materials resulting in the formation of corresponding chlorides (12a) and (12b). Since we found that primary and secondary alkyl alcohols were resistant towards transformations mediated with TMSCl, the $SN_1$ reaction course was found to be the most probable mechanistic characteristic of these valuable transformations.

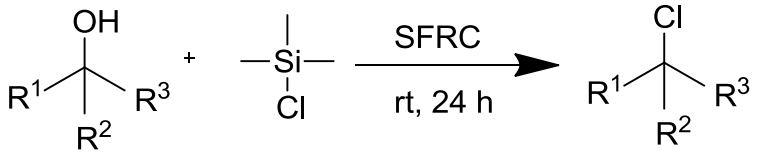


**11** **12**

**11a** : $R^1 = R^2 = R^3 = Et$ **12a** (100%)

**11b** : $R^1 = R^2 = Me$, $R^3 = -(CH_2)_2Ph$ **12b** (100%)

**Figure 4**: Chlorination of tertiary alkyl alcohols with TMSCl under SFRC

In order to expand the utility of silanes mediated transformations of alcohols we studied reactions of trimethylbromosilane (TMSBr) with some benzyl and alkyl alcohols and the results are shown in Figure 5. Trimethylbromosilane readily converted under SFRC phenyl(*p*-tolyl)methanol (1) to 1-(bromo(phenyl)methyl)-4-methylbenzene (14a) and 4-fluoro benzyl alcohol (13b) to 4-fluoro benzyl bromide (14b), as well as α,α-dimethylbenzenepropanol (11a) to (3-bromo-3-methylbutyl)benzene (16).

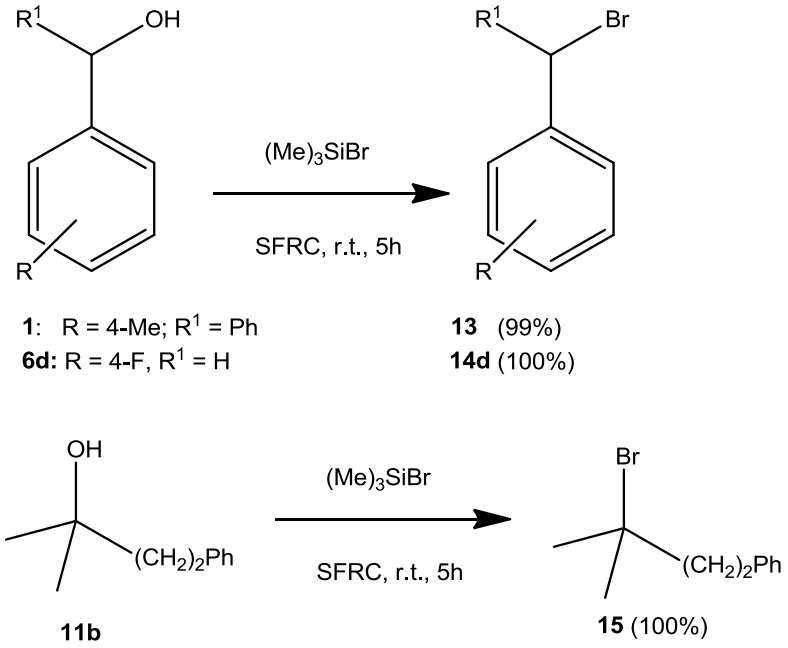


**Figure 5**: Bromination of benzyl and tertiary alkyl alcohols with TMSBr under SFRC

Based on transformations of alcohols with TMSCl and TMSBr we were curious to know if it is possible to introduce in the similar way various other functional groups, such as cyano or azido into organic molecules. We performed the reactions of phenyl(*p*-tolyl)methanol (1) as a model compound under the mentioned reaction conditions using cyanotrimethylsilane (TMSCN) or azidotrimethylsilane ($TMSN_3$) as the sources of cyano or azido functional group. The course of reactions were found to be different and the formation of trimethylsilyl ethers as the sole products were observed.

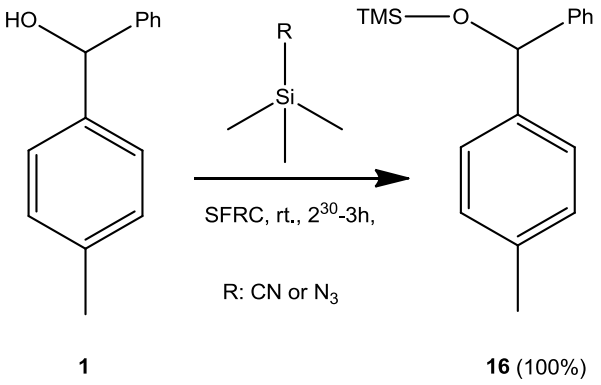


**Figure 6**: Trimethylsilylation of phenyl(p-tolyl)methanol with TMSCN or $TMSN_3$ under SFRC

## 3 Conclusions

We have demonstrated a novel and efficient method for direct conversion of benzylic and tertiary alkyl alcohols to corresponding chlorides or bromides by nucleophilic substitution of hydroxyl group using trimethylhalosilanes as sources of halogen moiety. Reactions performed under solvent-free reaction conditions gave high to quantitative yields of halogenated products, while under similar reaction conditions using cyanotrimethylsilane or azidotrimethylsilane resulted in the trimethylsilylation of the hydroxyl group in target molecules.

From the green chemical point of view newly developed methods represent a significant improvement of related known methodology.

## References:


[1] P. T. Anastas, J.C. Warner *Green Chemistry: theory and practice*, Oxford University Press, Oxford, 1998.

[2] H. A. Oskooie, M. M. Heravi, M. H. Tehrani, F. K. Behbahani, O. M. Heravi. *Phosphorus, Sulfur, and Silicon,* 184, 1729-1737, 2009

[3] J. G. Lee, K. K. Kang. *J. Org. Chem.* 53, 3634-3637, 1988

[4] M. Yasuda, S. Yamasaki, Y. Onishi, A. Baba. *J. Am. Chem. Soc.* 126, 7186-7187, 2004

[5] B. D. Kelly, T. H. Lambert. *J. Am. Chem. Soc.,* 131, 13930-13931, 2009

[6] M. Yasuda, K. Shimizu, S. Yamasaki, A. Baba. *Org. Biomol. Chem.* 6, 2790-2795, 2008

[7] G. A. Olah, B. G. B. Gupta, R. Malhotra, S. C. Narang. *J. Org. Chem.* 45, 1638-1639, 1980

## For wider interest

Aim of this work is to achieve direct conversion of alcohols to other functionalized derivatives using silanes under reaction conditions which follow as much as possible the principles of green chemistry We showed that various primary, secondary and tertiary benzyl alcohols and tertiary alkyl alcohols could be directly selectively and efficiently transformed to corresponding halides using trimethylhalosilanes (TMSCl or TMSBr) under solvent-free reaction conditions, while in the case with $TMSN_3$ and TMSCN under the same conditions silylation of hydroxyl group in target compounds took place..

These discoveries represent considerable contribution to the green chemical approach for transformation of alcohols into various valuable derivatives.

# Priprava porozne keramike svinčevega cirkonata titanata z uporabo polimetil metakrilata

**Tina Bakarič**[1,2], **Danjela Kuščer-Hrovatin**[1], **Barbara Malič**[1,2]

[1] Inštitut Jožef Stefan, Ljubljana, Slovenija

[2] Mednarodna podiplomska šola Jožefa Stefana, Ljubljana, Slovenia

tina.bakaric@ijs.si

**Povzetek**. V prispevku poročamo o pripravi porozne keramike s sestavo $Pb(Ti_{0,53}Zr_{0,47})O_3$ (PZT) s homogeno mikrostrukturo, ki bi bila uporabna kot podporni dušilec v ultrazvočnih pretvornikih. Keramiko smo pripravili iz mešanice PZT in polimetil metakrilata (PMMA), ki smo ga dodali kot tvorec por.

Delce PZT in PMMA smo razpršili v vodi pri pH 7, tako da so imeli na površini delci PZT pozitivni in delci PMMA negativni naboj. Po sušenju smo pridobili prah z enakomerno porazdelitvijo obeh faz. Prah smo stisnili v surovce, odstranili PMMA in vzorce sintrali pri temperaturi 1000 °C in 1050 °C. Mikrostrukturo keramike smo preučevali z vrstičnim elektronskim mikroskopom, količino poroznosti ter porazdelitev velikosti por pa smo določili z živosrebrovo porozimetrijo.

Keramika PZT je imela enakomerno razporejene pore okroglih oblik z velikostjo med 1 in 1,5 μm, kar je ustrezalo obliki in velikosti delcev PMMA. Poroznost je naraščala z večjo količino PMMA, zmanjševala se je z višjo temperaturo sintranja.

**Ključne besede**: svinčev cirkonat titanat, porozna keramika, metoda z uporabo tvorca por, hetero-koagulacija

## 1 Uvod

Ultrazvočni pretvorniki, ki jih v medicini uporabljajo za preiskovanje oči, kože ali žil, delujejo v frekvenčnem območju nekaj 10 MHz [1], [2]. Sestavni del vsakega pretvornika je piezoelektrik, ki ultrazvočno valovanje oddaja ali sprejema. Debelina

piezoelektrika v visoko-frekvenčnih ultrazvočnih pretvornikih je običajno nekaj 10 μm. Plast nanesemo na podlago z debeloplastno tehnologijo, običajno s sitotiskom [3], [4]. Plast nato sintramo pri temperaturi okoli 950 °C [4], [5]. Med sintranjem lahko pride do difuzije ionov iz plasti v podlago in obratno. Posledica so neželeni reakcijski produkti, ki lahko zmanjšajo učinkovitost piezoelektrične plasti [6], [7], [8]. Predlagana je bila rešitev, da je material, uporabljen za podlago enak piezoelektrični plasti [3]. Podlaga v ultrazvočnih pretvornikih lahko deluje kot dušilec ultrazvočnega valovanja (ang. backing), ki se širi v nasprotno smer od želene smeri širjenja ultrazvočnega valovanja [1], [9]. Kot dušilec pogosto uporabljajo različne polimerne materiale s kovinskimi delci [10] ali porozno keramiko [3], [9], [11]. Keramika na osnovi $Pb(Zr,Ti)O_3$ z enakomerno razporejenimi porami velikosti nekaj mikrometrov in debeline okoli 15 mm se je izkazala kot učinkovit material za dušilec [3], [11].

Porozno keramiko z enakomerno porazdeljenimi mikrometrskimi porami lahko pripravimo z različnimi metodami, kot so metoda direktnega penjenja, replika tehnika in metoda z uporabo tvorca por (ang. Sacrificial template method) [12], [13]. Slednja temelji na dodajanju tvorca por, naprimer: škrob, naftalen, polimetil metakrilat (PMMA), ki mora biti enakomerno porazdeljena med keramičnim prahom. Po odstranitvi tvorca por in sintranjem dobimo keramiko s porozno, homogeno mikrostrukturo [12], [14]. Učinkovita metoda za pripravo praha z enakomerno porazdelitvijo keramične in organske faze je hetero-koagulacija [15]. Metoda temelji na flokulaciji delcev z nasprotnim nabojem v topilu [15], [16]. Z uporabo te metode so pripravili keramiko $TiO_2$, $ZrO_2$ in $Al_2O_3$ s homogeno razporejenimi porami velikosti med 0,7 μm in 1 μm in poroznostjo okoli 70 % in kot tvorec por uporabili PMMA različnih velikosti [17], [18].

V prispevku poročamo o pripravi porozne keramike $Pb(Zr_{0,53}Ti_{0,47})O_3$ (PZT), ki bi bila primerna za izdelavo podpornega dušilca v visoko-frekvenčnih ultrazvočnih pretvornikih. Opisali bomo način priprave praha z enakomerno porazdeljenimi delci PZT in PMMA z metodo hetero-koagulacije in razložili vpliv količine dodanega PMMA ter temperature sintranja na velikost por in poroznost.

## 2 Metodologija

Prah $Pb(Zr_{0,53}Ti_{0,47})O_3$ (PZT) smo pripravili s sintezo v trdnem iz homogene mešanice oksidov PbO (99,9%; Sigma, Steinheim, Nemčija), $TiO_2$ (99,8%; Alfa, Karlsruhe, Nemčija) in $ZrO_2$ (99,9 %; Tosoh, Yamaguchi, Japonska). Mešanico oksidov smo dvakrat kalcinirali pri 1100 °C eno uro. Po drugi kalcinaciji smo prah mleli v planetarnem mlinu v izopropanolu 2 uri. Kot mlevna telesa smo uporabili z itrijem stabilizirane $ZrO_2$ (YSZ) kroglice premera 10 mm. Zatem smo prah mleli v atritorskem mlinu v izopropanolu 8 ur. Kot mlevna telesa smo uporabili kroglice YSZ premera 3 mm. Kot tvorec por smo uporabili prah PMMA (Soken Chemical & Engineering Co., Ltd, Japonska) z okroglimi delci enakomerne velikosti 1,5 μm. Delce PZT smo stabilizirali v vodi s polietileniminom (PEI) (Alfa Aesar, Karlsruhe, Nemčija) s povprečno molekulsko maso 10000. Količina PEI je podana kot masa PEI na gram prahu PZT (ut. %).

Vodno suspenzijo z vsebnostjo 10 vol. % PZT smo pripravili tako, da smo raztopili 0,5 ut. % PEI v vodi in nato dodali prah PZT. Suspenziji smo uravnali pH na 7 z 1 M $HNO_3$ in mešali z magnetnim mešalom 1 h. Nato smo suspenzijo homogenizirali v planetarnem mlinu pri 150 obratih/min eno uro. Vzporedno smo pripravili vodno suspenzijo PMMA z vsebnostjo delcev 10 vol. % tako, da smo v vodo dodali PMMA in uravnali pH na 7 z 1 mM $HNO_3$. Suspenzijo smo mešali z magnetnim mešalom 1 h ter jo nato postavili v ultrazvočno kopel za 15 min. Suspenziji PZT in PMMA smo nato zmešali skupaj, tako da je bilo volumensko razmerje PZT:PMMA 80:20 in 70:30. Suspenziji PZT:PMMA smo homogenizirali v planetarnem mlinu pri 150 obratih/min eno uro. Zatem smo suspenziji posušili pri 105 °C in tako pridobili prah PZT:PMMA.

Porozno keramiko PZT smo pripravili tako, da smo prahova PZT:PMMA stisnili v jeklenem modelu s premerom 8 mm enoosno s pritiskom 50 MPa in nato še izostatsko s pritiskom 300 MPa. Surovce smo predsintrali pri 400 °C 2 h ter jih nato žgali v komorni peči pri temperaturi 1000 °C in 1050 °C 2 h v lastnem zasipu. Za primerjavo smo sintrali tudi tablete, stisnjene iz prahu PZT brez dodatka PMMA. Vzorci bodo označeni kot referenčna keramika.

Zeta potencial (ζ) delcev PZT in PMMA smo merili v 1 mM $KNO_3$ v pH območju 2-12 z zeta metrom ZetaPALS (Brookhaven Instruments Corporation, ZDA). pH

smo uravnavali z raztopinama $HNO_3$ ali NaOH. Velikost in porazdelitev delcev smo merili v vodi z laserskim granulometrom Microtrac S3500 (Montgomeryville, PA, ZDA). Rezultate podajamo kot velikost delcev po volumnu ($d_v$). Prah PZT in PMMA ter mikrostrukturo porozne keramike PZT smo preiskali z vrstičnim elektronskim mikroskopom SEM JSM-5800 (JEOL, Tokio, Japonska). Poroznost keramike PZT smo določili s kvantitativno karakterizacijo mikrostruktur. Vsebnost por smo določili tako, da smo SEM posnetke pretvorili v binarne z uporabo programske opreme s slikovno analizo (ImageTools 3.0, Univerza v Texasu Health Science Center, ZDA). Iz binarnih posnetkov smo določili črne in bele slikovne pike, ki so predstavljali pore in gost material. Količino poroznosti smo nato izračunali iz razmerja med črnimi slikovnimi pikami in vsemi slikovnimi pikami. Količino poroznosti in porazdelitev velikost por v keramiki PZT, pridobljeni iz prahu PZT:PMMA smo izmerili z živosrebrovim porozimetrom (PASCAL 140 in 440 Series, Thermo SCIENTIFIC, ZDA).

# 3 Rezultati

Na sliki 1 je prikazan mikroskopski posnetek ter porazdelitev velikosti delcev prahu PZT po sintezi in mletju v atritorskem mlinu. Prah ima široko porazdelitev delcev s srednjo velikostjo 0,6 μm in največjimi delci ($d_{v100}$) 4,6 μm. Velikost delcev se ujema z velikostjo delcev na mikroskopskem posnetku.

Na sliki 2 je prikazan mikroskopski posnetek ter porazdelitev velikosti delcev prahu PMMA. Iz mikroskopskega posnetka je razvidno, da so vsi delci PMMA okrogle oblike in enakih velikosti. Porazdelitev delcev je ozka s srednjo velikostjo 1,5 μm, kar se ujema z mikroskopskim posnetkom.

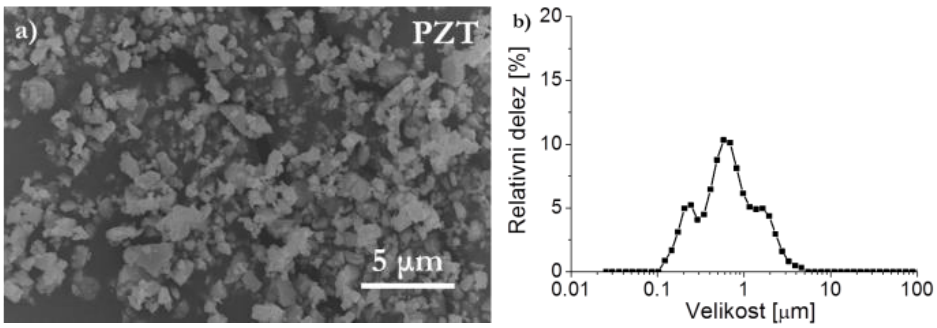


**Slika 1:** Prah PZT po sintezi pri 1100 °C in mletju v atritorskem mlinu. a) SEM posnetek. b) Porazdelitev velikosti delcev.

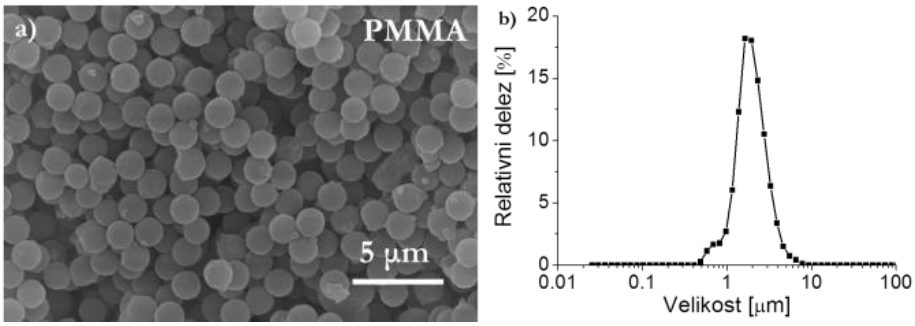


**Slika 2:** Prah PMMA. a) SEM posnetek. b) Porazdelitev velikosti delcev.

Prah PZT smo v vodi stabilizirali s PEI pri pH 7. Zeta potencial delcev je znašal +50(5) mV. Delce PMMA smo dispergirali v vodi pri pH 7, njihov zeta potencial je znašal -90(5) mV. Pri pH 7 so bili delci PZT pozitivno in delci PMMA negativno nabiti. Po mešanju obeh suspenzij se delci niso posedali., suspenzija je bila stabilna. Zaradi nasprotnega naboja na delcih PZT in PMMA je prišlo do hetero-koagulacije, kar je razvidno iz slike 3. Na sliki 3 je prikazan mikroskopski posnetek prahu z volumenskim razmerjem PZT:PMMA 70:30. Svetlejši delci velikosti okoli 1 μm so delci PZT, med katerimi so enakomerno razporejeni delci PMMA temnejše barve velikosti okoli 1,5 μm.

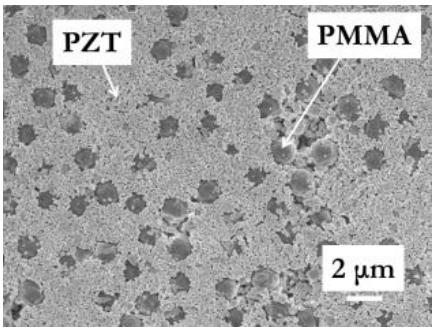


**Slika 3:** SEM posnetek prahu PZT:PMMA z volumenskim razmerjem 70:30 po sušenju na 105 °C.

Mikrostrukture referenčne keramike in keramike, pripravljene iz prahu PZT:PMMA z volumenskim razmerjem 80:20 in 70:30 sintrane pri 1000 °C so prikazane na sliki 4, sintrane pri 1050 °C pa na sliki 5.

Iz mikrostruktur keramike vidimo, da so pore homogeno razporejene in imajo okroglo obliko ne glede na temperaturo sintranja ali količino PMMA. Pore so velike med 1 in 1,5 μm in ustrezajo tako velikosti kot obliki PMMA. Opazimo tudi manjše pore nepravilnih oblik, ki jih pripisujemo zgoščevanju keramične matrice PZT [5].

Podobne pore smo opazili v referenčni keramiki. Por je sicer v referenčni keramiki manj in so nepravilnih oblik.

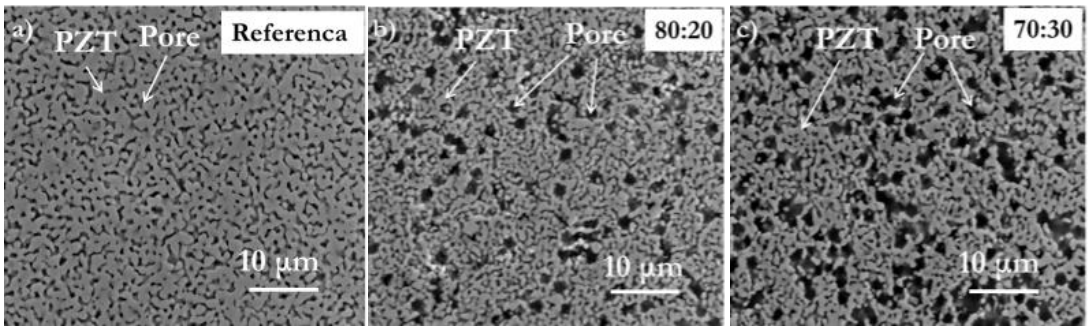


**Slika 4:** Mikrostruktura porozne keramike sintrane pri 1000 °C. a) Referenčna keramika. b) Keramika pripravljena iz prahu PZT:PMMA z volumenskim razmerjem 80:20. c) Keramika pripravljena iz prahu PZT:PMMA z volumenskim razmerjem 70:30.

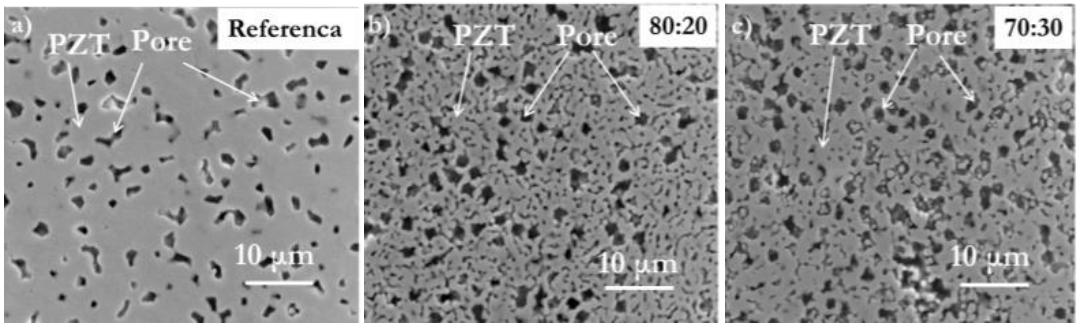


**Slika 5:** Mikrostruktura porozne keramike sintrane pri 1050 °C. a) Referenčna keramika. b) Keramika pripravljena iz prahu PZT:PMMA z volumenskim razmerjem 80:20. c) Keramika pripravljena iz prahu PZT:PMMA z volumenskim razmerjem 70:30.

Poroznosti keramike PZT, pridobljene iz volumskega razmerja PZT:PMMA 80:20 in 70:30, določene iz SEM posnetkov in izmerjene z živosrebrovo porozimetrijo so bile primerljive. Pri temperaturi 1000 °C znaša poroznost referenčne keramike 25(2) %, medtem ko znaša poroznost keramike PZT, pridobljene iz prahu PZT:PMMA z volumenskim razmerjem 80:20 in 70:30, 39(3) % in 48(3) %. Pri temperaturi 1050 °C se poroznost referenčne keramike zniža na 8(1) %, poroznost keramike PZT, pridobljene iz prahu PZT:PMMA z volumenskim razmerjem 80:20 in 70:30, se zniža na 25(3) % in 29(3) %. Iz dobljenih rezultatov vidimo, da se količina poroznosti v keramiki viša z dodajanjem delcev PMMA in je nižja pri višji temperaturi sintranja. Zato sklepamo, da je PMMA učinkovit tvorec por.

Na sliki 6 je prikazana velikost in porazdelitev velikosti por v keramiki pridobljeni iz prahu PZT:PMMA z volumenskim razmerjem 80:20 in 70:30. Predpostavimo lahko, da količina dodanega PMMA manj vpliva na velikost in porazdelitev por kot temperatura sintranja. Porazdelitev velikosti por v keramiki, sintrani pri 1000 °C, je bimodalna ne glede na volumensko razmerje PZT:PMMA z velikostmi por med 0,2 in 1,5 μm. Z zvišanjem temperature sintranja na 1050 °C se porazdelitev velikosti por zoži, velikost por znaša okoli 1 μm.

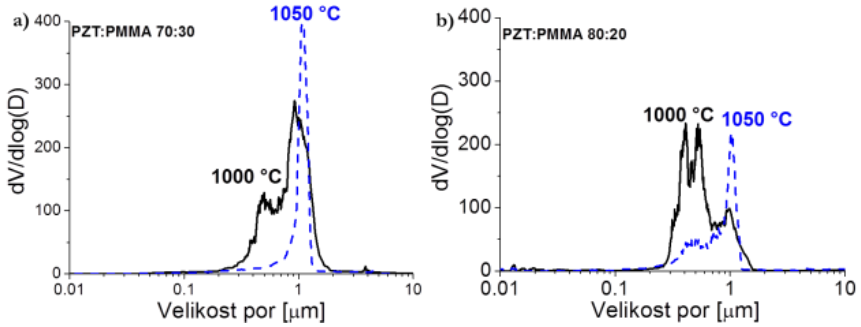


**Slika 6:** Porazdelitev velikosti por v porozni keramiki PZT pri temperaturi sintranja 1000 °C in 1050 °C. a) Keramika pridobljena iz prahu PZT:PMMA 70:30. b) Keramika pridobljena iz prahu PZT:PMMA 80:20.

## 4 Zaključki

Porozno keramiko PZT s kontrolirano velikostjo por in poroznostjo smo pripravili z dodatkom tvorca por PMMA. PZT in PMMA smo v vodi dispergirali tako, da so imeli delci nasprotni naboj na površini. Zaradi česar sta bili obe fazi po sušenju enakomerno razporejeni v prahu. Iz mešanice prahu smo nato s sintranjem pripravili keramiko z enakomerno razporejenimi porami v matrici PZT.

Velikost in oblika por v keramiki PZT je odgovarjala velikosti in obliki delcev PMMA. Prisotne so bile tudi manjše pore, ki so bile posledica zgoščevanja keramične matrice. Ugotovili smo, da na količino poroznosti vplivamo s količino PMMA in temperaturo sintranja. Z večjo količino PMMA se količina poroznosti zvišuje, z višanjem temperature sintranja pa zmanjšuje.

## Zahvala

Javni agenciji za raziskovalno dejavnost Republike Slovenije se zahvaljujemo za finančno pomoč (P2-0105 in PR-04362). Soken Chemical & Engineering Co. se zahvaljujemo za brezplačno dobavo PMMA.

## Literatura:

[1] M. Lethiecq, F. Levassort, D. Certon, in L. P. Tran-Huu-Hue. Piezoelectric Transducer Design for Medical Diagnosis and NDE. V *Piezoelectric and Acoustic Materials for Transducer Applications*, A. Safari and E. K. Akdoğan. Springer, 2008.

[2] S. K.Kirk. *Diagnostic ultrasound: imaging and blood flow measurements*, 1 izd. Taylor & Francis Group, 2006.

[3] F. Levassort, J. Holc, E. Ringgaard, T. Bove, M. Kosec, and M. Lethiecq. Fabrication, modelling and use of porous ceramics for ultrasonic transducer applications. *Journal of Electroceramics*, 19(1): 127–139, 2007.

[4] M. Kosec, D. Kuscer, and J. Holc. Processing of ferroelectric ceramic thick films. V *Multifunctional polycrystalline ferroelectric materials: processing and properties*, L. Pardo and J. Ricote. Springer, 2011.

[5] W. D. Kingery, H. K. Bowen, and D. R. Uhlman. *Introduction to Ceramics*, 2 izd. John Wiley & Sons, 1976.

[6] D. A. Northrop. Vaporization of Lead Zirconate-Lead Titanate Materials. *Journal of the American Ceramic Society*, 50(9), 1967.

[7] J. Holc, M. Hrovat, and M. Kosec. Interactions Between Alumina and PLZT Thick Films. *Materials Research Bulletin,* 34(14/15), 1999.

[8] Y. B. Lee, I. C. Cheon, S. J. Kim, S. K. Bang, C. J. Kim, and G. H. Lee. Low temperature firing of PZT thick films prepared by screen printing method. *Materials Letters*, 56(4), 2002.

[9] N. Ichinose, N. Miyamoto, and S. Takahashi. Ultrasonic transducers with functionally graded piezoelectric ceramics. *Journal of the European Ceramic Society*, 24(6), 2004.

[10] C. M. Sayers and C. E. Tait. Ultrasonic properties of transducer backings. *Ultrasonics*, 22(2), 1984.

[11] P. Marechal, F. Levassort, J. Holc, D. Kuscer, M. Kosec, G. Feuillard, and M. Lethiecq. Electromechanical Properties of Piezoelectric Integrated Structures on Porous Substrates. *Ferroelectrics*, 371(1), 2008.

[12] A. R. Studart, U. T. Gonzenbach, E. Tervoort, and L. J. Gauckler. Processing Routes to Macroporous Ceramics: A Review. *Journal of the American Ceramic Society*, 89(6), 2006.

[13] M. Scheffler and P. Colombo. *Cellular Ceramics*. Wiley-VCH Verlag GmbH & Co. KGaA, 2005.

[14] C. Galassi. Processing of porous ceramics: Piezoelectric materials. *Journal of the European Ceramic Society*, 26(14), 2006.

[15] E. Geuzens, G. Vanhoyland, J. D'Haen, S. Mullens, J. Luyten, M. K. Van Bael, H. Van den Rul, and J. Mullens. Synthesis of zirconia–alumina and alumina–zirconia core–shell particles via a heterocoagulation mechanism. *Journal of the European Ceramic Society*, 26(15), 2006.

[16] F. Tang, H. Fudouzi, T. Uchikoshi, and Y. Sakka. Preparation of porous materials with controlled pore size and porosity. *Journal of the European Ceramic Society*, 24(2), 2004.

[17] F. Tang, H. Fudouzi, and Y. Sakka. Fabrication of macroporous alumina with tailored porosity. *Journal of the American Ceramic Society*, 86(12), 2003.

[18] Y. Sakka, F. Tang, H. Fudouzi, and T. Uchikoshi. Fabrication of porous ceramics with controlled pore size by colloidal processing. *Science and Technology of Advanced Materials*, 6(8), 2005.

## Za širši interes

Porozno keramiko lahko uporabljamo v visokotemperaturnih izolatorjih, kostnih vsadkih, ultrazvočnih pretvornikih, itd. Namen naših raziskav je pripraviti porozno keramiko na osnovi svinčevega cirkonata titanata (PZT), ki bi bila primerna kot podlaga v ultrazvočnih pretvornikih.

Ultrazvok je zvočno valovanje z višjo frekvenco, kot je slušno območje pri človeku (nad 20 kHz). V medicini ultrazvok s frekvenčnim območjem med 2-10 MHz uporabljajo za pregledovanje mehkih tkiv ali ploda med nosečnostjo. Za pregledovanje površine kože, človeškega očesa ali žil je potrebno uporabiti ultrazvok, ki deluje pri frekvencah višjih od 20 MHz.

Naprava, ki ultrazvočne valove proizvaja, je ultrazvočni pretvornik. Glavni del takega pretvornika je piezoelektrični material, ki ultrazvočne valove oddaja in jih nato tudi sprejema, ko se ti odbijejo od preiskovanega vira. Ker se ultrazvok širi tudi v nasprotni smeri od želene, je potrebno te neželene valove zadušiti. Zato v pretvornikih uporabljajo podporne dušilce. Za dušilce uporabljajo različne materiale, kot so polimeri ali porozna keramika.

Pore v porozni keramiki dušijo ultrazvočno valovanje, zato je cilj našega raziskovanja pripraviti porozno keramiko, ki bi bila učinkovit dušilec v visoko-frekvenčnih ultrazvočnih pretvornikih. Da je dušenje učinkovito, morajo biti pore enakomerno razporejene v keramiki in morajo biti enakih oblik in velikosti. Zato je namen našega dela poiskati metodo, s katero lahko kontroliramo tako količino poroznosti, kot tudi velikost, obliko in porazdelitev por.

Porozno keramiko smo pripravili tako, da smo keramičnemu prahu PZT dodali organski material polimetil metakrilat (PMMA). Delce PMMA smo enakomerno razporedili med PZT delce z metodo hetero-koagulacije v vodi. Metoda temelji na flokulaciji delcev z nasprotnim nabojem v topilu. Za uspešen potek tega procesa je bilo zato potrebno urediti pozitivni naboj na površini delcev PZT in negativni naboj na površini delcev PMMA, da so se delci med seboj privlačili in sprijeli skupaj. Na ta način smo po sušenju pridobili prašno mešanico z enakomerno razporejenima fazama. Zatem smo prah oblikovali in odstranili PMMA delce, pri čemer so se tvorile pore v matrici PZT. Nato smo matrico žgali pri visokih temperaturah in tako pridobili porozno keramiko z enakomerno razporejenimi porami. Velikost in obliko por smo nadzorovali z velikostjo in obliko PMMA. Količino poroznosti smo uravnavali s količino PMMA in temperaturo žganja. Pripravili smo porozna keramiko, ki je primerna za uporabo podpornega dušilca v visoko-frekvenčnih ultrazvočnih pretvornikih.

# Synthesis of composite nanoparticles using coating of the core nanoparticles with cobalt ferrite layers

**Blaž Belec**[1,2]**, Darko Makovec**[1,2]

[1] Department for Material Synthesis, Jožef Stefan Institute, Ljubljana, Slovenia

[2] Jožef Stefan International Postgraduate School, Ljubljana, Slovenia

blaz.belec@ijs.si

**Abstract.** The synthesis of the composite nanoparticles, combining magnetic spinel cobalt ferrite ($CoFe_2O_4$) shell with different core nanoparticles was studied. In our research, the silica ($SiO_2$) nanoparticles were used as the cores to study the synthesis of cobalt-ferrite shell. The synthesis method was based on the known synthesis procedure for coating magnetic spinel iron oxide (maghemite - $\gamma$-$Fe_2O_3$) with heterogeneous nucleation at the core nanoparticles in an aqueous suspension. The problem of cobalt ferrite synthesis is in large difference of pH values where $Fe^{3+}/Co^{2+}$ ions precipitate. The cobalt-ferrite shell was formed with co-precipitation and heterogeneous nucleation of the solid product onto the core nanoparticles. The co-precipitation of the $Fe^{3+}/Co^{2+}$ ions was provoked by addition of solid hydroxide; a mixture of $Mg(OH)_2$ and CaO pressed into a tablet. The stoichiometric and nonstoichiometric Co/Fe atomic ratio was used. Although the pH value for cobalt precipitation was reached, the stoichiometric composition of cobalt-ferrite shell was not obtained, even the excess amount of Co was introduced into the starting suspension.

**Keywords**: composite nanoparticles, co-precipitation, heterogeneous nucleation, spinel, ferrites

## 1 Introduction

Composite nanoparticles are particles where at least one of their dimensions is in nanometre range and they consist of at least two different materials. Compared with the single-component nanoparticles, composite nanoparticles have large potential to

exhibit novel physical and chemical properties. Changes in particle properties can be observed when the particle size is less than a particular level, called the critical size. Additionally, novel properties of composite nanoparticles often arise from interaction of its phases at the interfaces. As dimensions reach the nanometre level, interactions at phase interfaces become largely improved and this is important to enhance material properties [1, 2].

The synthesis of composite nanoparticles is complex problem and in recent years considerable effort has been devoted to prepare such materials. One of the possible approaches to prepare the composite nanoparticles is to coat the core nanoparticle with a thin shell, thus producing core/shell structure (CSn). In our work, we investigated the synthesis of such composite nanoparticles with coting the thin shell of magnetic spinel cobalt ferrite onto core nanoparticles of different functional materials with the synthesis method that was proposed by Primc in her thesis [3]. She proposed an alternative approach to synthesize composite nanoparticles with coating soft magnetic spinel iron oxide - maghemite ($\gamma$-$Fe_2O_3$) onto different core nanoparticles ($SiO_2$ and $BaFe_{12}O_{19}$). The thin maghemite shell was formed with co-precipitation of $Fe^{3+}/Fe^{2+}$ ions and heterogeneous nucleation and growth of the solid phase at the cores. To enable exclusively heterogeneous nucleation leading to formation of the shell the supersaturation of the precipitating species has to be closely controlled and, above all, homogeneous throughout the whole reaction mixture. The low and heterogeneous supersaturation needed for heterogeneous nucleation was enabled by controlled release of the reactants during the precipitation of the Fe ions in the suspension of the core nanoparticles. The controlled release was enabled by thermal decomposition of a $Fe^{3+}$-urea complex ($[Fe((CO(NH_2)_2)_6)](NO_3)_3]$), while the homogeneous release of the $OH^-$ ions was enabled by use of solid $Mg(OH)_2$ as the precipitating agent. The reactants: $Fe^{3+}$-urea complex, $Fe^{2+}$ ions and $Mg(OH)_2$ were admixed into the colloidally-stable suspension of the core nanoparticles. At increased temperature the $Fe^{3+}$-urea complex slowly decomposes, the solubility of $Mg(OH)_2$ increases and the reactants, $Fe^{3+}$ and $OH^-$ ions are slowly released into the reaction mixture. After 10 minutes of thermal hydrolysis at an elevated temperature, oxo-hydroxide ϒ-FeOOH nucleates exclusively at the core nanoparticles. The oxo-hydroxide phase at the core nanoparticles transform to magnetic spinel during precipitation of $Fe^{2+}$ ions at higher pH values.

We choose cobalt ferrite because it exhibits different magnetic properties than maghemite. Cobalt ferrite is among all spinel ferrites the only one hard magnetic and has the highest magnetostriction from all oxide materials [4]. Because of his high magnetostriction it can be used in multiferroic, magnetoeletric composite materials. Multiferroic materials possess at least two of the ferroic properties (ferroeletricity, ferromagnetism and/or ferroelasticity). In such materials, the coupling between the different order parameters could produce new effects, for example magnetoeletric (ME) effect. ME effect in composite materials is known as a tensor property, that results from the interaction between the two phases in the composite. It is result of the product of the magnetostrictive effect (magnetic/mechanical effect) in the magnetic phase and the piezoeletric effect (mechanical/eletrical effect) in the piezoeletric phase [5].

The formation of the magnetic shell is the key step in synthesis of CS composite nanoparticles, combining magnetic shell with different functional cores. In our research, the silica nanoparticles were used as the cores to study the synthesis of the cobalt-ferrite shell. The goal of the first part of our research was to repeat the results from the previous research [3] of heterogeneous nucleation of maghemite on to the silica core nanoparticles. In the second part, the synthesis of cobalt ferrite shell onto the silica core nanoparticles with modified method as was proposed for deposition of the maghemite layer was investigated. The problem of cobalt ferrite synthesis arises from the large difference in pH values where $Fe^{3+}$ and $Co^{2+}$ ions precipitates, which is much larger than in the case of $Fe^{3+}$ and $Fe^{2+}$.

# 2 Experimental

## 2.1. Preparation of core nanoparticles

Suspension of silica core nanoparticles was prepared with dispersing the $SiO_2$ powder into 50 mL of deionized water in such amount that the overall surface of core nanoparticles is $5.45 \times 10^{18}$. This surface is determined in the previous research and it was estimated in a way, that the determined concentration of Fe precursor would form a 3 nm thick spinel shell [3].

## 2.2. Synthesis of ferrite shell

Composite nanoparticles with heterogeneous nucleated spinel ferrite shell were synthesized with co-precipitation of $Fe^{3+}/Fe^{2+}$ or $Fe^{3+}/Co^{2+}$ ions with the method that is reported in Ref. [3]. $Fe^{3+}$-urea complex with composition $[Fe((CO(NH_2)_2)_6)](NO_3)_3]$ was prepared as is described by Ashua et al. [6] and used as source of $Fe^{3+}$ ions.

For synthesis of thin layer of maghemite on to the silica core nanoparticles ($Fe@SiO_2$), firstly the suspension of core nanoparticles (d= 25 nm, n= 0.08 mmol, V= 50 mL) is heated under argon flow at 60 °C. At the temperature the $Fe^{3+}$-urea complex (0.12 mmol) and iron (II) chloride ($FeCl_2$, Alpha Aesar, 99.5%) (0.06 mmol) is added. After 10 minutes of thermal hydrolysis at 60 °C we added magnesium hydroxide ($Mg(OH)_2$, Alpha Aesar, 95%) (0.24 mmol). The reaction mixture is left with steering at the final temperature for another 2 hours. In the case of the cobalt ferrite layer onto the core nanoparticles, synthesis procedure was similar as in the $Fe@SiO_2$ case, except use of cobalt nitrate ($Co(NO_3)_2$, Alpha Aesar, 98%) (0.06 or 0.12 mmol), instead of iron (II) nitrate. Because the concentration of $OH^-$ ions needed for precipitation of $Co^{2+}$ (pH=8) could not be reached using $Mg(OH)_2$, we used the mixture of $Mg(OH)_2$ (0.24 mmol) and CaO (0.16 mmol or 0.24 mmol), pressed into tablets. For the synthesis of the cobalt ferrite shell the stoichiometric Co/Fe atomic ratio of 0.5 ($CoFe@SiO_2$-Mg24C16) and the nonstoichiometric Co/Fe atomic ratio of 1 ($CoFe@SiO_2$-Mg24C24) was used.

## 2.1. Characterisation of the materials

Core nanoparticles and spinel ferrite shell were characterized by conventional transmission electron microscope TEM JEOL 2100 coupled with energy dispersive X-ray spectroscopy (EDXD). For the TEM investigation the nanoparticles were deposited on a copper-grid-supported transparent carbon foil. Quantitative analyses of cobalt ferrite shell were performed using EDS microanalysis system (LINK ISIS EDS 300) and Oxford ISIS software. For quantification of the cobalt ferrite shell spectra the $CoFe_2O_4$ ceramic was used as a standard ($Co/Fe_{standard} = 0.502 \pm 0.003$).

The ξ-potential of the silica core nanoparticles in their aqueous suspension was measured using Brookhaven Instrument Corp. ZetaPALS.

# 3 Results and discussion

## 3.1. Core nanoparticles

Aqueous suspension of silica core nanoparticles was examined with TEM and ξ-potential measurements. Figure 1a presents TEM image of the amorphous $SiO_2$ core nanoparticles. From the image it is evident, that the sample consists of agglomerated particles with average size of 25 nm. From the ξ-potential measurements (Figure 1b) it was determined that silica core nanoparticles in the aqueous suspension exhibited a large negative ξ-potential at pH values above ~ 3. This enables their colloidal stability over large pH region. The silica nanoparticles were chosen as the core nanoparticles, because they are amorphous and making the characterization of the crystalline product on their surface easier.

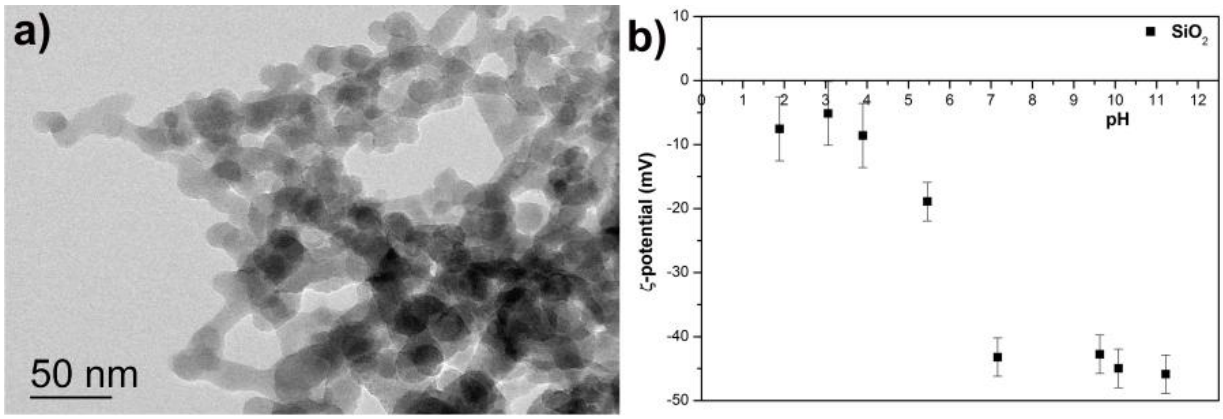


**Figure 1:** TEM image of silica core nanoparticles (a) and ξ -potential measurements of silica core nanoparticles in their aqueous suspension.

## 3.2. Core nanoparticles

For the synthesis of the spinel ferrite shell, which is heterogeneously nucleated at the core nanoparticles, low supersaturation is required. To keep the supersaturation low enough to avoid the homogeneous nucleation, the concentration of the reactants should be low and their release must be controlled. In our case, the controlled release of the $Fe^{3+}$ ions can be achieved with thermal decomposition of the $Fe^{3+}$-urea complex. Apart from the control of the $Fe^{3+}$ release from the complex, the release of the hydroxyl ions can also be controlled to improve the homogeneity of the reaction mixture and to maintain the desired level of the supersaturation [3, 7].

Synthesis of the composite nanoparticles with maghemite shell on the silica core nanoparticles was repetition of results from Primc research [3]. $Fe^{3+}/Fe^{2+}$ ions were dissolved into aqueous suspension of core nanoparticles heated at 60 °C under argon flow. After the suspension remained at the initial pH value of 2.2 for 10 minutes the $Mg(OH)_2$ was added. The addition of $Mg(OH)_2$ resulted in increase of pH during the reaction (Figure 2a). After approximately 17 minutes, the pH value needed for precipitation of the $Fe^{2+}$ ions was reached (pH=6.2), while in another 90 minutes pH increased to the maximum value of 6.9. Reaction mixture was maintained at final pH for another 30 minutes that overall reaction time was 2 hours.

Figure 2b represents the $Fe@SiO_2$ composite nanoparticles. The TEM image shows $SiO_2$ core nanoparticles with average size of 25 nm that are homogeneously covered with small spherical nanoparticles with average size of approximately 5 nm. Detailed TEM analysis revealed that spherical nanoparticles are nucleated exclusively on the core nanoparticles while the larger homogeneous nanoparticles of maghemite were never observed. This result showed the repeatability of the procedure invented by Primc [3].

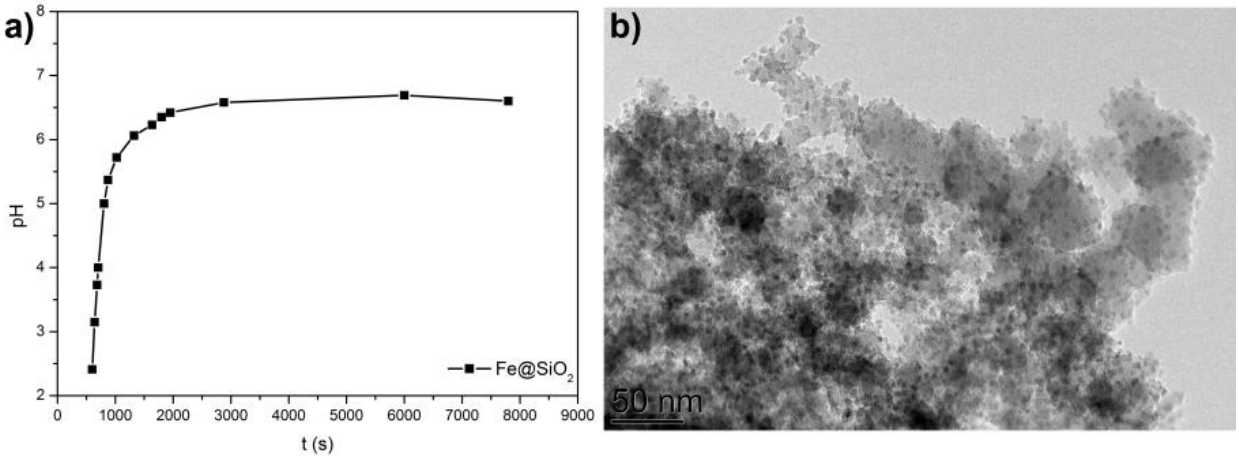


**Figure 2:** pH vs. time curve (a) and TEM image of the $Fe@SiO_2$ sample (b)

The cobalt-ferrite shell was coated onto the silica core nanoparticles using similar procedure as in the case of the maghemite shell. The $Fe^{3+}/Co^{2+}$ ions were added into the aqueous suspension of the core nanoparticles, heated at 60 °C under argon flow. After the suspension remained at initial pH of 2.3 for 10 minutes, the $Mg(OH)_2$ was added to increase pH (Figure 3a). After approximately 60 minutes, pH value raised to the maximum pH of 7.35. Afterwards the pH value increased another

60 minutes. For the precipitation of $Co^{2+}$ ions, pH = 8 must be reached [8]. As is seen from the figure 3a, with $Mg(OH)_2$ we could not reach pH value needed for precipitation of the cobalt ions, so we consider to use stronger base.

Figure 3b presents TEM image of the CoFe@$SiO_2$-M composite nanoparticles. The image shows silica core nanoparticles with small spherical nanoparticles on their surface. Although the pH value was not high enough for precipitation of all $Co^{2+}$ ions and forming the stoichiometric cobalt ferrite, small nanoparticles are nucleated on the surface of the core nanoparticles while homogeneous nucleated nanoparticles were not observed. However, EDXS analysis showed no cobalt present in the precipitated nanoparticles at the cores. As the material was slightly magnetic, the product is most probably of maghemite.

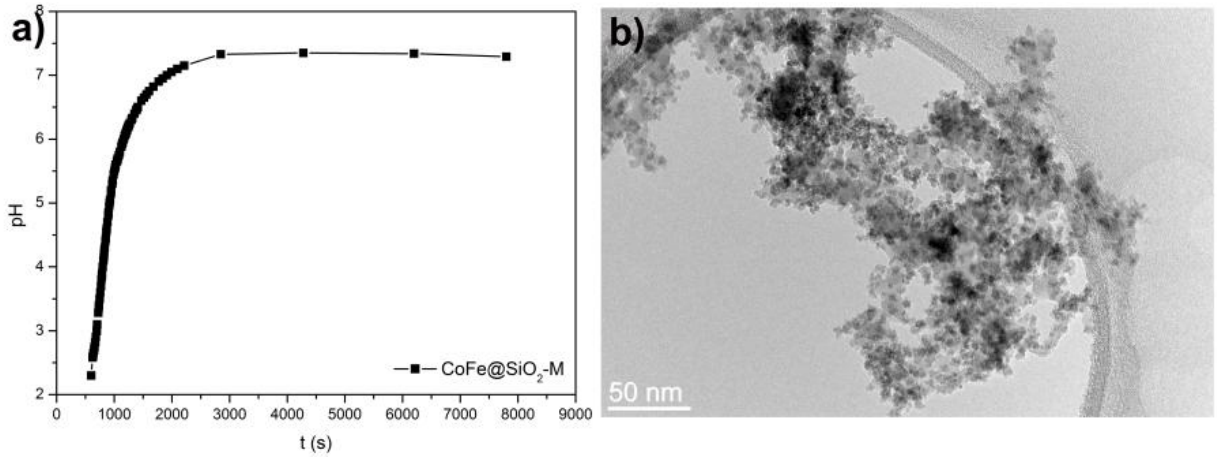


**Figure 3:** pH vs. time curve (a) and TEM image of the CoFe@$SiO_2$-M sample

According to the results in previous research, hydroxide ions must release slowly so that low saturation is achieved enabling heterogeneous nucleation. At the same time they must release fast enough, that oxo-hydroxide phase ϒ-FeOOH does not transform into α-FeOOH. For the formation of spinel ferrite layer onto the core nanoparticles, Primc find out that $M^{2+}$ ions must precipitate approximately 15 minutes after addition of hydroxide [3].

Because we could not reach the pH value where the $Co^{2+}$ ions precipitates with proposed hydroxide, we consider using stronger solid base, that also have low solubility. We used the mixture of $Mg(OH)_2$ and CaO pressed into tablets. With pressing the mixture into tablet we decrease surface to volume ratio and make the hydroxide ions release slower. The increase of the pH after addition of the $Mg(OH)_2$ /CaO tablet was followed in the separate experiments. The $Mg(OH)_2$ /CaO tablet

was added to the solution of the $Fe^{3+}/Co^{2+}$ ions after heating for 10 minutes at 60 °C. Figure 4 shows changing of the pH value with the time for different $Mg(OH)_2$ /CaO ratios. The addition of the mixture of $Mg(OH)_2$ (n=0.24) and CaO (n=0.12) (sample CoFe-M24C12) resulted in increase of the pH to the maximum value of 7.77, which is still below pH=8 required for the precipitation of the $Co^{2+}$ ions. When the mixture was consisted of $Mg(OH)_2$ (n=0.24 mmol) and CaO (n=0.16 – 0.24 mmol), the pH of 8 was reached in approximately 15 minutes. Moreover, maximum pH value was always above pH=9. As it is mentioned before, the hydroxide ions must release homogeneously with the time to maintain the conditions needed for the heterogeneous nucleation. According to this, for further research of the heterogeneous nucleation of cobalt ferrite layer onto the core nanoparticles we choose mixture of $Mg(OH)_2$ (n=0.24 mmol) and CaO (n=0.16 mm)(sample CoFe-M24C16) where pH=8 was reached 12 minutes after the tablet addition and the maximum pH value was 9.10. The pH value is first increased slowly to pH=4 and then the increase was faster to pH=7 when it becomes slower again.

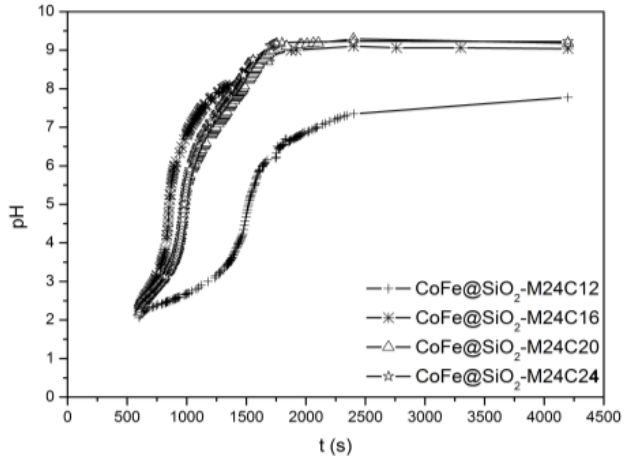


**Figure 4:** pH vs. time curve for different different $Mg(OH)_2$ /CaO ratios

The procedure of coating the cobalt-ferrite shell onto the core nanoparticles using the mixture of $Mg(OH)_2$ and CaO (CoFe@$SiO_2$-M24C16) was similar than in the previous case (CoFe@$SiO_2$-M). The $Fe^{3+}$and $Co^{2+}$ ions were added into the suspension of the core nanoparticles and heated at 60 °C under argon flow. After 10 minutes of thermal hydrolysis at initial pH, the tablet consisting mixture of $Mg(OH)_2$ (n=0.24 mmol) and CaO (n=0.16 mmol) was added to increase the pH (Figure 5a). After approximately 19 minutes pH of 8 needed for precipitation of the $Co^{2+}$ ions was reached. With time, the pH increased to the maximum value of 8.48 in another

10 minutes whereas in another 90 minutes it decreased to pH of 8.25. Figure 5b and c presents TEM images of the CoFe@$SiO_2$-m24C16 composite nanoparticles. The images show spherical amorphous core nanoparticles covered with small crystalline nanoparticles and some larger, sheet-like product nanoparticles, which were not attached to the cores (Figure 5b). The crystalline nanoparticles with size of 3 - 5 nm are heterogeneous distributed at the cores surfaces (Figure 5c). EDXS analysis of the shell on the surface of the core nanoparticle revealed, that shell contains only ≈ 4 at.% of cobalt instead of 14 at.% required by the stoichiometry of $CoFe_2O_4$. Even though the pH value needed for precipitation of $Co^{2+}$ ions was reached, the stoichiometric cobalt ferrite was not formed. EDXS analysis of sheet-like structures revealed, that they contain iron and cobalt in ratio Fe/Co ≈ 1. We assume that this phase is ferroxide (Co(Fe)COOH).

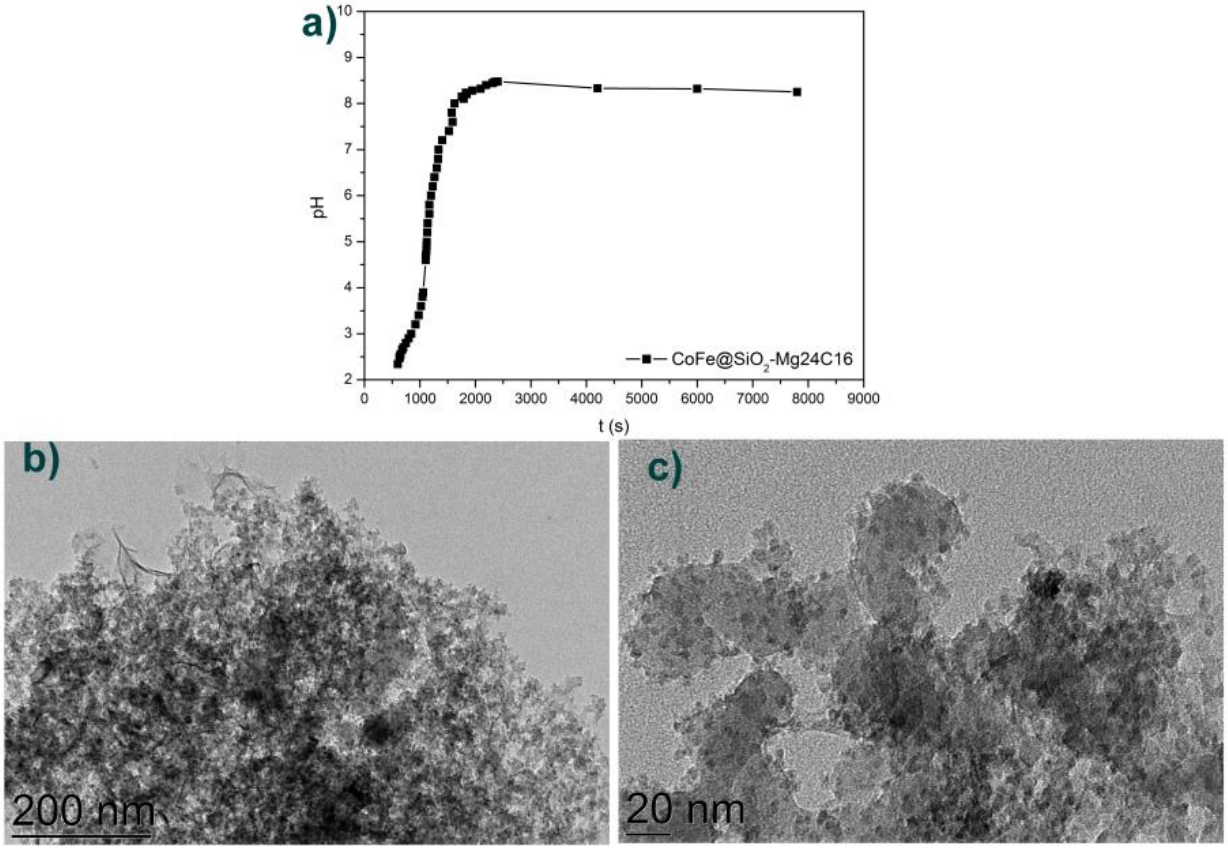


**Figure 5:** pH vs. time curve (a), representative TEM image of CoFe@$SiO_2$-M24C16 sample (b) and TEM image of small heterogeneous nucleated crystalline nanoparticles on the cores

When we added the stoichiometric Co/Fe atomic ratio, we do not get the stoichiometric composition of the cobalt ferrite nanoparticles at the surface of the core nanoparticles. In the next step the amount of $Co^{2+}$ ions was increased to favour its incorporation in the product spinel ferrite nanoparticles (CoFe@$SiO_2$-M24C24). The procedure for synthesis of composite nanoparticles was the same as in the previous case (CoFe@$SiO_2$-M24C16) in difference, that the atomic ratio between Co/Fe = 0.5 instead of stoichiometric 1. Because we added increase amount of ions into the reaction mixture, we also needed mode hydroxide ions to reach pH of 8 needed for precipitation of the $Co^{2+}$ ions. After 10 minutes of thermal hydrolysis, we added tablet of $Mg(OH)_2$ (n=0.24 mmol) and CaO (n=0.24 mmol) for increasing the pH (Figure 6a). Value of pH=8 where $Co^{2+}$ precipitates was reached after approximately 20 minutes and after 30 minutes the maximum pH= 8.17 was reached. Figure 6b and c represent the TEM images of CoFe@$SiO_2$-M24C24 composite nanoparticles. TEM images showed the silica core nanoparticles with covered with small crystalline nanoparticles and some larger, sheet-like nanoparticles (Figure 6b). The crystalline nanoparticles with size 3-5 nm are heterogeneous distributed at the core surfaces (Figure 6c). Homogeneous nucleated spinel nanoparticles are not observed. EDXS analysis of the shell on the core nanoparticles revealed that shell contains only ≈ 4 at.% of cobalt instead of 14 at.%. Also here we can observe the sheet-like structures (Figure 6c), which according to EDS analysis have got ratio of Fe:Co=1. EDS analysis on the composite nanoparticles showed that layer on the surface of the core nanoparticles contains just % of cobalt instead of 14 %. Although, we increased the concentration of $Co^{2+}$ ions, the stoichiometric cobalt ferrite was not formed. EDXS analysis of sheet-like structures revealed, that they contain iron and cobalt in ratio Fe/Co ≈ 1.

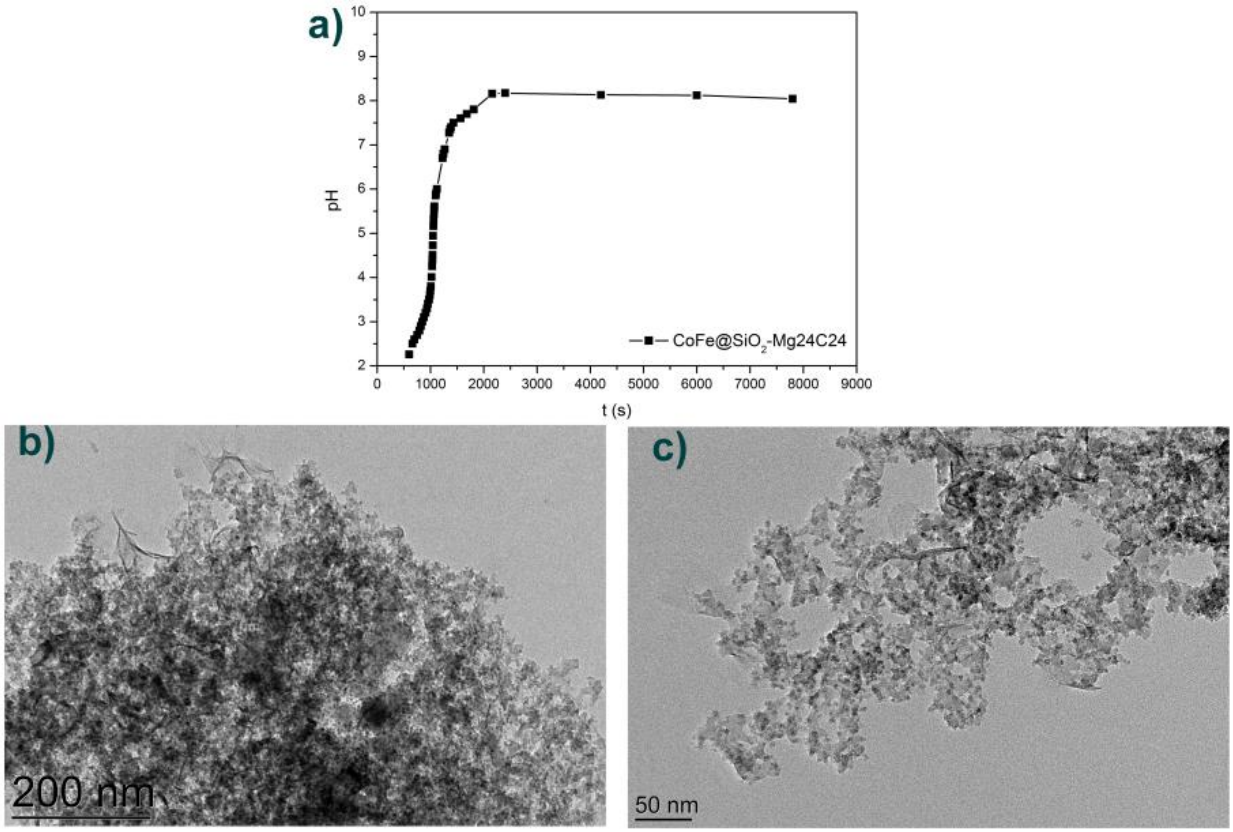


**Figure 6:** pH vs. time curve (a), representative TEM image of CoFe@$SiO_2$-M24C16 sample (b) and TEM image of small heterogeneous nucleated crystalline nanoparticles on the cores

## 4. Conclusions

The synthesis of the composite nanoparticles consisting of spinel cobalt-ferrite shell and the core of different functional materials was investigated. As a model core the silica nanoparticles were used. The spinel shell forms with heterogeneous nucleation and growth of the solid product during co-precipitation of the $Fe^{3+}/Co^{2+}$ ions in the aqueous suspension of the core nanoparticles. Different precipitating agents were tested. By using $Mg(OH)_2$ as the precipitating agent, the pH of 8 needed for $Co^{2+}$ precipitation could not be reached. As a result, the spherical spinel nanoparticles nucleated on the surface of the core nanoparticles contained no Co. Using the mixture of $Mg(OH)_2$ and CaO, the pH value of cobalt precipitation was reached. However, EDS and TEM analysis revealed that the cobalt-ferrite nanoparticles contained to low content of Co, even when the increased concentration of Co was used in the starting solution.

**References:**


[1] Caruso, F., *Nanoengieneering of Particle Surfaces.* Adv. Mater., 2001. **13**: p. 11-22.

[2] Camarago, P.H.C., K.G. Satyanaraya, and F. Wypych, *Nanocomposites: synthesis, structure, properties and new application opportunities.* Mat. Res., 2009. **12**: p. 2009.

[3] Darinka, P., *Heterogeneous nucleation of iron oxides (gama Fe2O3) in colloidal systems*. 2013, Jožef Stefan Postgraduate School: Ljubljana.

[4] Smith, J. and H.P.J. Wijn, *Ferrites: Physical properties of ferrimagnetic oxides in relation to their technical applications*. 2959, Eindhoven (Holland) Philips' technical library.

[5] Wang, Y., et al., *Multiferroic magnetoeletric composite nanoparticles.* NPG Asia Mater, 2010. **2**: p. 61-68.

[6] Ashua, S., et al., *One step synthesis of maghemite nanoparticles by direct thermal decomposition of Fe-urea complex and their properties.* J. Alloys Compd., 2009. **472**: p. l23-l25.

[7] Jolivet, J.P., *Metal oxide chemistry and synthesis: From solution to solid state*. 1994, Chichester: John Wiley & Sons.

[8] Gyergyek, S., M. Drofenik, and D. Makovec, *Oleic-acid-coated $CoFe_2O_4$ nanoparticles synthesized by co-precipitation and hydrothermal synthesis.* Mater. Chem. Phys., 2012. **133**: p. 515-522.

## For wider interest

Composite nanoparticles are composite materials, where one of their dimensions is in nanometre range (1 nm = $10^{-9}$ m). Within the individual composite nanoparticle at least two different materials displaying different, compositions, crystal structures and properties are combined. Such nanoparticles have potential to exhibit novel physical and chemical properties compared to single-material nanoparticles. Of particular interest are nanoparticles where properties of different materials are coupled. The coupling means, that one property can be tuned with influence on the other.

Typical example of composite material where properties are coupled is multiferroic composites. Multiferroics combine two "ferro" properties (ferroelecticity and ferromagnetism). The two properties are mechanically coupled in the composite, through the change in volume of the megnetosrtictive material in the magnetic field and piezoelectric material in the electric field. In such materials magnetic properties can be tuned by an applied electric field and the electric properties by an applied magnetic field. The multiferroic materials have great potentials in technological applications such as sensors, oscillators, memory devices, phase shifter etc.

In our work, we investigate the method for coating the different functional core nanoparticles with magnetic spinel cobalt ferrite ($CoFe_2O_4$) shell. Cobalt ferrite exhibit different magnetic properties that other spinel ferrites. Among all of spinel ferrites it is the only one hard magnetic and have the largest magnetostriction among oxides. On the basis of its properties, cobalt ferrite can be uses in storage and recording devices, drug-delivery systems, sensors etc.

The synthesis of cobalt-ferrite shell based on the known synthesis method for synthesis the maghemite shell with heterogeneous nucleation of the product of $Fe^{3+}/Fe^{2+}$ co-precipitation at the core nanoparticles. The main problem in cobalt-ferrite shell synthesis is the large difference of pH values where $Fe^{3+}/Co^{2+}$ ions precipitate. The pH value of 8 needed for $Co^{2+}$ precipitation can be reached by using strong base, however the release of the hydroxyl ions should be controlled and slow enough to enable low supersaturation needed for the heterogeneous nucleation.

# TNFα-induced apoptosis in U937 cell line is independent of cathepsin D and cysteine cathepsins

**Katja Bidovec**[1,2], **Veronika Stoka**[1,2], **Vito Turk**[1,2]

[1] Department of Biochemistry and Molecular Biology, Jožef Stefan Institute, Ljubljana, Slovenia

[2] Jožef Stefan International Postgraduate School, Ljubljana, Slovenia

katja.bidovec@ijs.si

**Abstract.** The role of cysteine and aspartic cathepsins in Tumor Necrosis Factor-alpha (TNFα)-induced apoptosis was investigated using U937 cell line. Apoptosis was caspase-dependent and accompanied by lysosome membrane permeabilization and release of cathepsin D into the cytosol. However, cysteine cathepsin inhibitor E64d and aspartic protease inhibitor pepstatin A did not prevent the initiation or progression of apoptosis, suggesting that neither cysteine cathepsins nor cathepsin D are critically involved in triggering or progression of the TNFα-induced apoptosis in U937 cell line. Cathepsins may, however, be involved in the amplification of the death receptor-mediated apoptosis pathway in certain cell lines or under different stimulation conditions.

**Keywords**: Apoptosis, TNFα, cathepsins

## 1 Introduction

Apoptosis is the major mechanism by which eukaryotic organisms eliminate potentially dangerous, superfluous and damaged cells [1]. Phenotypically, apoptosis is characterized by cell shrinkage, chromatin condensation, plasma-membrane blebbing and dismantling of the cell into small intact fragments (apoptotic bodies) that are removed by phagocytes [2]. Caspases, a family of cysteinyl aspartate-specific proteases, are central mediators of apoptotic and inflammatory pathways [3]. They are activated via two different signalling pathways, the intrinsic or mitochondrial pathway, and the extrinsic or death receptor pathway. In the intrinsic pathway, cellular stress results in the activation of proapoptotic proteins together with the inactivation of antiapoptotic proteins, both belonging to the Bcl-2 family of poteins.

Bax and Bak proteins oligomerize and form pores in the mitochondrial membrane which leads to the release of cytochrome c from the mitochondrial intermembrane space. In the cytosol, cytochrome c binds to the Apaf-1 protein, resulting in the formation of the apoptosome complex and subsequent procaspase -9 activation [4]. The death receptors, which are critical for the induction of extrinsic pathway, are all members of the tumor necrosis factor receptor (TNFR) superfamily which includes among others tumour-necrosis factor receptor-1 (TNF R1), the Fas receptor (FasR) and TNF-related apoptosis-inducing ligand (TRAIL) receptors: death receptor 4 (DR4 or TRAIL-RI) and death receptor 5 (DR5 or TRAIL-RII) [1, 4]. Binding of the ligands initiates oligomerization of receptors in the membrane, followed by assembly of the death inducing signalling complex (DISC). Initiator caspases -8 or -10 are then recruited to the DISC and activated. The two pathways converge at the level of the executioner caspases -3 and -7 [1]. The so called type I cells have been defined to be independent of mitochondria for the induction of death receptor-mediated apoptosis [5]. However, in certain cells, called type II cells [5], caspase-8 activates the proapoptotic Bcl-2 family protein Bid, which engages the mitochondrial pathway, thereby linking the pathways. Moreover, Bid seems to be a general sensor for apoptosis, as it can be cleaved by a number of other proteases, including calpains [6], granzyme B [7] and the lysosomal cathepsins [8]. A number of different stimuli were found to directly or indirectly target the lysosomal membrane, thereby inducing lysosomal membrane permeabilization and the release of cathepsins into the cytosol. Cathepsins are a family of proteases representing the largest group of proteolytic enzymes in the lysosomes [9]. In lysosomes, cathepsins execute non-specific bulk proteolysis. However, they were found to have specific physiological functions outside lysosomes, such as apoptosis mediation [9-11]. Massive lysosomal damages trigger necrosis, whereas more selective lysosomal permeabilization can lead to the induction of apoptosis [12] through activation of Bid and inactivation of the antiapoptotic Bcl-2 family members and subsequent activation of the the intrinsic pathway [10, 13]. The cathepsins were also suggested to be involved in the extrinsic pathway, however, the findings are contradictory [13-18]. In order to address this issue, we have investigated the role of cysteine cathepsins and cathepsin D in TNF-alpha mediated apoptosis in U937 cells that are known to express high levels of cathepsins and respond well to TNF-alpha.

## 2 Experimental work

*Cell culture and treatments:* Human Caucasian histiocytic lymphoma (U937) cells were obtained from European Collection of Cell Cultures and cultured at 37°C in a humidified atmosphere with 5% $CO_2$. Cells were grown in RPMI 1640 medium supplemented with 10% heat-inactivated foetal bovine serum, 1% glutamine and 1% streptomycin/penicillin. For all experiments, cells were seeded at a density $2x10^5$ cells/ml and maintained in the complete medium for 24 hours prior to any treatment. Human recombinant TNFα (ProSpec-Tany TechnoGene LTD, Rehovot, Israel). and cycloheximide (Sigma-Aldrich, St. Louis, USA) were added in fresh medium. Where indicated, Pepstatin A, Penetratin (Calbiochem; EMD Milipore, Billerica, MA, USA), E64d (Peptide Research Institute, Osaka, Japan) and z-VAD-FMK (Bachem AG, Bubendorf, Switzerland) were added two hours prior to the addition of TNF for the time indicated, to ensure inhibition of caspases and cathepsins. The total and cytosolic cell extracts were prepared as previously described [13, 19].

*Quantification of cell death:* Cells were seeded at a concentration of $4x10^5$ cells/ml in 24-well plates. After treatment, cells were pooled, collected by centrifugation (380 x g for 4 min) and stained with Annexin V-PE (BD, Franklin Lakes, NJ, USA) for 15 min at room temperature, followed by the staining with Propidium Iodide (PI) (Sigma-Aldrich St. Louis, USA). Annexin V-PE and PI were used to determine the phosphatidylserine exposure and the loss of membrane integrity according to the manufacturer's instructions. Analysis was made with FACSCalibur flow cytometer (BD, Franklin Lakes, NJ, USA) and the CellQuest software (FACSComp Software, BD, Franklin Lakes, NJ, USA). Acridine Orange was used to assess the integrity of the lysosomes as previously described [19].

*Caspase -3 activity measurement:* Proteins from total extracts were tested for DEVDase activity by measuring the proteolytic cleavage of the fluorogenic substrate Ac-DEVD-AFC. 50 μg of protein extracts, as determined by the Bio-Rad assay, were mixed in a 96-well plate with caspase buffer [100 mM HEPES, 200 mM NaCl, 0.2% (w/v) CHAPS, 20% (w/v) sucrose, 2 mM EDTA, and 20 mM dithiothreitol (pH 7.0)] to the final volume of 90 μl. After 15 min incubation at 37°C, the substrate was added to a final concentration of 10 mM and substrate hydrolysis was continuously

measured in a 96-well plate reader (Tecan Safire, Mannedorf, Switzerland) at excitation and emission wavelengths of 400 and 505 nm, respectively [20]

*Immunoblotting:* 50 μg of protein, as determined by the Bio-Rad assay, were loaded and resolved in 12.5% sodium dodecyl sulphate polyacrylamide gel electrophoresis gels and electrotransferred to the nitrocellulose membranes. Blots were probed with cathepsin D-specific mouse monoclonal antibodies (0.8 μg/ml) [21], caspase -8 p18 specific rabbit polyclonal antibodies (Santa Cruz Biotechnology, Inc., Dallas, TX, USA; 1:200 dilution) and Bid specific rabbit polyclonal antibodies (Cell Signaling Technology, Inc., Dancers, MA, USA; 1:500 dilution). Goat anti-mouse and goat anti-rabbit horseradish peroxidase-conjugated secondary antibodies (Abcam, Cambridge, UK; 1:5000 dilution) were added followed by visualization with enhanced chemiluminescence according to the manufacturer's instructions (GE Healthcare Bio-SciencesCorp., Piscataway, NJ, USA).

## 3 Results and discussion

*Triggering of TNF R1 death receptors induces caspase-dependent apoptosis that is independent of cysteine and aspartic cathepsin activity*

U-937 cells were initially tested for their sensitivity to apoptosis induction by TNFα in combination with cycloheximide, which sensitizes cells to TNFα induced apoptosis [22]. As shown in Fig 1, cells responded to TNFα. A significant number of cells entered apoptosis already after 12 hours with no major differences observed at 24 hour time point, except that few more cells underwent necrosis. A broad-spectrum caspase inhibitor Z-VAD-FMK did not protect against apoptosis as the cells underwent necroptosis (Figure 1, UR; [23, 24]).

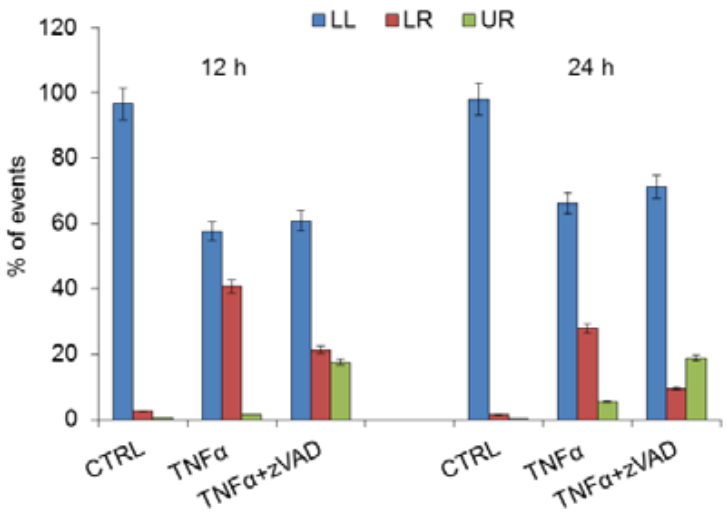


**Figure 1:** TNFα-induced apoptosis in U937 cell line. Cells were pretreated for 2 h with pan caspase inhibitor Z-VAD-FMK (20 μM) and incubated with TNFα (10 ng/ml) and cycloheximide (1 μg/ml) for 12 h and 24 h. Cells are distributed as follows: Ann-/PI- :living cells (LL); Ann+/PI- :apoptotic cells (LR); Ann+/PI+ (UR). The labelling for LL, LR and UR represents positions of cell populations in flow cytometric graphs (not shown).

We next tested DEVDase activity, characteristic of caspases, in total cell extracts following TNFα treatment. In agreement with a major role of caspases in death-receptor-induced apoptosis, DEVDase activity was significantly increased (Figure 2). A complete inhibition of DEVDase activity was observed in cells treated with the pan caspase inhibitor Z-VAD-FMK, in agreement with caspase activation in this model.

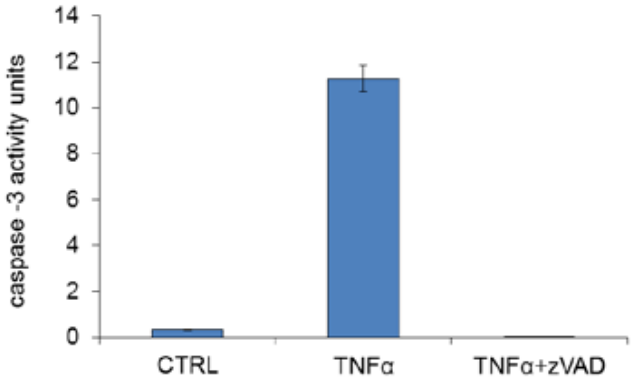


**Figure 2:** DEVDase activity after TNFα-induced apoptosis in U937 cell line. Cells were treated with 10 ng/ml TNFα and 1 μg/ml cycloheximide for 24 h. The inhibitor Z-VAD-FMK was added 2 h prior to TNF treatment at a concentration of 20 μM. Caspase activity was determined using the fluorogenic substrate Ac-DEVD-AFC. The results are expressed as relative fluorescence.

Next, we tested whether caspase -8, the critical upstream protease in the extrinsic apoptotic pathway was activated. As can be seen in Fig 3A, the band at 55 kDa,

corresponding to the preform of caspase-8 almost completely disappeared, whereas the band at 18 kDa, corresponding to the p18 subunit of activated caspase-8 appeared, indicating that caspase-8 was fully active. In addition, Fig 3B shows that the band at 22 kDa, corresponding to the full length Bid almost completely disappeared, indicating the cleavage of proapoptotic protein Bid (Figure 3B), most likely performed by activated caspase -8, although Bid is a potential target of many other proteases [6-8].

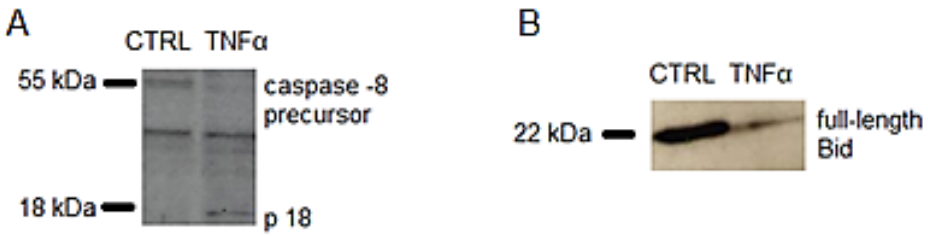


**Figure 3:** (A) Activation of caspase -8 and (B) Bid cleavage following treatment with 10 ng/ml TNFα and 1 μg/ml cycloheximide for 12 h.

Next, we tested if cysteine cathepsin inhibitor E64d and/or aspartic protease inhibitor pepstatin A prevent apoptosis, triggered by TNFα and cycloheximide. As shown in Fig 4, neither cysteine cathepsins nor cathepsin D are critically involved in TNFα-induced apoptosis in U937 cell line. Neither of the inhibitors by themselves exhibited cytotoxicity (not shown).

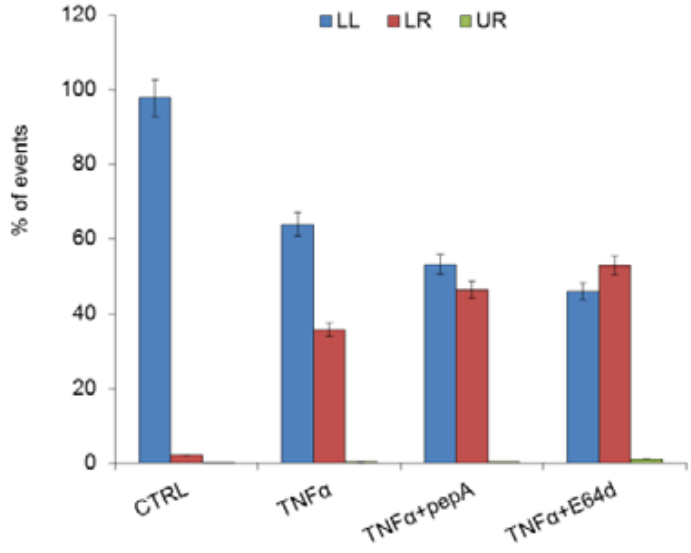


**Figure 4:** Cysteine and aspartic cathepsin inhibitors do not reduce the cytotoxic potential of TNFα. Cells were pretreated for 2 h with cysteine cathepsin inhibitor E64d (10 μM) and aspartic cathepsin

inhibitor Pepstatin A-Penetratin (1 μM ) and incubated with TNFα (10 ng/ml) and cycloheximide (1 μg/ml) for 12 h. Cells are distributed as follows: Ann-/PI- :living cells (LL); Ann+/PI-:apoptotic cells (LR); Ann+/PI+ (UR). The labelling for LL, LR and UR represents positions of cell populations in flow cytometric graphs (not shown).

*Lysosomal membrane is permeabilized in TNFa-induced apoptosis and cathepsin D is released to the cytosol*

We evaluated the stability of lysosomes after cell treatment with TNFα and cycloheximide by monitoring lysosome membrane permeabilization (LMP) at the 24 h time point. It is evident from figure 5A that about 20% of cells had damaged lysosomes. As TNFα-induced apoptosis was accompanied by LMP, we tested if cathepsin D was released to the cytosol. It has been previously shown that cathepsin D is released to the cytosol and actively mediates the death signal by TNFα [25]. As can be seen in Fig 5B, the bands at 48 kDa and 34 kDa, corresponding to the single-chain mature cathepsin D and heavy chain of mature cathepsin D, respectively, are strong in the control total cell extract and almost completely disappear in control cytosolic cell extract. In cytosolic cell extract, made after treatment with TNFα and cycloheximide, the band, corresponding to the heavy chain of mature cathepsin D becomes apparent, indicating the presence of cathepsin D in the cytosol following treatment.

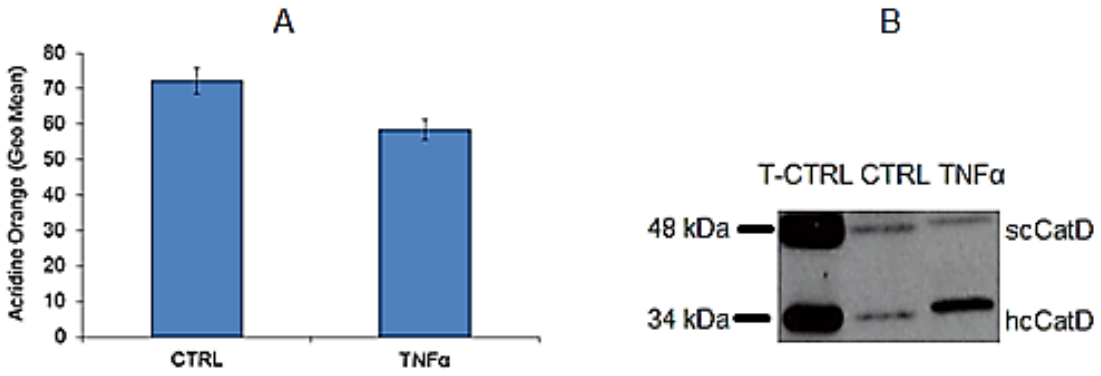


**Figure 5:** Lysosome integrity during TNFα-induced apoptosis in U937 cell line. (A) The cells were treated with TNFα (10 ng/ml) and cycloheximide (1 μg/ml) for 24 h. Acridine Orange uptake indicates the percentage of cells with decreased fluorescence. (B) Immunodetection of Cathepsin D in total cell extracts (T-CTRL) and cytosolic cell extracts without treatment (CTRL) and after treatment with TNFα (10 ng/ml) and cycloheximide (1 μg/ml) for 12 h. scCatD, single-chain mature cathepsin D; hcCatD, heavy chain of mature cathepsin D.

The role of caspases as major players in the death receptor pathway was clearly established, however, different opinions exist concerning the role of cysteine cathepsins and cathepsin D in this pathway. We showed that the activity of cysteine cathepsins and cathepsin D is not critical for the induction and/or progression of apoptosis induced by TNFα in U937 cell line, despite the fact that apoptosis induction was accompanied by damage to the lysosomes and release of cathepsin D to the cytosol. Our results are in agreement with the report from Klarić et al., who showed that TNFα induced apoptosis is independent of cysteine cathepsins, although lysosomes were found damaged and cathepsin B was released to the cytosol in U937 cell line [26]. U937 are type II cells which require an amplification of the apoptotic signal through engagement of the mitochondrial pathway [27, 28] via Bid cleavage to efficiently activate executioner caspase -3. In contrast to our results, several earlier studies suggested that cathepsins are important mediators of apoptosis upstream of mitochondrial outer membrane permeabilization (MOMP) in many different cell lines in TNFα induced apoptosis after being released to the cytosol [14, 15, 25]. However, apoptosis was only delayed, not abrogated in these studies, arguing against a critical role of cathepsins in the pathway. Cathepsins are more likely to be involved in the amplification loop involving mitochondria and lysosomes [11, 29] where the level of amplification may depend on cell type and the apoptotic stimulus.

## 4 Conclusions

The induction of apoptosis by TNFα and cycloheximide in U937 cell line results in caspase -8 and -3 activation, with subsequent cleavage of proapoptotic protein Bid. If caspases are blocked upon apoptosis induction, necroptosis becomes apparent. Lysosomal membrane is permeabilized during apoptosis progression and cathepsin D is released to the cytosol. Cysteine cathepsin inhibitor E64d and aspartic protease inhibitor Pepstatin A, did not rescue apoptosis, triggered by TNFα and cycloheximide, indicating that neither cysteine cathepsins nor cathepsin D are critically involved in the induction of this cell death pathway.

## Acknowledgement

Thanks to prof. ddr. Boris Turk for revision of the article and valuable comments.

## References:


[1] M. O. Hengartner. The biochemistry of apoptosis. *Nature,* 407, 6805: 770-776, 2000.

[2] J. Savill, V. Fadok. Corpse clearance defines the meaning of cell death. *Nature,* 407, 6805: 784-788, 2000.

[3] D. W. Lamkanfi M., Depuydt B., Kalai M., Saelens X., Vandenabeele P. The Caspase Family. In:*Caspases: Their Role in Cell Death and Cell Survival.* Edited by W. H. Los M., vol. Kluwer Acad./Plenum Publishers; 1-40, 2003.

[4] C. Adrain, S. J. Martin. The mitochondrial apoptosome: a killer unleashed by the cytochrome seas. *Trends in biochemical sciences,* 26, 6: 390-397, 2001.

[5] N. Ozoren, W. S. El-Deiry. Defining characteristics of Types I and II apoptotic cells in response to TRAIL. *Neoplasia,* 4, 6: 551-557, 2002.

[6] M. Chen, H. He, S. Zhan, S. Krajewski, J. C. Reed, R. A. Gottlieb. Bid is cleaved by calpain to an active fragment in vitro and during myocardial ischemia/reperfusion. *The Journal of biological chemistry,* 276, 33: 30724-30728, 2001.

[7] V. R. Sutton, J. E. Davis, M. Cancilla, R. W. Johnstone, A. A. Ruefli, K. Sedelies, K. A. Browne, J. A. Trapani. Initiation of apoptosis by granzyme B requires direct cleavage of bid, but not direct granzyme B-mediated caspase activation. *The Journal of experimental medicine,* 192, 10: 1403-1414, 2000.

[8] V. Stoka, B. Turk, S. L. Schendel, T. H. Kim, T. Cirman, S. J. Snipas, L. M. Ellerby, D. Bredesen, H. Freeze, M. Abrahamson *et al.* Lysosomal protease pathways to apoptosis. Cleavage of bid, not pro-caspases, is the most likely route. *The Journal of biological chemistry,* 276, 5: 3149-3157, 2001.

[9] V. Turk, V. Stoka, O. Vasiljeva, M. Renko, T. Sun, B. Turk, D. Turk. Cysteine cathepsins: from structure, function and regulation to new frontiers. *Biochim Biophys Acta,* 1824, 1: 68-88, 2012.

[10] V. Turk, B. Turk, D. Turk. Lysosomal cysteine proteases: facts and opportunities. *The EMBO journal,* 20, 17: 4629-4633, 2001.

[11] U. Repnik, V. Stoka, V. Turk, B. Turk. Lysosomes and lysosomal cathepsins in cell death. *Biochim Biophys Acta,* 1824, 1: 22-33, 2012.

[12] W. Li, X. Yuan, G. Nordgren, H. Dalen, G. M. Dubowchik, R. A. Firestone, U. T. Brunk. Induction of cell death by the lysosomotropic detergent MSDH. *FEBS letters,* 470, 1: 35-39, 2000.

[13] G. Droga-Mazovec, L. Bojic, A. Petelin, S. Ivanova, R. Romih, U. Repnik, G. S. Salvesen, V. Stoka, V. Turk, B. Turk. Cysteine cathepsins trigger caspase-dependent cell death through cleavage of bid and antiapoptotic Bcl-2 homologues. *The Journal of biological chemistry,* 283, 27: 19140-19150, 2008.

[14] M. E. Guicciardi, J. Deussing, H. Miyoshi, S. F. Bronk, P. A. Svingen, C. Peters, S. H. Kaufmann, G. J. Gores. Cathepsin B contributes to TNF-alpha-mediated hepatocyte apoptosis by promoting mitochondrial release of cytochrome c. *The Journal of clinical investigation,* 106, 9: 1127-1137, 2000.

[15] L. Foghsgaard, D. Wissing, D. Mauch, U. Lademann, L. Bastholm, M. Boes, F. Elling, M. Leist, M. Jaattela. Cathepsin B acts as a dominant execution protease in tumor cell apoptosis induced by tumor necrosis factor. *The Journal of cell biology,* 153, 5: 999-1010, 2001.

[16] T. Cirman, K. Oresic, G. D. Mazovec, V. Turk, J. C. Reed, R. M. Myers, G. S. Salvesen, B. Turk. Selective disruption of lysosomes in HeLa cells triggers apoptosis mediated by cleavage of Bid by multiple papain-like lysosomal cathepsins. *The Journal of biological chemistry,* 279, 5: 3578-3587, 2004.

[17] N. Fehrenbacher, L. Bastholm, T. Kirkegaard-Sorensen, B. Rafn, T. Bottzauw, C. Nielsen, E. Weber, S. Shirasawa, T. Kallunki, M. Jaattela. Sensitization to the lysosomal cell death pathway by oncogene-induced down-regulation of lysosome-associated membrane proteins 1 and 2. *Cancer research,* 68, 16: 6623-6633, 2008.

[18] A. Spes, B. Sobotic, V. Turk, B. Turk. Cysteine cathepsins are not critical for TRAIL- and CD95-induced apoptosis in several human cancer cell lines. *Biol Chem,* 393, 12: 1417-1431, 2012.
[19] S. Ivanova, U. Repnik, L. Bojic, A. Petelin, V. Turk, B. Turk. Lysosomes in apoptosis. *Methods in enzymology,* 442, 183-199, 2008.
[20] J. Rozman-Pungercar, N. Kopitar-Jerala, M. Bogyo, D. Turk, O. Vasiljeva, I. Stefe, P. Vandenabeele, D. Bromme, V. Puizdar, M. Fonovic *et al.* Inhibition of papain-like cysteine proteases and legumain by caspase-specific inhibitors: when reaction mechanism is more important than specificity. *Cell Death Differ,* 10, 8: 881-888, 2003.
[21] N. Kopitar-Jerala, V. Puizdar, S. Berbic, T. Zavasnik-Bergant, V. Turk. A cathepsin D specific monoclonal antibody. *Immunol Lett,* 77, 2: 125-126, 2001.
[22] B. Pajak, B. Gajkowska, A. Orzechowski. Cycloheximide-mediated sensitization to TNF-alpha-induced apoptosis in human colorectal cancer cell line COLO 205; role of FLIP and metabolic inhibitors. *Journal of physiology and pharmacology : an official journal of the Polish Physiological Society,* 56 Suppl 3, 101-118, 2005.
[23] P. Vandenabeele, T. Vanden Berghe, N. Festjens. Caspase inhibitors promote alternative cell death pathways. *Science's STKE : signal transduction knowledge environment,* 2006, 358: pe44, 2006.
[24] J. Hitomi, D. E. Christofferson, A. Ng, J. Yao, A. Degterev, R. J. Xavier, J. Yuan. Identification of a molecular signaling network that regulates a cellular necrotic cell death pathway. *Cell,* 135, 7: 1311-1323, 2008.
[25] M. Demoz, R. Castino, P. Cesaro, F. M. Baccino, G. Bonelli, C. Isidoro. Endosomal-lysosomal proteolysis mediates death signalling by TNFalpha, not by etoposide, in L929 fibrosarcoma cells: evidence for an active role of cathepsin D. *Biol Chem,* 383, 7-8: 1237-1248, 2002.
[26] M. Klaric, S. Tao, V. Stoka, B. Turk, V. Turk. Cysteine cathepsins are not critical for TNF-alpha-induced cell death in T98G and U937 cells. *Biochim Biophys Acta,* 1794, 9: 1372-1377, 2009.
[27] C. Scaffidi, S. Fulda, A. Srinivasan, C. Friesen, F. Li, K. J. Tomaselli, K. M. Debatin, P. H. Krammer, M. E. Peter. Two CD95 (APO-1/Fas) signaling pathways. *The EMBO journal,* 17, 6: 1675-1687, 1998.
[28] A. D. Terrisse, C. Bezombes, S. Lerouge, G. Laurent, J. P. Jaffrezou. Daunorubicin- and Ara-C-induced interphasic apoptosis of human type II leukemia cells is caspase-8-independent. *Biochim Biophys Acta,* 1584, 2-3: 99-103, 2002.
[29] K. Schrader, J. Huai, L. Jockel, C. Oberle, C. Borner. Non-caspase proteases: triggers or amplifiers of apoptosis? *Cellular and molecular life sciences : CMLS,* 67, 10: 1607-1618, 2010.

## For wider interest

Apoptosis is genetically regulated energy-dependent process, characterized by specific morphological and biochemical features in which caspase activation plays a central role. It is the major mechanism by which eukaryotic organisms eliminate potentially dangerous, superfluous and damaged cells. Many of the key apoptotic proteins that are activated or inactivated in the apoptotic pathways have been identified to date, however, the molecular mechanisms of action or activation of these proteins are not fully understood and are thus the focus of continued research. The importance of understanding the mechanistic machinery of apoptosis is vital because apoptosis is a component of both health and disease, namely being initiated by various inducing stimuli. Moreover, the widespread involvement of apoptosis in the pathophysiology of disease makes the process of apoptosis amenable to therapeutic intervention at many different checkpoints.

TNFα is one of the most important pro-inflammatory cytokines and has a crucial role in the pathogenesis of immune disorders and tumor development. Detailed understanding of TNFα triggered pathways will enable the development of a new generation of anti-TNFα therapies that will cause fewer side effects, whilst maintaining high efficacy in the treatment of cancer and immune disorders.

Our results have confirmed caspases as critical for induction and progression of apoptosis induced by TNFα in U937 cells, whereas, neither cysteine cathepsins nor cathepsin D are critically involved in the induction of this pathway. Although lysosomes are damaged and cathepsin D released to the cytosol, the inhibition of cysteine cathepsin and cathepsin D activity by its inhibitors, has no effect on apoptosis progression. However, cathepsins may be involved in the amplification rather than initiation of death receptor-mediated apoptosis.

# Tailoring relaxor dielectric response by blending P(VDF-TrFE-CFE) terpolymer with a ferroelectric P(VDF-TrFE) copolymer

**Goran Casar**[1,2], **Xinyu Li**[3], **Barbara Malič**[4], **Qiming Zhang**[3], **Vid Bobnar**[1,2],

[1] Condensed Matter Physics Dept., Jožef Stefan Institute, Ljubljana, Slovenia

[2] Jožef Stefan International Postgraduate School, Ljubljana, Slovenia

[3] Materials Research Institute, The Pennsylvania State University, USA

[4] Electronic Ceramics Dept., Jožef Stefan Institute, Ljubljana, Slovenia

goran.casar@ijs.si

**Abstract.** We report dielectric properties of relaxor P(VDF-TrFE-CFE) terpolymer (a polymer system that exhibits fast response speeds and high electric energy density, giant electrostriction and large electrocaloric effect) blended with ferroelectric P(VDF-TrFE) copolymer. We show that blends exhibit a relaxor-like linear dielectric response at low copolymer content. In samples with 20-50 wt. % of P(VDF-TrFE) the ferroelectric and relaxor states coexist and nonlinear dielectric spectroscopy appears as a very appropriate tool for revealing such coexistence. Moreover, the temperature dependence of the third harmonic dielectric response reveals the onset of ferroelectric behavior also in blends with a low copolymer amount, due to a high VDF content in the P(VDF-TrFE-CFE) terpolymer, which increases the ferroelectric interactions. In addition, the coexistence of ferroelectric and relaxor states is confirmed by differential scanning calorimetry, DSC, which further reveals the influence of blending on the terpolymer crystallinity and melting point.

**Keywords**: ferroelectric, relaxor, polymer blends, nonlinear dielectric spectroscopy, differential scanning calorimetry.

## 1 Introduction

Polyvinylidene fluoride, PVDF, has played an important role in sensor and actuator applications, ever since its high piezoelectric response has been reported [1]. Similary high piezoelectric response was found in poly(vinylidene fluoride-trifluoroethylene), P(VDF-TrFE), copolymer, which, contrary to PVDF, spontaneously crystallizes into a polar phase [2]. When P(VDF-TrFE) system is further manipulated either with

high-energy electrons irradiation or with additional monomers that contain large chlorine atoms, such as chlorofluoroethylene, CFE, or chlorotrifluoroethylene, CTFE, polar all-trans chains in normal P(VDF-TrFE) are converted into nanopolar regions in P(VDF-TrFE-CFE) and P(VDF-TrFE-CTFE), thus transforming the material into a typical relaxor system [3]. Such systems have in recent years been proposed for many advanced applications since they possess giant electrostriction [4], high energy densities with fast discharge speeds [5] and large electrocaloric effect [6]. Most of the investigations have, however, focused on either normal ferroelectric polymers or polymers that are completely transformed into a relaxor (e.g., terpolymers or P(VDF-TrFE) copolymer, irradiated with a high dose). Only recently properties of P(VDF-TrFE) copolymer, irradiated with low and moderate doses of high-energy electrons, have been reported - a clear evidence that ferroelectric and relaxor states coexist in the system has been provided on the basis of dielectric and thermal investigations and it has furthermore been shown that such a coexistence strongly influences some materials' properties [7]. Since it is known that irradiation can cause some undesirable effects, such as crosslinking of polymer chains and formation of free radicals, we have developed a polymer system, where similar coexistence of states could be expected - blends of a relaxor terpolymer and ferroelectric copolymer. Here we thus report dielectric properties of P(VDF-TrFE-CFE) terpolymer/P(VDF-TrFE) copolymer blends.

## 2 Materials and methods

P(VDF-TrFE-CFE) terpolymer and P(VDF-TrFE) copolymer powders (62.5/29/8.5 and 55/45 mol. %, respectively), synthesized by a suspension polymerization method, were dissolved in N,N-dimethylformamide at room temperature. Then, the two solutions were mixed together by proper ratios for different blend compositions. The final solution was filtered using 0.2 μm sized polytetrafluoroethylene filters and then cast on cleaned glass plates and dried at 70 °C for 24 h. Afterwards, the films were peeled on from the glass plates and further annealed at 70 °C for 24 h. For dielectric measurements, surfaces of 11-15 μm thick polymer films were covered by sputtered electrodes (100 nm of gold on 10 nm of chromium for better adhesion, diameter of 4.6 mm). Complex linear dielectric constant $\varepsilon^*=\varepsilon'-i\varepsilon''$ was measured in the frequency range of 30 Hz - 1 MHz by using HP4284A Precision LCR Meter. The amplitude of the probing ac electric signal was 0.1 V.

After heating the samples up to 375 K, the dielectric response was detected during cooling runs with the rate of 0.5 K/min. Similar heating/cooling procedure was used for the nonlinear dielectric response measurements, which were carried out at various frequencies by using HP35665A Dynamic Signal Analyzer. Here, the first ($\varepsilon$), the second ($\varepsilon_2$) and the third ($\varepsilon_3$) harmonic dielectric responses were measured simultaneously, which, in comparison to the separate measurement runs, reduces mistake in the subsequent computation of the ratio $a_3 = -\varepsilon'_3/\varepsilon_0^3\,\varepsilon'^4$. The differential scanning calorimetry (DSC) curves were recorded on a Netzsch DSC 204 F1 calorimeter. The sample was packed in an Al crucible with a lid, loaded into the calorimeter and heated up to 473 K with a heating rate of 10 K/min. The temperatures of the phase transitions are reported as the maxima of the peaks. The temperature and enthalpy calibrations were performed prior to the measurements using the standard calibration materials with well-defined transition temperatures and enthalpies.

## 3 Results and Discussion

Fig. 1 shows the temperature dependences of the real, $\varepsilon'$, and imaginary, $\varepsilon''$, parts of the complex linear dielectric constant, at various frequencies in the pure P(VDF–TrFE–CFE) terpolymer (100:0), its blends with different wt. % (5–50) of P(VDF–TrFE) copolymer, and in the pure copolymer (0:100). The terpolymer exhibits a typical relaxor broad dispersive maximum, i.e., temperatures at which $\varepsilon'$ and $\varepsilon''$ exhibit maximum are dependent on frequency. A small admixture of the P(VDF–TrFE) copolymer does not qualitatively influence the spectra, but only slightly increases the maximum values. However, in samples with higher copolymer amount (≥ 20 wt. %), a frequency independent peak due to the ferroelectric phase transition in the copolymer starts to form in addition to the broad terpolymer's relaxor maximum, which indicates that in these blends ferroelectric and relaxor states coexist. The linear dielectric spectra of the pure copolymer distinctively shows this ferroelectric phase transition; and in addition, a dielectric relaxation at lower temperatures. It should thus be stressed here that in polymer systems the ferroelectric phase transition and/or relaxor dynamic behavior take place only in the crystalline part of the system. It is namely well known, from x-ray, heat capacity, and infrared investigations, that PVDF and its copolymers are semicrystalline systems

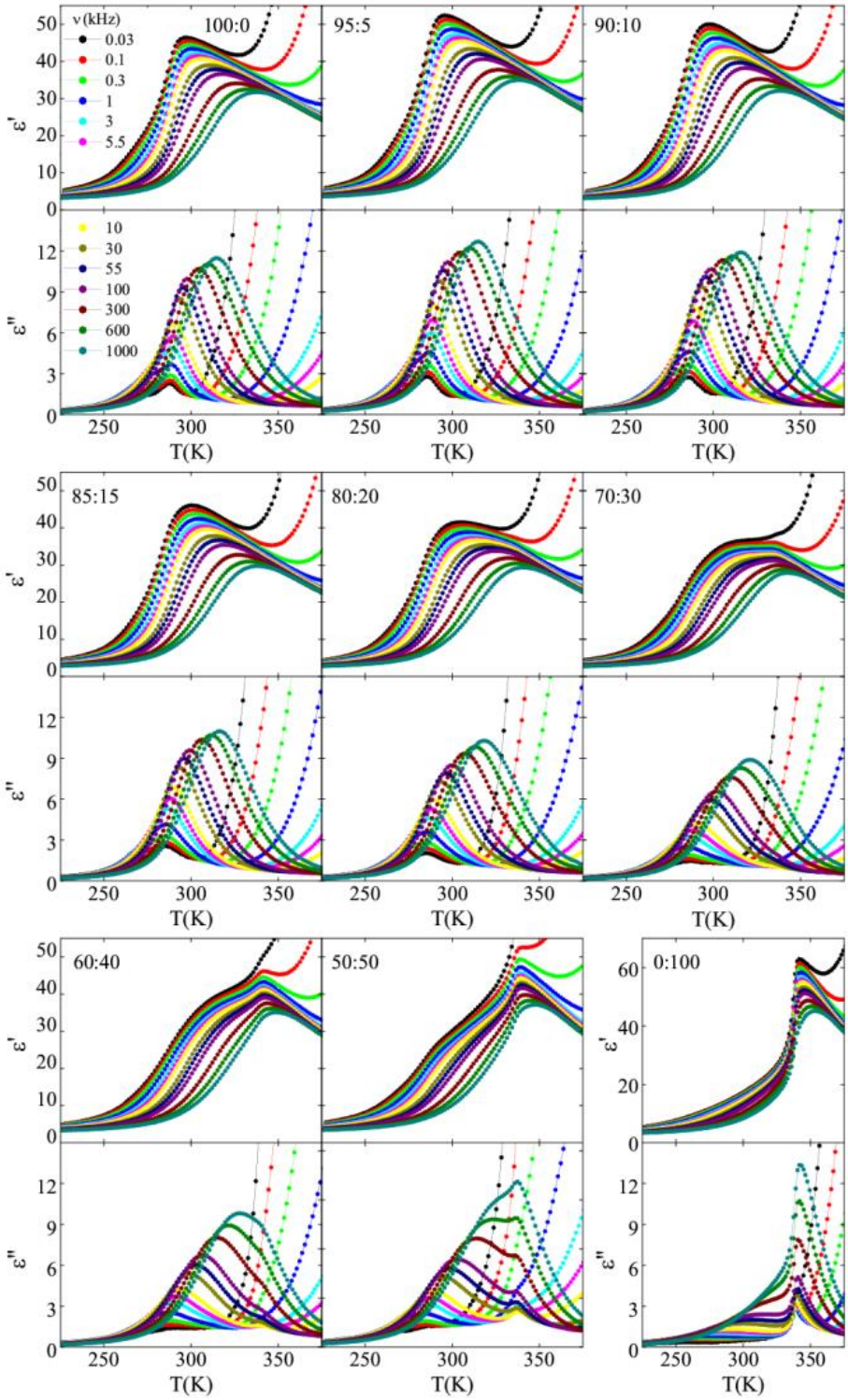


**Figure 1**: Temperature dependences of the real, ε', and imaginary, ε", parts of the complex linear dielectric constant, detected at various frequencies in the pure P(VDF–TrFE–CFE) terpolymer (100:0), its blends with different wt.% (5–50) of P(VDF–TrFE) copolymer, and in the pure copolymer (0:100). Due to clarity, the y-scale of the copolymer sample, which shows a ferroelectric behavior, is different to those of other samples, which exhibit either relaxor behavior or relaxor–ferroelectric coexistence.

comprising noncrystalline, i.e., amorphous regions, and crystalline regions with a spontaneous polarization associated with parallel packing of all-trans chains [2]. While on heating the crystalline region, adopted ferroelectric or relaxor phase undergoes a transition into a paraelectric phase, and finally melts, the amorphous region undergoes a transition from glassy to a rubbery state below room temperature [2]. This glass transition (sometimes called β-process) is dynamically manifested as an additional dielectric relaxation in the temperature region of 250–300K and is in fact present in all our investigated samples—it is only much less pronounced in samples, which comprise terpolymer, since it is overrided by the broad relaxor maximum.

The linear dielectric response thus reveals that ferroelectric and relaxor states coexist in the P(VDF–TrFE–CFE) terpolymer/P(VDF–TrFE) copolymer blends with 20–50 wt. % of P(VDF–TrFE), while no sign of ferroelectricity has been detected in samples with lower copolymer amount. Differential scanning calorimetry (DSC) results have in fact already revealed that in relaxor terpolymer/ferroelectric copolymer blends with a low amount of copolymer (≤10 wt. %), although both components form separate crystalline phases, (i) the interfacial couplings to the bulky defects in the terpolymer convert the normal ferroelectric copolymer into a relaxor and that (ii) the addition of the copolymer increases the crystallinity of blends. These findings can explain the facts that (i) 95:5, 90:10, and 85:15 blends entirely exhibit relaxor linear dielectric response and (ii) the increase in dielectric data (compare maximum $\varepsilon'$ values of 100:0 and 95:5 blends in Fig. 1) as a consequence of larger polarization which mostly originates in the crystalline phase.

The linear dielectric constant $\varepsilon$ is defined only in low electric fields $E$. For higher field strengths, the polarization $P$ can be represented as the power series expansion of the variable $E$ as $P/\varepsilon_0=(\varepsilon'-1)E+\varepsilon_2'^{2}+\varepsilon_3'^{3}$, where $\varepsilon_2'$ and $\varepsilon_3'$ are the real parts of the second- and the third-order nonlinear dielectric constants, respectively. While $\varepsilon_2'$ is nonzero only for the macroscopically noncentrosymmetrical systems and is proportional to the net polarization, $\varepsilon_3'$ can distinguish between the continuous or discontinuous ferroelectric phase transitions and the relaxor behavior [8]. The same applies for the dielectric nonlinearity coefficient $a_3=-\varepsilon'_3/\varepsilon_0^3\,\varepsilon'^4$, which is equal to the coefficient $B$ in the inverted $P(E)$ relation $E=AP+BP^3+CP^5\cdots$ (this is in fact the equation of state, obtained via the equilibrium condition from the order parameter expansion

of free energy). $a_3$ has often been used for the description of the nonlinear properties of relaxors as it can distinguish between the glass and the ferroelectric state—in spin and dipolar glasses $a_3$ namely diverges at the freezing temperature.

The temperature dependences of the real part of the third-order nonlinear dielectric constant, detected at 1 kHz in the pure P(VDF–TrFE–CFE) terpolymer, its blends with the P(VDF–TrFE) copolymer, and in the pure copolymer, are presented in Fig. 2. $\varepsilon_3'(T)$ data for the pure P(VDF–TrFE) copolymer show a typical ferroelectric behavior with the change of sign at the ferroelectric-to-paraelectric phase transition temperature of $T_C=339\pm1.5$ *K*. The change of $\varepsilon_3'$ sign indicates continuous, i.e., the second-order ferroelectric phase transition [8], which indeed is known to take place in the P(VDF-TrFE) 55/45 mol. % copolymer [2]. Similarly, $\varepsilon_3'(T)$ changes sign for blends with copolymer ratio above 20 wt. %, where the coexistence of ferroelectric and relaxor states has already been figured out from the linear dielectric results. The temperature of the $\varepsilon_3'$ sign change is however decreasing with lower copolymer amount (see the data for the samples with 20–50 wt. % of copolymer in the inset to Fig. 2) as a consequence of the fact that the ferroelectric transition temperature is reduced with decreased size of ferroelectric crystallites.

Moreover, the $\varepsilon_3'$ sign change has been detected at ≈287 K in all samples with the copolymer content below 20 wt. %, although they exhibit a relaxorlike linear dielectric behavior, and even in the pure terpolymer, despite the fact that the thermodynamic theory predicts that the third-order nonlinear dielectric constant changes sign only for a second-order ferroelectric phase transition [8]. In accordance with these theoretical predictions, solely positive values of $\varepsilon_3'(T)$ have in fact been detected in inorganic relaxors as well as in the P(VDF–TrFE–CFE) stretched and non-stretcthed terpolymer [8]. However, the terpolymer (59.2/33.6/7.2 mol. %) reported have lower VDF content than the terpolymer used in this study (62.5/29/8.5 mol. %), and it is known that ferroelectric interactions are stronger in P(VDF–TrFE) samples with higher VDF content: (i) Not only that *Tc* increases with increasing VDF content, (ii) the irradiation with high-energy electrons at a dose of 40 Mrad completely transforms the P(VDF–TrFE) 50/50 mol. % into a relaxor (only a broad dispersive linear dielectric maximum has been detected) while in the case of P(VDF–TrFE) 80/20 mol.% sample even after irradiation at a dose of 80

Mrad ferroelectric states clearly persist in the system. Obviously on increasing the VDF content, the P(VDF–TrFE) copolymer is more resistant to be converted into a relaxor, and our data reveal that in the P(VDF–TrFE–CFE) 62.5/29/8.5 mol. % terpolymer the VDF content is already high enough that even after addition of 8.5 mol. % of CFE the ferroelectric component is still present in the system.

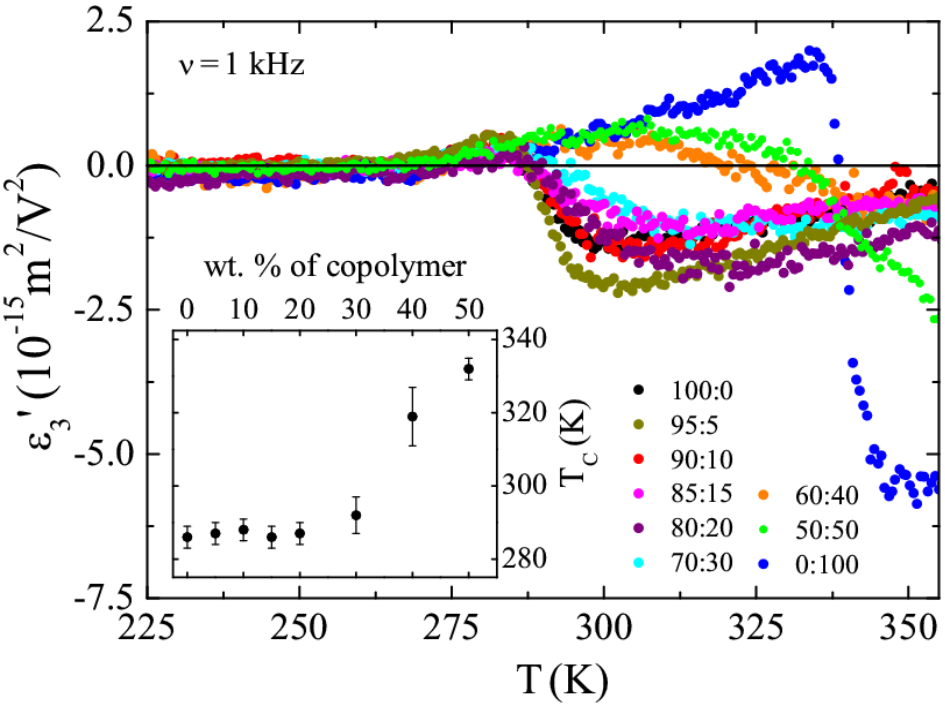


**Figure 2**: Temperature dependences of the $\varepsilon_3'$, detected at 1 kHz in the pure P(VDF–TrFE–CFE) terpolymer (100:0), its blends with the P(VDF–TrFE) copolymer, and in the pure copolymer (0:100). The inset shows the temperature where $\varepsilon_3'$ changes sign vs. copolymer content.

The temperature dependence of the real part of the second-order nonlinear dielectric constant, shown in Fig. 3 for two blend samples and for the pure copolymer, additionally confirms the presence of ferroelectric states in investigated samples. $\varepsilon_2'$ is non-zero only if the net polarization is present, and data for the pure copolymer clearly reveal that, like in ferroelectric crystals [8], $\varepsilon_2'$ reaches minimum at *Tc* (the arrow indicates the temperature where the corresponding $\varepsilon_3'$ changes sign), and below this temperature the nonzero $\varepsilon_2'$ values originate from the non-compensated domain structure, while above *Tc* the still existing net polarization can be due to the presence of charged surface layers. In the other two samples, where ferroelectric states coexist with relaxor states, the $\varepsilon_2'$ data are more scattered, however, their average (solid lines) also reveal minima near temperatures where the corresponding

$\varepsilon_3'$ changes sign. Finally, similar information can be obtained from the temperature dependence of the dielectric nonlinearity $a_3 = -\varepsilon'_3/\varepsilon_0^3\,\varepsilon'^4$, which also changes sign at *Tc* and is shown in the inset for the copolymer and 60:40 (smoothed data) samples.

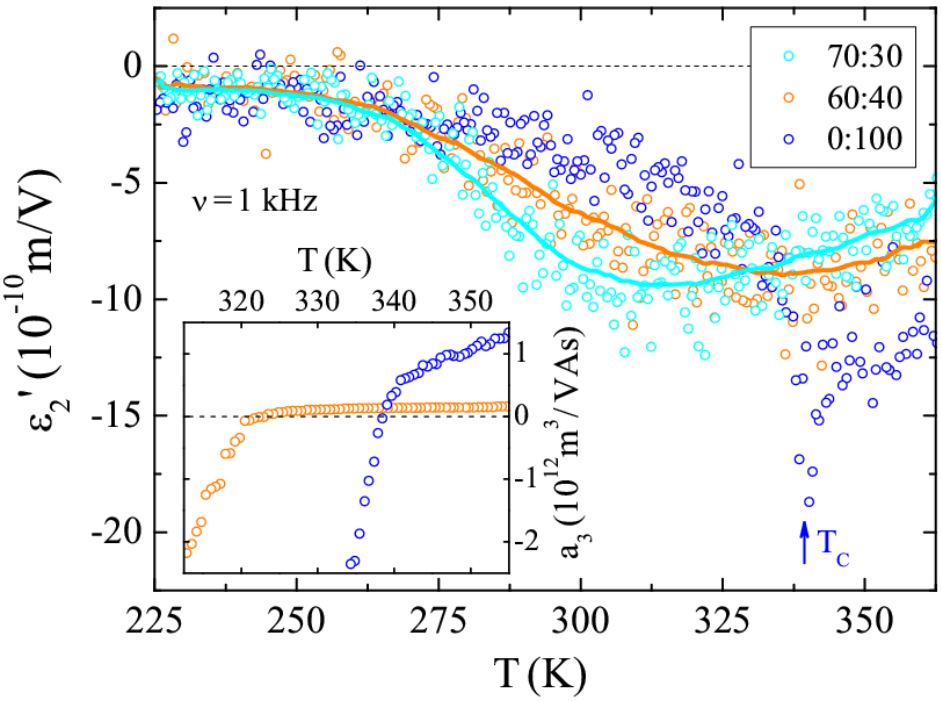


**Figure 3**: The real part of the second-order nonlinear dielectric constant, detected at 1 kHz in two terpolymer/copolymer blends with coexisting ferroelectric and relaxor states and in the pure copolymer. The $\varepsilon_2'$ data in the copolymer sample clearly exhibit a minimum at the ferroelectric phase transition. In the other two samples, the average of the data (solid lines) also reveal minima near temperatures where the corresponding $\varepsilon_3'$ changes sign. Similar information can be obtained from the temperature dependence of the dielectric nonlinearity $a_3$.

The final confirmation that in P(VDF–TrFE-CFE) terpolymer/P(VDF-TrFE) copolymer blends the ferroelectric and relaxor states coexist has been obtained by DSC experiments. Fig. 4 reveals DSC peaks at around three different temperatures, 340 K, 400 K, and 430 K. The peak at ~340 K, which appears in the pure copolymer and in blends with large amount of copolymer, denotes the ferroelectric phase transition. The other two peaks are due to the melting of the terpolymer (~400 K) and copolymer (~430 K) crystallites with their entalpy being proportional to the terpolymer/copolymer amount in the samples. DSC traces thus clearly reveal the coexistence of relaxor terpolymer crystallites and copolymer crystallites, the latter undergoing the ferroelectric transition in samples with their high enough amount.

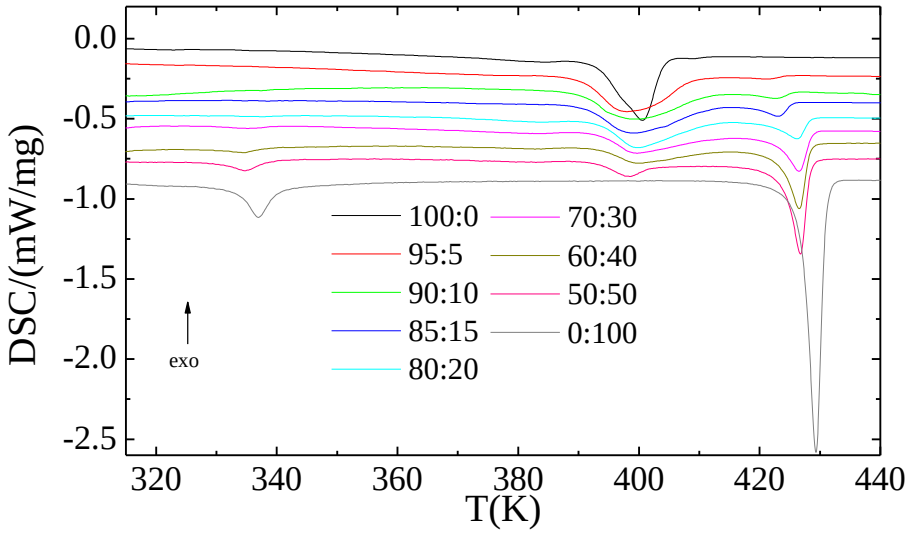


**Figure 4:** DSC traces of the pure P(VDF–TrFE–CFE) terpolymer (100:0), its blends with the P(VDF–TrFE) copolymer, and of the pure copolymer (0:100).

## 4 Summary

Blending a relaxor terpolymer with the ferroelectric copolymer resulted in the system with coexisting ferroelectric and relaxor states, showing similar properites to P(VDF-TrFE) copolymer, irradiated with low doses of high-energy electrons, where such a coexistence has been shown to strongly influence materials' properties [7]. This blend polymer system could thus be suggested as a model system for tailoring various materials' properties, not only the dielectric response, reported in this work.

## References:

[1] H. Kawai. The Piezoelectricity of poly(vinylidene fluoride). *Japanese Journal of Applied Physics*, 8(1): 975-976, (1969).

[2] T. Furukawa. Ferroelectric properties of vinylidene fluoride copolymers. *Phase Transitions*, 18(3-4): 143-211, (1989).

[3] V. Bobnar, B. Vodopivec, A. Levstik, M. Kosec, B. Hilczer, and Q. M. Zhang. Dielectric Properties of Relaxor-like Vinylidene Fluoride−Trifluoroethylene-Based Electroactive Polymers. *Macromolecules*, 36(12): 4436-4442, (2003).

[4] B. Chu, X. Zhou, K. Ren, B. Neese, M. Lin, Q. Wang, F. Bauer, and Q. M. Zhang. A Dielectric Polymer with High Electric Energy Density and Fast Discharge Speed. *Science*, 313(334): 334-336, (2006).

[5] F. Xia *et al.*. High Electromechanical Responses in a Poly(vinylidene fluoride–trifluoroethylene–chlorofluoroethylene) Terpolymer. *Advanced Materials*, 14(21): 1574, (2002).

[6] B. Nesse, B. Chu, S. G. Lu, Y. Wang, E. Furman, Q. M. Zhang. Large Electrocaloric Effect in Ferroelectric Polymers Near Room Temperature. *Science*, 321(5890): 821-823, 2008.

[7] G. Casar, X. Li, J. Koruza, Q. M. Zhang, and V. Bobnar. Electrical and thermal properties of vinylidene fluoride–trifluoroethylene-based polymer system with coexisting ferroelectric and relaxor states. *Journal of Materials Science*, 48(22): 7920-7926, (2013).

[8] S. Miga and J. Dec. Non-Linear Dielectric Response of Ferroelectric and Relaxor Materials. *Ferroelectrics*. 367(1): 223-228, (2008).

## For wider interest

Dielectric spectroscopy investigates electrically-induced properties of a material as a function of frequency and/or temperature. Dielectric properties are related to polarizability and thus depends on the structure and molecular properties of a material. That is why it is an useful tool for material characterization and is used in pharmacy, biotechnology and material science. The basic quantity in dielectric spectroscopy is complex dielectric constant $\varepsilon^*$, which consists of the real, $\varepsilon'$, and imaginary, $\varepsilon''$, part. The real part is related to stored energy within the medium, whereas the imaginary part describes the losses. That is why the dielectric constant is very important in devices for storing electrical energy (capacitors).

Numerous materials are also able to convert the electrical energy into mechanical work (electromechanical effect) or into heat (electrocaloric effect) note that in electrocalorics this is not due to the electrical current. Such properties of a material can be utilized in many devices such as actuators, sonars, integrated microelectro-mechanical systems or artificial muscles, which use the electro-mechanical effect, or in heating/cooling devices of new generation, which use the electrocaloric effect.

Ferroelectrics and relaxors are materials that possess giant electromechanical and electrocaloric effect. Subgroup of them are also polymers based on P(VDF-TrFE) copolymer. Pure P(VDF-TrFE) is a ferroelectric and can be transformed into a relaxor by irradiating it with large doses of high-energy electrons or by the addition of the third monomer, such as CFE. Most of the investigations up to now have focused either on pure, non-processed, ferroelectric P(VDF-TrFE) copolymer, or polymer that is completely transformed into a relaxor. It has recently been shown that in P(VDF-TrFE), irradiated with low doses of high-energy electrons, ferroelectric and relaxor states coexist. Since high-energy electron irradiation can cause some undesirable effects, such as cross-linking of polymer chains and formation of free radicals, we have developed a polymer system, where similar coexistence of states could be expected - blends of relaxor terpolymer and ferroelectric copolymer. In our work we show, by means of dielectric spectroscopy and differential scanning calorimetry, that ferroelectric and relaxor states indeed coexist in blends of P(VDF-TrFE-CFE) terpolymer and P(VDF-TrFE) copolymer. In addition we demonstrate how such coexistence influences some of the materials properties.

# Bioactive Peptides Derived from Egg White Hydrolyzate

**Ana Gluvić**[1]

[1] Jožef Stefan International Postgraduate School, Ljubljana, Slovenia

anadgluvic@gmail.com

**Acknowledgements**: I would like to thank the supervisor, prof. Dr. Eva Žerovnik (J. Stefan Institute and J. Stefan International Postgraduate School, Ljubljana) for discussion and correcting the paper.

**Abstract.** Hen egg white has exceptional potential as an inexhaustible source for a variety of peptide products with unique properties. These active peptides are valuable for human health and nutrition and can be used as raw material for diverse purposes in the cosmetic and pharmaceutical industries. The studies thus far have established that enzymatic hydrolysis of egg white water solution can release **active peptides**. Possible therapeutic effects of these peptides are antioxidant, antihypertensive, anti-inflammatory and antimicrobial, while functional properties of egg white hydrolyzate are better foaming, digestion, and solubility of food products. The aim of this work is to determine and describe which peptides have mentioned abilities and to propose some new abilities such as anti-aggregation and autophagy-stimulating effects and their possible application as drug or functional food.

**Keywords**: Egg white, enzymatic hydrolysis, bioactive peptides, functional food, antihypertensive, antioxidant, antimicrobial, anti-aggregation;

## 1 Egg White

In every day human diet, hen eggs represent significant food. With that being said, it is important to explore the properties of eggs as plausible source of therapeutic compounds. Nowadays, numerous commercial synthetic drugs are available but all of them have side effects. That is why an interest in therapeutic application of natural active components such as bioactive peptides grows. Egg white as a source of bioactive peptides is safer alternative to drugs.

## 1.1. Composition of Egg White

Hen egg is consistent of four parts: shell, membrane, egg yolk and egg white also known as albumen. Each part of hen egg has its own nutritional value. The biggest potential, as bioactive peptides pool, is the egg white. Albumen is liquid, viscous, tasteless solution with transparent yellowish-colour. It consists of 88, 5 % water and 13-20 % dry mass. This liquid mixture contains proteins of high nutritious value, amino acids like tryptophan, lysine, cysteine, and in amount of 1% carbohydrate and ions of atoms Na, K and Cl. Egg white has 10,5% (w-w) [1] of proteins per one average egg weight. It is composed of more than 70 different proteins [2], from which the most important and most well examined are those that are shown in table 1 below.

**Table 1**: Characteristics of the principal egg white proteins[3]

| No. | Protein | Percent of albumen(%) weight per weight (w-w) | Isoelectric point (pH) | Size (Da) |
|---|---|---|---|---|
| 1. | Ovalbumin | 54 | 4,5 | 45 000 |
| 2. | Ovotransferrin | 12 | 6,1 | 76 000 |
| 3. | Ovomucoid | 11 | 4,1 | 28 000 |
| 4. | Ovomucin | 3,5 | 4,5-5,0 | 5,5-8,3 x $10^6$ |
| 5. | Lysozyme | 3,4 | 10,7 | 14 300 |

| | | | | |
|---|---|---|---|---|
| 6. | G2 globulin | 4,0 | 5,5 | 3,0-4,5 x $10^4$ |
| 7. | G3 globulin | 4,0 | 4,8 | / |
| 8. | Ovoinhibitor | 1,5 | 5,1 | 49 000 |
| 9. | Ovoglycoprotein | 1,0 | 3,9 | 24 400 |
| 10. | Ovoflavoprotein | 0,8 | 4,0 | 32 000 |
| 11. | Ovomacroglobulin | 0,5 | 4,5 | 7,7 x $10^5$ |
| 12. | Chicken Egg White Cystatin | 0,05 | 5,1 | 12 700 |
| 13. | Avidin | 0,05 | 10 | 68 300 |

The proteins that are listed above have shown many positive as well as some negative effects, such as allergic reactions, on human health. Albumen properties can be improved by different treatments.

**Ovalbumin** is the biggest and predominant protein of egg white with antibacterial activity. This protein has potential to become source of many bioactive peptides with various functions[4]. It has one unwanted property, causation of allergic

response. This is one more reason to digest ovalbumin, and to potentially produce bioactive peptides and remove allergenicity. With hydrolysis of egg white it is possible to generate more a suitable form for oral intake especially for children under age of five that are within the allergy prone group. Beside ovalbumin, ovomucoid, ovotransferin and lysozyme have also shown allergen effects which are IgE-mediated immediate reactions[5].

**Ovotransferrin** also known as conalbumin has the propensity to bind to metallic iron ion[6]. It has antibacterial activity which is reflected in its ability to permeate bacterial outer membranes[4].

**Lysozyme** has antibacterial properties that are related to its capability to hydrolise ß (1-4) bonds of peptidoglycan, structural component of bacterial cell wall. Lysozyme is well known as natural food conservation agent against gram positive bacteria. Its antiviral activity against skin infections has also been confirmed[4].

**Avidin** has the ability to bind to biotin- water soluble vitamin B, that is necessary for bacterial and yeast growth[4].

Albumen **chicken egg-white cystatin** (CWEC) has shown antimicrobial activity by preventing group A streptococcus growth[4].

### 1.2. Albumen and protein aggregation

Chicken white egg cystatin (CWEC) is a member of cystatin family type 2. Cystatins are cysteine proteases inhibitors, that inhibit enzymes from peptidase papain family [7]. Some of the members of cystatin family were shown to be part of amyloid-plaques and to interfere with protein aggregation or form amyloid aggregates themselves [8]. As well, some variants of human cystatin C proved to be a risk factor for old-onset Alzheimer's disease [9].

Amyloids are fibril like proteinaceous formations, that form elongated spines consisted of antiparallel ß-sheets that can be identified by Congo red colour[10]. These formations are often found to be the final step in the mechanism of protein aggregation. Their precursors have shown different cytotoxic effects. Interaction of

amyloids has been studied using stefin B and cystatin C as model proteins[11]. Mutations of their genes or protein damage by oxidative stress or metal interactions can lead to amyloid formations and aggregation[12].

CWEC was used to determine the type of inhibition of Cathepsin C, a papain type of proteinase, and to locate the active site and mode of binding[7]. An exogenous amyloidogenic protein can present a potential seed for aggregation or it could contribute to diseases connected to amyloid formation in humans[13]. This is why CWEC is examined side by side to stefin B and human cystatin C, with the goal to better understand aggregation and the way of its prevention. Ultrasound treatments of CWEC could change its propensity towards cathepsin binding and cathepsin inactivation as well as its aggregation propensity.

## 2 Effect of Hydrolysis on Egg White

Usage of albumen is restricted to minimum commercial application because of its allergenic properties, thermal liability and unsatisfying digestivity. One way to improve egg white properties is with partial and controlled enzymatic hydrolysis. When comparing the egg white and its hydrolyzate, hydrolyzate has better digestivity, less viscosity, better solubility and it has no allergenic proteins. This has been also confirmed in the literature where it was reported that even pre-treatments such as cooking or ultrasound decreases allergenic potential[14].

Thus far four different enzymes have been used for hydrolysis optimisation: alcalase, neutrase, flevourzyme and papain. Alcalase is serine peptidase with endogenic activity, neutrase is serine peptidase with endogenic activity and both are isolated from bacteria. Papain is plant cysteine peptidase with endopeptidase activity while flavourzyme is a fungal enzyme with both endo- and exo-peptidase activity. Two different approaches have been used, single-step and two-step hydrolysis. Single-step was performed with above mentioned enzymes in order to determine their capability to reach the highest degree of hydrolysis. With two-step hydrolysis high percentage of hydrolysis was also one of goals and the other goal was to produce bioactive peptides. Also, two different pretreatments preceded hydrolysis. Pretreatments presented physical hydrolysis of 10% egg white solution by heat and ultrasound. Reaction conditions during experiments were constant with pH and temperature

adapted to each protease. Pretreatmen with high temperature was conducted at 75°C degres for 30 minutes and ultrasound treatment was cinducted at room temperature with frequency of 20 kHz. The results are shown in figure 1 and 2[15].

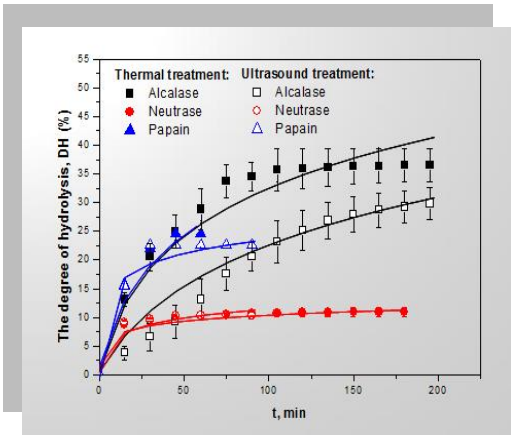


**Figure 1:** Schematic presentation of single-step hydrolysis of 10% egg white water solution with termic and ultra sound pre-treatment.

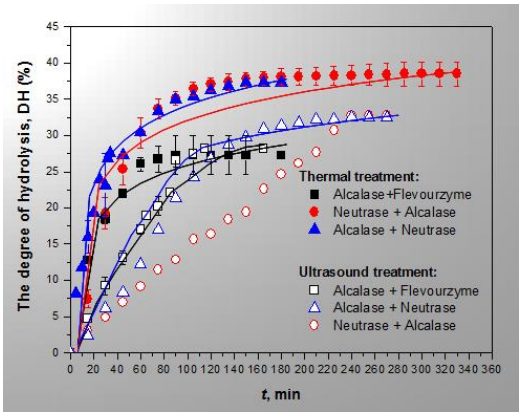


**Figure 2:** Schematic presentation of two-step hydrolysis of 10% egg white water solution with termic and ultra sound pre-treatment

Figure 1 shows influence of pretreatment on single step hydrolysis. The best result was obtained with termal pretreatment using alcalase, which was espected, because of better accessibility of its endopeptidase activity after partial cleavage of proteins. Ultrasound pretreatment had a little bit slower kinetics than termal pretreatment but it also reached the same hydrolysis persentage. The advantage of ultrasound was lack of side effects such as chainge of solution colour that was observed in termal pretreatment.

Two- step hydrolysis which was shown on figure 2 was obtained under the same conditions as the one-stape hydrolysis with same prereatments with the addition of second enzyme when 20 % degree of hydrolysis was achived.

During hydrolysis antioxidative parameter was followed. The highest activity was determined in two-step hydrolysis with combination of alcalse and flevourzyme. Also, this treatment has shown very good functional propetrties, table 2. The results shown below were derived from 27% deggre of hydrolisis solution of one and two-step enzyme hydrolisis with termal and ultrasound treatment. The data within table 2

are important to food industry and for formulation of functional food. The two-step enzyme, alcalase-neutrase, hydrolisate treated with ultrasound has the biggest foaming stability and capacity. The digestivity is also improved which is suitable for products for consumers with difficulties with digestion. Taste is very interesting clause and it shoud not be neglected in formulation of functional food.

**Table 2:** Functional properties of egg white protein hydrolyzate with same hydrolysisi degree, *DH*=27%.

| Parameters | Albumen | Alcalase | | Alcalase and neutrase | | Alcalase and flevourzyme | | Papain | |
|---|---|---|---|---|---|---|---|---|---|
| | | T | UZ | T | UZ | T | UZ | T | UZ |
| Degree of hydrolysis, DH(%) | 0,00 | 27,00 | 27,00 | 27,00 | 27,00 | 27,00 | 27,00 | 27,00 | 27,00 |
| Foaming capacity, (%) | 77,68 | 81,06 | 77,68 | 80,92 | 81,06 | 69,10 | 80,47 | 73,68 | 74,75 |
| Foam stability, (%) | 73,96 | 72,83 | 64,29 | 73,96 | 73,12 | 72,22 | 73,12 | 70,24 | 46,81 |
| Digestibility, (%) | 69,29 | 79,44 | 79,17 | 81,86 | 79,83 | 79,05 | 79,30 | 90,43 | 90,72 |
| Solubility at pH 6, (%) | 70,69 | 93,11 | 89,27 | 100,00 | 77,43 | 88,31 | 100,99 | 95,68 | 95,41 |
| Solubility at pH 8, (%) | 81,85 | 93,12 | 87,34 | 92,13 | 81,19 | 92,99 | 97,73 | 91,94 | 100,00 |
| DPPH activity, (%) | 35,62 | 77,68 | 70,49 | 51,35 | 33,29 | 44,92 | 77,65 | 73,84 | 89,93 |
| Reduction power | / | 0,15 | 0,11 | 0,11 | 0,15 | 0,15 | 0,05 | 0,49 | 0,45 |
| Taste | pleasant | salty and bitter | | bitter | | sweet and pleasant | | unpleasant | |

In some studies they have improved antioxidative properties of egg white by adding minerals like selenite and thus improving egg white powder[16].

One of the important factors in the hydrolyzate solution are electrolytes, especially ions of $Na^+$ and $Cl^-$ which have influence changes of the protein backbone and thus the protein activity[17].

## 3 Bioactive peptides derived so far from Egg White

There are many different peptides that have bioactive functions. From egg white protein ovotransferin two peptides IRW and IQW have shown capability to attenuate tumour necrosis factor (TNF) and to attenuate inflammatory stress response in endothelial cells. These three-peptides have influence on prevention of atherosclerotic lesions. They are potent ACE inhibitors that have been tested on

endothelial cells by 20 hour treatment[18]. Some longer peptides like 92- amino acid residue peptides of ovotransferin have shown antibacterial activity against Gram-negative bacteria[19].

Enzymatic hydrolysis of Lysozyme has even enhanced its anti-bacterial activity by mediating its insertion into bacterial membrane. Orally inserted lysozyme showed antiviral propensity against herpes simplex and chicken pox[19].

Ovalbumin peptides OA 77-84 and OA 126-134 derived from peptic or chymotryptic digestion increased macrophages activity. Digestion of ovokinin ovalbumin by chymotrypsin gave peptide OA 358-365 with vasodilating effect. This propensity was confirmed in vivo, on spontaneously hypertensive rats. Peptide OA 183-184 derived by peptic and OA 200-2018 derived by tryptic digestion showed antihypertensive activity[19].

Some researchers suggested that cystatins may be involved in inflammatory response. Verdot at al. found that cystatin induces the synthesis of TNF-α resulting up-regulation of nitric oxide[20]

## 4 Future plan for bioactive peptide isolation and identification from egg white

Food-derived active components- bioactive peptides are the future of pharmaceutical and healthy-food industry. With such products and drugs one could expect to avoid side effects of synthetic drugs but still keep their therapeutic effect.

As it was mentioned before, many studies have shown in vitro and not that many in vivo that egg white proteins have a propensity to become part of functional food products. By enzymatic hydrolysis the bioactive peptides are exempt from egg white proteins. Different enzymes derive different active peptides with different properties. This opens a whole range of possibilities. By variation of enzymes we will be able to produce peptides with properties that have potential in treatment of different illnesses.

This work will focus on detection, isolation and characterization of active peptides derived from egg white chosen, most abundant proteins hydrolysed by one-step hydrolysis with alcalase and two-step hydrolysis with combination of alcalase and flevourzyme or, if necessary some other combination of digestive enzymes. In the previous studies of albumen proteins and their peptides, anti-aggregation properties of bioactive peptides derived from white egg were not probed, therefore, this will be a new additional feature.

The goal of this research is to identify active peptides that can be used as antioxidants or ROS inhibitors and others (or the same), which would have anti-aggregation or autophagy simulating properties. With that said it is possible to prevent age-dependent diseases by preventing ROS caused cell death and on the other hand, obtain repression of aggregation of other amyloid peptides.

## References:


[1] Mann, K. (2007) The chicken egg white proteome. *Proteomics*, 3558-3568
[2] Mann, K. (2011) In-depth analysis of the chicken egg white proteome using an LTQ Orbitrap Velos. *Proteome Science* 9
[3] Belitz, H. (2009) *Food Chemistry*. Springer
[4] Kovacs-Nolan, J. (2005) Advances in value of eggs and egg components for human health. *Journal of agriculturaland food chemistry* 53, 8421-8431
[5] Aabin, B. ( 1996) Identification of IgE-binding egg white proteins: comparison of results obtained by different methods. *Int Arch Allergy Immunol* 109, 50-57
[6] Ibrahim, H. (2000) Ovotransferrin. *Natural Food Antimicrobial Systems*, 211-226
[7] Dolenc, I. (1996) Interaction of human cathepsin C with chicken cystatin. *FEBS*, 277-280
[8] Levy, E. (2008) Cystatin C a potential target for Alzheimer´s treatment. *Expert Rewiew of Neurotherapeutics* 8, 687-689
[9] Benussi, L. (2003) Alzheimer disease-associated cystatin C variant undergoes impaired secretion. *Neurobiology of Disease* 13, 15-21
[10] Rode, W. (1988) The 2.0 A X-ray crystal structure of chicken egg white cystatin and its plosible mode of interaction with cysteine proteinases. *Cell Death and Disease* 4, 2593-2599
[11] Žerovnik, E. (2002) Amyloid Fibril Formation. Proposed mechnisms and relevance to conformational disease. *the FWBS Journal*, 3362-3371
[12] Žerovnik, E. (2011) Mechanisms of amyloid fibril formation – focus on domain swapping.*The FEBS Journal*, 2263-2282
[13] Kenjiro, O. (2014) Exogenous amyloidogenic proteins function as seeds in amyloid ß-protein aggregation. *Biochimica et Biophysica Acta* 1842, 646-653
[14] Mine, Y. (2008) Recent advances in the understanding of egg allergens: Basic, industrial, and clinical perspectives. .*Journal of Agricultural and Food Chemistry* 56, 4874-4900
[15] KneževićJugović, Z. (2013) Effects of hydrolysis degree and type of protease on antioxidant activity and functionality of egg white protein hydrolysates In *40th International Conference of SSCHE* (Markoš, J., ed), pp. 14331439
[16] Zhao, J. (2013) Characteristics and enhanced antioxidant activity of egg white protein selenized by dry-heating in the presence of selenite. *Journal of agriculturaland food chemistry* 61, 3131-3139

[17] Raikos, V. (2007) Effects of sucrose and sodium chloride on foaming properties of egg white proteins. *Food Research International* 40, 347-355
[18] Majumder, K. (2013) Structure and Activity Study of Egg Protein Ovotransferrin Derived Peptides (IRW and IQW) on Endothelial Inflammatory Response and Oxidative Stress. *Agricultural and food chemistry* 61, 2120-2129
[19] Nolan, J.K.-. (2005) Advances in the Value of Eggs and Egg Components for Human Health. *Journal of Agricultural and food chemistry* 53, 8421-8431
[20] Verdot, L. (1999) Chicken cystatin stimulates nitric oxide relese from interferon-gama activated mouse peritoneal macrophages via cytokine synthesis. *European Journal of Biochemistry*

## For wider interest

Egg white is a major row material in food industry. Its hydrolyzate can be added to meat, bakery and cookie products because of its foaming, emulsifying and better digesting properties. Eggs also contribute a clean, natural image of packaged or prepared foods to look consumer-friendly. Enzymatic egg white hydrolyzate contains in addition bioactive peptides which have beneficial effects in comparison to non-hydrolysed egg white. The aim of this work is to study anti-oxidant and some novel effects of bioactive peptides, for possible usage as aging preventive, healthy-food.

# The role of different niobium pentoxide precursors in the solid-state synthesis of potassium sodium niobate

**Jitka Hreščak**[1,2], **Andreja Benčan**[1,2], **Tadej Rojac**[1], **Barbara Malič**[1,2]

[1] Electronic Ceramics Department, Jožef Stefan Institute, Ljubljana, Slovenia

[2] Jožef Stefan International Postgraduate School, Ljubljana, Slovenia

jitka.hrescak@ijs.si

**Abstract.** The lead-free ceramics based on the solid solution of potassium sodium niobate have been extensively studied in recent years. Different authors reported preparation of qualitatively extremely different ceramics, although they used comparable processing methods. The repeatability of the preparation of the potassium sodium niobate systems thus is an issue. In this study, two batches of $K_{0.5}Na_{0.5}NbO_3$ were prepared, using the orthorhombic and the monoclinic $Nb_2O_5$ polymorphs for the solid-state synthesis. Our results showed a clear influence of the $Nb_2O_5$ polymorhic form on the formation of a homogeneous potassium sodium niobate solid-solution and its further densification behaviour. To achieve a perfect reproducibility in the potassium sodium niobate ceramics processing this point is crucial and was not considered so far.

**Keywords**: Potassium sodium niobate; Niobium pentoxide; Solid-state synthesis

## 1 Introduction

Piezoelectric materials based on the solid solution of sodium potassium niobate have been the most studied lead-free piezoelectric materials over the past few years [1, 2]. A high electromechanical coupling factor and a low dielectric permittivity make potassium sodium niobate ceramics interesting for ultrasonic applications [1]. However, despite there being many reports on the preparation and properties of this material, problems with densification and grain growth control remain. In general, the reproducibility of the solid-state synthesis is an issue.

Malič [3] studied the solid-state reaction of $K_{0.5}Na_{0.5}NbO_3$ from alkaline carbonates and niobium pentoxide by diffusion couples. They found that at 600°C, $K_{0.5}Na_{0.5}NbO_3$ is formed via an intermediate phase that best corresponds to the solid solution $(K_xNa_{1-x})_2Nb_4O_{11}$. The reaction proceeds by the diffusion of $K^+$, $Na^+$ and $O^{2-}$ ions through the reaction layer of the intermediate phase and $K_{0.5}Na_{0.5}NbO_3$ toward $Nb_2O_5$. The reaction rate is determined by the diffusion of the slower species, i.e., $K^+$. As known from the studies made on an analogous but better-known system, i.e., $BaTiO_3$ [4, 5], the particle size distribution (PSD) of the starting powders plays a crucial role in the synthesis of $K_{0.5}Na_{0.5}NbO_3$. In principle, the carbonates should have a uniform PSD and a small particle size to obtain good homogeneity of the potassium and sodium carbonates around the particles of niobium pentoxide in the initial mixture. Based on the work of Malič et al. [3], the PSD of $Nb_2O_5$ would determine the rate of the overall diffusion-controlled reaction since at the usual calcination temperature the diffusion of $Nb^{5+}$ is negligible and only the diffusion of $K^+$, $Na^+$ and $O^{2-}$ takes place.

$Nb_2O_5$ is the most commonly used source of Nb in the solid-state synthesis of potassium sodium niobate and is known to exist in different polymorphs [6]. The most common polymorphs are the orthorhombic γ-phase and the high-temperature-stable monoclinic α-phase. The phase composition is not specified in commercially available $Nb_2O_5$, and neither is it usually reported in the literature when $Nb_2O_5$ is used for synthesis.

The aim of this study was to investigate the influence of the polymorphic form of $Nb_2O_5$ on the solid-state synthesis of $K_{0.5}Na_{0.5}NbO_3$. Two batches of $K_{0.5}Na_{0.5}NbO_3$ were prepared using identical procedures from two different $Nb_2O_5$ polymorphs, i.e., orthorhombic and monoclinic. The reactions of the two homogenized mixtures were studied. The possible reasons for the $Nb_2O_5$ polymorphs' different reactivity with the alkaline carbonates during the synthesis of $K_{0.5}Na_{0.5}NbO_3$ are discussed. The paper clearly shows the importance of different $Nb_2O_5$ polymorphs on the course of the solid-state reaction and further densification behaviour of $K_{0.5}Na_{0.5}NbO_3$, which has not been considered so far.

## 2 Experimental procedure

Two batches of $K_{0.5}Na_{0.5}NbO_3$ were prepared from the following starting powders: $K_2CO_3$ (anhydrous, 99.9+ %, ChemPur, Karlsruhe, Germany), $Na_2CO_3$ (anhydrous, 99.9+ %, ChemPur, Karlsruhe, Germany) and two types of $Nb_2O_5$. The first $Nb_2O_5$ (325 mesh, 99.9 %, Sigma-Aldrich, Steinheim, Germany) was orthorhombic and had median particle diameter $d_{50}$ = 0.48 μm and $d_{90}$ = 3.77 μm. The second $Nb_2O_5$ (99.9985 %, Alfa Aesar, Karlsruhe, Germany) was monoclinic with bimodal PSD and $d_{50}$ = 0.70 μm.

All the powders were ball milled in a planetary mill in acetone for 4 h and dried. The milling of all powders resulted in the elimination of the larger particles and a $d_{50}$ = 0.33 μm for the orthorhombic $Nb_2O_5$ and $d_{50}$ = 0.40 μm for the monoclinic $Nb_2O_5$. The milled and dried precursors were weighed in the exact stoichiometric ratio to prepare $K_{0.5}Na_{0.5}NbO_3$ from two different $Nb_2O_5$ in a dry box and the two mixtures were homogenized in a planetary mill for 4 h in acetone. The homogenized mixtures were dried, compacted into pellets and calcined two times at 800°C for 4 h with intermediate and final planetary milling for 4 h in acetone. For the densification study, the powders were compacted with a uniaxial press into cylindrical samples, cold isostatically pressed at 200 MPa and sintered at 1120°C for 2 h, with heating and cooling rates of 5 K/min, in a tube furnace.

The phase composition and structure of the precursors and the ceramic powders were determined by X-ray diffraction (XRD) analyses performed on a PANalytical X'Pert PRO diffractometer with a Cu Kα1 radiation source and a Ge monochromator. The data were collected in the 2θ range from 10° to 90° with a step of 0.016°/100 s. A Rietveld refinement was carried out using the Topas program. Orthorhombic (ICSD 1840) and monoclinic (ICSD 16605) $Nb_2O_5$ were used as model structures for the refinement. The morphology of the precursors and the ceramic powders was analyzed using a Jeol JSM-7600F field-emission scanning electron microscope (SEM) and a Jeol JEM-2100 transmission electron microscope (TEM). For the SEM analysis of the ceramics, the samples were cut with a diamond wire saw, mounted in epoxy and polished. Thermal etching of the ceramics was carried out at 1020°C for 40 minutes. Prior to the analysis, the samples were coated with a 4-nm-thick carbon layer in a Gatan PECS 682. The dimensional changes of

the pellets of the calcined and milled mixtures with comparable green densities during heating, were recorded with a Leitz heating-stage microscope, Version 1A, at a heating rate of 5 K/min.

In the subsequent text the monoclinic $Nb_2O_5$ and the potassium sodium niobate prepared from the monoclinic $Nb_2O_5$ are denoted as $Nb_2O_5$-mono and KNN-mono, respectively, and the orthorhombic $Nb_2O_5$ and the potassium sodium niobate prepared from this orthorhombic $Nb_2O_5$ are denoted as $Nb_2O_5$-ortho and KNN-ortho, respectively.

# 3 Results and discussion

## 3.1 $Nb_2O_5$ precursors

The XRD patterns of the $Nb_2O_5$-ortho and mono before and after milling are shown in Figure 1. The XRD patterns of the as-received $Nb_2O_5$-ortho and the as-received $Nb_2O_5$-mono can be indexed to the orthorhombic [7] and monoclinic [8] $Nb_2O_5$ unit cells, respectively. After milling, in the $Nb_2O_5$-mono new broad peaks were detected at 22.6, 28.5 and 36.7 °2θ. These peaks can be indexed to the orthorhombic $Nb_2O_5$ unit cell [7]. According to the Rietveld refinement of the milled $Nb_2O_5$-mono XRD spectra, the powder contained 53% of the monoclinic and 47% of the orthorhombic phase. Thus, our results show that with wet planetary milling the $Nb_2O_5$-mono was partially transformed to orthorhombic, while the $Nb_2O_5$-ortho retained its crystal structure.

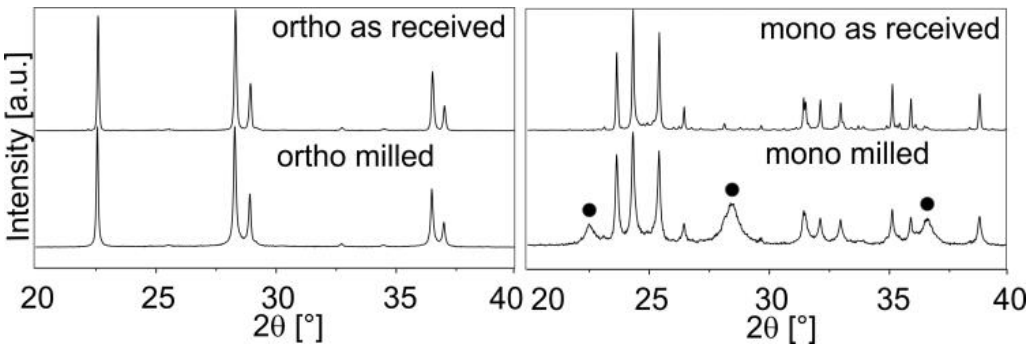


**Figure 1**: XRD patterns of $Nb_2O_5$ precursors: $Nb_2O_5$-ortho as-received and milled, $Nb_2O_5$-mono as-received and milled. Peaks marked with • correspond to the newly introduced orthorhombic phase.

According to Holtzberg et al. [6] the transformation from orthorhombic to the high-temperature-stable monoclinic $Nb_2O_5$ at 830°C is irreversible. Rojac [9] confirmed, that with cooling to room temperature the monoclinic $Nb_2O_5$ did not transform back to the orthorhombic form. However, after 10 hours of high-energy milling he observed a complete transformation of the monoclinic $Nb_2O_5$ to the orthorhombic one. Rojac explained the transformation of the monoclinic $Nb_2O_5$ to orthorhombic by the increased pressures of the collisions during the high-energy milling. Similarly, Senna [10] assigned the mechanochemical polymorphic transformation of PbO in the form of massicot to litharge by isothermal, wet ball-milling to mechanical effects. We therefore assume that similar mechanical effects during wet planetary milling caused the phase transformation of the monoclinic $Nb_2O_5$ to orthorhombic.

A closer look at the milled $Nb_2O_5$-mono powder was made possible by the high-resolution TEM (HR-TEM) (Figure 2). Nanocrystals of tens of nm are clearly seen on the surface of the larger particle. The diffraction spots of these nanocrystals obtained with a fast Fourier transform (FFT) (Figure 2 – inset left) correspond to the orthorhombic (001) plane reflections [7], while the spots from the larger particle (inset right) correspond to the monoclinic (-101) plane reflections [8].

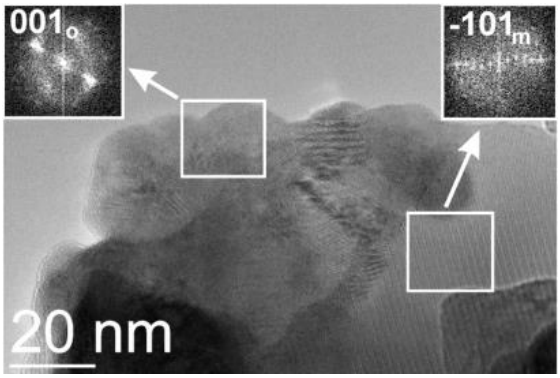


**Figure 2**: HR-TEM image of the milled $Nb_2O_5$-mono particles with insets showing FFTs of the selected areas.

The results from the TEM analysis are consistent with the XRD pattern in Figure 1. In addition, as revealed by the TEM analysis, the broader XRD peaks of the new orthorhombic phase introduced by milling are attributed to the orthorhombic nanocrystals attached to the surface of the relatively large monoclinic crystals.

### 3.2 Synthesis of $K_{0.5}Na_{0.5}NbO_3$

From the results above it is expected that the $Nb_2O_5$-mono would react in a different way with the carbonates than the $Nb_2O_5$-ortho. As shown in Figure 3a, the XRD pattern of the calcined KNN-ortho can be indexed with the $K_{0.5}Na_{0.5}NbO_3$ monoclinic perovskite unit cell according to Tellier [11]. In addition to the expected $K_{0.5}Na_{0.5}NbO_3$ perovskite peaks, the shoulders at higher °2θ are visible on the XRD pattern of the calcined KNN-mono (Figure 3a: KNN-mono calcined). These shoulders can be indexed to the $NaNbO_3$ unit cell (Figure 3b), e.g., [12]. Assuming the presence of the $NaNbO_3$ perovskite in the stoichiometric mixture of $K_{0.5}Na_{0.5}NbO_3$, a phase rich in potassium should also be present. The peaks of the $KNbO_3$ [13] perovskite overlap with the $K_{0.5}Na_{0.5}NbO_3$ peaks. Nevertheless, the XRD pattern of the KNN-mono after calcination could be indexed completely with a range of perovskite solid solutions of $(K_x, Na_{1-x})NbO_3$ with varying contents of K and Na throughout the material (Figure 3b). This suggests A-site inhomogeneities.

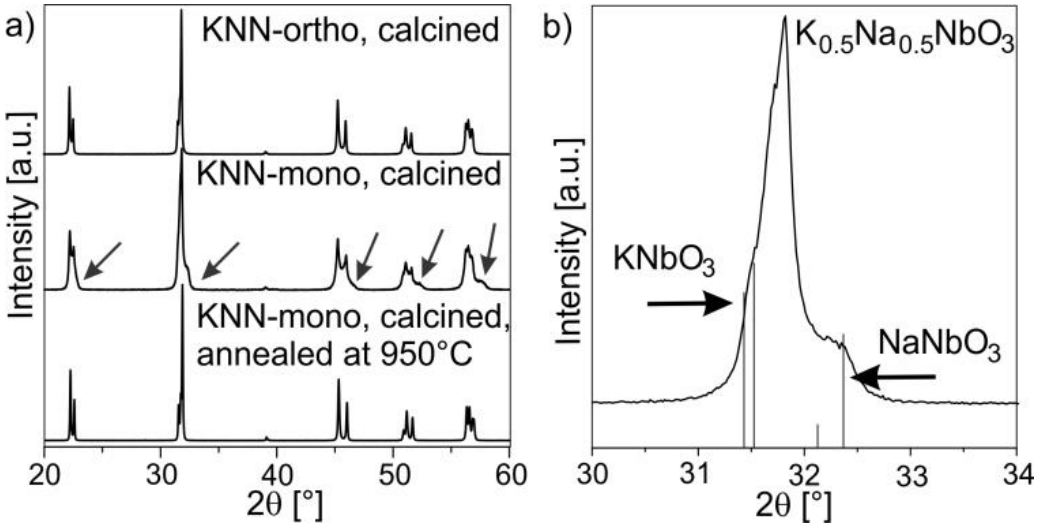


**Figure 3**: XRD patterns of powders: a) KNN-ortho, calcined, KNN-mono, calcined and KNN-mono, calcined and annealed at 950°C, 4h. The shoulders are marked with arrows b) enlarged view of {110} peaks of the calcined KNN-mono with the inserted patterns of $KNbO_3$ [13] and $NaNbO_3$ [12].

According to Malič et al. [14], homogeneous $K_{0.5}Na_{0.5}NbO_3$ is formed when annealed at temperatures as high as 950°C. With an additional annealing of our inhomogeneous, calcined KNN-mono powder (Figure 3a: KNN-mono, calcined) at 950°C for 4 h, a homogeneous $K_{0.5}Na_{0.5}NbO_3$ was obtained as well, i.e., the XRD pattern of the KNN-mono, calcined and annealed at 950°C, is consistent with the

XRD pattern of the calcined KNN-ortho (Figure 3a: KNN-mono, calcined, annealed at 950°C and KNN-ortho, calcined).

The probable origin of the different reaction of the $K_{0.5}Na_{0.5}NbO_3$ when using milled $Nb_2O_5$-ortho or -mono is the presence of the orthorhombic $Nb_2O_5$ nanocrystallites in the milled $Nb_2O_5$-mono. In a study of the diffusion couples in $K_{0.5}Na_{0.5}NbO_3$ [3], the reaction in the $Na_2CO_3/Nb_2O_5$ diffusion couple started at 500°C, while for the $K_2CO_3/Nb_2O_5$ diffusion couple it started only at 600°C. Besides that, the parabolic rate constant at 600°C for the $Na_2CO_3/Nb_2O_5$ diffusion couple was ten times higher than for the $K_2CO_3/Nb_2O_5$ diffusion couple ($1x10^{-14}$ $m^2/s$ versus $3x10^{-15}$ $m^2/s$, respectively). This means that $Na_2CO_3$ starts reacting at a lower temperature and at 600°C it diffuses faster into the $Nb_2O_5$ than the $K^+$. It is also necessary to consider the higher reactivity of the $Nb_2O_5$ nanoparticles, because of the high curvature and high surface free energy of the crystals in the nanorange [15]. Moreover, the nanocrystals are on the surface of the $Nb_2O_5$ particles (Figure 2), so they are the first in contact with the carbonates. Since the $Na_2CO_3$ starts reacting with nanocrystalline $Nb_2O_5$ at lower temperatures and the diffusion paths through the $Nb_2O_5$ nanocrystals are very short (tens of nm), $Na_2CO_3$ and $Nb_2O_5$ nanocrystals would react predominantly, forming the $NaNbO_3$. The $K_2CO_3$ and a part of the unreacted $Na_2CO_3$ would then react at higher temperatures during heating with the remaining larger monoclinic $Nb_2O_5$ crystals. This would result in the coexistence of phases like $NaNbO_3$, $KNbO_3$ and/or inhomogeneous $(K_x, Na_{1-x})NbO_3$ solid solutions, at the end of the reaction, as shown in the XRD pattern of the calcined powders in Figure 3.

### 3.3 Densification of $K_{0.5}Na_{0.5}NbO_3$

The shrinkage curves together with SEM images of the sintered ceramics are presented in Figure 4. The densities of the sintered ceramics are shown in Table I. While the shrinkage behaviour of the calcined KNN-ortho is comparable to the one usually reported for $K_{0.5}Na_{0.5}NbO_3$ [16], both KNN-mono and KNN-mono additionally annealed have modified densification behaviour (Figure 4). This suggests the effect of the $Nb_2O_5$-mono precursor manifested in the A-site inhomogeneity in the KNN-mono after the calcination, could not be completely eliminated by further annealing and has an impact on the sintering behavior and final microstructure.

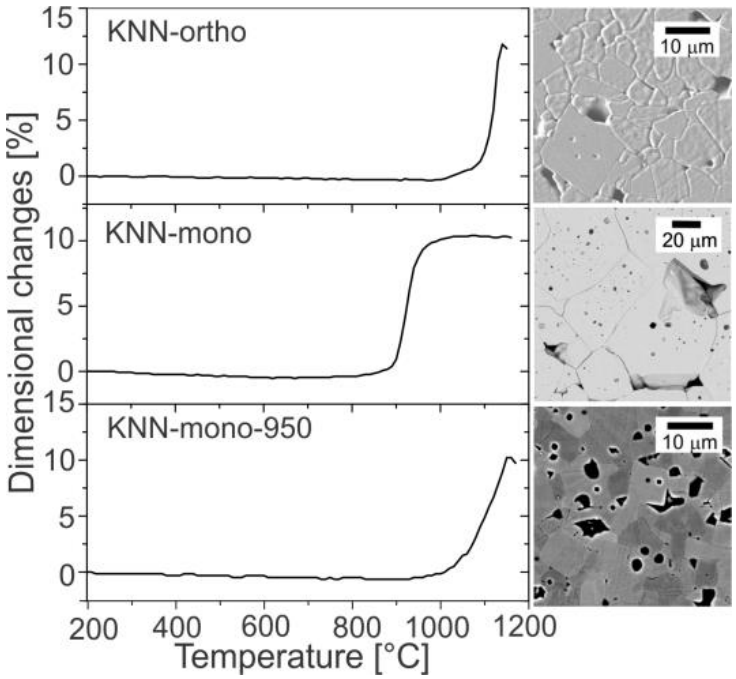


**Figure 4**: Dimensional changes with temperature of the calcined KNN-ortho, calcined KNN-mono and calcined and additionally annealed KNN-mono and corresponding SEM images of the ceramics sintered at 1120°C, 2h

**Table I**: Archimedes densities of the sintered ceramics

| Powder | Density [g/cm3] | Theoretical density* [%] |
|---|---|---|
| KNN-ortho | 4.17(2) | 92.4(4) |
| KNN-mono | 4.21(3) | 93.4(7) |
| KNN-mono-950 | 3.91(1)† | 86.6(1)† |

* theoretical density of $K_{0.5}Na_{0.5}NbO_3$ = 4.51 g/cm$^3$ (based on the Rietveld refinement of the monoclinic unit cell according to Tellier [11])
† measured as geometric density

The reason for the difference between the KNN-ortho and the KNN-mono sinterabilities and microstructures is most probably the starting A-site inhomogeneity of the KNN-mono after calcination. The densification and grain growth of the $(K_xNa_{1-x})NbO_3$ solid solution, which is richer in K, occurs at different rates and lower temperatures than in the case of the solid solution that is richer in Na. This results in the observed abnormal growth of certain grains (Figure 4: KNN-mono). Abnormal grain growth was not observed in the case of KNN-mono-950 sintered ceramics, however, this ceramic had a lower density (see Table I) than the KNN-ortho ceramic. The poor density of the KNN-mono-950 is most probably related to the high temperature of the additional annealing which caused coarsening of the

particles. Although the powder was subsequently planetary milled, it was not possible to obtain as fine particles as in the case of the calcined KNN-ortho.

## 4 Conclusion

This study shows that the partial transformation of the monoclinic $Nb_2O_5$ to the orthorhombic nanocrystals during wet planetary milling and the resulting bimodal particle size distribution of $Nb_2O_5$ play a crucial role in determining the A-site homogeneity of the potassium sodium niobate solid solution and crucially influence the densification behaviour of the KNN powders. To achieve a higher reproducibility in the processing of the $K_{0.5}Na_{0.5}NbO_3$, this point is important and was not considered so far.

## References:


[1] A. Safari, E. K. Akdogan. *Piezoelectric and acoustic materials for transducer applications*. New York: Springer; 2008.

[2] J. Rödel, W. Jo, K. T. P. Seifert, E. M. Anton, T. Granzow, D. Damjanovic. Perspective on the Development of Lead-free Piezoceramics. *Journal of the American Ceramic Society*, 92(6): 1153-1177, 2009

[3] B. Malic, D. Jenko, J. Holc, M. Hrovat, M. Kosec. Synthesis of sodium potassium niobate: A diffusion couples study. *Journal of the American Ceramic Society* 91: 1916-1922, 2008.

[4] L. K. Templeton, J. A. Pask, Formation of $BaTiO_3$ from $BaCO_3$ and $TiO_2$ in Air and in $CO_2$. *Journal of the American Ceramic Society* 42: 212-216, 1959.

[5] M. T. Buscaglia, M. Bassoli, V. Buscaglia, R. Alessio. Solid-State Synthesis of Ultrafine $BaTiO_3$ Powders from Nanocrystalline $BaCO_3$ and $TiO_2$. *Journal of the American Ceramic Society* 88: 2374-2379, 2005.

[6] F. Holtzberg, A. Reisman, M. Berry, M. Berkenblit. Chemistry of the Group VB Pentoxides. VI. The Polymorphism of $Nb_2O_5$. *Journal of the American Chemical Society* 79: 2039-2043, 1957.

[7] 01-071-0336, JCPDS-ICCD. *International centre for powder diffraction data*, 2002.

[8] 00-037-1468, JCPDS-ICCD. *International centre for powder diffraction data*, 2002.

[9] T. Rojac. Mechanochemical Synthesis of $NaNbO_3$. *University of Ljubljana, Faculty of Chemistry and Chemical Technology*, PhD Thesis, Ljubljana, 2007

[10] M. Senna, H. Kuno. Polymorphic Transformation of PbO by Isothermal Wet Ball-Milling. *Journal of the American Ceramic Society* 54: 259-262, 1971.

[11] J. Tellier, B. Malic, B. Dkhil, D. Jenko, J. Cilensek, M. Kosec. Crystal structure and phase transitions of sodium potassium niobate perovskites. *Solid State Sciences* 11: 320-324, 2009.

[12] 01-077-0873, JCPDS-ICCD. *International centre for powder diffraction data*, 2002.

[13] 01-071-0947, JCPDS-ICCD. *International centre for powder diffraction data*, 2002.

[14] C. Herring. Some Theorems on the Free Energies of Crystal Surfaces. *Physical Review* 82: 87-93, 1951.

[15] B. Malic, J. Bernard, A. Bencan, M. Kosec. Influence of zirconia addition on the microstructure of $K_{0.5}Na_{0.5}NbO_3$ ceramics. *Journal of the European Ceramic Society* 28: 1191-1196, 2008.

[16] M. Kosec, D. Kolar. On activated sintering and electrical properties of $NaKNbO_3$. *Materials Research Bulletin* 10: 335-339, 1975.

## For wider interest

In the last decade, a lot of effort has been dedicated in the field of piezoelectric ceramics to finding environmentally friendly lead-free materials which would substitute the currently mostly used lead zirconate titanate (PZT). In 2004, Saito et al. from Toyota Central Research Laboratory reported a high-performing material based on potassium sodium niobate solid solution (KNN).

Difficult processing of KNN-based materials hinders them from being used in larger scale. This ceramic system is sensitive to development of secondary phases during synthesis, tends to exhibit abnormal grain growth and is difficult to obtain in high densities by conventional sintering.

$Nb_2O_5$ is mostly used as a precursor for the solid-state synthesis of KNN materials. We observed that when using different $Nb_2O_5$ precursors for the solid-state synthesis of $K_{0.5}Na_{0.5}NbO_3$, ceramics of extremely different quality would be obtained.

Two batches of $K_{0.5}Na_{0.5}NbO_3$ were prepared using the same procedure, but different $Nb_2O_5$; i.e. orthorhombic and monoclinic. In order to reduce the large particle size of the as received $Nb_2O_5$ precursors, both powders were planetary milled. Although, the as-received orthorhombic $Nb_2O_5$ remained unchanged by the milling step, the as-received monoclinic $Nb_2O_5$ after milling partially transformed to nanoparticles with orthorhombic syngony, which were attached to the surface of the remaining micron-sized monoclinic particles. This two-phase $Nb_2O_5$ reacted to form inhomogeneous potassium sodium solid solution, which resulted in the abnormal grain growth during the densification. The inhomogeneous powder was additionally homogenized by annealing at elevated temperature and sintered. Sintering of this powder resulted in the ceramics with very poor density (86.6% TD). The as-received orthorhombic $Nb_2O_5$ yielded ceramics with uniform grain size and usual density of 92.4% TD.

This study shows that the choice of the $Nb_2O_5$ precursor phase is of a key importance for the quality of the final ceramics. Care should be taken with the phase composition and the particle size distribution of the starting powders as they are received from the producer.

# Pump-probe reflectivity study of $HgBa_2CuO_{4+\delta}$ cuprate superconductor

**Ivan Madan**[1,2], **Janusz Karpinski**[3], **Tomaž Mertelj**[1], **Dragan Mihailović**[1]

[1] Department of Complex matter, Jožef Stefan Institute, Ljubljana, Slovenia

[2] Jožef Stefan International Postgraduate School, Ljubljana, Slovenia

[3] ETH Zuirch, Zurich, Switzerland

ivan.madan@ijs.si

**Abstract.** $HgBa_2CuO_{4+\delta}$ (Hg-1201) cuprate compound is a single Cu-O layer member of mercury cuprate superconductor family. We present general characterization of the nonequilibrium relaxation dynamics: focusing on its temperature and polarization dependence. We also investigate photodestruction of superconducting condensate by ultrafast laser pulses and the ensuing recovery. We find that superconducting fluctuations make a significant contribution to the transient reflectivity in the temperature region >25 K above $T_c$.

**Keywords**: high-temperature superconductivity, fluctuations.

## 1 Introduction

Copper oxide (cuprate) superconductors are a family of compounds with highest known critical temperatures, in a wide zoo of currently known superconductor families: BCS, pnictides, organic salts, $MgB_2$ and others. An enormous amount of research has been done since 1986 and still ongoing for clarifying the physical mechanism responsible for superconductivity in cuprates. Cuprates are interesting from the physical point of view not only as superconductors, but because a number of different orders coexist and compete in these compounds. Insulating antiferromagnet, spin glass, pseudogap, "strange" metal, conventional Fermi liquid metal and in some cases charge density wave are the states which, apart from superconductivity mark different regions on the phase diagram of cuprates (see fig. 1).

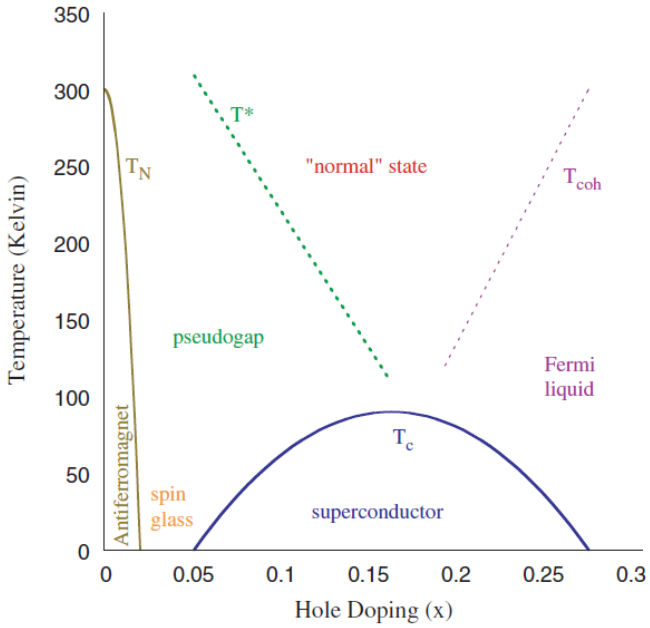


**Figure 1**: Phase diagram of cuprate superconductor (figure is copied from [1])

Superconducting properties in cuprates appeared to be distinct from those observed in conventional BCS superconductors – cuprates are strong type II superconductors with 0K coherence length of the order of just 1 nm and d-wave symmetry of the superconducting gap [2]. The superconducting transition itself is not completely understood even from thermodynamic point of view [3], especially in highly anisotropic compounds such as BiSCO and HBCCO in underdoped region of phase diagram. Here the possibility of separate pairing and phase coherence are discussed within several models. 1) Bose-Einstein condensation (BEC)[4] of bipolarons assumes that hole-polarons form a bipolaron at the pseudogap temperature T*. This leads to the formation of temperature independent gap in single-particle excitation spectra. At the critical temperature Tc bipolaron form Bose-condensate, and macroscopic phase coherence is established. 2) Berezinski-Kosterlitz-Thouless (BKT)[5]–[7] theory is a distinct approach to the problem. With increase of temperature in the superconducting state the number of thermally activated vortex-antivortex pairs increases accordingly to the Boltzman law. At the critical temperature vortices start to overlap and screen each other, thus destroying the macroscopic phase coherence. The instantaneous pair density however remains finite and obeys mean field law disappearing at $T_{onset}>T_c$.

In this work we perform pump-probe characterization of the model compound of Hg based superconductors and particularly discuss the presence of the transient reflectivity signal above the critical temperature.

# 2 Results

## 2.1 Samples and techniques

Samples were prepared in Zurich by a high-gas-pressure synthesis. Samples, of the lateral size of 100-200 μm were glued on a sapphire substrate and mounted in a liquid flow He-cryostat. 250 KHz 50 fs 800 nm laser pulses from Ti:Saphire regenerative amplifier were used.

Laser beam was split in three shoulders with variable delay in between. For all the experiments apart from recovery of the superconducting state two shoulders were used. In the text we use following abbreviation for the pulses from different shoulders: destruction (D) pulse, comes first and is most powerful, aimed for photodestruction of superconducting condensate, pump (P) pulse with fluence lower compared to photodestruction threshold (typically 1 $\mu J/cm^2$) and probe (pr) pulse for probing changes in reflectivity. We use lock-in detection with modulation of the pump beam, so only the changes in reflectivity caused by pump are seen.

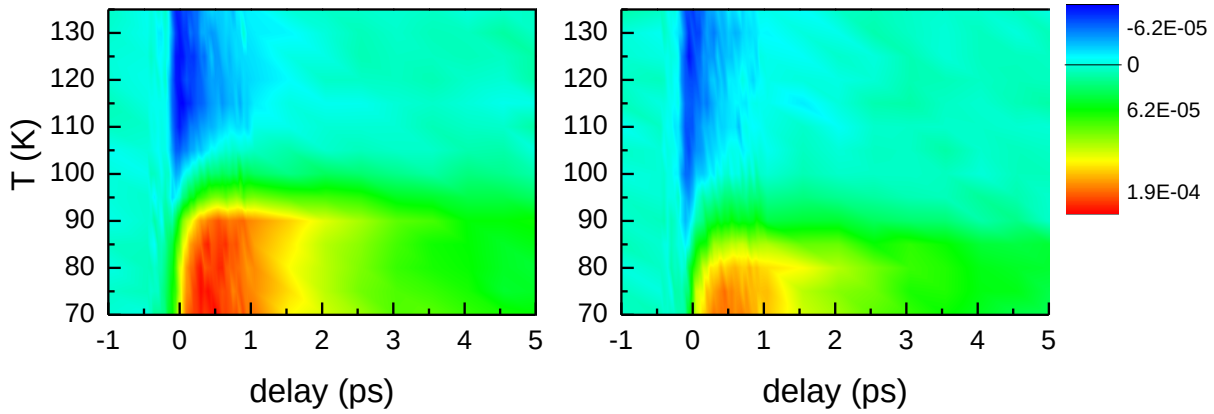


**Figure 2**: Temperature dependence of transient reflectivity for two measured sample consists of negative shortlived pseudogap component and slow positive divergent at $T_c$ superconducting component. Colour represents ΔR/R, for delays before 0 ps. signal is equal to 0.

In fig. 2 we show transient reflectivity change in the vicinity of the superconducting transition for two available samples. The critical temperature of the sample strongly depends on the oxygen doping level. Optimally doped Hg1201 has critical temperature of 94 K [8]. In pump-probe response the critical slowing down of positive superconducting signal at the critical temperature is clearly observed, so we can estimate $T_c$ for our samples to be ~90 and 79 K. Further in text we discuss nearly optimally 90 K sample.

It has been previously shown that the pseudogap response monotonically increase with decrease of temperature [9]. Since the pseudogap component has negative sign the presence of the positive component in the response above $T_c$ is attributed to the superconducting fluctuations. Optical response is sensitive to the gap and insensitive to the phase of the condensate[10], thus suggesting presence of superconducting pairs up to ~ 112 K and 125 K for the samples with 90 and 79 K $T_c$ respectively, larger onset temperature for the sample with smaller $T_c$ suggests that 79 K $T_c$ sample is underdoped [11].

## 2.2 Fluence dependence

Energy of absorbed pump photon is dissipated into non-equilibrium phonons during initial sub-ps equilibration process. Phonons with frequency $w>2\Delta$ destroy superconducting pairs, creating two quasiparticles above the gap [12]. We use a simple model which assumes that change in reflectivity is directly proportional to the number of quasiparticles excited and is limited by complete destruction of superconducting condensate [13].
Taking into account the inhomogeneity of depth and lateral profiles we obtain the fit value of photodestruction fluence $F_{sat}$=10.1±0.3 μJ/cm$^2$.

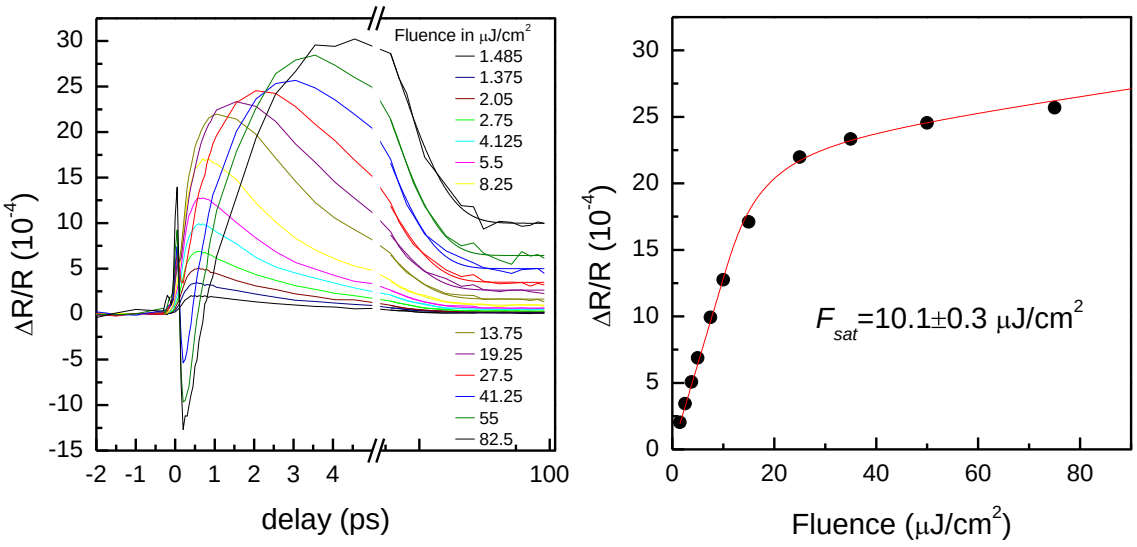


**Figure 3**: Fluence dependence of ΔR/R at 70 K. Left – superconducting component linearly grows and eventually saturates, at high *F* negative pseudogap component appears. After the break the relaxation is fitted by an exponential function with an offset. Right – fluence dependence of the amplitude and fit curve (see text).

## 2.3 Polarization dependence

Previously anisotropy of pump probe response was reported for YBCO [14] and BSCCO [10] cuprate superconductors, which is not expected for systems with $D_{4h}$ symmetry in dissipative process of quasiparticle excitation. It can be related either to the presence of Cu-O chains [14], which is not the case for Hg1201, or to the symmetry reduction due to the presence of some hidden order [10].

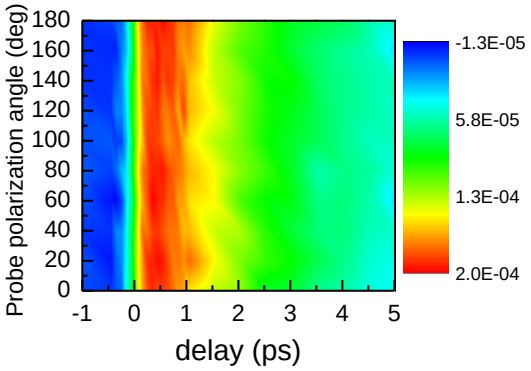


**Figure 4**: Probe polarization angle dependence at 70 K. Colour represents ΔR/R, for delays before 0 ps. signal is equal to 0.

In fig. 4 we present dependence of the pump-probe response on the initial probe polarization angle. No signature of anisotropy within the noise level is observed. This implies that there is no symmetry breaking in this compound which can be associated with the pseudogap or superconducting state at low temperatures

## 2.4 Superconducting state recovery

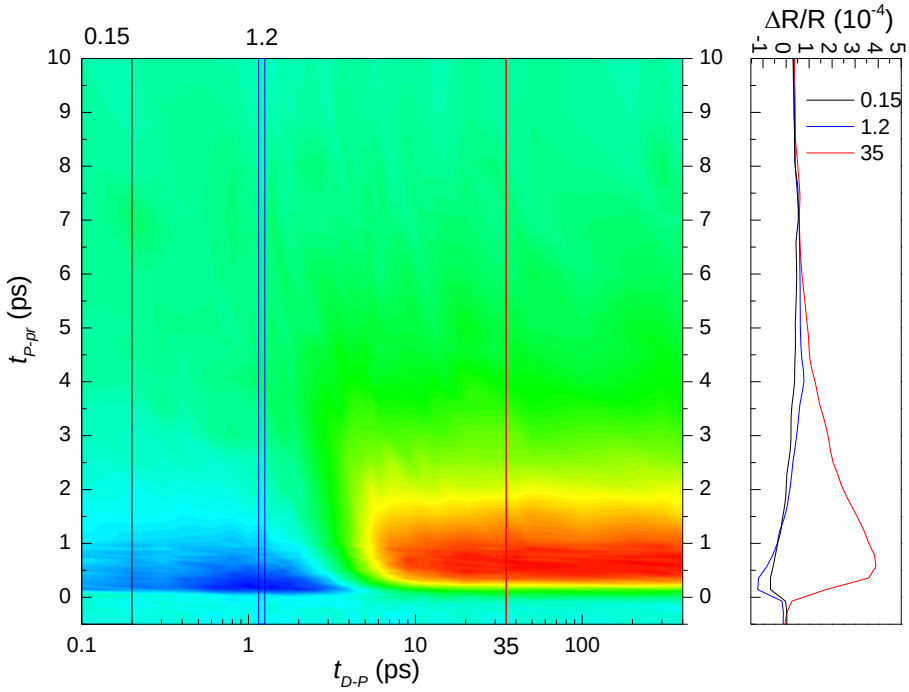


**Figure 5**: Recovery of the pseudogap and superconducting component after the photodestruction. On the right panel traces for three characteristic delays between D and P pulses: 0.15 ps pseudogap and superconducting responses are suppressed, 1.2 ps - pseudogap response has recovered, 35 ps – superconducting response has recovered. Colour represents ΔR/R.

Previously we have seen that superconducting condensate can be effectively destroyed by a femtosecond laser pulse. In this section we perform advanced 3-pulse experiment conducted to study the recovery of superconducting signal after photodestruction. Immediately after D pulse arrival disappearance of the superconducting signal is observed (fig. 5), with ensuing recovery. For the highest fluence also the pseudogap signal is suppressed and recovers prior the recovery of the superconducting component.

Plots of the readout of the amplitude at 0.7 ps P-pr delay is shown in fig. 6. Two characteristic features are observed: 1) For high fluences the recovery of the superconducting state is delayed and 2) Recovery is faster than exponential unlike exponential relaxation of quasiparticles seen in 2-pulse experiment, which implies that not solely photoinduced quasiparticles are involved in the gap recovery. These features, however, might also appear as an artefact of the overlap of two recovering signals of different sign. For more solid statements one needs to be able to separate components experimentally.

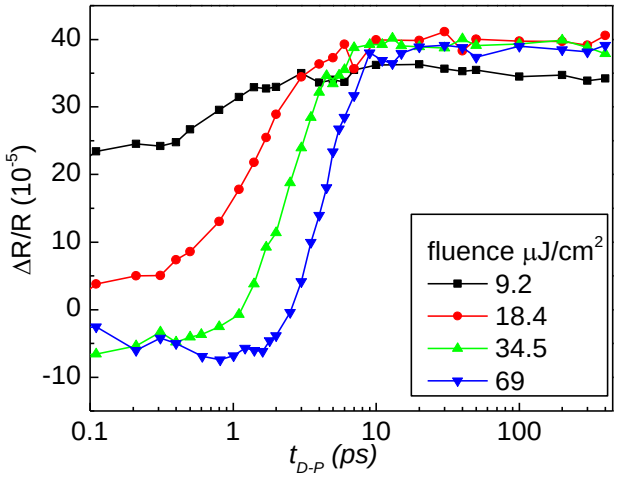


**Figure 6**: ΔR/R at $t_{P\text{-}pr}$=0.7 ps as a function of delay between D and P pulses

## 3 Conclusions

Temperature, fluence, polarization dependences and recovery after the photodestruction have been studied. Large region of superconducting fluctuations ~25 K is observed in favour of separate pairing and phase coherence scenario. Destruction of superconducting response occurs above $F_{sat}$=10.1±0.3 μJ/cm² with an ensuing superexponential delayed recovery.

# References:


[1] M. R. Norman, D. Pines, and C. Kallin, "The pseudogap: friend or foe of high T c ?," *Adv. Phys.*, vol. 54, no. 8, pp. 715–733, Dec. 2005.

[2] N. Plakida, *High-Temperature Cuprate Superconductors*, vol. 166. Berlin, Heidelberg: Springer Berlin Heidelberg, 2010.

[3] J. W. Loram and J. L. Tallon, "Thermodynamic transitions in inhomogeneous cuprate superconductors," pp. 1–5, 2008.

[4] A. S. Alexandrov, "Theory of high-temperature superconductivity in doped polar insulators," *EPL (Europhysics Lett.*, vol. 95, no. 2, p. 27004, Jul. 2011.

[5] V. L. Berezinsii, "Destruction of long-range order in one-dimensional and two-dimensional systems having a continuous symmetry group i. classical systems," *Sov. Phys. JETP*, vol. 32, no. 3, pp. 2–9, 1971.

[6] J. M. Kosterlitz and D. J. Thouless, "Ordering, metastability and phase transitions in two-dimensional systems," *J. Phys. C Solid State Phys.*, vol. 6, no. 7, pp. 1181–1203, Apr. 1973.

[7] V. J. Emery and S. A. Kivelson, "Importance of phase fluctuations in superconductors with small superfluid density," *Nature*, vol. 374, no. 6521, pp. 434–437, Mar. 1995.

[8] S. N. Putilin, E. V. Antipov, O. Chmaissem, and M. Marezio, "Superconductivity at 94 K in HgBa2Cu04+δ," *Nature*, vol. 362, no. 6417, pp. 226–228, Mar. 1993.

[9] Y. Liu, Y. Toda, K. Shimatake, N. Momono, M. Oda, and M. Ido, "Direct Observation of the Coexistence of the Pseudogap and Superconducting Quasiparticles in Bi2Sr2CaCu2O8+y by Time-Resolved Optical Spectroscopy," *Phys. Rev. Lett.*, vol. 101, no. 13, pp. 1–4, Sep. 2008.

[10] Y. Toda, F. Kawanokami, T. Kurosawa, M. Oda, I. Madan, T. Mertelj, V. V Kabanov, and D. Mihailovic, "Dynamics of broken symmetry nodal and anti-nodal excitations in Bi_{2} Sr_{2} CaCu_{2} O_{8+\delta} probed by polarized femtosecond spectroscopy," no. Dm, pp. 1–5, Nov. 2013.

[11] L. Li, Y. Wang, S. Komiya, S. Ono, Y. Ando, G. D. Gu, and N. P. Ong, "Diamagnetism and Cooper pairing above T_{c} in cuprates," *Phys. Rev. B*, vol. 81, no. 5, pp. 1–9, Feb. 2010.

[12] L. Stojchevska, P. Kusar, T. Mertelj, V. V. Kabanov, Y. Toda, X. Yao, and D. Mihailovic, "Mechanisms of nonthermal destruction of the superconducting state and melting of the charge-density-wave state by femtosecond laser pulses," *Phys. Rev. B*, vol. 84, no. 18, p. 180507, Nov. 2011.

[13] P. Kusar, V. V Kabanov, J. Demsar, T. Mertelj, S. Sugai, and D. Mihailovic, "Controlled Vaporization of the Superconducting Condensate in Cuprate Superconductors by Femtosecond Photoexcitation," *Phys. Rev. Lett.*, vol. 101, no. 22, pp. 1–4, Nov. 2008.

[14] D. Dvorsek, V. Kabanov, J. Demsar, S. Kazakov, J. Karpinski, and D. Mihailovic, "Femtosecond quasiparticle relaxation dynamics and probe polarization anisotropy in YSrxBa2-xCu4O8 (x=0,0.4)," *Phys. Rev. B*, vol. 66, no. 2, p. 020510, Jul. 2002.

## For wider interest

Superconductors - materials which can conduct electricity without losses. Highest temperature at which known material exist in a superconducting state is -135 C at ambient pressure. Even though this temperature seems to be very low these materials are already widely used in industry, particularly due to their magnetic properties. In this work we study dynamical properties of the superconducting state of one of such materials. How fast can superconductor react to external perturbation? To which extent can we control this process?

To answer these questions we first excite the superconductor by very short laser pulse (50 femtosecond, i.e. 50 millionth of a billionth of a second long) and afterwards by the similar pulse study how the state response. It appears that for this particular mercury based superconductor superconductivity is perturbed already in 300 fs and in 10000 fs relaxes to its initial state. We can not only perturb, but also completely destroy the superconducting state, and the sample will stay for a while in a non-superconducting state, the harder we excite the longer it will stay.
One can think of a practical application of these properties. Most basic element for computing – a transistor (or in simpler words a switch) can be made of a superconductor and switched by light on an extremely short timescales, which are several orders of magnitude faster than today's electronics.

Not only electric but also optical properties can be changed if the metamaterials are constructed from superconductors. Optical switches are extremely important in laser and communication technologies.

Hopefully one day the main disadvantage of these materials – low working temperature will be overcome, and superconductors will enter every house.

# Synthesis and functionalization of α-$NaYF_4$ nanoparticles

**Olivija Plohl**[1,2], **Darja Lisjak**[1,2], **Maja Ponikvar-Svet**[4], **Slavko Kralj**[1], **Darko Makovec**[1,2,3]

[1] Department of K8, Jožef Stefan Institute, Ljubljana, Slovenia

[2] Jožef Stefan International Postgraduate School, Ljubljana, Slovenia

[3] CENN Nanocenter, Ljubljana, Slovenia

[4] Department of K1, Jožef Stefan Institute, Ljubljana, Slovenia

olivija.plohl@ijs.si

**Abstract.** In this paper the synthesis of α-$NaYF_4$ nanoparticles with coprecipitation under reflux using ethylene glycol as a solvent and polyvinylpyrrolidone as stabilizing agent is described. The polyvinylpyrrolidone stabilized nanoparticles in ethanol were coated with silica using modified Stöber procedure. The silica coated nanoparticles were further functionalized with aminopropyltriethoxysilane and dispersed in water. The efficiency of the two processes was confirmed with electrokinetic measurements (from zeta potential and isoelectric point). Morphology and chemical composition of the synthesized nanoparticles was characterized with transmission electron microscopy combined with energy-dispersive X-ray spectroscopy while their crystal structure was analysed with X-ray powder diffraction. The chemical instability of the as-synthesized nanoparticles was observed in aqueous media and the released fluoride ion in aqueous media was measured with fluoride ion selective electrode. The efficiency of the silica coating against the dissolution of fluoride was examined.

**Keywords**: functionalization, lanthanides, nanoparticles, coprecipitation under reflux

## 1 Introduction

There is a growing interest for the development of fast, inexpensive and sensitive techniques that enable the analysis of biocomponents in one step. Bioimaging provides most of these options using biolabels. Recently, lanthanide-doped nanoparticles, which show upconversion (i.e., process, where the emission

wavelength is smaller than the excitation wavelength), were proposed as alternative biolabels for fluorescence bioimaging. In lanthanide-doped upconverting nanoparticles the crystalline host matrix is doped with sensitizer ion (e.g., $Yb^{3+}$), which absorbs the excitation radiation with specific wavelength and with active ions (e.g., $Er^{3+}$, $Tm^{3+}$, $Ho^{3+}$), which emit at shorter wavelength after a nonradiative energy transfer from the sensitizer (Figure 1). The most extensively studied host matrices are fluorides, because they can incorporate lanthanide ions, exhibit low phonon energies and high chemical stability. Therefore, they are often used as host materials for the upconversion process [1,2]. One such host matrix is cubic phase of sodium yttrium fluoride (α-$NaYF_4$). In this report we describe precipitation synthesis under reflux of α-$NaYF_4$ nanoparticles using ethylene glycol (EG) as a solvent and polyvinylpyrrolidone (PVP) as a stabilizing agent. Synthesized nanoparticles were coated with a silica layer and functionalized with aminopropyltriethoxysilane (APS). The purpose of this work was to examine the chemical stability of α-$NaYF_4$ in aqueous media.

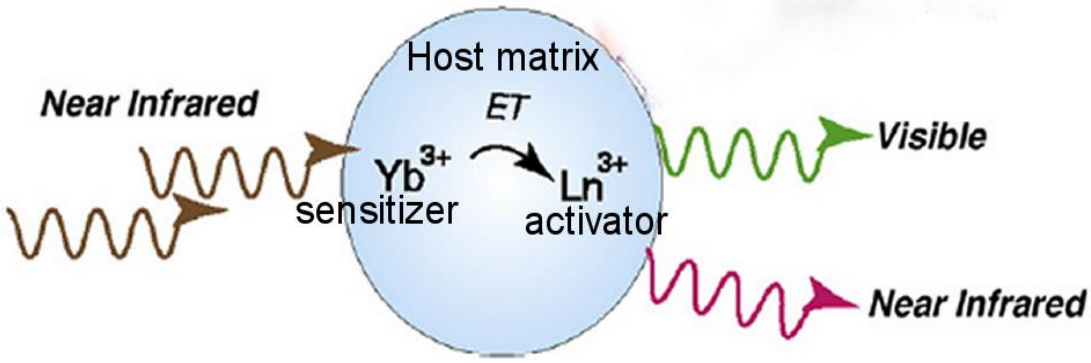


**Figure 1:** Schematic presentation of the upconverting mechanism in lanthanide-doped nanoparticles [3].

## 2 Experimental work

α-$NaYF_4$ nanoparticles were synthesized in EG with coprecipitation [4] at 160 °C for 2 h. 1 mmol of $Y(NO_3)_3x6H_2O$ was added to 30 mL of EG to dissolve the obtained precursor. PVP40 (0.556 g) and NaCl (1 mmol) were subsequently added and the solution was heated to 80 °C until a homogeneous solution was formed. $NH_4F$ (4 mmol) was dissolved in 20 mL of EG at 80 °C and added dropwise to the previous solution, which was maintained at 80 °C for 10 min under stirring. The mixed solution was heated to 160 °C under reflux for 2 h and then cooled to room temperature. The product was isolated by centrifugation and washed twice with absolute ethanol.

A typical procedure [4] for the coating of silica onto the α-$NaYF_4$/PVP nanoparticles was applied. As-synthesized α-$NaYF_4$/PVP nanoparticles were dispersed in ethanol (20 mL) and mixed with water (4 mL) and ammonia (0.6 mL, 25 %). Tetraethoxysilane (TEOS, 0.1 or 0.2 mL) dissolved in 10 mL of ethanol was then added slowly to the solution with continuous stirring. The product α-$NaYF_4$@$SiO_2$ nanoparticles were isolated by centrifugation and washed twice with ethanol.

The obtained purified α-$NaYF_4$@$SiO_2$ nanoparticles were dispersed in 30 mL of ethanol and then 3 mL of APS was added to form a mixture that reacted under refluxing at 80 °C for 3 h [5]. The resultant was washed with deionized water for several times and dried to obtain α-$NaYF_4$@$SiO_2$-APS. The nanoparticles were dispersed in water.

The crystal structure of synthesized nanoparticles was verified by X-ray powder diffraction (XRD). The crystallite size was determined from the X-ray diffractograms with the Pawley method [6] using the crystallographic program Topas2R 2000 (Bruker AXS). Morphology and chemical compositions of the synthesized nanoparticles was analysed with transmission electron microscopy (TEM) combined with energy dispersive X-ray spectroscopy (EDXS). Zeta potential of the nanoparticles and isoelectric point was determined from electrokinetic measurements in aqueous solution at pH range from 2 to 11. pH was corrected with HCl or NaOH. The concentration of released fluoride ion from nanoparticles in

aqueous media was determined with fluoride ion selective electrode. Solutions for the fluoride analysis were prepared by centrifugation of the aqueous suspensions to remove the synthesized nanoparticles and then supernatant was ultrafiltrated to eliminate the potentially remaining nanoparticles from the solution. Such prepared samples were used for measurements of released fluoride ion.

## 3 Results and discussion

We synthesized α-$NaYF_4$ nanoparticles with coprecipitation under reflux and checked their stability in aqueous media. The stability of the as-synthesized α-$NaYF_4$ in water was poor. A high concentration of the dissolved fluoride ion, 20.0 mg/l, suggested that such nanoparticles would degraded severely in aqueous suspensions and are therefore not suitable for the biomedical applications. According to our knowledge, no studies on the stability of α-$NaYF_4$ in water has been reported yet. Our aim was to coat the α-$NaYF_4$ nanoparticles with a protective layer that would prevent their decomposition. For this purpose we coated as-synthesized α-$NaYF_4$ nanoparticles with silica coatings.

The XRD patterns of the α-$NaYF_4$ and α-$NaYF_4$@$SiO_2$ nanoparticles agree well with the data for the cubic $NaYF_4$ structure (JCPDS card No. 77-2042, a=5.470, space group: Fm3m), thus indicating a high purity of the obtained nanoparticles (Figure 2). Well defined XRD peaks suggest on the high crystallinity of nanoparticles. The size of nanocrystallites was around 70 nm for α-$NaYF_4$ and for α-$NaYF_4$@$SiO_2$ nanoparticles. These results are in good agreement with TEM analyses, described below.

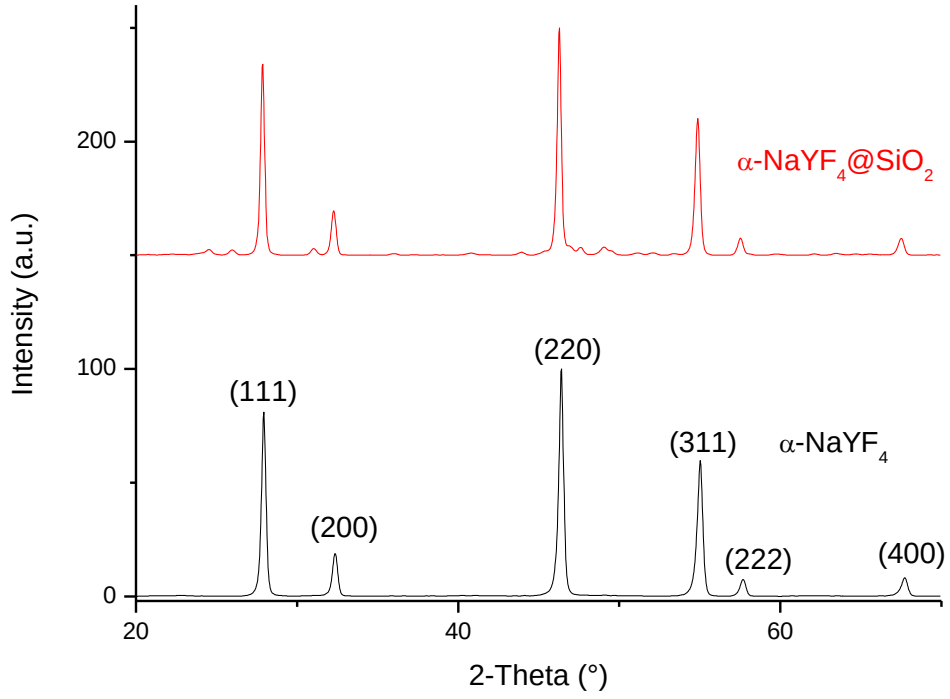


**Figure 2:** XRD patterns of α-$NaYF_4$ and α-$NaYF_4$@$SiO_2$.

The as-synthesized α-$NaYF_4$ nanoparticles are polyhedral in shape (Figure 3a). TEM images of the silica coated α-$NaYF_4$ nanoparticles show core-shell structured α-$NaYF_4$@$SiO_2$ nanoparticles with very uniform layer of silica shell. As suggested from selected area electron diffraction (SAED) particles are well crystalline with the cubic structure of α-$NaYF_4$ (see insets in Figure 3). TEM studies show that the size of α-$NaYF_4$ nanoparticles synthesized in EG is around 75 nm and the thickness of silica coatings of α-$NaYF_4$@$SiO_2$ is around 3 nm (Figure 3b), when 0.1 mL TEOS was added, and 8 nm (Figure 3c), when 0.2 mL TEOS was added.

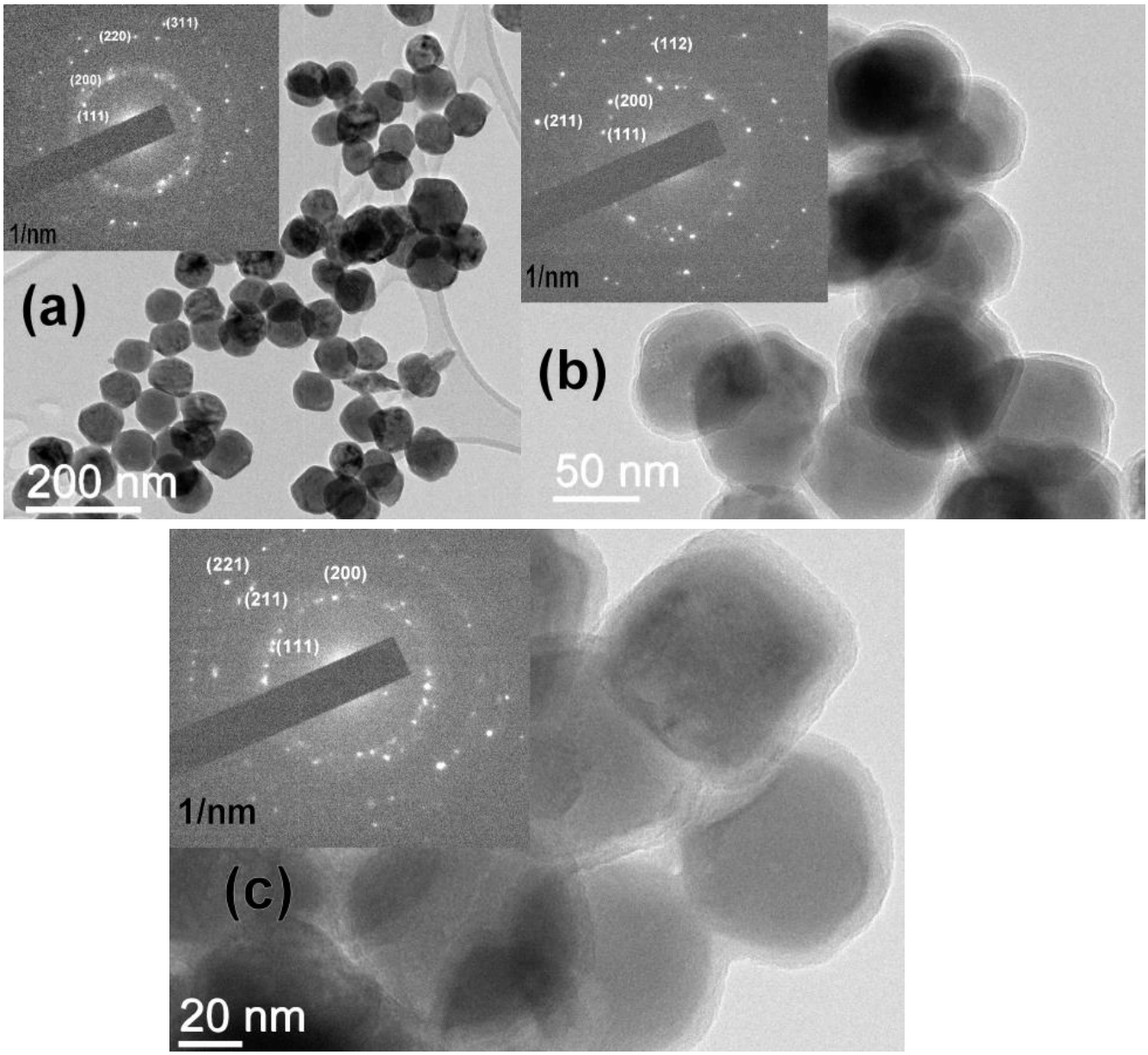


**Figure 3:** TEM images of α-$NaYF_4$ nanoparticles synthesized at 160 °C for 2 h (a), α-$NaYF_4$@$SiO_2$ nanoparticles, with uniform silica shell of about 3 nm (b) and α-$NaYF_4$@$SiO_2$ nanoparticles with uniform silica shell of about 8 nm (c).

EDXS analysis of the α-$NaYF_4$ nanoparticles confirmed that the main present elements are Na, Y, F, together with a minor fraction of oxygen. The later may originate from EG or PVP. EDXS analysis of the α-$NaYF_4$@$SiO_2$ confirmed that the main elements are Na, Y, F, Si and O.

The efficiency of the silica coating process was determined from the zeta potential measurements in aqueous suspensions. First, we measure zeta potential of the α-$NaYF_4$ (Figure 5, black dots). Positive values of the zeta potential of α-$NaYF_4$ are in the range of pH between 2 and 7 while negative values are in the range of pH between pH=7.5 and pH=11. Isoelectric point of nanoparticles is around pH= 7.4. Values of the zeta potential of α-$NaYF_4$@$SiO_2$ are negative in all pH range indicating the negative charge is on the surface of nanoparticles. This negative charge is due to silanol groups from the silica coatings (Figure 5, red dots).

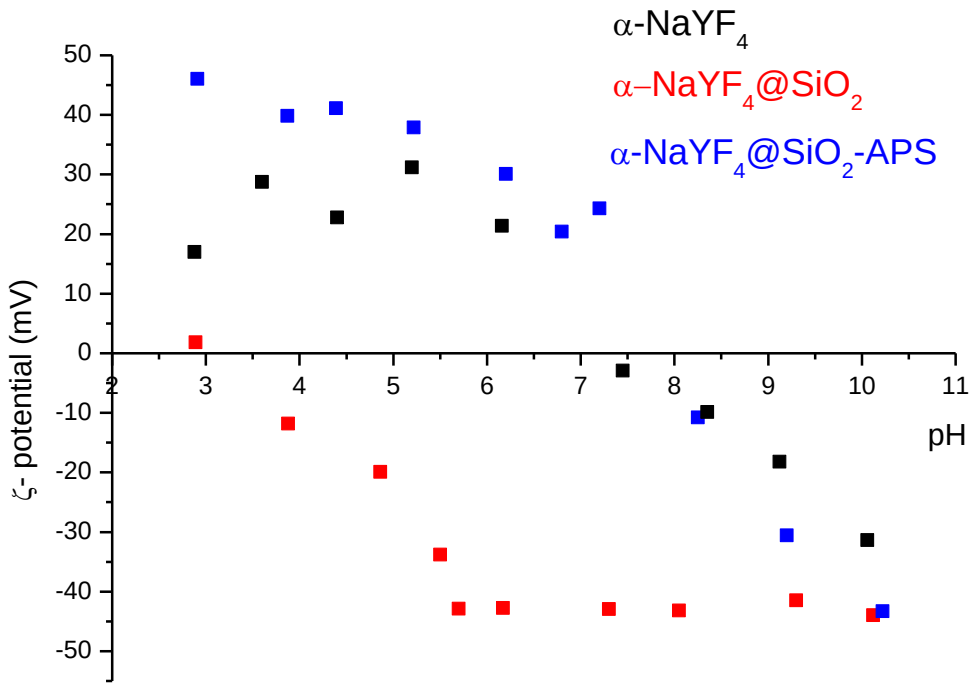


**Figure 4:** Zeta potential of α-$NaYF_4$, α-$NaYF_4$@$SiO_2$ and α-$NaYF_4$@$SiO_2$-APS nanoparticles.

Unexpectedly, the silica coating did not provide any protection for the α-$NaYF_4$ nanoparticles since the fluoride analysis of the α-$NaYF_4$@$SiO_2$ aqueous suspensions

confirmed 22.4 mg/l of the dissolved fluoride ions even for the suspension of α-$NaYF_4$@$SiO_2$ nanoparticles with the 8 nm thick silica layer. This was similar to that of the uncoated sample. Therefore we intend to apply additional protective coatings in the future. For this purpose we functionalized the α-$NaYF_4$@$SiO_2$ with APS that provided amino groups for the attachment for additional protective coatings.

Zeta potential of α-$NaYF_4$@$SiO_2$-APS show positive values in the range of pH=2 to pH=7.5. Positive values are due to protonated amino groups from APS on the surface of nanoparticles (Figure 5, blue dots). Isoelectric point is at pH= 8. Negative values of zeta potential at pH values higher than 8 is due to deprotonated amino groups of the APS functionalization. The differences between the zeta potential and isoelectric point values between the α-$NaYF_4$ and α-$NaYF_4$@$SiO_2$-APS suggest that the functionalization of the silica with APS was successful. We are planning to use this as a basis for further protective coating of the nanoparticles.

## 4 Conclusion

We have successfully synthesized α-$NaYF_4$ nanoparticles by coprecipitation synthesis under reflux and stabilized them with PVP. The as-synthesized nanoparticles were not chemically stable in aqueous suspensions. The dissolution of the fluoride was detected. The nanoparticles were coated with 3 nm or 8 nm thick silica layer and we further functionalized them with APS. The concentration of the released fluoride ion did not differ between uncoated and coated nanoparticles. Therefore different protective coatings will be tested in future.

## References:


[1] J. F. Wang, X. Liu Recent advances in the chemistry of lanthanide-doped upconversion nanocrystals. *Chemical Society Reviews*, 38: 976-989, 2009.

[2] A. Gnach, A. Bednarkiewicz Lanthanide-doped up-converting nanoparticles: Merits and challenges. *Nano today,* 7: 532-563, 2012.

[3] J. Shen, L. Zhao, G. Han Lanthanide-doped upconverting luminescent nanoparticle platforms for optical imaging-guided drug delivery and therapy. *Advanced Drug Delivery*, 2012.

[4] Z. Li, Y. Zhang Monodisperse Silica-Coated Polyvinylpyrrolidone/$NaYF_4$ Nanocrystals with Multicolor Upconversion Fluorescence Emission. *Angewandte Chemie*, 118: 7896-7899, 2006.

[5] J. Ma, P. Huang, M. He, L. Pan, Z. Zhou, L. Feng, G. Gao, D. Cui Folic Acid-Conjugated $LaF_3$:Yb,Tm@$SiO_2$ Nanoprobes for Targeting Dual-Modality Imaging of Upconversion Luminescence and X-ray Computed Tomography. *The Journal of Physical Chemistry*, 116: 14062-14070, 2012.

[6] G.S. Pawley Unit-cell refinement from powder diffraction scans. *Journal of Applied Crystallography*, 14: 357-361, 1981.

## For wider interest
## Materials synthesis – K8

**Head of department:** prof. dr. Darko Makovec

*Magnetic nanoparticles (ferrofluids, nanocomposites)*

New methods for the controlled synthesis of iron oxide nanoparticles are developing. Therefore, our department is focused on the functionalization of magnetic nanoparticles for biomedical applications. The surface properties of nanoparticles are tuned with organic/inorganic coatings (e.g., thin layer of amorphous silica). The coating prevents the agglomeration of nanoparticles and further enables easier preparation of their dispersion in various liquids.

*Multifunctional materials*

By mastering the surface properties of nanoparticles nanocomposites combining the various properties of the constituent materials can be prepared. For example, our studies include combinations of ferrimagnetics and dielectrics materials. Current studies are also related to the development of new magneto-optic materials for sensors and magneto-catalytic materials for environmental applications.

*Magnetic materials for micro- and mm-wave*s

Magnetic materials suitable for the absorbers of electromagnetic waves and for the non-reciprocal ferrite devices are being developed. Ceramics and composites based on ferrites are studied for the microwave applications and a new method for the preparation of magnetically oriented thick hexaferrites films for self-biased mm-wave applications has been developed.

*Inorganic fluorescent nanoparticles*

Inorganic fluorescent nanoparticles are considered as a promising alternative for biomedical applications. Lanthanide-doped nanoparticles with appropriate surface modification can be used in bioapplications such as bioimaging.

# Analyzing non-metallic inclusions in spring steel using Auger electron spectroscopy

**Besnik Poniku**[2], **Igor Belič**[1], **Monika Jenko**[1]

[1] Institute of Metals and Technology, Ljubljana, Slovenia

[2] Jožef Stefan International Postgraduate School, Ljubljana, Slovenia

besnik.poniku@gmail.com

**Abstract.** Auger Electron Spectroscopy (AES) is a suitable technique for surface characterization. It is very surface sensitive, with the characteristic information coming from the top 0.4 -5 nm. Since also the electron beam can be focused down to about 10 nm in diameter, AES provides a powerful technique for performing analysis on the nano – scale.

In the scope of this work AES was used to characterize non-metallic inclusions in spring steel. During this investigation a total of 52 analyses were performed on the first sample, and 41 on the second. Elements such as S, O, Ca, Mg, Mn, V, Cu, Al, Ti, Mo and C were found to be present. Having in mind the composition of spring steels, it is concluded that most of the inclusions which have a detrimental effect on their mechanical properties originated from the interaction of steel components with impurities during various stages of steel production.

**Keywords**: Auger electron spectroscopy, spring steel, non-metallic inclusions

## 1 Introduction

The last couple of decades have witnessed a growing interest in the study of surface phenomena. Processes occurring at solid surfaces are of great practical importance, particularly for the study of heterogeneous catalysis, corrosion, semiconductor technology, metallurgy, etc. [1] Along with this growing interest on understanding the surfaces of materials and their composition, the growing necessity for adequate analytical techniques also became apparent. Different analytical techniques are used to study surfaces. One of them is Auger electron spectroscopy.

## 1.1 Principles of AES

Auger electron spectroscopy as an advanced and modern analytical technique first started being used in the 1960's [2]. It is based on the Auger effect, a phenomenon that was discovered by Pierre Auger, a French scientist, in 1923 [3]. The emission of the Auger electron is illustratively presented in Figure 1 [4].

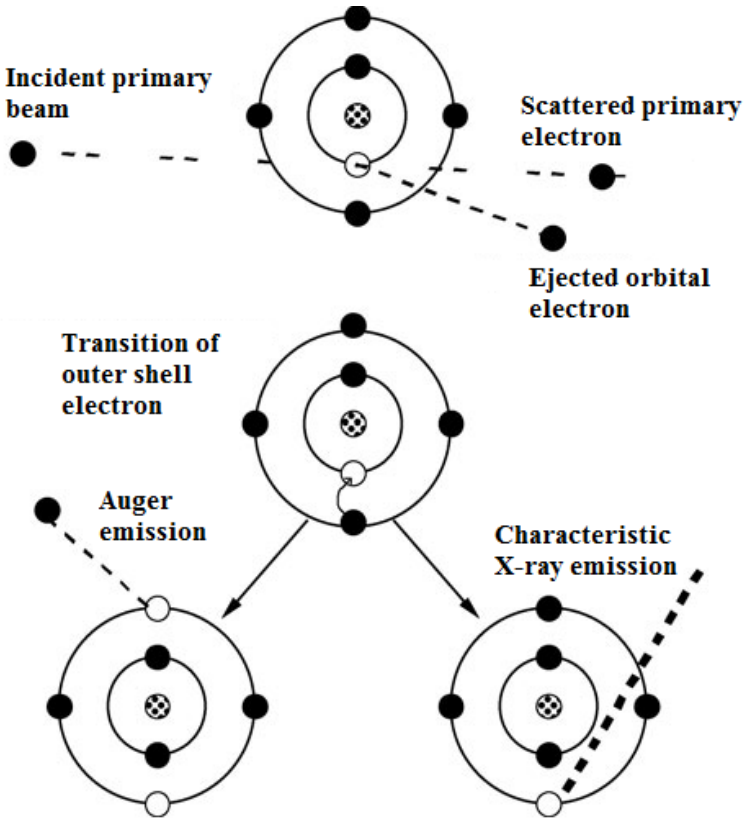


**Figure 1 :** Inner shell ionization and de-excitation tree for carbon.

Since the differences in energy levels are characteristic for atoms of different elements, as a consequence so are the energies given to the Auger electron through this process. The fact that the Auger electrons of different atoms eject under different kinetic energies, yet specific for atoms of the same kind, the detection of this kinetic energy makes a valuable means for elemental characterization.

## 1.2 Surface sensitivity of AES

Surface sensitivity is one of the factors that set Auger electron spectroscopy apart from most of the other analytical techniques. When the primary electron beam penetrates the solid surface that is being analyzed, characteristic Auger electrons, secondary electrons, backscattered electrons, and X-ray photons emerge. Figure 2 [5]

shows the volume of interaction, and different types of emissions taking place during this interaction of the incident (primary) electron beam with the solid sample.

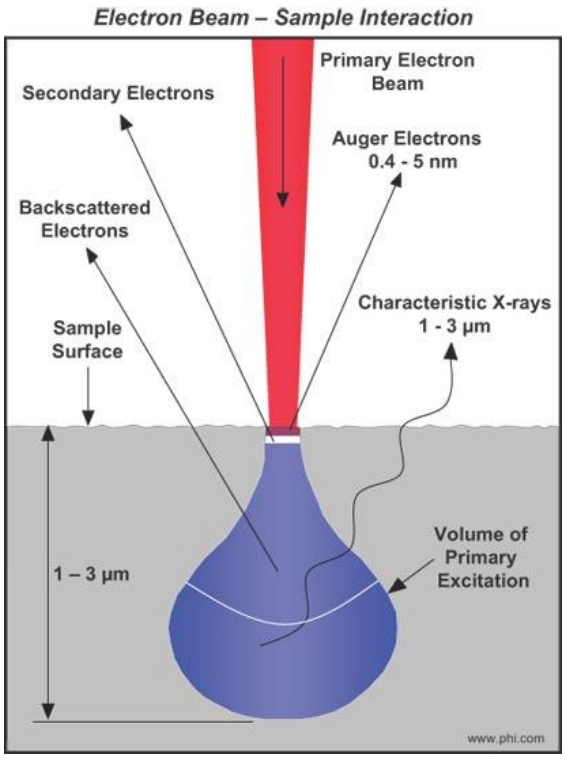


**Figure 2:** The interaction between an incident electron beam and a solid sample.

The volume of interaction is dependent on the energy of the primary electron beam and the nature of the sample material. Figure 2 shows that Auger electrons which successfully escape the sample come from the top 0.4 to 5 nm of the sample surface. Auger electrons may emerge also deeper within the solid as they do near the surface. But these electrons will inevitably get scattered while moving to the surface, and either they will not manage to escape the surface at all, or will escape while having lost much of their characteristic energy. This is due to their short inelastic mean free path. This parameter indicates the range of depth within a solid from which Auger electrons of various energies will be able to come to the surface and escape it while still maintaining their initial energy. This is very important, because only those electrons that escape the sample with their characteristic Auger energy are useful in identifying the atoms in the sample. [3] Figure 3 [6] shows a graph of the mean free path of electrons represented in monolayers as a function of electron kinetic energy.

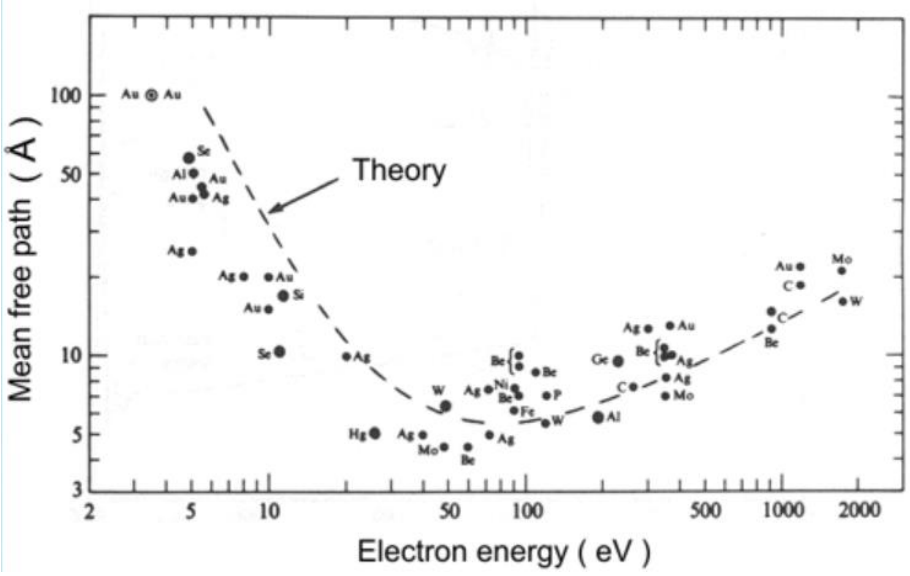


**Figure 3 :** The dependence of the inelastic mean free path of electrons on kinetic energy.

Because of this high surface sensitivity keeping the surface of the material to be analyzed very pure is of outmost importance, because even a couple of monolayers of contamination on the surface will interfere with the analysis. For this reason the analysis is performed in a special chamber under Ultra High Vacuum (UHV) conditions.

Another important factor in Auger electron spectroscopy is the fact that the primary electron beam in modern instruments can be focused down to app. 10 nm [7], giving the possibility to perform analysis not only of very good depth resolution due to the high surface sensitivity, but of very good lateral resolution as well. This fact makes it possible to characterize the smallest inclusions which reside on the surface of metals, or on the surfaces revealed after a fracture has occurred, in order to understand the real effects such inclusions have on materials and to take proper action to improve their properties. Such an example of using Auger electron spectroscopy to characterize non-metallic inclusions in spring steel will be presented in the following chapter.

## 2 Characterization of non-metallic inclusions

A non metallic inclusion is an impurity present in steel which might have been formed from the reaction of different additives in steel mostly with oxygen and sulfur, but also with the strengthening element, carbon, and in some cases with

nitrogen or phosphorus. These components are formed during various stages of steel production. To a certain degree non-metallic inclusions are welcomed in steel, because they improve the machinability of steel, for example. But in general they have a degrading effect on the quality of steel. Often when present in the surface of the alloy they can initiate cracks. [8]

When systematically monitoring the content of non-metallic inclusions in steels, AES is not the first technique of choice. By means of optical microscopy they can be classified into major groups, and by EDS (Energy Dispersive Spectroscopy) or WDS (Wavelength Dispersive Spectroscopy) combined with SEM valuable information about their chemical composition can be obtained. But for getting information about the inclusions that fall into the nanometer range, AES is an invaluable technique. Compared to EDS and WDS, Auger electron spectroscopy is much more surface specific. If the really small or thin inclusions were to be analyzed by EDS or WDS, much misleading information during the same measurement will be included also from the bulk material.

The experimental work presented in this paper was carried out by the surface analysis team at IMT, where two samples taken from spring steel produced at Štore Steel were investigated.

## 2.1 Sample preparation

First of all, the samples were prepared for analysis. Two specimens were taken from the bulk material, both of the dimensions 10 x 10 x 4 mm. First, samples were cut from the bulk material through abrasive wet cutting. Afterwards, grinding of the samples was done through plane grinding and then fine grinding. And at the end they were polished, first through diamond polishing and then oxide polishing. Oxide polishing produces a finer surface, which is necessary for Auger electron spectroscopy. And when all these steps were taken, the samples were cleaned in ultrasound to remove any impurities that may have been introduced on the surface during preparation. Afterwards the samples were taken to be analyzed in Auger electron spectroscopy.

## 2.2 Cleaning the surface with ions

Prior to starting the experiment, after the sample has been introduced to the analysis chamber, its surface must be cleared off of the contaminating layer present there. This is achieved through sputtering of the surface for a specific amount of time through bombardment of the sample with Ar+ ions from the ion gun. Ar+ ions and the ion gun are also used when depth profiling is required. It reveals the chemical composition at different depths from the surface of the sample, and is achieved by taking sequential AES measurements while removing successive layers of the sample by means of ion etching.

An area of 16 mm² of the samples in this investigation was sputtered for 5 minutes in each case under the stream of Argon ions with 3 keV energy and 0.5 μA intensity. Previous experience with similar metallic samples shows removal of most of the surface contamination within the sputtered area without affecting the sample.
After the cleaning procedure, Secondary Electron (SE) imaging capability of the instrument was used to image the cleaned surface of the sample and search for the inclusions, as shown in Figure 4:

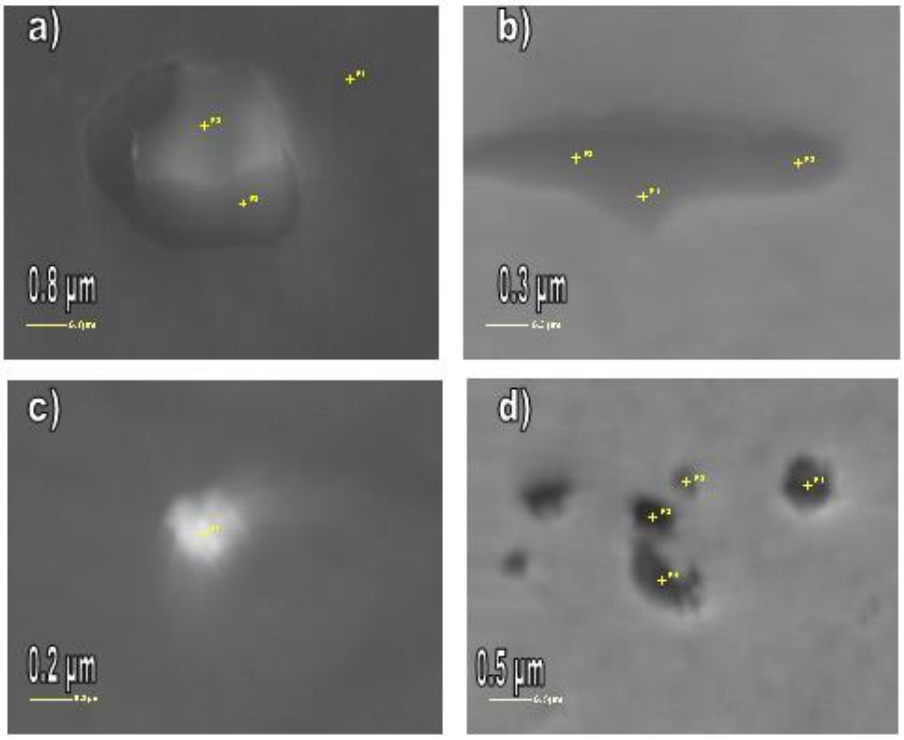


**Figure 4 :** SE images of inclusions in sample 1 (a, b) and sample 2 (c, d). The length of the marker is indicated by the number above it (ex. for sample 1 (a) the marker is of 0.8 μm length)

## 2.3 Charging of the sample

It is obvious that the inclusion in Figure 4 c) is much brighter than the rest. This is usually the case with the charging inclusions, which represent a specific challenge during characterization of non-metallic inclusions. The charging of the surface occurs usually when electrons from the primary beam accumulate at one spot due to the poor conductivity of the sample in the area which is being probed. This phenomenon can either shift the peaks from their usual position and slightly distort them, or it can make the spectrum completely unrecognizable. To counter this phenomenon the same ion gun with low energy Ar+ ions is used for charge compensation.

## 2.4 Probing the non-metallic inclusions

Through point analysis after spotting the inclusions, their "direct" spectra were obtained. The primary electron beam used was of 10 keV energy, 10 nA intensity, and 10 nm spot size.

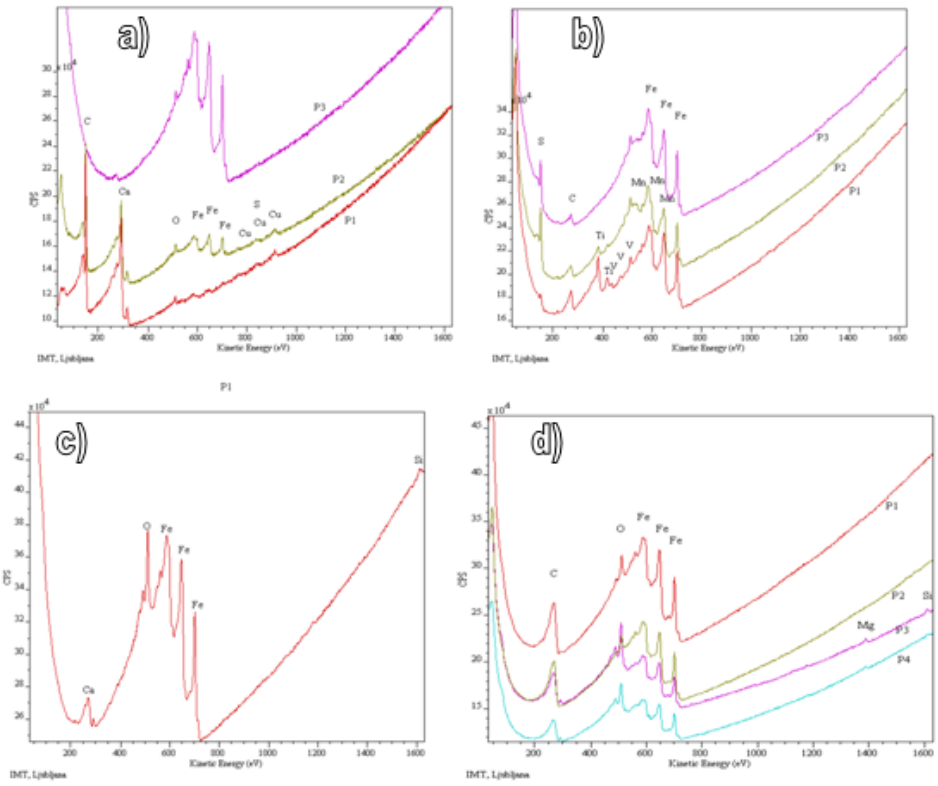


**Figure 5 :** "Direct" spectra of the previously shown inclusions from sample 1 and 2.

The elements detected were identified by comparing these measured spectra with the standard reference spectra of the pure elements. Afterwards CasaXPS, a program for

processing electron spectra was used. From the derivative form of the spectra obtained through this program, by using peak to peak heights the composition in relative atomic % was obtained.

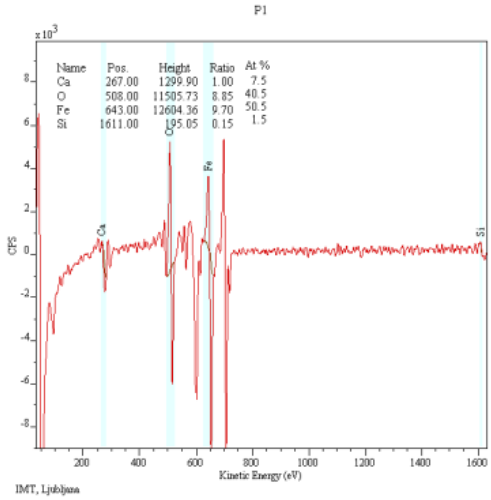


**Figure 6 :** At.% composition of the inclusion in Figure 4 c).

"Scanning Auger Microscopy" is a powerful feature of AES through which mapping of specific elements within an area of interest is done. By setting the energy analyzer to read specific energy values and then scanning the area of interest, a visual representation of the distribution of elements will be obtained.

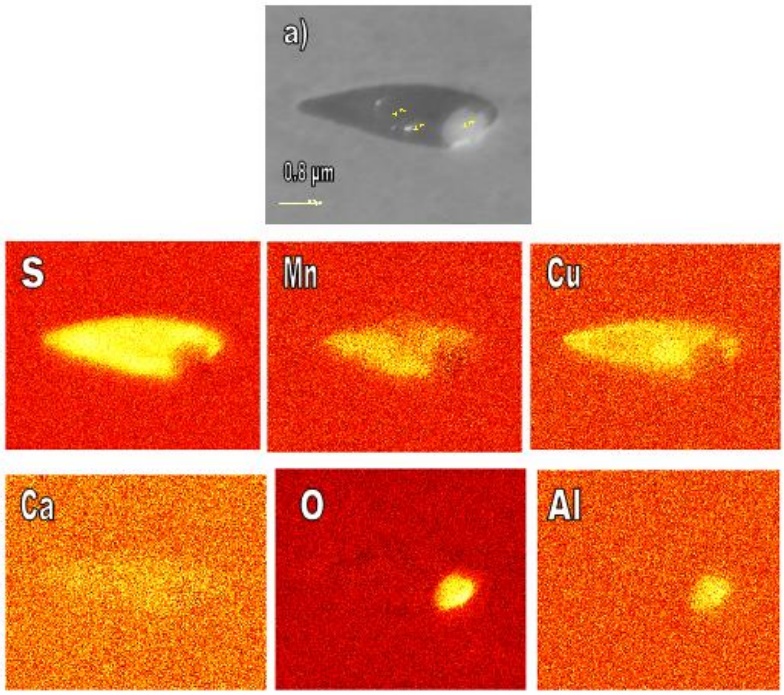


**Figure 7 :** a) - SE image of the inclusion,
S, Mn, Cu, Ca, O, Al – distribution of elements (presented by their symbols).

## 2.5 Conclusions reached from the investigation

During this investigation a total of 52 analyses were performed on the first sample, and 41 on the second. Elements such as S, O, Ca, Mg, Mn, V, Cu, Al, Ti, Mo and C were found to be present. Spring steels generally have the chemical composition as presented in Table 1 [9]:

**Table 1 :** Chemical constituents of spring steel (in wt.%) other than iron.

| C% | Si% max | Mn% | P% max | S% max | Cr% | V% |
|---|---|---|---|---|---|---|
| 0,47-0,55 | 0,40 | 0,70-1,10 | 0,025 | 0,025 | 0,90-1,20 | 0,10-0,25 |
| ± 0.02 | ± 0.03 | ± 0.05 | + 0.005 | + 0.005 | ± 0.05 | ± 0.02 |

By referring to table 1, we may conclude that most of the inclusions present in the samples originated from the interaction of steel components with impurities during various stages of steel production. And according to the analysis, the failure of the spring steel was influenced greatly by the presence of these inclusions.

## References:


[1] J. T. *Grant. Auger Electron Spectroscopy*. Unpublished Manuscript. Dayton, Ohio, n.d.

[2] F. A. Settle (ed.). *Handbook of Instrumental Techniques for Analytical Chemistry*. Prentice Hall, New Jersey, 1997.

[3] C. R. Brundle, C. A. Evans Jr., and S. Wilson (eds.). *Encyclopedia of Materials Characterization: Surfaces, Interfaces, Thin Films*. Butterworth – Heinemann, Massachusetts, 1992.

[4] N. Yao and Z. L. Wang (eds.). *Handbook of Microscopy for Nanotechnology*. Kluwer Academic Publishers, New York, 2005.

[5] N/A. *Auger Electron Spectroscopy (AES): What is AES?* http://www.phi.com/techniques/aes.html (accessed April 2014). Physical Electronics, Inc. Chanhassen, MN, 2006 – 2014.

[6] Z. Postawa. *How to investigate solid surface ?* http://users.uj.edu.pl/~ufpostaw/2_Pracownia/D1/jak_badac_powierzchnie_eng.htm (accessed April 2014).

[7] N/A. *Microlab 310-F: Operators Manual*. V.G. Scientific, United Kingdom, 1997.

[8] R. Kiessling and N. Lange. *Non – metallic inclusions in steel, 2nd Edition*. The Metals Society, London, 1978.

[9] N/A. *Spring steel 51CrV4 Technical card: Chemical composition*. Lucefin Group. http://www.lucefin.com/wp-content/files_mf/1.815951crv452.pdf (accessed April 2014).

## For wider interest

Auger Electron Spectroscopy (AES) is a very suitable technique for surface characterization of different materials. This technique is very surface sensitive, where the characteristic information comes from the top 0.4 -5 nm of the sample surface. Having in mind the fact that also the electron beam can be focused down to about 10 nm in diameter, AES provides a powerful tool for performing analysis on the nano – scale. Also the Scanning Auger Microscopy capability of this technique which does elemental mapping can produce a microscopy - type image of the distribution of selected elements over a certain region of the sample.

In the scope of this work AES was used to characterize non – metallic inclusions in spring steel. The above mentioned facts make it possible to characterize the smallest of the inclusions which cannot be reliably characterized by any other technique. During this investigation a total of 52 analyses were performed on the first sample, and 41 on the second. Elements such as S, O, Ca, Mg, Mn, V, Cu, Al, Ti, Mo and C were found to be present. Having in mind the chemical composition of spring steels, it is concluded that most of the inclusions present in the spring steel samples which have a detrimental effect on their mechanical properties originated from the interaction of steel components with impurities during various stages of steel production.

# Molecular dynamics study of incipient plasticity of the (1,1,19) nickel surface

**Nuša Pukšič**[1,2], **Monika Jenko**[1], **Matjaž Godec**[1]

[1] Institute of Metals and Technology, Ljubljana, Slovenia

[2] Jožef Stefan International Postgraduate School, Ljubljana, Slovenia

nusa.puksic@imt.si

**Abstract.** Molecular dynamics simulations are used to study defect nucleation in nickel in response to uniaxial strain. The incipient plasticity of two nickel mono-crystalline substrates is investigated and compared, one with the nominal (0,0,1) surface and the other with the vicinal (1,1,19) surface. Surface relaxation at 0 K is performed by minimization, and then the substrates are equilibrated to 10 K and subjected to uniaxial tensile and compressive strain in accordance with the "strain-and-equilibrate" method, with a cumulative strain rate of 2.5% $ps^{-1}$. The surface condition influences the mechanical properties and the nucleation of defects. The defects form at smaller strain in the case of the Ni(1,1,19) surface and the defects mirror the regularity of the surface absent in the case of the nominal surface.

**Keywords**: molecular dynamics, nickel, vicinal, uniaxial, tension, compression, defect nucleation

## 1 Introduction

The onset of plasticity in materials marks a point when strain cannot be accommodated by reversible elastic deformation any longer and defects begin to form. Molecular dynamics studies give insight into incipient plasticity, providing an opportunity to follow the nucleation of defects on an atomic level. This study is focused on the incipient plasticity of nickel, used as a sample metal with a face centred cubic (fcc) lattice. There are multiple studies of fcc metals subject to nano-indentation [1-3] and uniaxial tension or compression [4-10].

Nano-indentation studies focus on the vacancy and dislocation nucleation beneath the indenter. The stress applied via the frictionless rigid indenter is non-uniform, but can lead to homogeneous defect nucleation in a perfect crystal. The indenter is applied to a surface cut along a dense plane.

The simulations employing uniaxial tension or compression generate more uniformly distributed stress and require larger simulation cells to avoid self-interaction of defects. The studies centre on defect mobility and the effects of grain boundaries on the mechanic response of the material.

This study brings into focus the importance of the surface condition for the onset of plasticity. Steps on the surface of a metal substrate generate an elastic field of their own, which affects the distribution and redistribution of the stress generated by the tension or compression of the sample. A free surface also allows for greater mobility.

## 2 Simulation details

Nickel single crystal substrate was used in all the simulations. The simulations were carried out using the LAMMPS Molecular Dynamics Simulator [11,12] and the EAM potential file provided by H. W. Sheng, included with the LAMMPS distribution.

The simulations were performed on a substrate with the (0,0,1) surface and a substrate with the vicinal (1,1,19) surface, consisting of a sequence of terraces and steps. The terraces have (0,0,1) faces and the steps are along the (1,1,0) direction. The substrate is divided into two layers: the layer of fixed atoms (5 atomic layers) and the layer of equilibrated atoms. The boundaries of the simulation box are periodic in the $x$ and $y$ directions and non-periodic in the $z$ direction.

The size of the Ni(0,0,1) sample is 40×40×27.5 unit cells and the simulation box is a cube. The unit cell vectors of the sample are oriented in the (1,-1,0), (1,1,0) and (0,0,1) directions. The size of the Ni(1,1,19) sample is 40×38×30 unit cells and the simulation box is a parallelepiped, tilted in the $x$ direction enough to line up the faces of the box with the sample's crystallographic plane with the (1,-1,0) normal. The unit cell vectors of the sample are oriented along the (1,-1,0), (19,19,-2) and

(1,1,19) directions. The coordinate systems are depicted in Figure 1, in black for the simulation box, labelled $x$, $y$ and $z$, and in blue for the unit cell vectors, labelled $x'$, $y'$ and $z'$.

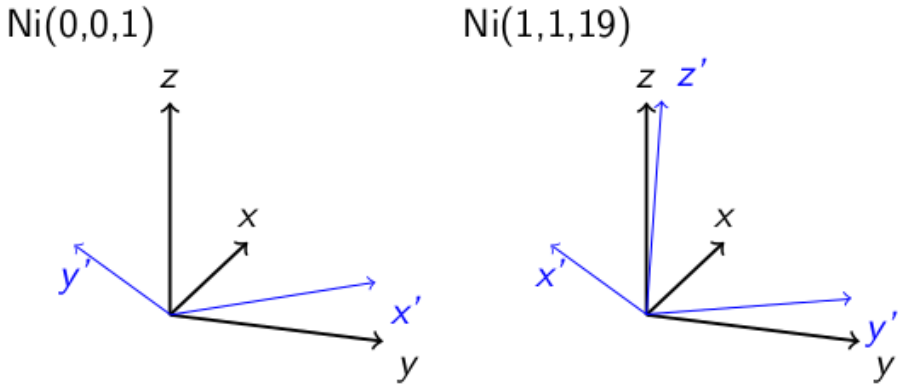


**Figure 1**: Coordinate systems for both cases: in black for the simulation boxes, labelled $x$, $y$ and $z$, and in blue for the unit cell vectors, labelled $x'$, $y'$ and $z'$.

Damped dynamics method [13] was used to calculate surface relaxation at 0 K. Each sample was then equilibrated to 10 K, before compressive and tensile strains are applied. The axis of the compressive or tensile strains in the simulations is along the (1,-1,0) direction, perpendicular to the steps on the vicinal surface.

The strain in the simulations is applied in accordance with the "strain-and-equilibrate" method, in this case applying strain in increments of 0.5% and equilibrating for 200 steps before applying additional strain. With the chosen time step, this results in the strain rate of 2.5% $ps^{-1}$.

## 3 Results and discussion

An analysis of the response of the nickel substrates to the uniaxial compression and tension is given, first for the Ni(0,0,1) and then for the Ni(1,1,19) sample. The post-processing was done using OVITO [14].

### 3.1 Ni(0,0,1)

The relaxation of the Ni(001) surface at 0 K spans the top three layers, all of which relax outwards, where the second layer is displaced more than the first and the third layers.

During compressive deformation of the Ni(001) sample defects begin to form right at the surface and spread into the bulk from there, as shown in Figure 2a,b. A disordered network of dislocations forms and because of the irregular slip of the near-surface layers, the surface gradually becomes rougher, as shown in Figure 3a.

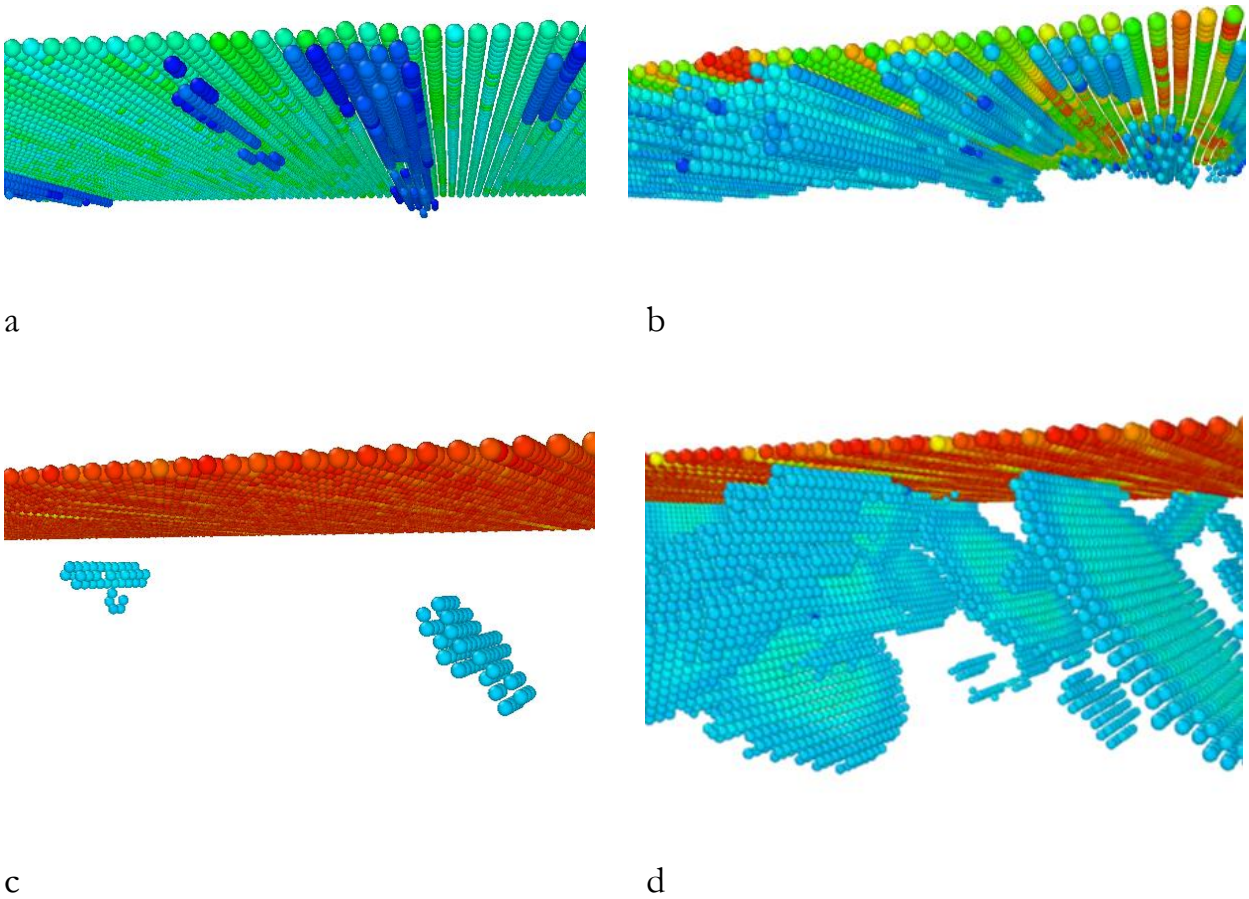

a b

c d

**Figure 2**: Nucleation of defects in the Ni(0,0,1) case. The atoms are coloured according to the central-symmetry parameter (csym), the atoms with csym < 2 are removed. Top: compressive deformation, dislocation nucleation at the strain of a) -0.079 and b) -0.080. Bottom: tensile deformation, dislocation nucleation at the strain of c) 0.090 and d) 0.091.

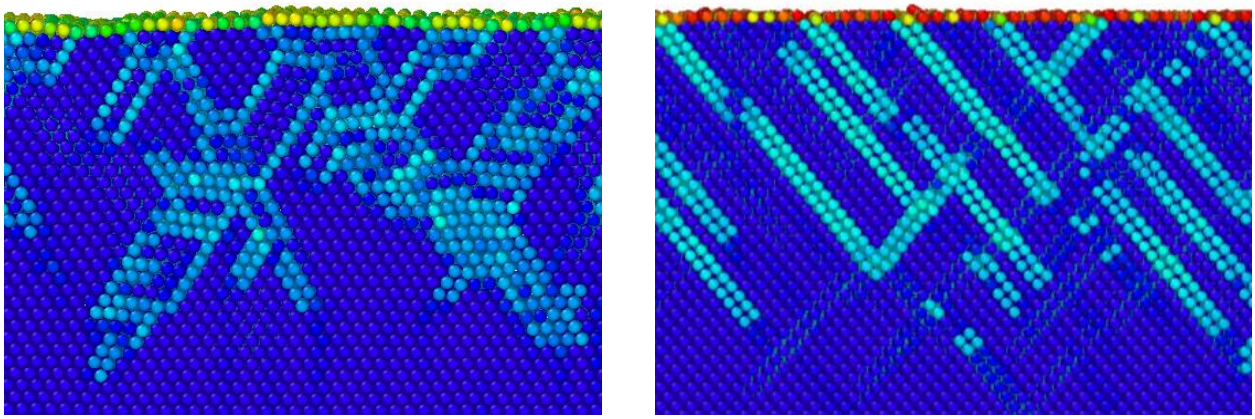

a b

**Figure 3**: Dislocation networks: a) compressive deformation at the strain of -0.085, b) tensile deformation at the strain of 0.093.

During tensile deformation defects begin to form multiple layers below the surface and spread into the bulk and towards the surface from there, as shown in Figure 2c,d. A more regular network of dislocations forms, compared to the compressive strain case (Figure 3b).

### 3.2 Ni(1,1,19)

The relaxation of the Ni(1119) surface is more complex than the relaxation of the nominal surface. A representation of the displacement field is shown in Figure 4. The terrace edge atoms relax towards the lower terrace (dark blue), and the corner atoms relax towards the edge of the upper terrace (dark red). The neighbouring atoms relax accordingly to gradually approach bulk positions. The relaxations reach deeper into the bulk than the top three layers.

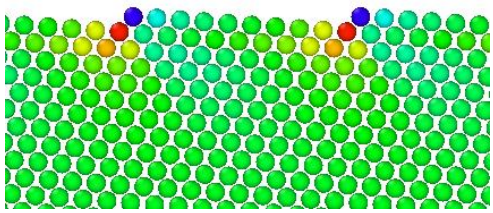

**Figure 4**: Relaxation of the Ni(1,1,19) surface in the $z$ direction. The displacement is the greatest for the terrace edge atoms, which relax towards the lower terrace (dark blue), and the corner atoms, which relax towards the edge of the upper terrace (dark red).

With the Ni(1,1,19) surface under compression, defects begin to form 10 layers beneath the surface under the step edges as rows of dumbbell pairs. Then dislocations begin to spread from those and from the surface. After connecting with the surface, the dislocation loops grow deeper into the bulk form there. The ordered steps are lost when slip occurs. Defect formation for this case is shown in Figure 5.

During tensile deformation, similar rows of dumbbell pair defects begin to form, then additional rows spread towards the surface. The dislocation loops first reach towards the surface then extend into the bulk. Slip begins first in one direction at the strain of 0.065, then also in the perpendicular direction at the strain of 0.075. As with the first set of dislocation loops, they start at the site of first defects and grow first towards the surface and then into the bulk. The surface periodicity is lost at this point. With additional tensile strain, voids begin to form at the sites of the first defects. Defect formation for this case is shown in Figure 6.

## 4 Conclusions

In all the cases, the near-surface layers plastically deform at lower strain than the deeper bulk layers.

Compared to the Ni(0,0,1) case, the defects begin to form at lower strain in the case of the Ni(1,1,19) surface. Additionally, the regularity of the nucleated defects mirrors the regularity of the steps, absent in the case of the Ni(0,0,1) surface.

The condition of a free nickel surface influences its mechanical response to external uniaxial strain: the stability of the surface, the position and type of defects and the strain at which the defects nucleate are all subject to the state of the surface before deformation.

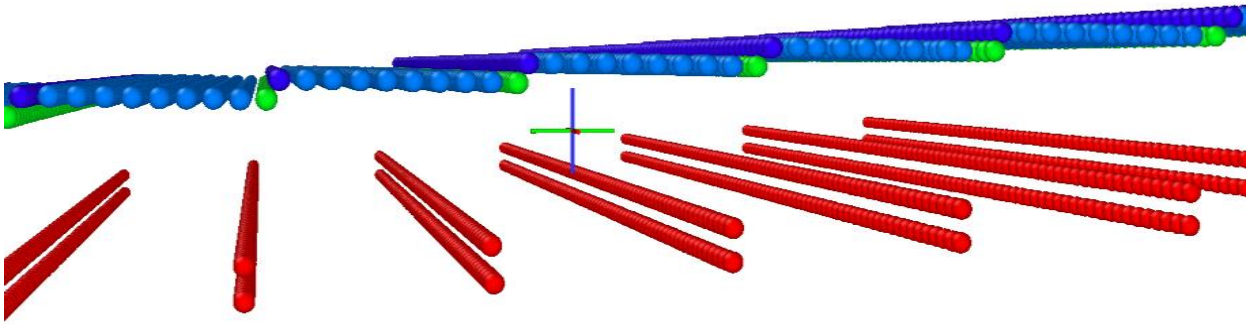

a

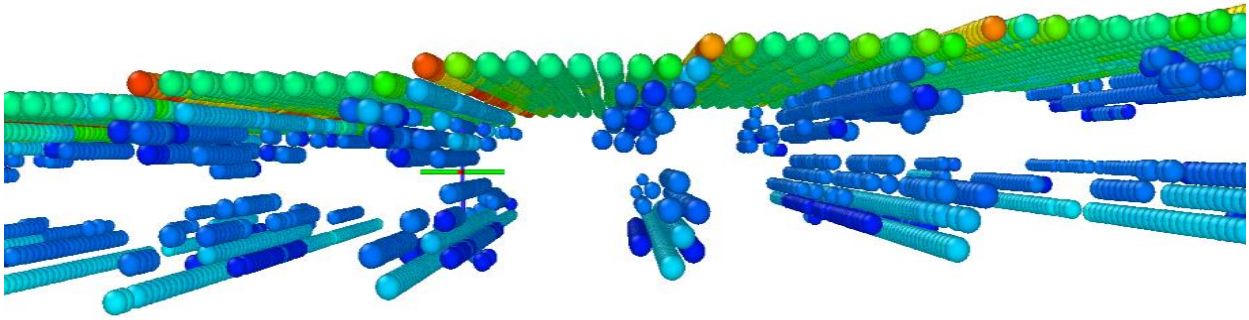

b

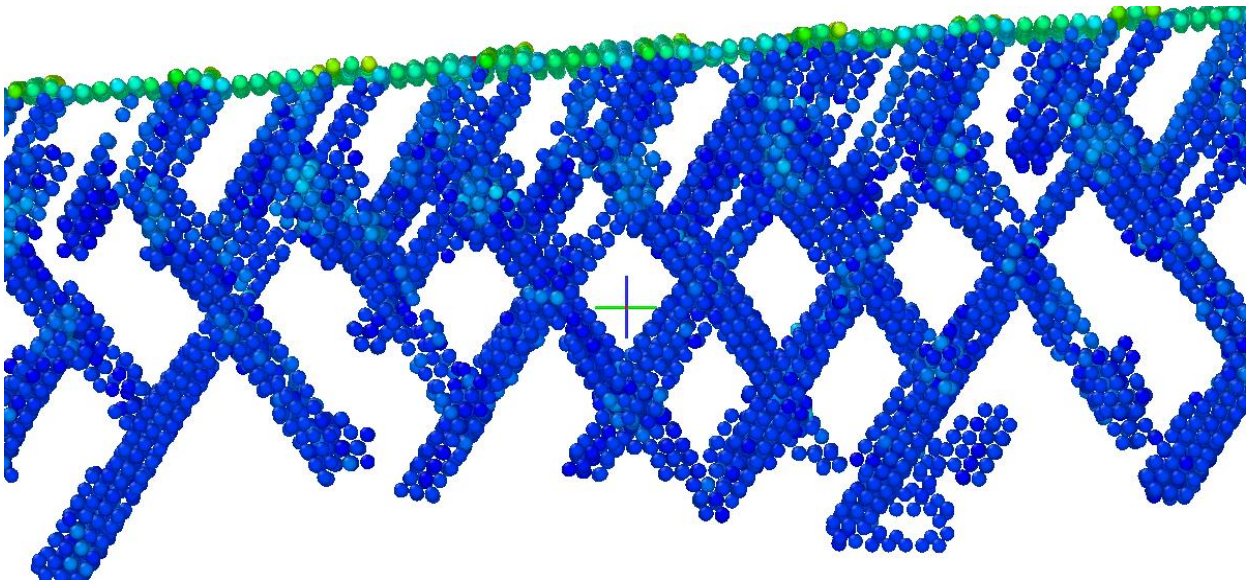

c

**Figure 5**: Defect nucleation and progress in the case of compressive strain of Ni(1,1,19): a) rows of dumbbell pairs below the surface coloured by coordination at the strain of -0.063, b) nucleation of dislocation loops at the strain of -0.078, c) dislocation loops at the strain of -0.080. The cases of b) and c) are coloured by csym, the atoms with csym < 2 are removed.

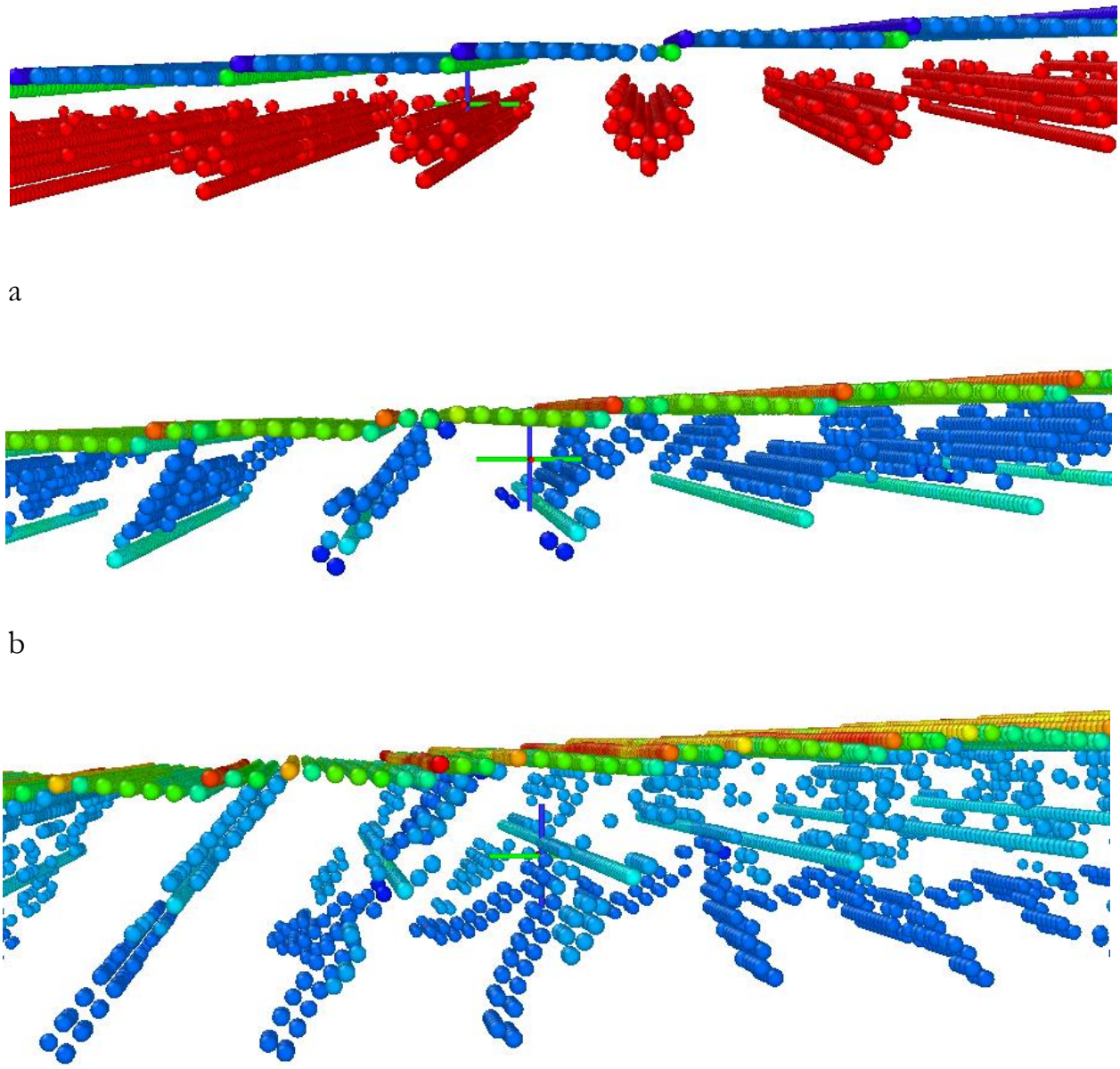

**Figure 6:** Defect nucleation and progress in the case of tensile strain of Ni(1,1,19): a) rows of dumbbell pairs below the surface coloured by coordination at the strain of 0.060, b) nucleation of dislocation loops at the strain of 0.065, c) dislocation loops at the strain of 0.068. The cases of b) and c) are coloured by csym, the atoms with csym < 2 are removed.

## References:


[1] I. Salehinia and S. N. Medyanik. Effects of Vacancies on the Onset of plasticity in Metals—An Atomistic Simulation Study. *Metallurgical and Materials Transactions A*, 42(13):3868–3874., 2011

[2] Y. Cao et al. Mechanical and tribological properties of Ni/Al multilayers—A molecular dynamics study. *Applied Surface Science*, 257(3):847–851, 2010

[3] S. N. Medyanik and S. Shao. Strengthening effects of coherent interfaces in nanoscale metallic bilayers. *Computational Materials Science*, 45(4):1129–1133, 2009

[4] J. Zhang and S. Ghosh. Molecular dynamics based study and characteri-zation of deformation mechanisms near a crack in a crystalline material. *Journal of the Mechanics and Physics of Solids*, 61(8)1670–1690, 2013

[5] D. Huang, Q. Zhang, and P. Qiao. Molecular dynamics evaluation of strain rate and size effects on mechanical properties of FCC nickel nanowires. *Computational Materials Science*, 50(3):903–910, 2011

[6] D. Bachurin, D. Weygand, and P. Gumbsch. Dislocation–grain boundary interaction in <111> textured thin metal films. *Acta Materialia*, 58(16):5232–5241, 2010

[7] C. Wang et al. A single vacancy diffusion near a Fe(110) surface: A molecular dynamics study. *Computational Materials Science*, 50(2):291–294, 2010

[8] A. Alavi et al. Molecular dynamics simulation of mechanical properties of Ni–Al nanowires. *Computational Materials Science*, 50(1):10–14, 2010

[9] A. Setoodeh, H. Attariani, and M. Khosrownejad. Nickel nanowires under uniaxial loads: A molecular dynamics simulation study. *Computational Materials Science*, 44(2):378–384, 2008

[10] Y.-H. Wen et al. The uniaxial tensile deformation of Ni nanowire: atomic-scale computer simulations. *Physica E: Low-dimensional Systems and Nanostructures*, 27(1-2):113–120, 2005

[11] S. Plimpton. Fast Parallel Algorithms for Short-Range Molecular Dynamics. *Journal of Computational Physics*, 117:1–19, 1995

[12] Sandia National Laboratories. LAMMPS Molecular Dynamics Simulator. http://lammps.sandia.gov/, 2014.

[13] D. Sheppard, R. Terrell, and G. Henkelman. Optimization methods for finding minimum energy paths. *The Journal of chemical physics*, 128(13):134106, 2008

[14] A. Stukowski. Visualization and analysis of atomistic simulation data with OVITO–the Open Visualization Tool. *Modelling and Simulation in Materials Science and Engineering*, 18(1):015012, 2010

## For wider interest

Research of mechanical properties of metallic materials has been extended in the last decades into the studies on the atomic level. And although testing of mechanical properties is a well established field, some of the finer points of the plastic deformation and failure of crystalline materials are not well understood or documented. Recently the atomistic simulations began to extend beyond the most basic simulations of single crystal samples and into a range of more realistic configurations, *e.g.* multi-layered thin films and polycrystalline samples.

Such studies will bring a better understanding of how the results of nano-indentation depend on the local configuration of the sample (the presence of a grain boundary, an inclusion or a void). Also, how the mechanical properties of the sample depend on the type of grain boundaries prevalent in the sample and their volume fraction.

Studies of the influence of strain on mechanical properties of metals are also important in the field of thin films, as lattice mismatch often induces stress when thin films are grown on various substrates.

This study shows in detail how the surface condition of a nickel substrate influences its mechanical response to external uniaxial strain: the stability of the surface, the position and type of defects and the strain at which the defects nucleate are all subject to the state of the surface before deformation. In the case of the nickel surface consisting of regular terraces and steps, the defects form at lower strain compared to the perfectly flat surface, and mirror the regularity of the surface absent in the case of the flat surface.

# Superhydrophilic surface of selectively plasma etched polyphenol composite

**Harinarayanan Puliyalil**[1,2], **Gregor Filipič**[1,2], **Uroš Cvelbar**[1,2]

[1] Department of Surface Engineering and Optoelectronics-F4, Jožef Stefan Institute, Ljubljana, Slovenia

[2] Jožef Stefan International Postgraduate School, Ljubljana, Slovenia

hari.puliyalil@ijs.si

**Abstract.** Surface hydrophilicity is an important property of polymer materials for applications, where we bond or attach other materials to its surface. For tuning the hydrophilicity, plasma treatment has greater advantage over the commonly used chemical treatments, due to its efficiency and localized functionalization with polar or non-polar groups. In this work, we created a superhydrophilic surface of glass filled polyphenol composite by plasma selective etching of the composite matrix. The weakly ionized highly dissociated plasma was generated in oxygen gas at 35 Pa. Due to high concentrations of oxygen atoms in plasma, we achieved high selectivity of etching the polymer, leaving fillers unattached. The systematic studies of surface morphology and composition were performed using X-ray Photoelectron Spectroscopy (XPS) and Scanning Electron Microscopy (SEM) after different exposure times. The surface energy was measured with Water Contact Angle measurements. Whereas plasma etching process was controlled by optical emission spectroscopy. The superhydrophilic surface was achieved after polymer was selectively removed and surface was populated with polar oxygen functional groups after 9 s treatment.

**Keywords**: oxygen plasma, selective etching, superhydrophilicity.

## 1 Introduction

Plasma technology is one of the most rapidly emerging techniques for material processing in polymer technology. The chemical changes on a polymer surface after plasma treatment depend on various discharge parameters as well as nature of gas used for generating plasma [1]. Weakly ionized and highly dissociated oxygen plasma

generated at low pressure has been reported for the functionalization and selective removal of polymer materials from the composite surfaces. The reactive oxygen neutrals inside the plasma can react with atoms of the polymer chain even at room temperature [2]. Oxygen neutrals first physically adsorb to the surface and then chemically react with the atoms from surface layer to form small volatile molecules. During the plasma treatment of multicomponent materials etching rate of various components depends on their chemical stability. Carbon polymers are easier to etch by oxygen plasma than many of the commonly used fillers such as glasses, ceramics, metals or graphite [1,2]. This makes the removal the polymer from the surface selective without affecting the bulk or fillers.

In this work, our aim is to study selective removal of polymer matrix material in order to generate a superhydrophilic surface on the glass fiber filled polyphenol composites with reactive oxygen plasma.

## 2 Materials and methods

### 2.1 Composite preparation

Duroplast from polyphenol containing 60% glass fiber was molded and compressed into sheets under pressure in industrial environment. Samples used for the experiments were of a size 2.2cm×2.2cm×5mm (lbh). .

### 2.2 Plasma treatment

The plasma was created with Dressler CESAR plasma generator in inductively coupled RF discharge. The plasma was generated at 35 Pa with RF power 700 W and frequency of 13.56 MHz. The oxygen gas flow rate, leaked into the system, was maintained at 40 sccm in order to get the density of neutral atoms about $8x10^{21}$ $m^{-3}$. A schematic of the experimental setup is presented in Figure 1. Throughout the treatments, the coil and the reactor chamber were air cooled to prevent overheating or the glass discharge chamber. To prevent overheating, samples were treated in pulses of 3 s. The treated times of each sample are presented in Table 1. Optical emission spectroscopic (OES) measurement was carried out with Avantes AvaSpec-3648 spectrometer.

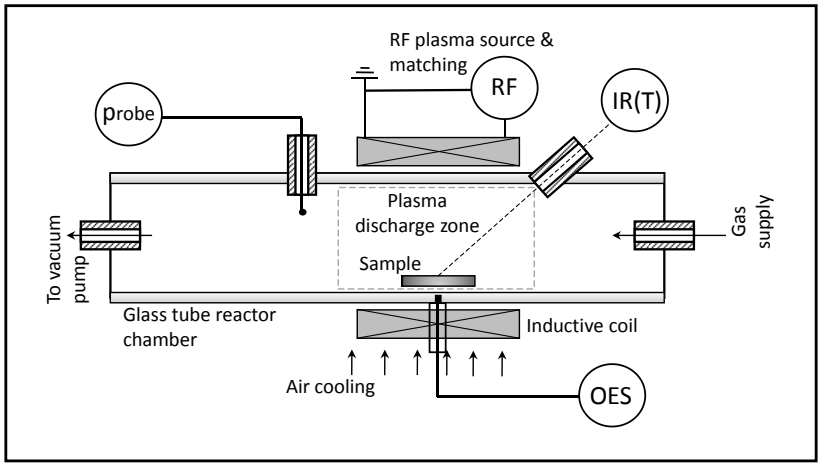


**Figure 1:** Schematic of the plasma system**.**

### 2.3 Surface analyses

The X-ray photoelectron spectroscopy (XPS or ESCA) analyses were carried out on the PHI-TFA XPS spectrometer produced by Physical Electronics Inc. Sample surfaces were excited by X-ray radiation from monochromatic Al source. The samples were also imaged with a field emission scanning electron microscope (FE-SEM) Jeol JSM-7600F with electron beam energy 15kV. Whereas, the surface wettability was measured immediately after plasma treatment by determining the water contact angle (WCA) with a demineralized water droplet. The setup was equipped with a CCD camera, and a computer was used for taking pictures of the water drop on the sample surface.

## 3 Results and discussion

The OES spectra of the oxygen plasma during the treatment times of 6s and 60s are presented in Fig 2. Various spectral features such as: O atom emission lines, hydrogen Balmer series and OH band are typical for water vapor containing oxygen plasmas due to residual gas in the vacuum system. Other spectral features including CO molecules, Na, CN and NH molecules are result from chemical reaction between the residual gas and the composite during etching. The intensity of the peak at 519 nm in the OES spectrum, that corresponds to transitions between the vibrational levels (0→2) of the carbon monoxide Angstrom system $B\,^1\Sigma - A\,^1\Pi$, increases with the treatment time and later decreased, indicates the removal of the polymer from the surface [3]. Disappearance of this peak after prolonged treatment

time pointed out that almost no polymer is present on the surface. On the other hand, the rich OH emission at 309 nm ($A^2\ \Sigma^+$- $X^2\ \Pi$) still persists and probably comes from material degassing. The emission line of Na was recorded at 589 nm and arises from the evaporation of Na species from the glass fiber to the gaseous phase due to increased surface temperature and Na high reactivity. The important oxygen species recorded during our treatments like atomic oxygen indicate the consumption of atoms during etching and how much material remains on the surface [4]. After the etching is done, the emission of O species increase to levels typical for empty reactors.

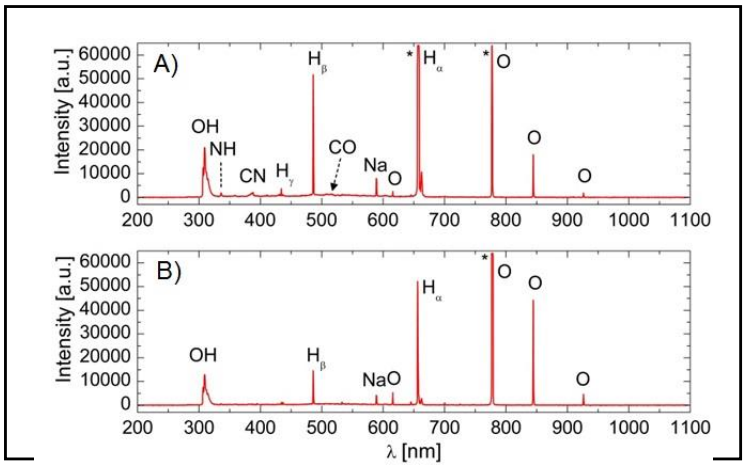


**Figure 2:** OES spectrum for the treatment A) at 6 s B) at 60s.

The morphology changes of the surface were analyzed using SEM presented in Fig. 3. On the untreated sample, the surface is almost covered with polymer and no glass fillings are visible.

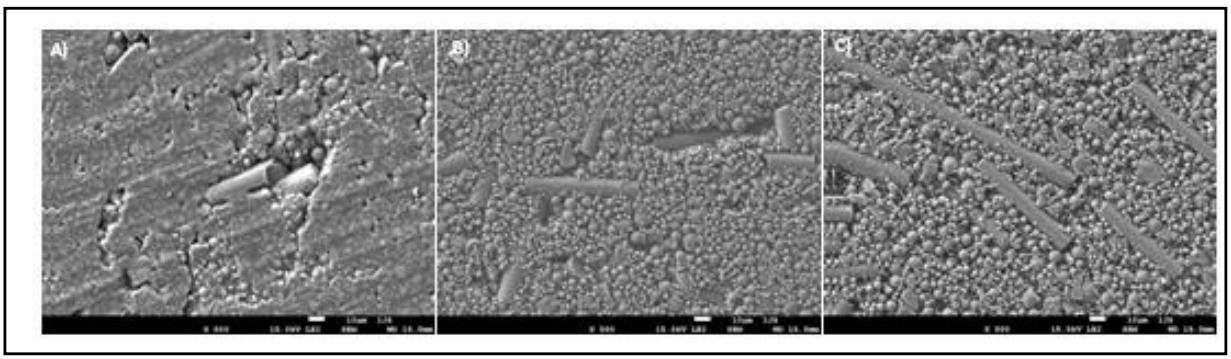

**Figure. 3.** SEM images for various plasma treated samples; A) Non-treated surface, B) treated for 15 s and C) 60 s.

After the treatment, the surface polymer is removed and fillers are exposed. Typically, the polymer disappears from surface after 15 s of plasma treatment, and

the glass balls and fibers are visibly exposed. During the plasma treatments the surface energy is increased and this leads to decrease in the water contact angle. This is a simultaneous effect of functionalization as well as roughening due to etching [5]. Functionalization of the surface increased the oxygen content, as observed by XPS measurements (Fig.4). Percentage of elements including Si, Ca, Na, Mg, etc. increased with the treatment time because of the exposure of the glass fibers on to the surface. Surface roughening is a permanent change, whereas the polar functional groups, including C-O, C=O, O-C=O, etc. tend to move into the bulk of the material or decay with time [5].

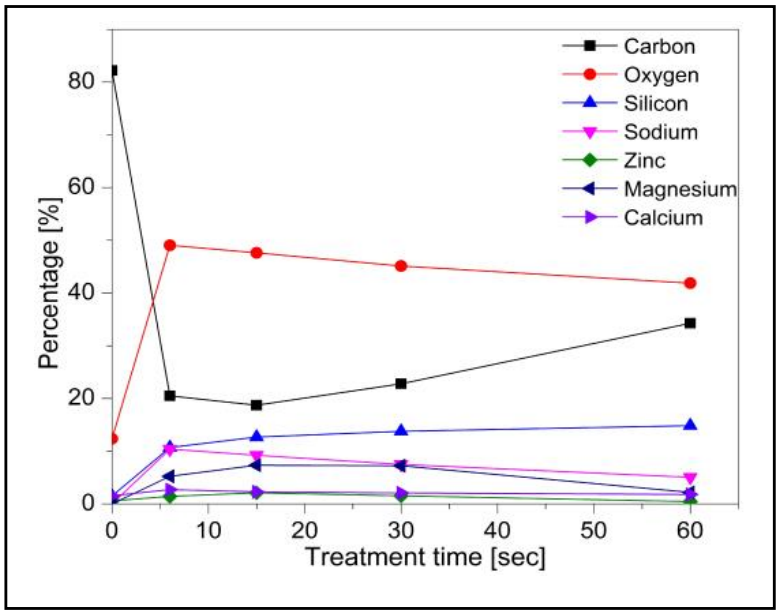


**Figure 4:** XPS measurement for the elemental composition on the surface with treatment time.

The ageing of treated material was studied by measuring the water contact angle for various time intervals (Fig. 5). The surface immediately turned super hydrophilic after treating the surface for 9 s. Due to unstable surfaces this was temporary phenomena, and wettability increased back with ageing time. However in some cases of prolonged treatments, the sample surface demonstrated superhydrophilicity even after longer periods of ageing of 8 days. For the case of 45s and above cumulative surface treatment, the contact angle increased only after 30 days.

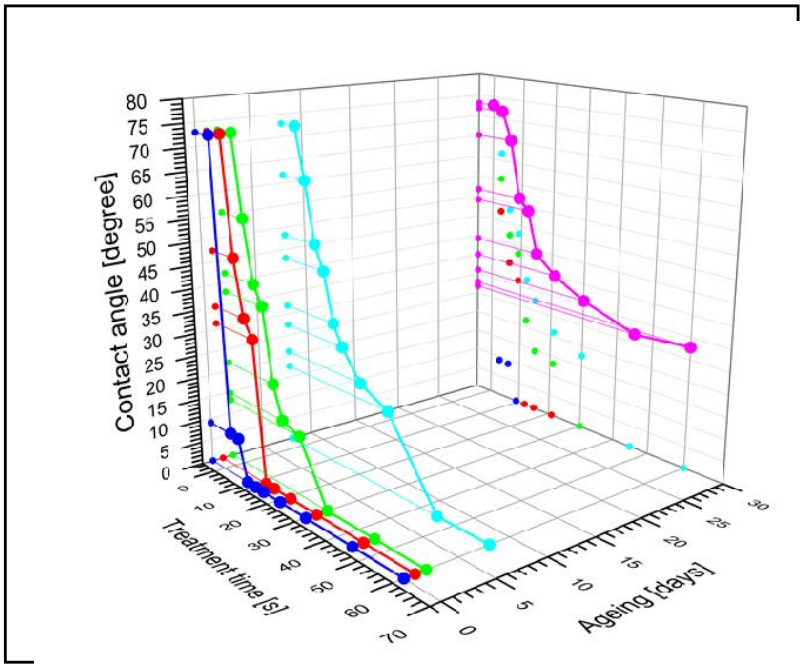


**Figure 5:** Variation of contact angle with treatment time and ageing.

## 4 Conclusions

In this paper, a method for attaining the superhydrophilic surface on the glass filled polyphenolic composite by an oxygen plasma etching was demonstrated. Reactive oxygen neutrals selectively etched the polymer matrix from the surface while keeping the glass fibers intact. The superhydrophilicity phenomena were achieved by the implementation of oxygen polar functional groups and increasing the surface roughness. The surface superhydophilicity was achieved already after 9 s of treatments. The oxygen plasma selective removal of the polymers proves to be a promising technique for the enhancement in the flame resistant properties of polyphenolics, widely used in electrical and thermal insulation applications.

## References:


[1] M. Mozetič, A. Zalar, P. Panjan, M. Bele, S. Pejovnik, R. Grmek. A method of studying carbon particle distribution in paint films. *Thin Solid Films*, 376(1–2):5-8, 2000

[2] M. Kunaver, M. Klanjsek-Gunde, M. Mozetic, M. Kunaver, A. Hrovat. The degree of dispersion of pigments in powder coatings and the origin of some surface defects. *Surface Coatings International Part B: Coatings Transactions*, 86(3):175-179, 2003

[3] E. Vassallo, A. Cremona, F. Ghezzi, D. Ricci. Characterization by optical emission spectroscopy of an oxygen plasma used for improving PET wettability. *Vacuum*, 84(7):902-906, 2010

[4] V. Milosavljević, M. Donegan, P.J. Cullen, D.P. Dowling. Diagnostics of an O2–He RF Atmospheric Plasma Discharge by Spectral Emission. *Journal of the Physical Society of Japan*, 83(1):014501, 2013

[5] B. Tissington, G. Pollard, I.M. Ward. A study of the effects of oxygen plasma treatment on the adhesion behaviour of polyethylene fibres. *Composites Science and Technology*, 44(3):185-19, 1992

## For wider interest

Our work is mainly related to the selective etching of the polymer matrix composites for various applications. Plasma treatment is very efficient for functionalization and etching. By using our techniques, we shall tune the hydrophilicity of surface which helps to improve biocompatibility of various polymer materials for preparing artificial organs, blood vessels, etc. Our current research mainly concentrates to improve the fire resistance and electrical insulation properties of polymer composites by means of selective etching.

# The effect of silica and alumina co-doping on the properties of dental zirconia ceramic

**Anastasia Samodurova**[1,2], **Andraž Kocjan**[2], **Tomaž Kosmač**[2]

[1] Department of Engineering Ceramics, Jožef Stefan Institute, Ljubljana, Slovenia

[2] Jožef Stefan International Postgraduate School, Ljubljana, Slovenia

anastasia.samodurova@ijs.si

**Abstract.** We report on the addition of alumina and silica as dopants to an 3-mol%-yttria-doped tetragonal zirconia (3Y-TZP) ceramic as an effective strategy to significantly decelerate the low temperature degradation (LTD), without any loss of fracture toughness of as-sintered materials. The results of transmission electron microscopy (TEM) and energy dispersive X-ray spectroscopy (EDS) analyses revealed that silica was mainly present as an amorphous phase concentrated at triple grain junctions. Focused ion beam scanning electron microscopy (FIB-SEM) studies of sub-surface region of aged for 24 h samples show substantially smaller transformed layer with lower amount of microcracks in alumina or silica doped 3Y-TZP. At the same time crack-free sub-surface with only 2-3 grains transformed was observed for alumina/silica-doped 3Y-TZP. Results indicate that alumina and silica has different mechanism behind the suppression of LTD and when combined they add-up resistance.

**Keywords**: 3Y-TZP, low temperature degradation.

## 1 Introduction

3-mol%-yttria-doped tetragonal zirconia (3Y-TZP) is an attractive material for biomedical applications due to its excellent biocompatibility, mechanical properties and chemical durability. One of the issues concerning tetragonal (t) zirconia ceramics is their sensitivity to low temperature degradation (LTD), i.e. ageing. [1]. LTD is a slow transformation of metastable t-phase to a more stable monoclinic phase in the presence of moisture at temperatures lower than 400°C. The transformation initiates from surface grains and proceeds into the bulk, resulting in severe microcracking,

grain pull out, and finally surface roughening, which leads to strength degradation [1].

LTD resistance of t-zirconia can be improved by doping with other oxides. In fact, commercial 3Y-TZP powders, such as E-types or TZ-PX-242A from Tosoh contain 0.25 and 0.05 wt% of alumina, which lowers the sintering temperature and improves the aging properties of t-zirconia [2]. It was also reported that the addition of a small amount of silica to Y-TZP improves the aging resistance of t-zirconia [3,4].

By co-doping of 3Y-TZP with alumina and silica, possibly good stability of the t-phase can be achieved. However, to the best of the author's knowledge, no systematic study of the effect of co-doping has been performed so far.

In the present work, the combined effect of silica and alumina on the ageing resistance and mechanical properties of 3Y-TZP ceramics was evaluated. Specimens were prepared by the infiltration silica sol into the pre-sintered porous 3Y-TZP pellets, produced from commercially available powders, containing different amounts of alumina (0, 0.05 and 0.25 wt%). After final sintering ceramic specimens were verified for density, phase composition, mean grain size, fracture toughness and subjected to *in vitro* accelerated ageing. The sub-surface regions of aged samples were also studied using focused ion beam microscopy (FIB/SEM).

The final aim was to improve LTD resistance of 3Y-TZP without affecting the fracture toughness.

## 2 Experimental

Three commercially available, ready-to-press, granulated, biomedical-grade Y-TZP powders (Tosoh, Japan) with different amount of alumina were used for the preparation of specimens: TZ-3YSB-E contains 0.25 wt. % alumina, TZ-PX-242A contains 0.05 wt. % alumina and the TZ-3YB grade is essentially alumina-free. All powders contain 3 mol% yttria in the solid solution to stabilize the tetragonal structure and~3 wt% of an acrylic binder. In the following, the alumina-free ceramic will be referred to as "TZ-3Y" and the ceramics containing 0.05 and 0.25 wt.% of alumina will be referred to as "0.05A-TZ-3Y" and "0.25A-TZ-3Y".

Uni-axial dry pressing at 150 MPa in a floating die was used to shape green disks of 20 mm in diameter and 2 mm in thickness. Afterwards they were pre-sintered in air for 2 h at 900 ˚C (TZ-3Y, 0.05A-TZ-3Y) and 1000 ˚C (0.25A-TZ-3Y). After pre-

sintering specimens of each material were randomly divided into two groups. One group was left untreated and served as a control group. Other group of specimens was infiltrated with silica sol, synthesized in situ by the sol–gel method through hydrolysis of dynasylan (Dynasylan® 6490, Evonik, Germany): specimens were immersed in a mixture of absolute ethanol and dynasylan; the hydrolysis was carried out by dropwise addition of an aqueous ammonia (25%) at room temperature. The concentration of $SiO_2$ in final solution was 0.24 mol/l. Specimens were infiltrated for 1 cycle, soaking for 30 min. Thereafter they were dried and finally sintered at 1450 ˚C for 4 h together with the controls.

The fractional density of sintered disks was determined with Archimedes method using distilled water as the immersion liquid. The relative densities were calculated by adopting a theoretical density of $\varrho_T$ = 6.08 g/cm$^3$. The grain size evaluations were made on FE-SEM (Jeol JSM-7600F, Japan) micrographs of polished (3 μm diamond paste) and thermally etched (1350 ˚C, 1 h) specimens, using the planimetric method. The specimens for the TEM were prepared by cutting 3-mm diameter discs from the ceramic bodies. These discs were reduced to ~120 μm by grinding. A region about 20-μm thick at the centre of the disc was produced using a dimple grinder. Finally, the specimens were thinned by argon-ion erosion at 4 kV with an incident angle of about 10˚.

The indentation technique was used to determine fracture toughness of $SiO_2$-doped and undoped Y-TZP. A load of 30 N was applied to the specimens with a Vickers hardness indenter. Fracture toughness was calculated using the length of the cracks emanating from the Vickers impression [5].

No surface treatment, such as grinding and/or polishing was applied to specimens' surface before *in vitro* ageing experiments. These were conducted in distilled water under isothermal conditions at 134 ˚C for 6–48 h.

X-ray diffraction patterns in the 25–40˚ 2$\theta$ range were collected from the specimen's surfaces before and after accelerated ageing experiments using Cu Kα radiation (Endeavor D4, Bruker AXS). The relative amount of the transformed monoclinic zirconia (m-$ZrO_2$) on all the surfaces was determined from the integral intensities of

the monoclinic $(\bar{1}\ 1\ 1)_m$ and $(1\ 1\ 1)_m$, and the tetragonal $(1\ 0\ 1)_t$ peaks according to the method of Garvie and Nicholson [6], which is the most commonly applied to determine the phase composition of zirconia powders and compacts with randomly distributed m-$ZrO_2$ and t-$ZrO_2$ phases at any distance from the surface exposed to the XRD analysis.

A study of the sub-surface microstructure of aged zirconia ceramics was carried out using FIB/SEM (FEI, Helios Nanolab 650). 0.5 μm thick platinum film was first deposited onto a surface, where the cross section was intended to be made, using ion beam assisted gas injection system at 30 kV and 0.43 nA to protect the area of interest from the formation of extensive curtain effect. The regular cross sections were then made by using the ion beam machining at 30 kV and 65 nA and were finalized by ion polishing at 30 kV and 21 nA. As-prepared cross sections were observed in situ, under an angle of 52°, using the electron probe at 2 kV and 100 pA.

## 3 Results and discussion

The relative densities and the mean of grain size of the pure and alumina- and/or silica-doped sintered samples are listed in Table 1.

This result revealed, that the addition of alumina or/and silica into the 3Y-TZP has negligible effect on density and grain size of material.

The indentation toughness values of pure and silica-doped materials are listed in Table 1. No significant differences in indentation toughness were observed between pure and alumina- or/and silica-doped specimens. These results in agreement with practically the same grain sizes of all grades of materials.

**Table 1:** Relative densities, grain sizes and fracture toughness of sintered for 4 h at 1450°C pure and silica-doped TZ-3Y, 0.05A-TZ-3Y and 0.25A-TZ-3Y materials.

| Sample | Relative densities (%) | Grain sizes (mm) | Indentation toughness, $K_{IC}$ (MPa·m$^{1/2}$) |
|---|---|---|---|
| TZ-3Y | 99.7 | 0.31 ± 0.12 | 4.6 ± 0.2 |
| TZ-3Y/SiO2 | 99.4 | 0.29 ± 0.13 | 4.7 ± 0.1 |

| | | | |
|---|---|---|---|
| 0.05A-TZ-3Y | 99.8 | 0.31 ± 0.13 | 4.7 ± 0.1 |
| 0.05A-TZ-3Y/$SiO_2$ | 99.5 | 0.28 ± 0.12 | 4.7 ± 0.1 |
| 0.25A-TZ-3Y | 99.8 | 0.35 ± 0.13 | 4.9 ± 0.1 |
| 0.25A-TZ-3Y/$SiO_2$ | 99.1 | 0.4 ± 0.15 | 4.6 ± 0.1 |

TEM and EDS analyses of sintered silica-doped 0.05A-TZ-3Y material revealed the presence of amorphous silica phase, which is mainly located in triple grain junctions rather than grain-boundaries (Fig. 1.).

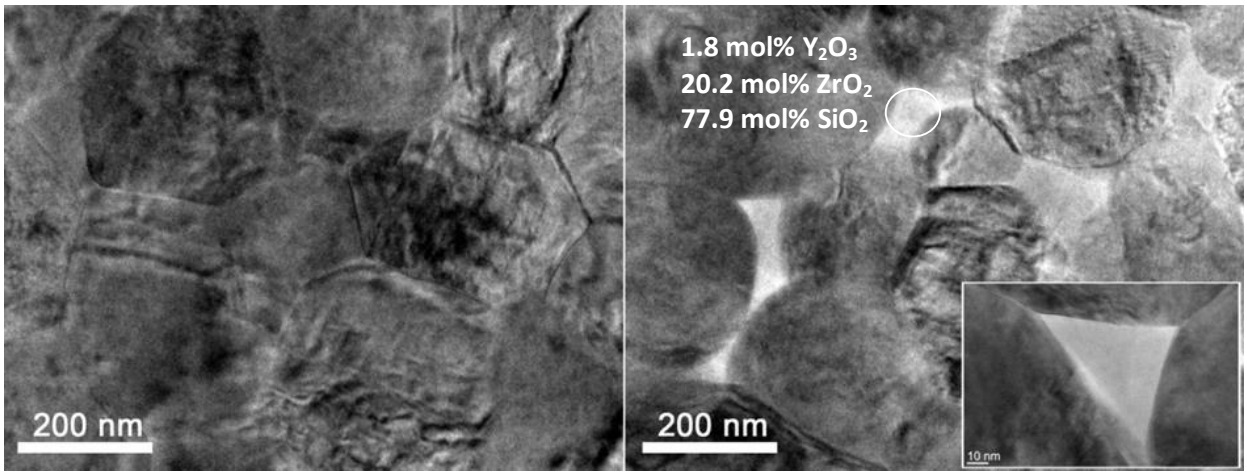


**Figure 1:** TEM micrographs of 0.05A-TZ-3Y(a) and 0.05A-TZ-3Y/$SiO_2$ (b, c) specimens, sintered at 1450 ˚C for 4 h and aged for 24 h.

Characteristic XRD patterns obtained in the 21–36 2$\theta$ range from silica-doped 0.05A-TZ-3Y and TZ-3Y ceramic surfaces sintered for 4 h at 1450 ˚C, before and after accelerated ageing at 134 ˚C in water for different periods of time (6, 12, 24 and 48 h), are represented in Fig. 2a and 2b, respectively. The pattern for as sintered surfaces displays three characteristic peaks positioned at 2$\theta$ of 30.2˚, 34.7˚ and 35.2˚ corresponding to the $(1\ 0\ 1)_t$, $(0\ 0\ 2)_t$ and $(1\ 1\ 0)_t$ planes of the tetragonal zirconia phase, respectively.

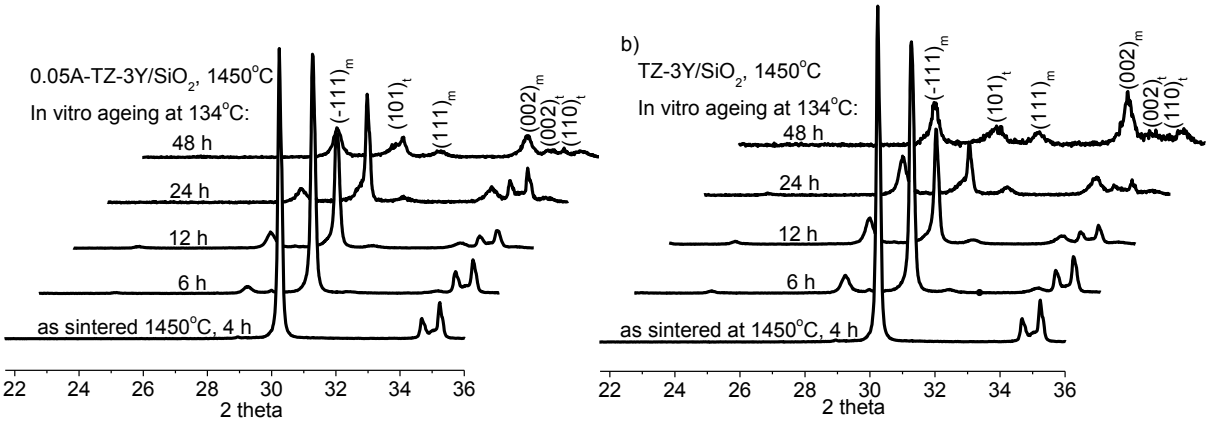


**Figure 2:** XRD patterns obtained from a) 0.05A-TZ-3Y/$SiO_2$ and b) TZ-3Y/$SiO_2$ ceramic surfaces, sintered for 4 h at 1450 ˚C and aged in water at 134 ˚C for 6, 12, 24 and 48 h.

After 6 h of ageing, monoclinic $(\bar{1}\ 1\ 1)_m$, $(1\ 1\ 1)_m$, and $(0\ 0\ 2)_m$ peaks (positioned at $2\theta$ of 28.15˚, 31.3˚, and 34˚, respectively) start emerging with a tendency for their intensity to increase with still longer ageing times at the expense of reduced intensity of the tetragonal $(1\ 0\ 1)_t$, $(0\ 0\ 2)_t$ and $(1\ 1\ 0)_t$ peaks. Notice that the intensity of the monoclinic peaks of the aged 0.05A-TZ-3Y/$SiO_2$ material is considerably lower, compared to the peaks of TZ-3Y/$SiO_2$ material aged for the same time.

The time-dependent variation of the calculated fraction of the monoclinic zirconia for the silica-doped and pure TZ-3Y, 0.05A-TZ-3Y and 0.25A-TZ-3Y materials sintered at 1450 ˚C during *in vitro* ageing is presented in Fig. 3. The rate of *t-m* transformation substantially decreases when either alumina or silica is present in the 3Y-TZP. Notice that the LTD decelerates with an increasing amount of alumina in the initial 3Y-TZP powders. The rate of monoclinic phase nucleation and growth was subsequently decreased, when both silica and alumina were present in the 3Y-TZP.

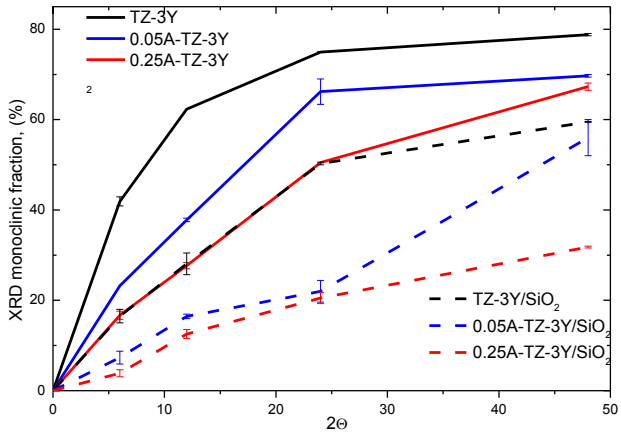


**Figure 3:** Calculated monoclinic fraction versus *in-vitro* ageing time for pure and $SiO_2$-doped TZ-3Y, 0.05A-TZ-3Y and 0.25A-TZ-3Y materials.

The FIB-SEM study of the sub-surface microstructures of 3Y-TZP materials aged for 24 h revealed that the LTD leads to the formation of a transformed surface layer (Fig. 4). The interface between the unaffected and the transformed material shows a well-defined border. Significant amount of intragranular microcracks, running nearly parallel to the surface layer of TZ-3Y material (Fig. 4a), are related to the large shear strains produced by twinning during *t–m* transformation. The measured thickness of transformed layer was ~ 9 μm for TZ-3Y material. The monoclinic layer of alumina- or silica-doped 3Y-TZP has substantially smaller amount of grain-boundary microcracks (Fig. 4b,c), compared to the TZ-3Y material aged under the same conditions. The thickness of the transformed layer was practically the same for the 0.25A/TZ-3Y and TZ-3Y/$SiO_2$ ( ~ 6,5 μm). This result is in agreement with the almost overlapped ageing curves for these materials (Fig. 3). The SEM micrograph of the 0.25A-TZ-3Y/$SiO_2$ material aged for 24 h shows a crack-free sub-surface microstructure with only 3-4 surface grains transformed (Fig. 4d).

The substantial deceleration of LTD by alumina and silica co-doping indicates indicate that alumina and silica has different mechanism behind the suppression of ageing and when combined they add-up resistance. Silica, locating at multiple grain junctions, reduces stresses at grain corners, where the nucleation of LTD usually occurs [7]. Alumina is known to locate at grain boundaries of 3Y-TZP [7] and, most probably, increases the cohesion between grain boundaries, thereby reducing the proneness to microcracking during the LTD [8].

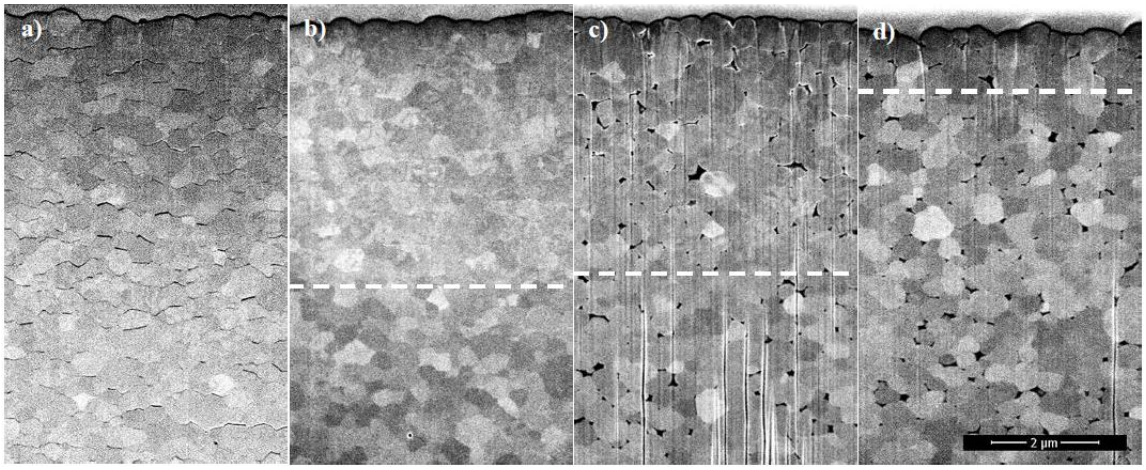


**Figure 4:** FIB-SEM sub-surface microstructures of the TZ-3Y (a), 0.25A-TZ-3Y (b), TZ-3Y/$SiO_2$ (c) and 0.25A-TZ-3Y/$SiO_2$ (d) materials aged for 24 h.

## 4 Conclusions

By alumina and silica co-doping, 3Y-TZP ceramics with round-shaped grain corners and strong cohesion between the grains could be obtained. As modified 3Y-TZP ceramics does not show any significant effect on fracture toughness of 3Y-TZP ceramics. Moreover, these two features of the alumina/silica-doped 3Y-TZP results in a substantial deceleration of the LTD.

## References:

[1] I. Denry, J. Kelly. State of the art of zirconia for dental applications. *Dental materials*, 24:299-307, 2008.

[2] I.M. Ross, W.M. Rainforth, D.W. McComb, A.J. Scott, R. Brydson. The role of trace additions of alumina to yttria-tetragonal zirconia polycrystals (Y-TZP). *Scripta Mater*, 45:653–60, 2001.

[3] L. Gremillard, T. Epicier, J. Chevalier, G. Fantozzi. Microstructural study of silica-doped zirconia ceramics. *Acta mater,* 48:4647-4652, 2000.

[4] T. Nakamura, H. Usami, H. Ohnishio, M. Takeuchit, H. Nishida, T. Sekino and H. Yatani. The effect of adding silica to zirconia to counteract zirconia's tendency to degrade at low temperatures. *Dental Materials Journal,* 30(3):330-335, 2011.

[5] K. Niihara, R. Morena and D. P. H Hasselman, Evaluation of $K_I c$ of brittle solids by the indentation method with low crack-to-indent ratios. *J. Mater. Sci. Lett*, 1:13–16, 1982

[6] R. C. Garvie, P.S. Nicholson. Phase analysis in zirconia systems. *J Am Ceram Soc,* 55:303–305, 1972.

[7] S. Schmauder, H. Schubert. Significance of Internal Stresses for the Martensitic Transformation in Yttria-Stabilized Tetragonal Zirconia Polycrystals During Degradation. *J. Am. Ceram. Soc*., 69:534-540, 1986.

[8] H. Tsubakino, R. Nozato, M. Hamamoto. Effect of alumina addition on the tetragonal-to-monoclinic phase transformation in zirconia-3 mol% yttria. J. Am.Ceram. Soc. 74: 440–443, 1991

## For wider interest

3-mol%-yttria-doped tetragonal zirconia (3Y-TZP) is becoming increasingly popular as an alternative material in restorative dentistry. One of the issues concerning tetragonal Y-TZP ceramics is their sensitivity to low temperature degradation (LTD), i.e. ageing. LTD appears from spontaneous transformation of metastable tetragonal grains to a more stable monoclinic phase in the presence of water or water vapour.

LTD resistance of dental zirconia can be improved by decreasing grain size or increasing the yttria content in the starting powder. Unfortunately, both of these approaches lead to the reduction of the mechanical properties of zirconia, thus making it unattractive for dental applications. Other way to tackle the problem is by adding of dopants.

Our research is focused on the study of the effects of silica and alumina on the phase composition, microstructure, indentation toughness and LTD of the 3Y-TZP ceramics in order to understand, whether ageing resistance can be increased without decreasing mechanical properties. The other goal of work is to understand the mechanism, by which silica and alumina gives rise to increasing ageing resistance of Y-TZP. The understanding of this can helps to explain the mechanism of LTD. In order to reach the desired final properties of tetragonal zirconia ceramics, the mechanism of LTD must be known.

# Kazalo Avtorjev (Index of Authors)


separation
human
activity
PPCPs
data
samples
exist
organic
temperature
provide
compounds
tea
bread
ECO
care
products
results
fate
high
mercury
release
environment
different
materials
chromatographic
columns
fractionation
MoS2
work
stable
presence
enables
Monolithic
information
represent
experiments
ketoprofen
catalytic
applied
years
confirm
spite
run
structure
speciation
follow
low
milk
gas
coal
solid
small
based
useful
monolithic
several
chromatography
50Cr
added
recent
found
soaps
chemical
sites
related
substrates
sunscreen
higher
factors
natural
rate
acid
effects
offer
isotope
reduced
analysis


new
materials
data
work
magnetic
compounds
activity
using
sensor
properties
coding
nanoparticles
applications
sensors
process
based
IPS
high
learning
wireless
network
methods
drug
model
measured
organic
mercury
physical
information
node
temperature
machine
iron
samples
rules
devices
body
models

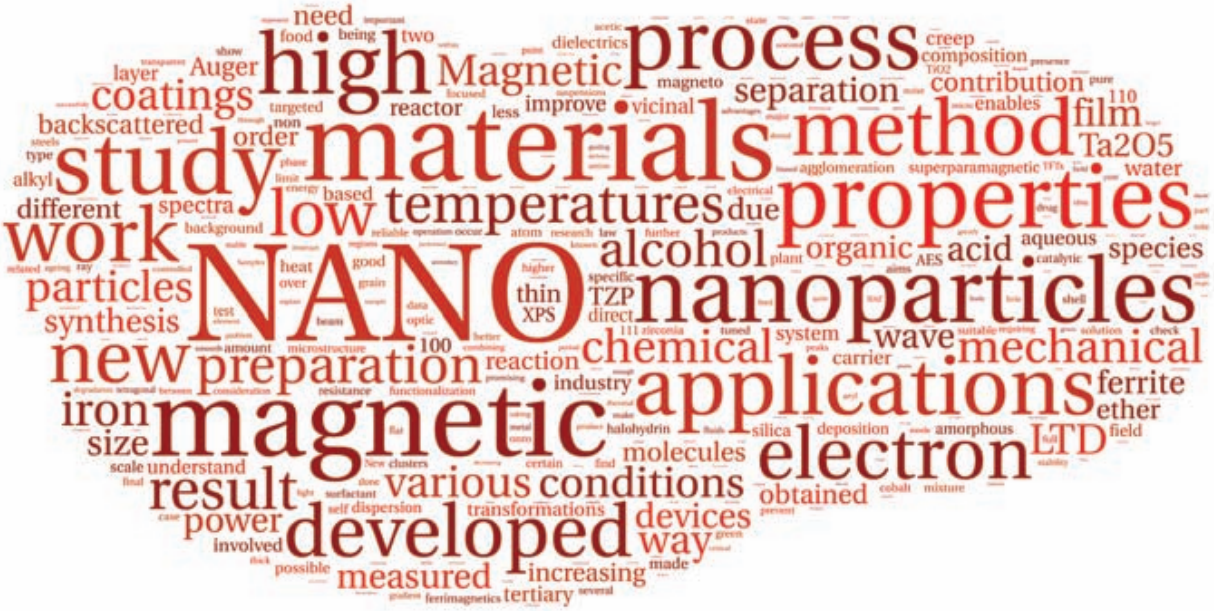
process
high
Magnetic
materials
method
study
NANO
properties
nanoparticles
work
low
temperatures
alcohol
applications
magnetic
electron
new
preparation
chemical
mechanical
developed
coatings
separation
contribution
film
Ta2O5
particles
synthesis
wave
ferrite
ether
LTD
iron
size
result
various
conditions
obtained
power
devices
way
measured
increasing
tertiary
reactor
improve
vicinal
backscattered
order
different
spectra
temperatures
due
organic
acid
aqueous
species
water
thin
XPS
TZP
reaction
carrier
industry
molecules
deposition
amorphous
field
understand
dispersion
transformations
involved
possible
made
need
food
being
two
layer
Auger
dielectrics
creep
composition
magneto
agglomeration
superparamagnetic
enables
110
alkyl
heat
over
good
grain
system
100
111 zirconia
tuned
suitable
requiring
solution
check
peaks
silica
halohydrin
cobalt
mixture
scale
New clusters
certain
find
surfactant
self
case
power
involved
flask
ferrimagnetics
several

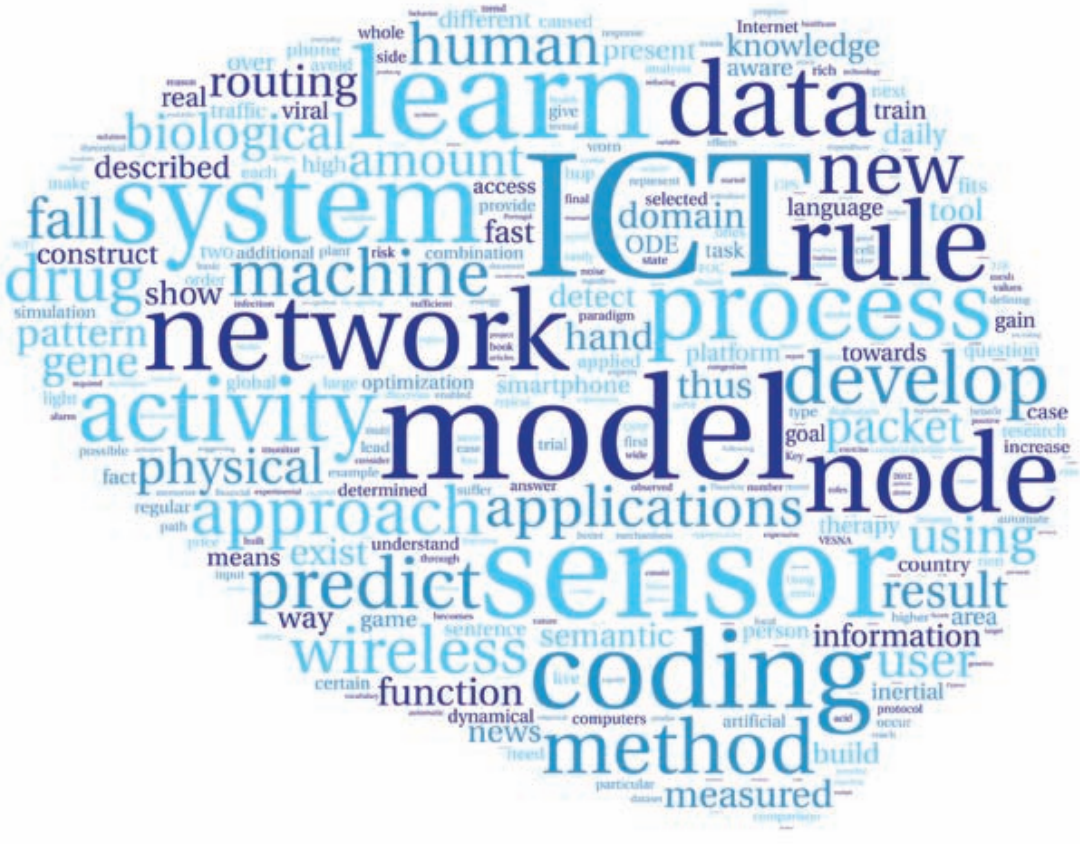
learn
data
human
ICT
Rule
system
network
model
node
process
activity
develop
machine
drug
physical
sensor
predict
coding
wireless
approach
applications
method
routing
biological
amount
fall
new
domain
fast
construct
detect
hand
gene
pattern
smartphone
thus
packet
using
result
function
user
measured
knowledge
present
Internet
aware
described
access
language
tool
ODE
task
show
platform
towards
exist
means
semantic
information
inertial
build
real
viral
traffic
daily
train
whole
side
different
over
avoid
phone
rich
next
selected
combination
optimization
fact
determined
answer
regular
path
understand
through
sentence
person
area
country
game
way
certain
dynamical
computers
artificial
news
protocol
particular
increase
case
goal
trial
lead
therapy
VESNA
automate

**MEDNARODNA PODIPLOMSKA ŠOLA JOŽEFA STEFANA**

***JOŽEF STEFAN INTERNATIONAL POSTGRADUATE SCHOOL***

Jamova 39, SI-1000 Ljubljana

**T** +386 (0)1 477 31 00
**F** +386 (0)1 477 31 10

**E** info@mps.si
www.mps.si

ISBN 978-961-92871-6-3